A stylized, blue-toned illustration of a knee joint. The femur (thigh bone) is at the top, and the tibia (shin bone) is at the bottom. A mechanical implant is visible on the tibia, consisting of a rectangular base with several vertical posts. The joint space is filled with a textured, fibrous material representing cartilage or ligaments. The overall style is clean and modern, using various shades of blue and black.

Diarthrodial joint resurfacing: Multi-scale biofabrication of mechanically stable implants

**Osteochondral tissue regeneration
in the knee joint**

Mylène de Ruijter

**Diarthrodial joint resurfacing: Multi-scale
biofabrication of mechanically stable implants**
Osteochondral tissue regeneration in the knee joint

Mylène de Ruyter

Diarthrodial joint resurfacing: Multi-scale biofabrication of mechanically stable implants
Osteochondral tissue regeneration in the knee joint
PhD Thesis Utrecht University

ISBN: 978-90-393-7348-4

Author: Mylène de Ruijter

Cover design: Mylène de Ruijter and Guus Gijben, Proefschrift All In One (AIO)

Layout and printing: Guus Gijben, Proefschrift All In One (AIO)

The research in this thesis is financially supported by the European Research Council (ERC) under grant agreement 647426 (3D-JOINT) and de Hofvijverkring Fellowship 2019.

Financial support for printing this thesis was kindly provided by the Netherlands Society for Biomaterials and Tissue Engineering (NBTE).

Copyright © M. de Ruijter 2020. All rights reserved. No parts of this thesis may be reproduced, stored in a retrieval system of any nature, or transmitted in any form or by any means, without prior written consent of the author. The copyright of the articles that have been published has been transferred to the respective journals.

Diarthrodial joint resurfacing: Multi-scale biofabrication of mechanically stable implants

Osteochondral tissue regeneration in the knee joint

Vervanging van het articulaire gewrichtsoppervlak: Geavanceerde (bio)fabricatie van mechanisch stabiele knie-implantaten.

(met een samenvatting in het Nederlands)

Proefschrift

ter verkrijging van de graad van doctor aan de
Universiteit Utrecht
op gezag van de
rector magnificus, prof.dr. H.R.B.M. Kummeling,
ingevolge het besluit van het college voor promoties
in het openbaar te verdedigen op

woensdag 9 december 2020 des middags te 2.30 uur

door

Mylène de Ruijter

geboren op 16 augustus 1989
te Heemskerk

Promotor: Prof. dr. ir. J. Malda

Co-promotor: Dr. ir. M. Castilho

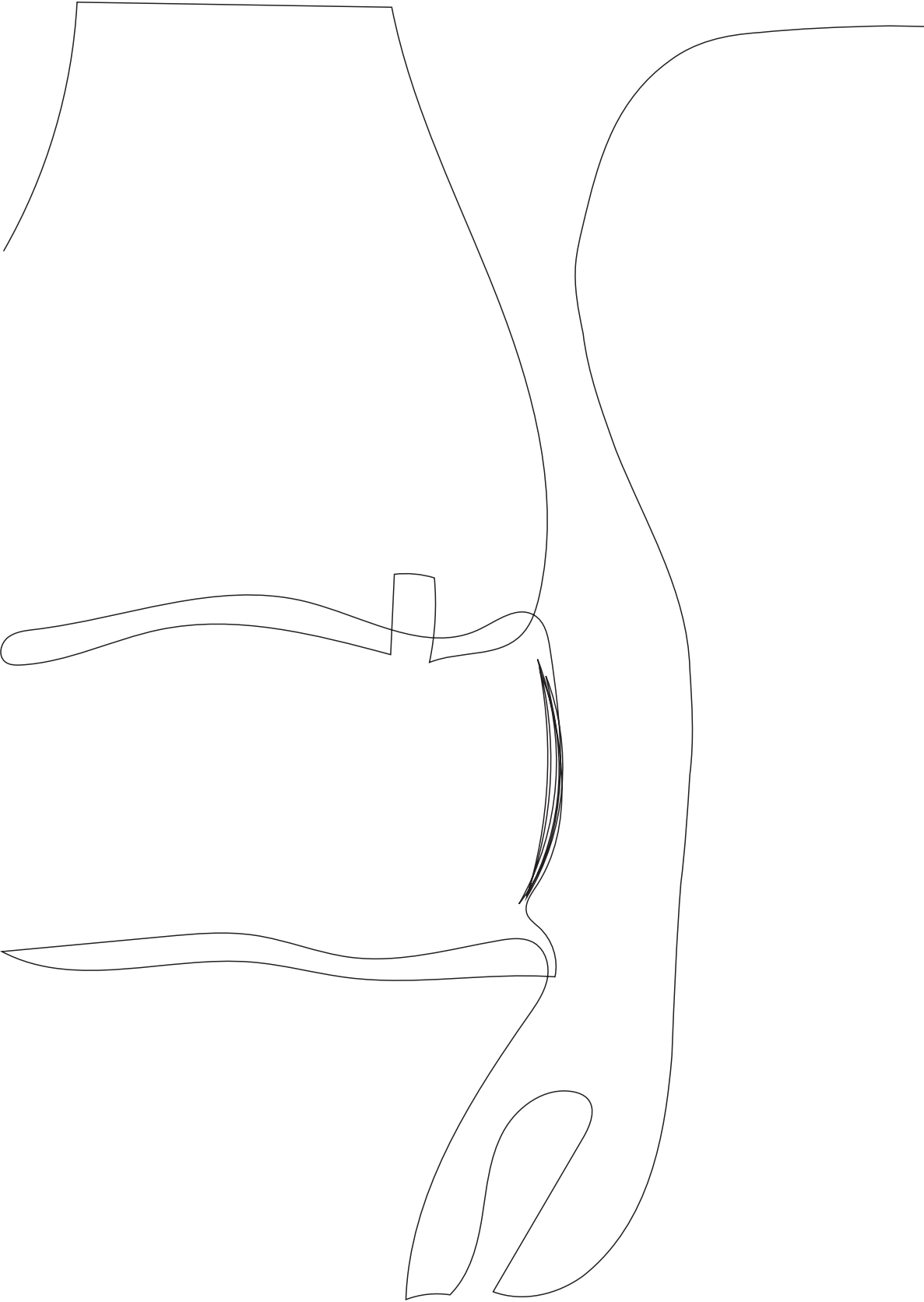
Fear is the mind-killer

- Frank Herbert, Dune (1965)

Table of contents

Chapter1:	General introduction, outline and aim of thesis	9
Part I:	Melt electrowriting to improve the mechanical properties of implants	25
Chapter 2:	Out-of-plane 3D-printed microfibrils improve the shear properties of hydrogel composites	27
Chapter 3:	Combining multi-scale 3D printing technologies to engineer reinforced hydrogel-ceramic interfaces	41
Part II:	Incorporating melt electrowriting in the bioprinting process for multi-scale biofabrication	71
Chapter 4:	Multi-technology biofabrication: a new standard for manufacturing of functional tissues	73
Chapter 5:	Simultaneous Micro-patterning of fibrous meshes and bioinks for the fabrication of living tissue constructs	93
Chapter 6	Melt electrowriting onto anatomically relevant substrates: resurfacing a diarthrodial joint	107

Part III:	Application and <i>in vivo</i> translation of multi-scale biofabrication	131
Chapter 7:	Bone morphogenic protein 9 stimulates efficient cartilage-like matrix production by articular cartilage-resident chondroprogenitor cells onto 3D melt electrowritten scaffolds	133
Chapter 8:	Pivotal importance of reinforcement of cartilage implants confirmed in challenging large animal model; presence of transplanted cells probably secondary	147
Chapter 9:	Scaling up from osteochondral plug to patient-specific condyle resurfacing: 178 fabrication, <i>in vitro</i> and mechanical characterization under physiological conditions of clinically relevant osteochondral implants.	173
Chapter 10:	General discussion	197
	Annexes	211
	- Annex 1	213
	- Annex 2	225
	References	235
	List of Abbreviations	259
	English Summary/Nederlandse Samenvatting	263/267
	Acknowledgements	271
	Publications	283
	Curriculum Vitae	289



Chapter 1

General introduction, outline and aim of thesis

The impact of diarthrodial joint problems

Mobility, autonomy, and physical activity are key aspects in modern society. As the average life expectancy of the population continues to increase, therefore, long-term mobility and the ability to remain physically active is an important healthcare challenge.^{1,2} In turn, physical activity is vital in relation to healthy aging³⁻⁶ and has been proven to positively affect quality of life as it improves both fitness^{7,8} and cognitive^{7,9-11} capabilities. Diarthrodial joints, in particular those of the knee, play a pivotal role in enabling this physical mobility, thus impaired joint movement significantly hampers not only quality, but eventually also life expectancy.¹²⁻¹⁴ The cause of impaired joint movement is multifactorial and includes swelling and pain that can be caused by chondral and osteochondral (OC) defects. Chondral defects present partial thickness or full thickness lesions, where in the latter the lesion protrudes all the way through the cartilage to the subchondral bone plate, which consequently leads to type I collagen-rich scar tissue formation induced by bone marrow cells.¹⁵ Osteochondral defects are lesions that involve the cartilage, as well as the underlying bone. Chondral defects are generally caused by trauma, whereas OC defects can additionally be caused by joint related diseases, such as osteochondritis dissecans, a hereditary disease in which part of the bone starts to separate from the surrounding tissue because of a lack of blood supply.¹⁶ Chondral and OC defects can, if left untreated, increase in size or in severe cases, and especially for OC defects, eventually lead to osteoarthritis (OA), a progressive degenerative joint disease that causes pain, reduces mobility, and decreases the patient's quality of life.¹⁷⁻¹⁹ Furthermore, an increased life expectancy and active life style, together with an increased average bodyweight^{20,21}, contributes to prolonged and intensified loading of the joints. This further increases the risk of chondral and OC defects as well as faster progression and onset of OA.^{22,23}

Chondral and OC defects frequently occur and, in the Netherlands alone, an estimated total of 3000 – 5000 patients per year require surgical treatment for such defects combined.²⁴ Approximately 60% of the patients that undergo arthroscopic surgery because of joint-related complains exhibit chondral or OC defects. Together, these defects occur more frequently in male patients, with an average age of 40 years, and most defects are located at the medial femoral condyle with an average of 2.7 lesions per knee.^{25,26} The severity of chondral and OC damage is dependent on variables such as the location, size, depth, and age of the defect, but also on the alignment of the leg, stability of the knee joint, and status of the meniscus.²⁴ Therefore, treatment of chondral and OC defects can be regarded as a complex challenge that concerns the entire joint.

Articular cartilage: structure and mechanical functioning

In diarthrodial joints, articular cartilage is the white and smooth tissue that covers the ends of long bones to achieve efficient load transfer and to provide frictionless, smooth sliding of the opposing bone structures upon joint movement. Initially, femoral AC was considered a rather simple tissue of about 2 mm thick, that is not innervated nor vascularized and contains only few matrix components. However, more thorough analysis of this tissue elucidated a highly complex, multi-material composition with matrix components of different sizes (multi-scale) and a distinct structure that enables AC to sustain the range of motion patterns and loading conditions that arise from normal movement.^{27,28} Rotational movement in the knee joint is partially restricted by the ligaments, leaving flexion-extension the main motion.²⁹ Joint loading is dependent on a person's bodyweight plus the activity involved, and the main loading conditions include compressive and shear loading.²⁹ Peak axial loading is generally between 8 to 14 times bodyweight during running³⁰, the expected maximum compressive stress in the human knee joint is approximately 6 MPa, and the maximum shear stress due to sliding and subsequent fluid movement is 0,085 MPa.³¹ If an (osteo)chondral defect is treated with an implant, it will therefore be exposed to a mechanically challenging environment of combined compressive and shear loads.

The aforementioned structurally imperative composition and architecture of AC tissue is identified along the distinctive superficial tangential, middle, and deep zone (**Figure 1**). The material composition of AC matrix can roughly be divided into a non-fibrous (*e.g.* cells, proteins, growth factors, enzymes) and a fibrous (*e.g.* type II collagen) component. The cell population in human AC comprises 2 – 5% of the total volume of AC and mainly includes chondrocytes (with a diameter close to 13 μm) and a subpopulation of 0.1 – 1.0 % articular cartilage-resident chondroprogenitor cells (ACPCs), which are mainly present in the superficial tangential zone.³² The overall cell density is highest in the superficial tangential zone and the overall cell morphology ranges from flattened or ellipsoid in the superficial tangential zone to spheroid-shaped, columnar arranged in the intermediate and deep zone (**Figure 1**).^{33–35} A chondrocyte plus its directly surrounding, type VI collagen-rich pericellular matrix is called a chondron, and all that is surrounding the cells and chondrons is considered the extracellular matrix (ECM). Overall, the ECM contains 65 – 80 % water, over 200 different types of proteins³⁶, including ECM modifying enzymes and ECM-binding growth factors.³⁷

Key components of the tissue that contribute to the extreme compressive and shear properties of AC in the non-fibrous ECM are the negatively charged glycosaminoglycans (GAGs). Due to their negative charge, GAGs attract water which subsequently induces an osmotic swelling. This swelling is resisted by the structure of type II collagen, key player in the fibrous part of the ECM.³⁹ Structurally, collagen fibre sheets (Benninghoff arcades⁴⁰) are connected to the subchondral bone, where they provide the interconnection between the AC and bone tissue, and transform from a perpendicular, normal-to-the-articular-surface-orientation in the deep zone, to a parallel-to-the-surface-orientation in the superficial zone.⁴⁰ The type II collagen fibre orientation allows for load distribution throughout the tissue. Type II collagen fibres have a high tensile strength, which not only limits the swelling behaviour initiated by GAGs, but also effectively provides resistance to shear stress at the superficial-tangential region.⁴¹ Once the architecture of AC tissue has been destroyed, the tissue is not able to withstand the mechanical loading conditions, leading to tissue failure.

(Osteo)chondral defects of the knee joint: current treatments

As AC tissue has a low regenerative capacity and does not heal by itself, surgical intervention is needed to repair the damaged tissue, decrease clinical symptoms, and therewith restore joint function.^{42,43} The type of surgical treatment mainly depends on the age and health of the patient (*i.e.*, BMI, and level of activity⁴⁴), the status of the defect (*i.e.*, defect size, location of the defect, and the ICRS grade¹ of the defect), and the condition of the whole joint (*i.e.*, alignment of the leg, patella and biological age of the joint). Chondral defects are treated differently than osteochondral defects. Surgical treatments that are currently available to treat chondral defects include bone marrow stimulation techniques⁴⁵⁻⁴⁷, synthetic, non-resorbable implants^{48,49}, and cartilage-focused cell therapies^{42,50-52}, whereas surgical strategies to treat osteochondral defects include tissue replacement surgeries⁵³⁻⁵⁶ and synthetic, non-resorbable implants^{48,49} (**Table 1**). Fortunately, of the currently used surgical techniques, osteochondral autologous transplantation (OAT) and osteochondral allografting (OAG) do show promising results, as hyaline cartilage is retained and no synthetic non-degradable materials are used.^{56,57} However, specifically for larger OC defects, donor site morbidity (OAT), availability (OAT and OAG), size and fit of the transplants (OAT and OAG) pose significant challenges.⁵⁶

¹ ICRS grade refers to the scoring system as established by the International Cartilage Regeneration & Joint Preservation Society (ICRS). The grade ranges from grade 0 (normal cartilage) to grade 1 (Nearly normal, soft indentations and/or superficial fissures), to grade 2 (abnormal (lesions extending down to < 50% of cartilage depth), to grade 3 (severely abnormal, lesions extend down to > 50% of cartilage depth and down to but not through the subchondral bone) and to grade 4 (severely abnormal with the lesions protruding through the subchondral bone as well).⁴²³

In severe cases, total knee replacement (TKR) surgery is needed. TKR is considered a last resort option to restore patient mobility, as revision surgery is limited and implant survival, especially in younger patients, is low.⁵⁸ It is therefore important to postpone or eliminate TKR.

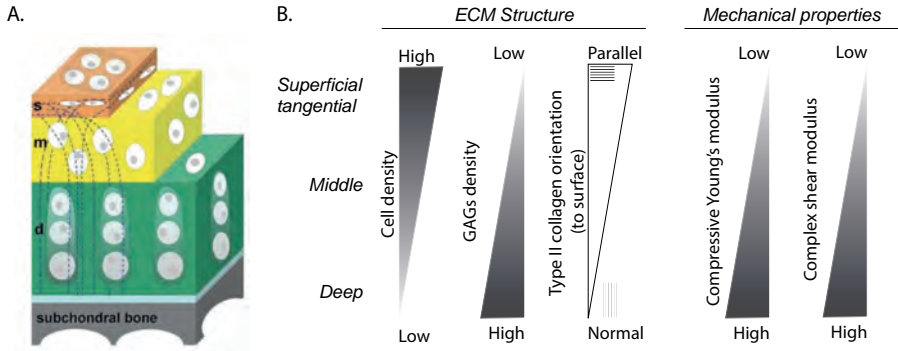


Figure 1. Representation of the zonal architecture of native AC tissue. A) Schematic of the three zones. Adapted from Klein et al. (2009)³⁸ B) Extra cellular matrix (ECM) component distribution and mechanical properties along the superficial tangential, intermediate, and deep zone.

Table 1. Current surgical treatment for chondral and osteochondral defects to eliminate or postpone Total Knee Replacement (TKR) surgery.

Type of lesion	Surgical technique	Advantages	Challenges
Bone marrow stimulation techniques (BST)	Microfracture (MF) ⁴⁵ (< 2 cm ²)	Introducing micro-sized fractures to the bone to introduce bone marrow cells to the cartilage defect area.	Repair tissue is fibrocartilage. ⁶⁰ Mid-term to long-term clinical functionality limited (especially for young and active patients). ⁵⁹
	Autologous matrix induced chondrogenesis (AMIC) ^{46,47} (< 2 cm ²)	Type I/II collagen membrane on top of MF. Chondro-Gide®, BST-Cargel®	More expensive, invasive, and time consuming as compared to MF. Not enough evidence that AMIC > MF or autologous chondrocyte implantation (ACI) ⁶²
Synthetic and metallic implants	Metallic implants (> 2 cm ²)	Partial cartilage resurfacing HemiCAP®, UniCAP®, PF Wave®, PF Wave Kahuna®, Episealer	Non-biodegradable. Low implant survival rate. 20% of patients that underwent partial resurfacing are in need for a TKA within 4 years. ⁴⁹
Chondral cell therapies	1 st and 2 nd generation autologous chondrocyte implantation (ACI) ⁴² (> 2 cm ²)	ACI with periosteal flap (ACI-P), ACI with collagen membrane (ACI-C) ⁶³ , ACI with characterized cells (ACI-CCI) ^{51,64}	No mid- to long-term confirmation of quality of repair tissue as results after 5 years of follow-up differ. ^{51,66,67}
	3 rd generation autologous chondrocyte implantation (> 2 cm ²)	(3D) Matrix assisted ACI (M-ACI) ⁵⁰	Quality of repair tissue similar as to ACI. ⁵⁰ Not available in Europe.
	4 th generation autologous chondrocyte implantation (> 2 cm ² , < 10 cm ²)	3D matrix, including spheroids of chondrocytes. Spherex®	Use of only human material. Arthroscopic surgery. Clinical improvement up to 3 years of follow up. ^{52,70}

2 Western Ontario and McMaster universities osteoarthritis index (WOMAC) score indicates the level of pain, stiffness and functional limitations of the knee and hip joints on a scale from 0 (none) to 4 (extreme).

Tissue replacement surgery	Osteochondral autologous Transplantation (OAT) ^{53,54} (< 2cm ²)	Transplanting osteochondral plugs from less load-bearing parts of the joint to the defect site.	Better short- to long-term clinical outcomes as compared to MF. ⁵⁷ Quick implant stability. 34% of patients show hyaline repair tissue after 1 year. ⁷¹ Arthroscopic surgery.	Limited donor material availability. Donor site morbidity. ⁷² Technical difficulty in mimicking the contours of the defect.
Osteochondral allografting (OAG) ^{55,56} (> 2cm ²)	Transplanting osteochondral plugs from diseased donors	Metabolically active chondrocytes. Hyaline repair tissue. High implant survival rates and good long-term clinical outcomes for younger patients. ⁵⁶	Technical challenge to fit to defect. Limited to non-availability in the EU. Expensive treatment. ⁷³ Risk of limited integration and disease transmission including infections. Conservation of grafts only up to 24-28 days. ⁷⁴	
Synthetic and metallic implants	Synthetic scaffolds (< or > 2cm ²)	Synthetic osteochondral plug. MatioRegen [®] , Agill-C [®] ⁵⁵	Biological, resorbable materials used. No donor site morbidity. Relatively easy surgery. For deep osteochondral defects, some clinical improvement is shown. ⁷⁶	Inconsistency in success of implants. Filling, integration, and quality of repair tissue is varying between fibrous and hyaline cartilage. ^{77,78}

Osteochondral

Regenerative approaches, including aforementioned cell-based surgical treatments, aim to restore and repair native tissue with use of biodegradable materials, generally combined with cells. However, current surgical therapies along this regenerative approach result in sub-optimal healing or fibrous cartilage tissue formation which is composed of more type I collagen fibres compared to hyaline cartilage tissue and therefore only provides limited mechanical resilience, resulting in eventual mechanical failure of the initially repaired defect.¹⁵

An alternative, patient-specific approach can potentially aid in restoring (osteo)chondral defects and postpone or eliminate TKR surgery. Therefore, the overarching aim of this thesis is to provide such an approach by fabricating an osteochondral implant where special attention is given to the mechanical stability of the chondral compartment, while allowing substantial matrix deposition. The individual challenges that arise throughout the search for this solution are specifically highlighted in the boxes at the end of each of the following sections. To start, as the knee joint is a mechanically challenging environment, the first challenge to be tackled is the fabrication of an osteochondral plug with engineered AC tissue that is structurally capable to withstand the mechanical loading conditions upon implantation. This underscores the **structural/mechanical challenge (Box 1)** in the restoration of the AC.

Box 1

Structural/mechanical challenge

To fabricate mechanically stable implants, it is required to address the compressive, as well as the shear properties of the implant. This could be achieved by more closely mimicking the multi-material and multi-scale complexity of the matrix composition and structure, as the structure of AC is essential for the mechanical functioning of the tissue.

(Bio)fabrication: multi-scale AC mimicry and mechanical reinforcement

(Bio)fabrication enables the fabrication of living complex tissue structures (**Intermezzo 1**) and has been proposed to more closely mimic the multi-scale structure of native AC and consequently improve the mechanical properties of cartilage equivalents.^{79,80} Extrusion-based bioprinting is most frequently used to recreate the AC zonal architecture within fabricated implants using cell-laden hydrogels.⁸¹ Said technique generally uses cell-laden hydrogels which have been combined with fibre reinforcing scaffolds that have been fabricated by technologies such as Fused Deposition Modelling (FDM)⁸², Solution ElectroSpinning (SES)⁸³ and melt electrowriting (MEW)^{84,85}, to provide structural integrity to these intrinsically soft hydrogels. Where FDM generally generates thick fibres of 100 – 200 µm in diameter^{82,86}, and SES⁸⁷ results in random fibre deposition, MEW successfully

achieves control over (sub)micro-meter scale fibres.⁸⁸⁻⁹¹ Due to the high control over network fibre architecture, MEW scaffolds have been shown to enhance the compressive properties of hydrogel constructs while providing ample space for cartilage-like matrix production.^{84,92} The working mechanism behind this synergistic reinforcing effect is a combination of strong polymeric fibres that restrict lateral gel expansion⁸⁴ and load carrying ability of the fibre scaffold intersections⁹³ upon axial compressive loading. Although this composite material, fibre reinforcing approach, seems promising, only the compressive and not shear loading is addressed. Additionally, to use these constructs for AC regeneration a two-step cast approach is currently employed. This considerably limits simultaneous control over the non-fibrous and fibrous components of engineered AC and consequently does not result in multi-scale AC mimicry of both the fibrous and non-fibrous ECM components. This illustrates the **challenge in the fabrication (Box 2)** of composite implants for the treatment of (osteo)chondral damage: Multi-scale, high-resolution fabrication has not yet been achieved with the readily available techniques.

Box 2**Fabrication challenge**

To fabricate an (osteo)chondral implant with native tissue mimicry elements, multi-scale fabrication is hypothesized to be key. Multi-scale fabrication can only be achieved by converging multiple biofabrication technologies, preferably into a single fabrication platform.

Diarthrodial joint resurfacing: an *in vivo* translational challenge

To translate the use of advanced biofabrication technologies to the fabrication of patient-specific osteochondral implants, the patient's femoral size and shape has to be considered. Moreover, as chondral and OC damage may affect large proportions of the joint an average of 2.7 lesions per knee therapeutic strategies require resurfacing of large parts of the diarthrodial joint.^{25,26} Thus, a shift from regenerating smaller osteochondral plugs to large, patient-specific, convex and concave surfaces has to be made. This shift gives rise to challenges related to the fabrication process, cell source and cell availability, but also regarding the mechanical survival of these implants. A larger resurfaced area increases the need for implant stability, as insufficient load distribution can potentially lead to mechanical failure, subsequent total joint failure, pain and immobility. Moreover, the adult femoral condyle differs per patient, yet macroscopically shows a convex geometry with an average sagittal radius of 22 to 32 mm⁹⁴ and patient-specific, convex and concave surface irregularities exist. For therapeutic strategies, medical imaging techniques such as magnetic resonance imaging (MRI) and computed tomography (CT) can be used to generate a patient-specific template for an implant based on the healthy contralateral joint.

Intermezzo 1

Additive manufacturing and biofabrication: towards patient-specific solutions

Additive manufacturing (AM) is the process of creating a 3-dimensional (3D) structure by depositing materials in a layer-by-layer fashion, based on a computer-aided-design (CAD) and using computer aided manufacturing (CAM) software and technologies. AM-techniques have been present in the manufacturing industry since the late 20th century, are referred to as “the third industrial revolution”⁴²⁴, and have inspired development in the field of biofabrication. However, not all of these technologies are cell-compatible, and are consequently not applicable to the biofabrication field, as cells need a water-rich environment at a temperature close to body-temperature that also allows for sufficient nutrient and waste exchange.²⁴¹

Biofabrication was pioneered in 2002 with inkjet printing of proteins and bovine endothelial and smooth muscle cells⁴²⁵, evolved to the first *in vivo* laser-assisted printing study in 2010 in mice⁴²⁶, and is as of 2016 defined as “*The automated generation of biologically functional products with structural organization from living cells, bioactive molecules, biomaterials, cell aggregates such as micro-tissues, or hybrid cell-material constructs through bioprinting or bioassembly and subsequent tissue maturation processes.*”²⁴⁰ Biofabrication technologies have evolved rapidly and have been categorized into extrusion-based 3D bioprinting^{80,150}, droplet-based or inkjet printing^{215,319,427}, light or laser-based printing or stereolithography and digital light processing^{172,428,429}, and electrohydrodynamic-based printing.^{89,90} A wide range of subgroups exist such as (microfluidic-assisted) co-axial^{420,430}, multi-material^{182,247,260,376}, and multi-nozzle³⁷⁶ printing. Additionally, convergence of biofabrication technologies with other AM techniques is of key interest to best take advantage of the benefits of these different technologies and therefore achieve higher versatility in the design and properties of 3D (bio)printed constructs. Recently, some exciting developments have been made to increase the size of high-resolution printed constructs while substantially decreasing the printing time by means of volumetric printing.³⁷³

Another important building block of biofabrication research is biomaterial development. As most biofabrication technologies use these versatile materials as cell-carriers, maturation-mechanisms, or bioactive release -mechanisms, (smart) hydrogels with dynamic properties³⁷² can be considered a field of its own. The development and adaptation of these biomaterials, and their ability to be processed using (bio)fabrication techniques has been studied in depth.⁴³¹

The holy grail of using (bio)fabricated tissue equivalents is for patient-specific implantation to repair or replace damaged tissue. However, (bio)fabricated tissue equivalents could also be used for high-throughput screening, as advanced *in vitro* culture models, or as organ-on-a-chip devices to answer fundamental research questions.⁸⁰ Up until now, most biofabrication research has focused on cartilage and bone regeneration, followed by cardiovascular regeneration applications.^{432–434}

Cell-cell communication is key for neocartilage formation in engineered cartilage constructs.⁹⁵ As high cell densities are used for engineered cartilage constructs, resurfacing larger surface areas requires an abundant number of cells. Cell type-specific challenges, such as the limited expansion capacity of chondrocytes and hypertrophic fate of MSCs can both be overcome when using ACPCs. However, expanding ACPCs to higher quantities is

time consuming. Hence, more efficient culture systems should be explored, such as the use of chondrogenic stimulating growth factors (e.g., Bone Morphogenic Protein-9 (BMP-9)⁹⁶) and inducing cell-cell contact by aggregating these cells.⁹⁷ Additionally, the origin (allogeneic or autologous) of the selected cell source with respect to an adverse immune response is important to enable safe clinical translation.^{98,99}

Mimicry of patient-specific condyle geometries, and upscaling from small osteochondral plugs to larger joint resurfacing gives rise to **translational challenges** both in fabrication aspects as well as cell source and availability (**Box 3**).

Box 3

Translational challenge

Translating (bio)fabricated (osteo)chondral plugs to a potential therapeutic solution for (osteo)chondral defects includes challenges regarding cell source and cell availability, together with the ability to induce (stem)cell differentiation and production and maturation of neo-tissue. Once translating from smaller (osteo)chondral plugs towards larger personalized implants, the translational challenge also includes adapting current technologies to resurface the complexity of the patient-specific geometry of the joint.

Aim and outline of this thesis

Current surgical therapies are sub-optimal for articular cartilage repair as mechanically inferior fibrous repair tissue is formed and a patient-specific fit of the implants is challenging. It is envisioned that biofabrication technologies may provide a solution by generating osteochondral implants that are inspired by native tissue architecture. As described above, the challenges that arise while aiming to use (bio)fabrication technologies to fabricate (osteo)chondral implants are structural/mechanical, fabrication, and translational in nature, with implant stability and patient-specific fit as shared core challenges (**Figure 2**). More specifically, the compressive and shear properties of cell-laden hydrogels for cartilage repair, as well as their fixation to the underlying bone have to be sufficiently stable to restore the mechanical environment, which is imperative for the success of osteochondral implants.¹⁰⁰ Additionally, convergence of (bio)fabrication technologies is required to aid multi-scale fabrication and further help mimicking the native tissue composition and architecture. Lastly, the step towards generating patient-specific implants and selecting a cell source that efficiently produces large quantities of cartilage-like tissue is imperative. These challenges regarding diarthrodial resurfacing will be addressed along the following main and specific aims.

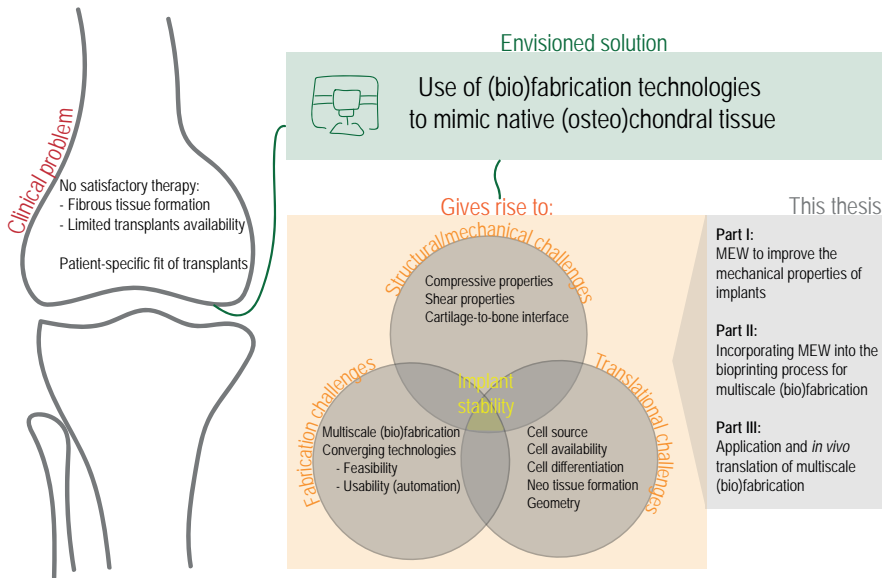


Figure 2. Schematic representation of the clinical problem and the envisioned solution of using (bio) fabrication technologies (Box 3) to mimic osteochondral transplants. The structural/mechanical, fabrication, and translational challenges that arise when developing this solution share the core challenge of implant stability. These challenges are addressed in part I, II, and II of this thesis.

Main aim

To fabricate a functional (osteo)chondral implant, inspired by native tissue composition and architecture and made from biodegradable materials, by combining 3D (bio) fabrication technologies.

Specific aims

- Improve mechanical properties (i.e., shear, and compression) of engineered cartilage- and osteochondral tissue equivalents, including the cartilage-to-bone-interface, using melt electrowriting (MEW) as a technology to produce fibre reinforced hydrogel constructs.
- Converge MEW into the extrusion-based 3D bioprinting technology to achieve control over fibre deposition and cellular distribution.
- Generate multi-scale osteochondral implants of anatomically relevant shapes and sizes.
- Evaluate multi-scale biofabricated implants in a relevant *in vivo* model.

Outline of this thesis

To fabricate a mechanically stable osteochondral implant, the architecture of the native tissue is used as inspiration, as it is known that nature has remarkably efficient ways to deal with the tremendous loading that articular cartilage is subjected to. With state-of-the-art (bio)fabrication technologies, a plethora of biomaterials can be processed. Also, the spatial resolution that is seen in nature can be more closely equalled.

Part I of this thesis focusses on how one (bio)fabrication technology, MEW, can be used to produce scaffolds that enable mechanical reinforcement of (cell-laden) hydrogel constructs. MEW fibre scaffolds have been shown to increase the compressive properties of (cell-laden) hydrogel constructs. However, the potential of MEW to produce specific scaffold designs to enhance other mechanical properties such as the shear modulus and the interfacial strength between the cartilage-and-bone interface, are yet to be investigated.

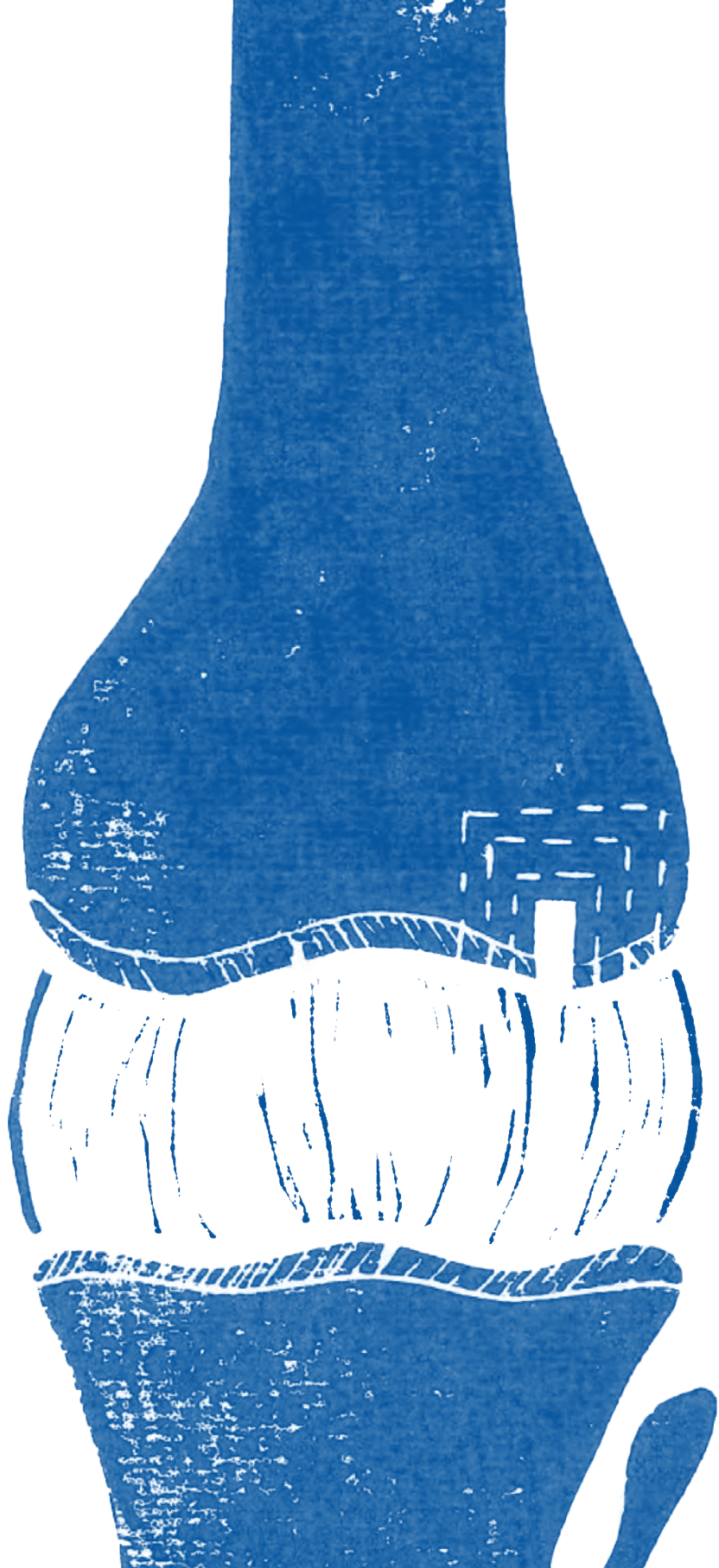
Chapter 2 shows how MEW can be used to print fibres that are out-of-plane by design and are subsequently used to improve the shear modulus of hydrogel constructs. Furthermore, in **Chapter 3**, MEW fibres are combined with extrusion-based ceramic printing (EBCP) to improve the strength of the interface between the cartilage and bone component of osteochondral tissue equivalents.

As part I demonstrates the potential of MEW for improving the mechanical properties of engineered, biodegradable, cartilage and osteochondral tissue equivalents, **part II** of this thesis focuses on how to incorporate MEW in the bioprinting process to create multi-scale constructs and enable control over both fibre deposition and cellular distribution in a single-step fabrication approach. First, **Chapter 4** reviews the opportunities and challenges of multi-scale biofabrication, including implant digital design strategies, as well as artificial intelligence to improve the efficiency of named technologies. Second, **Chapter 5** demonstrates successful incorporation of MEW into the extrusion based (cell-laden) hydrogel printing process and investigates the effect of this incorporation on cell viability and chondrogenic differentiation capacity. Third, the potential of the developed hybrid printing technology is demonstrated for the fabrication of anatomically relevant geometries and materials in **Chapter 6**. Key printing parameters and the effect of frequently used biomaterials on fibre deposition accuracy are investigated.

Based on the key aspects and technological developments that are demonstrated in part I and part II of this thesis, **part III** addresses the translation of multi-scale bioprinting and presents *in vivo* evaluation of bioprinted, multi-scale implants. One of the major

challenges in upscaling and clinical translation of engineered constructs is cell source and availability. Therefore, **Chapter 7** demonstrates efficient chondrogenic matrix deposition through the use of BMP9 as a growth factor. In **Chapter 8**, multi-scale osteochondral implants undergo long-term evaluation in a large *in vivo* model (equine). Here, mechanical stability of biodegradable osteochondral implants is achieved for the first time. **Chapter 9** concludes the experimental work of thesis by applying the developments achieved throughout previous chapters in a large-scale, converged biofabrication approach to resurface the diarthrodial knee joint of an ovine.

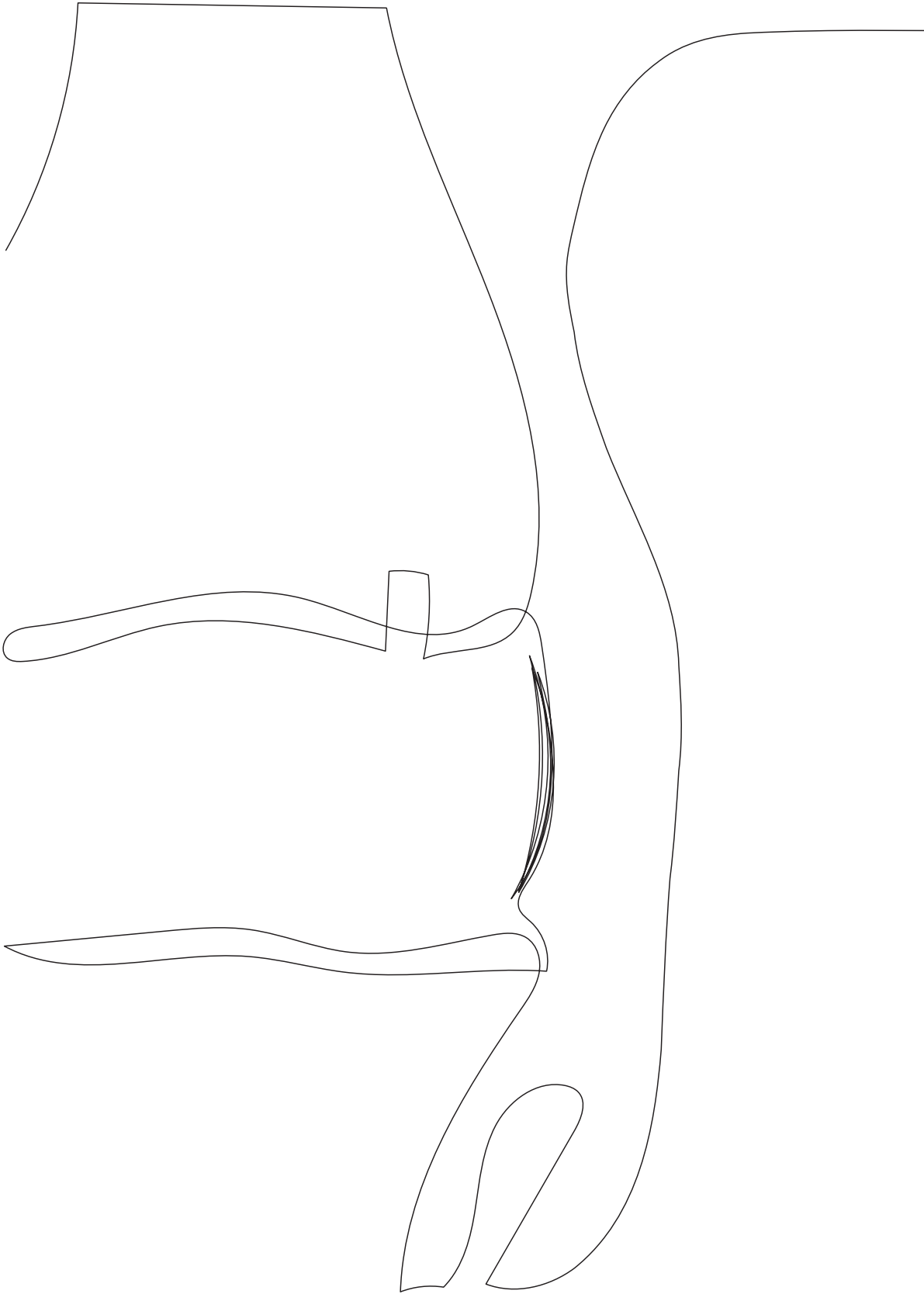
The overarching key findings of this thesis are discussed in **Chapter 10** and includes future directions to further improve diarthrodial joint resurfacing for the treatment of (osteo)chondral defects.

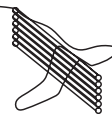


Part I



Melt electrowriting to improve the mechanical properties of osteochondral implants





Chapter 2

Out-of-plane 3D-Printed Microfibres Improve the Shear Properties of Hydrogel Composites

Mylène de Ruijter¹
Andrei Hrynevich²
Jodie N. Haigh²
Gernot Hochleitner²
Miguel Castilho^{1,3}
Jürgen Groll²
Jos Malda^{1,4}
Paul D. Dalton²

Published in Small (2017)
DOI: 10.1002/smll.201702773

¹Department of Orthopaedics, Regenerative Medicine Utrecht, UMC Utrecht, University of Utrecht, The Netherlands

²Department of Functional Materials in Medicine and Dentistry and Bavarian Polymer Institute, University Hospital of Würzburg, Germany

³Department of Biomedical Engineering, Eindhoven University of Technology, The Netherlands

⁴Department of Clinical Sciences, Faculty of Veterinary Medicine, Utrecht University, The Netherlands.

Abstract

One challenge in biofabrication is to fabricate a matrix that is soft enough to elicit optimal cell behaviour while possessing the strength required to withstand the mechanical load that the matrix is subjected to once implanted in the body. Here, melt electrowriting (MEW) is used for the first time to direct-write poly(ϵ -caprolactone) (PCL) fibres “out-of-plane” by design. These out-of-plane fibres are specifically intended to stabilize an existing structure in x, y and z-directions and subsequently improve the shear modulus of hydrogel-fibre composites. The stabilizing fibres (diameter = $13.3 \pm 0.3 \mu\text{m}$) are sinusoidally direct-written over an existing MEW wall-like structure ($330 \mu\text{m}$ height) using a programmed amplitude of $500 \mu\text{m}$, wavelength of $400 \mu\text{m}$, and collector velocity of 400 mm/min . The printed constructs are embedded in different hydrogels (5, 10, and 15 wt.% polyacrylamide; 65% poly(2-hydroxyethyl methacrylate) (pHEMA) and a frequency sweep test ($0.05 - 500 \text{ rad/s}$, 0.01% strain, $n = 5$) was performed to measure the complex shear modulus within the linear viscoelastic range. For the rheological measurements, stabilizing fibres are deposited with a radial-architecture prior to embedding to correspond to the direction of the stabilizing fibres with the loading of the rheometer. Stabilizing fibres increase the complex shear modulus irrespective of the percentage of gel, or crosslinking density. The capacity of MEW to produce well-defined out-of-plane fibres and the ability to increase the shear properties of fibre-reinforced hydrogel composites is highlighted.



Introduction

Melt electrowriting (MEW) is an additive manufacturing technique that direct-writes ultra-fine fibres onto a surface using molten fluid columns that are stabilized with an applied voltage^{89,91,101}. The process is different to polymer melt¹⁰², hydrogel¹⁰³, and colloidal ink^{104,105} extrusion through nozzles which all operate with direct-contact deposition for each layer. In this study, the electrified molten jet is periodically written back and forth across a wall-like structure with remarkable consistency, with minimal variation in structural dimensions. When embedded within a hydrogel, these “out-of-plane fibres” distinctly increase the shear modulus of the composite, even though they partake in a small fraction of the total composite volume. Previously MEW has been used for “in-plane” printing, meaning that the fibre is aligned along a single plane for cartesian coordinates⁹¹, or a single curvature for rotating collectors.¹⁰⁶ The technique is capable of producing micron-scale diameter fibres, ranging from 45 μm ⁹¹ to as small as 820 nm⁸⁸. In addition, MEW results in a narrow fibre diameter distribution (3 - 5% coefficient of variation), emphasizing the reproducibility of this technique.¹⁰⁷ The accurate and reproducible fibre deposition is a crucial characteristic for the use of such a technology in biomedicine, filtration, and energy applications.¹⁰⁸⁻¹¹²

The mechanical advantage of accurate control over fibre placement was shown in a recent study, where a weak hydrogel matrix was reinforced with either small-diameter MEW (2–7 vol.%) fibres or with thicker (16 vol.%) fused deposition modelling (FDM) fibres.⁸⁴ The MEW-reinforced constructs were able to recapitulate the compressive properties of native articular cartilage, whereas the FDM fibres-containing structures were significantly stiffer than the native tissue and failed at comparatively low deformations (less than 10% strain).⁸⁴ The implications for tissue engineering (TE) applications is that such fibre/hydrogel composites enable the use of a mechanically weak hydrogel for cell differentiation and matrix formation, while still providing a structural support required for high compressive loading conditions.¹¹³

Other methods to reinforce hydrogels include using random solution electrospun meshes⁸³, interpenetrating polymer networks¹¹⁴, or the inclusion of carbon nanofibre tubes¹¹⁵. However, the restricted control over the fibre meshes architectures limits their reinforcing potential of soft hydrogels by such meshes. MEW is distinct from these approaches as it allows for fibre placement control with highly organized architecture that synergistically reinforces hydrogels in compression.^{84,116} Control over design in reinforcing techniques is also shown with FDM and extrusion based bioprinting for PCL-based and hydrogel-based reinforcement, respectively.^{82,84} Nonetheless, the accuracy and fibre resolution limits of such extrusion-based fabrication methods hinders the reinforcing potential. Extrusion direct writing is also associated to a high volume fraction of reinforcing materials than in

turn potentially results in stress shielding that can compromise a favourable mechano-regulated environment for the cells to differentiate and excrete extracellular matrix.¹¹⁷ The reinforcement with “woodpile” MEW fibres showed promising results with regards to the resistance to compressing forces⁸⁴, however, it did not address the interplay of compressive, shear, and tensile stresses that tissues in the human body are subjected to. Therefore, to generate hydrogel-based constructs for the replacement of damaged tissues, additional scaffold design elements for fibre-reinforcement are required.

Materials and Methods

Materials


For all experiments PCL (PURASORB PC 12, Lot# 1412000249, 03/2015, Corbion Inc., Gorinchem, Netherlands) was used for MEW. The PCL was stored and retrieved using procedures previously outlined.¹⁰⁷ In order to erase previous thermal history before first use, the polymer was heated to 90 °C for 30 minutes, cooled down to room temperature, and heated up to 90 °C again. After this, each PCL sample was used for a maximum period of 100 h to avoid degradation of the polymer.

MEW Device

A custom-built MEW device that included high precision x-y-z linear axes (Aerotech Inc., Pittsburgh, USA) with a reported resolution of 1 µm was used. The opposed aluminium collector plate was grounded and moved in X- and Y-direction via PRO115-05MM-150-UF positioning stage while the nozzle was moved in the Z-direction via an ATS03005 stage. The axes were controlled via G-code, using A3200 Motion Composer (A3200, version 4.09.000.0126, Aerotech Inc., Pittsburgh, USA). A precision pressure control valve, (FESTO, Berkheim, Germany) was operated with nitrogen gas for pushing the melt to the nozzle. The PCL pellets were heated in a glass syringe (3mL FORTUNA OPTIMA Luer Lock Tip, Poulten & Graf GmbH, Wertheim, Germany) with an electrical heating element connected to a PID controller (cTRON, JMMO, Metz Cedex, France). A metal flat-tipped nozzle (25G, Unimed Switzerland) was heated separately from the glass syringe and connected to a high voltage source (HCP 14-20000 Power supply, FuG Electronic GmbH, Schechen, Germany).

MEW Fibre Collection

Fibres were direct-written onto uncoated microscope slides (ECN 631-1552, VWR international GmbH, Germany). In a first step, a wall of sequentially layered PCL fibres was printed with 20 layers to reach a height of approximately 265 µm (set temperature = 90 °C, applied voltage = 6.0 kV, feeding pressure = 2.0 bar, collector velocity = 900 mm/min, collector distance = 3 mm). In a second step a crossing fibre was deposited over this



wall, while the collector velocity (200 – 1200 mm/min), amplitude (20 – 1000 μm) and wavelength (100 – 3200 μm) were varied. To assess the influence of these crossing fibres on the shear properties of composites, MEW structures were printed in a radial manner to accommodate the loading direction of the rheometer. Afterwards they were embedded into the different hydrogels. A variety of stabilizing architectures was tested. The control samples include a hydrogel only and one with walls only and no crossing fibres.

Visualization

Images were obtained using scanning electron microscopy (SEM) (Zeiss CB 340, Carl Zeiss Microscopy GmbH, Göttingen, Germany), accelerating voltage = 2.0 kV. Prior to imaging, samples were coated with platinum (approximately 2 nm thick) (EM ACE600, Leica, Germany).

Embedding samples in hydrogel composites

PCL scaffolds were embedded in 5 %, 10 %, and 15 % polyacrylamide, as well as in 15 % PG-ACR-DTT and PHEMA. For the polyacrylamide, a 30 % acrylamide + bis-acrylamide solution (37.5:1 ratio, BIO-RAD) was diluted in PBS and polymerized using 0.5 % ammonium persulfate (APS, 10 % w/v solution, Sigma Aldrich) as initiator and 0.05 % N,N,N',N' Tetramethylethylenediamine (TEMED, Sigma Aldrich) as a catalyst. To test the effect of the mesh size, acrylamide powder (BIO-RAD) and bis-acrylamide powder (Sigma Aldrich) were diluted in PBS and polymerized with APS and TEMED. A solution of 65 % 2-hydroxyethyl methacrylate (Sigma Aldrich) and 35 % deionized water was polymerized using 0.5 % ammonium persulfate (APS) (Sigma Aldrich) as an initiator and 0.5 % TEMED a catalyst. All percentages are stated in wt.% of the total volume. The hydrogel-fibre composites were all 26 mm in diameter and 1 mm in height.

Shear testing

The complex shear modulus of the hydrogel composites ($n = 5$) was measured via oscillatory rheometry (plate-plate, diameter = 25 mm, gap = 1 mm) (Physica MCR301, Anton Paar GmbH, Baden-Württemberg, Germany). A frequency sweep was performed (0.05 – 500 rad/s, 0.01 % strain) within the linear viscoelastic range, and the complex shear modulus at 10 rad/s was measured. Prior to testing, (physical) contact between plate and sample was ensured by applying a pre-load of 5 % compression.

Statistics

An ANOVA, post hoc Bonferroni was used to test the difference between the groups. For the quantitative span measurements, $n = 3$ and 10 lines per sample were measured and $n = 5$ for the shear measurements. A difference was determined to be significant when $p < 0.05$, while data is presented as mean \pm standard deviation.

Results and Discussion

The effect of introducing a fibre that crosses through a layered MEW structure (described herein as a “wall”) is quantitatively explored, using out-of-plane deposition. Such crossing fibres (described herein as “stabilizing fibres”) are fabricated to stabilize the wall under shear forces when embedded in a hydrogel. To accurately evaluate the shear properties, the fibre/hydrogel composite samples were designed for analysis with a rotational shear rheometer. An understanding of the basic requirements for improving the resistance to shear stresses is investigated prior to enable these elements to be combined into physiologically relevant fibre/matrix composites for TE applications. The unit structure for a stabilizing fibre is shown in **Figure 1A** and has a specific wavelength, amplitude and fibre span. Scanning electron microscopy (SEM) revealed that the out-of-plane MEW fibre contains very defined and reproducible features (**Figure 1B**). This reproducibility was emphasized by the outcomes of the quantitative SEM analysis (**Figure 1C**) that revealed that the span of the ascending ($114.02 \pm 5.98 \mu\text{m}$) and descending fibre ($151.24 \pm 6.69 \mu\text{m}$) was significantly different ($p < 0.05$) from each other, and increased with an increase of the wall height. Unlike for extrusion direct-writing, for MEW the high voltage applied between the nozzle and collector affects accurate fibre deposition, particularly when existing structures are present on the collector. This includes previously deposited MEW fibres (*i.e.* the wall), which can consequently attract (or repulse) the subsequently deposited layer, depending on the polymer composition.^{91,107,118,119}

The fibre diameter for both the wall and stabilizing fibres was $13.3 \pm 0.3 \mu\text{m}$. Nevertheless, the collector movement amplitude and wavelength, the collector velocity, and height of the wall, all affect morphology of the stabilizing fibres. Optimal stabilizing fibre morphology included fibres that cross the wall in a straight manner (*i.e.* without being deflected or overlapping) and were created with a collector movement amplitude of $500 \mu\text{m}$, wavelength of $400 \mu\text{m}$, collector velocity of 400 mm/min , at a wall height of 20 layers ($265 \mu\text{m}$). When the amplitude was decreased to the lower limit of $200 \mu\text{m}$, stabilizing fibres only minimally spanned the wall to the collector, and often adhered to the side of the wall (**Figure 1D**). When increasing this amplitude to $1000 \mu\text{m}$, the span remained constant while the length of the fibre that adheres to the collector increased (**Supplementary Figure S1A**). Fibres that were deposited with a small wavelength resulted in stabilizing fibres that intersected already deposited stabilizing fibres (**Figure 1E**). Increasing the wavelength decreased both the span and the total length of the fibre (**Supplementary Figure S1B**).

It is important to note that the electrified molten jet for MEW deposits onto the collector in a similar manner to non-charged viscoelastic fluids.^{107,120–122} To deposit linear fibres, the

collector speed must at least match the speed of the electrified jet. The speed at which the electrified jet and collector match has been previously termed the critical translation speed (CTS).^{91,107,123} When depositing stabilizing fibres with a velocity below the CTS, an irregular pattern was clearly observed and the fibres buckled and collapsed onto the wall (**Figure 1F**). An increase in collector velocity did not affect the span of the stabilizing fibre (**Figure S1D**), however, it did decrease the total length of the stabilizing fibre, due to writing with a viscoelastic fluid. A clear increase in span was observed when the wall-height was increased (**Figure 1G, 1C**). However, an upper limit of 20 layers (265 μm) was found with the selected parameters since stabilizing fibres started to adhere to the wall at a wall-height of 25 layers (330 μm).

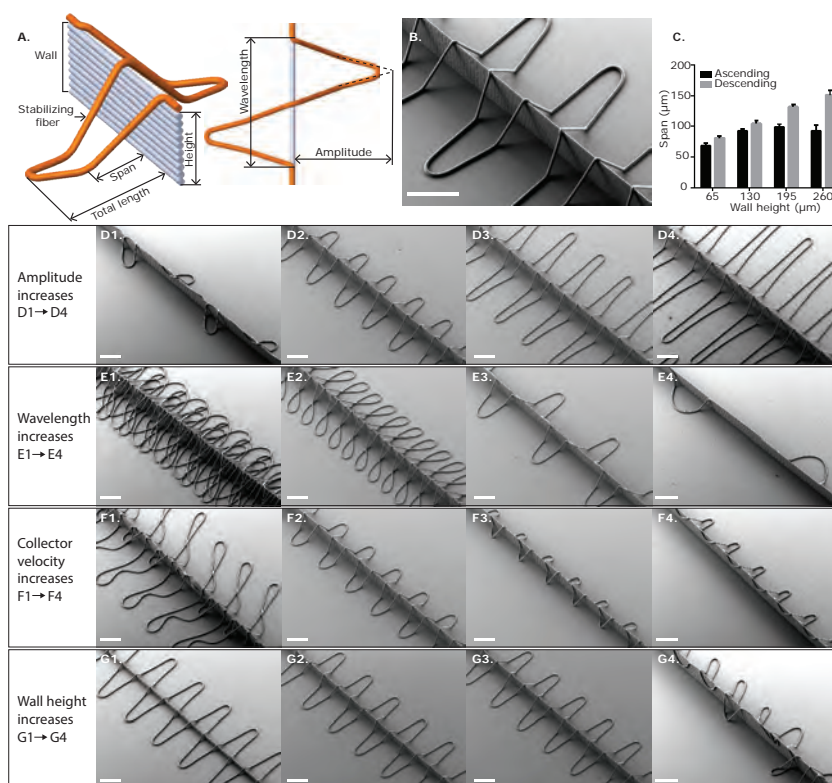


Figure 1. Fabrication of stabilizing fibres. A) Illustration and nomenclature of stabilizing fibres that were deposited out-of-plane. B) Stabilizing fibres crossing the wall with programmed amplitude = 500 μm , wavelength = 400 μm , collector velocity = 400 mm min^{-1} . Scale bar = 100 μm . C) Effect of the height of the wall on the span of the ascending and descending fibre. D) Effect of amplitude on stabilizing fibre fabrication. Wavelength and collector velocity similar as B. E) Effect of wavelength on the morphology of the stabilizing fibres. Amplitude and collector velocity similar as B. F) Effect of collector velocity on stabilizing fibre fabrication. Amplitude and wavelength similar to B. G) Effect of height on stabilizing fibre fabrication with parameters as in B. Scale bar = 200 μm .

Overall, these data show the influence of the instrument parameters on fibre morphology. For the first time, the morphology of fibres fabricated with MEW includes an intentionally introduced out-of-plane component. By tailoring the machine parameters, fibre morphology could be altered resulting in highly reproducible structures (**Figure 1B**) that could potentially be used to reinforce hydrogels.

While there are potential applications of spanning microstructures within electronics^{124–126}, our interest in such stabilizing fibres was to enhance the shear properties of fibre/hydrogel composites for use in medical and TE applications. Therefore, MEW scaffolds were fabricated in a radial configuration so that the stabilizing fibres were in the same direction as the applied load of the rotational shear rheometer (SF1; **Figure 2A**), and walls only (**Figure 2B**) were used as the control. A single fibre grid layer was first direct written under all samples to assist in fibre adhesion and handling during hydrogel embedding (**Figure 2C**).

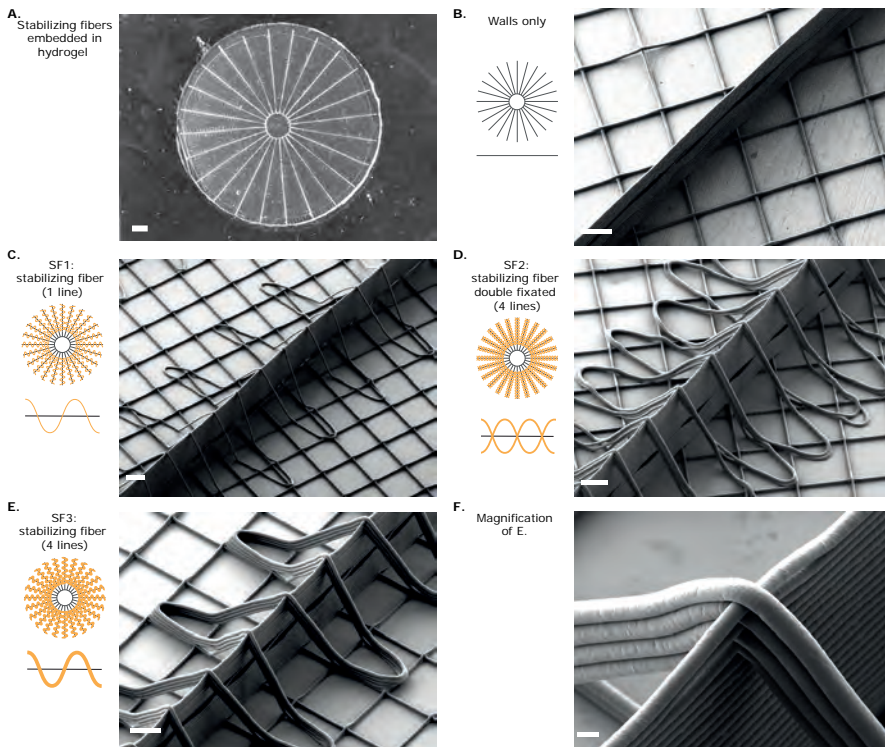


Figure 2. Different variants of stabilizing fibres produced in a radial manner for shear stress measurements. A) Overview image of a MEW PCL scaffold embedded in a model hydrogel. B) Control group, walls only, no stabilizing fibres. C) Stabilizing fibres, 1 line. D) Stabilizing fibres, 4 lines of which 2 out of phase. E) Stabilizing fibres, 4 lines, in-phase. F) Magnification of E, where the stabilizing fibres cross the wall. Scale bar A = 1 mm, scale bar B-D = 100 μ m, scale bar F = 10 μ m.

In order to determine the effect of fibre architecture on the resistance to shear, multiple designs, with extra stabilizing fibres incorporated within the structure, were also fabricated (**Figure 2D-E**). For these additional groups, the stabilizing fibres were integrated within the top of the wall by alternating the stabilizing fibres with the fibres being placed upon the wall (**Figure 2F**). One variant had four stabilizing fibres in total, with half of them out-of-phase with each other (SF2; **Figure 2D**) while the other one had all four stabilizing fibres in phase (SF3; **Figure 2E**). To analyse the effect of the stabilizing fibres on the shear modulus of PCL/hydrogel composites, these 3D MEW structures were embedded in different concentrations of polyacrylamide with a range of crosslinking densities, as well as in pHEMA. All fibre/hydrogel constructs had a relatively low PCL component of only 0.24–0.29 vol.% (*i.e.* a hydrogel content between 99.71–99.76 vol.%) (**Figure 2B – 2F**).

The inclusion of stabilizing fibres within the various hydrogels did increase the shear modulus for all different geometries (Walls only, SF1, SF2 and SF3, see **Figure 3A**), both in the pHEMA and in the relatively soft 5% polyacrylamide (**Figure 3B, 3C**). Remarkably, no significant differences were found between the variant groups geometries (SF1, SF2 and SF3) with additional fibres integrated into the structure – as long as there was a stabilizing fibre, the shear modulus increased to a similar level. To investigate the effect of hydrogel-concentration and crosslink-density of the hydrogel on the fibre reinforcement effect, stabilizing fibres were tested in 5%, 10%, and 15% polyacrylamide and with 0.2, 0.3, and 0.5 % bis-acrylamide (**Figure 3D-F**).

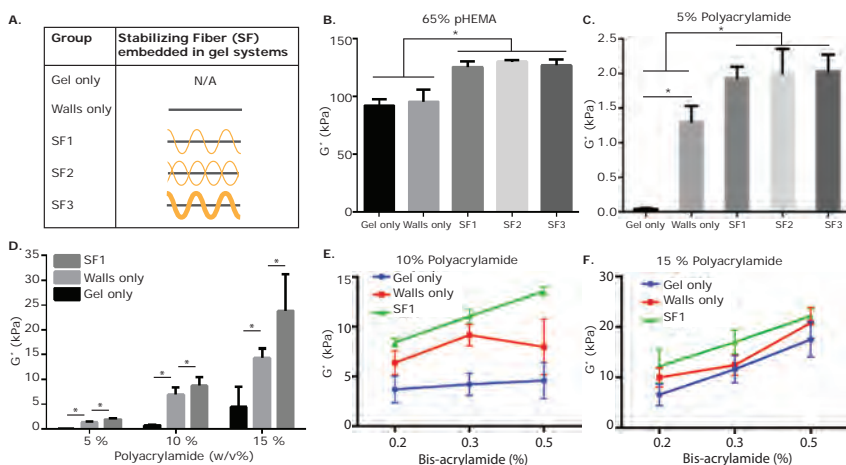


Figure 3. Effect of stabilizing fibres within fibre/hydrogel composites. A) Nomenclature of the stabilizing fibre structures when embedded within a hydrogel. B) Different designs of stabilizing fibres in pHEMA. C) Different designs of stabilizing fibres in the softer 5% polyacrylamide. D) Effect of stabilizing fibres (SF1) in 5%, 10%, and 15% polyacrylamide. E) Effect of stabilizing fibres in 10% polyacrylamide with 0.2%, 0.3%, and 0.5% bis-acrylamide representing an increase in hydrogel mesh size. F) Effect of stabilizing fibres in 15% polyacrylamide with 0.5%, 0.3%, and 0.2% bis-acrylamide. Data represented as mean \pm SD, * = $p < 0.05$.

Although no correlation was found, the reinforcing effect of the stabilizing fibres was shown in all gels, irrespective of hydrogel-concentration, or crosslink-density. A deeper understanding of this reinforcing effect for shear forces could be achieved using numerical methods to investigate the influence of out-of-plane fibres, including their morphology and more complex organizations, on the mechanical behaviour and reinforcement mechanism of soft hydrogels. The use of continuum Finite Element methods, combined with experimental data, can provide a better understanding of the construct's mechanical response with different boundary conditions, e.g. confined compression, shear loading or other boundary conditions that mimic a specific physiological application and eventually facilitate the reinforcing strategy design process. This in turn would provide reinforcement designs for MEW with even more efficiency and complexity.

Conclusion

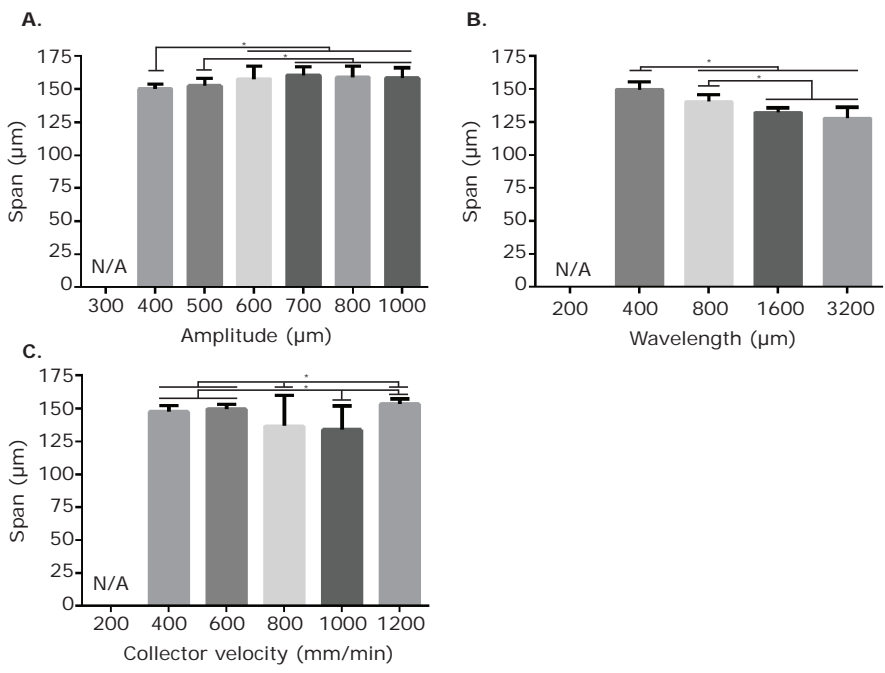
In conclusion, this study shows the highly reproducible out-of-plane deposition of an electrically charged polymer melt, resulting in stabilizing fibres. Stabilizing structures, irrespective of the number and arrangement of fibres (in phase or out of phase), increased the shear modulus in both weak and strong hydrogels, with different crosslinking densities and different hydrogel concentrations. The ability to fabricate highly reproducible MEW structures that include an out-of-plane component, and the capacity to increase the shear response of hydrogel/fibre composites, while maintaining a soft hydrogel, are key outcomes of this study.

Acknowledgements

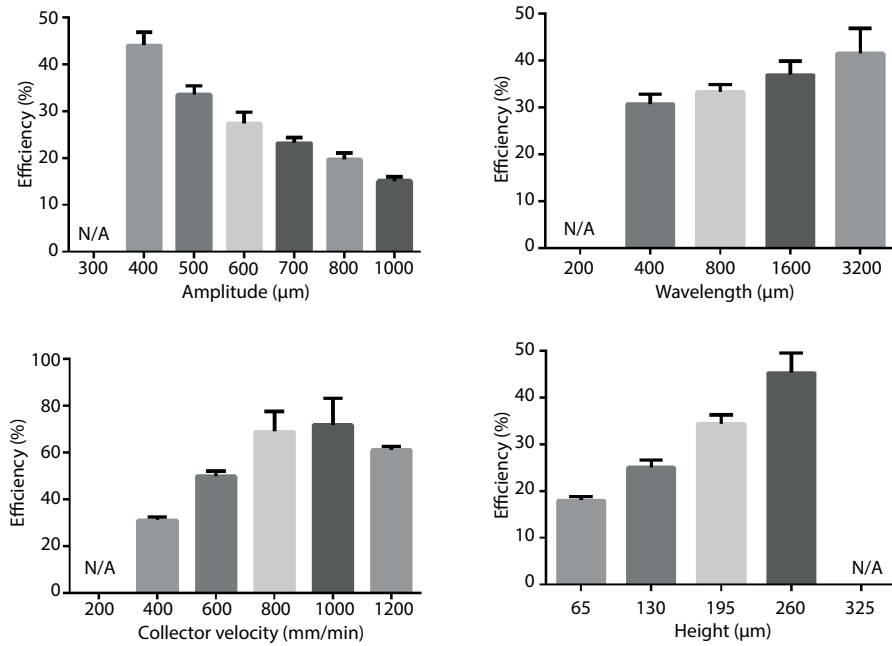
This work was financially supported by the Dutch Arthritis Foundation (LLP-12); the European Community's Seventh Framework Programme (FP7/2007-2013) under grant agreement 309962 (HydroZONES). Further, we gratefully acknowledge the European Research Council under grant agreements 647426 (3D-JOINT) and 617989 (Design2Heal), as well as the German Research Foundation (DFG) State Major Instrumentation Programme for funding the Zeiss Crossbeam CB 340 scanning electron microscope (INST 105022/58-1 FUGG). The MEW device used for this study was built by GH, while the support of the Hofvijverkring for PD is appreciated.



Supplementary data

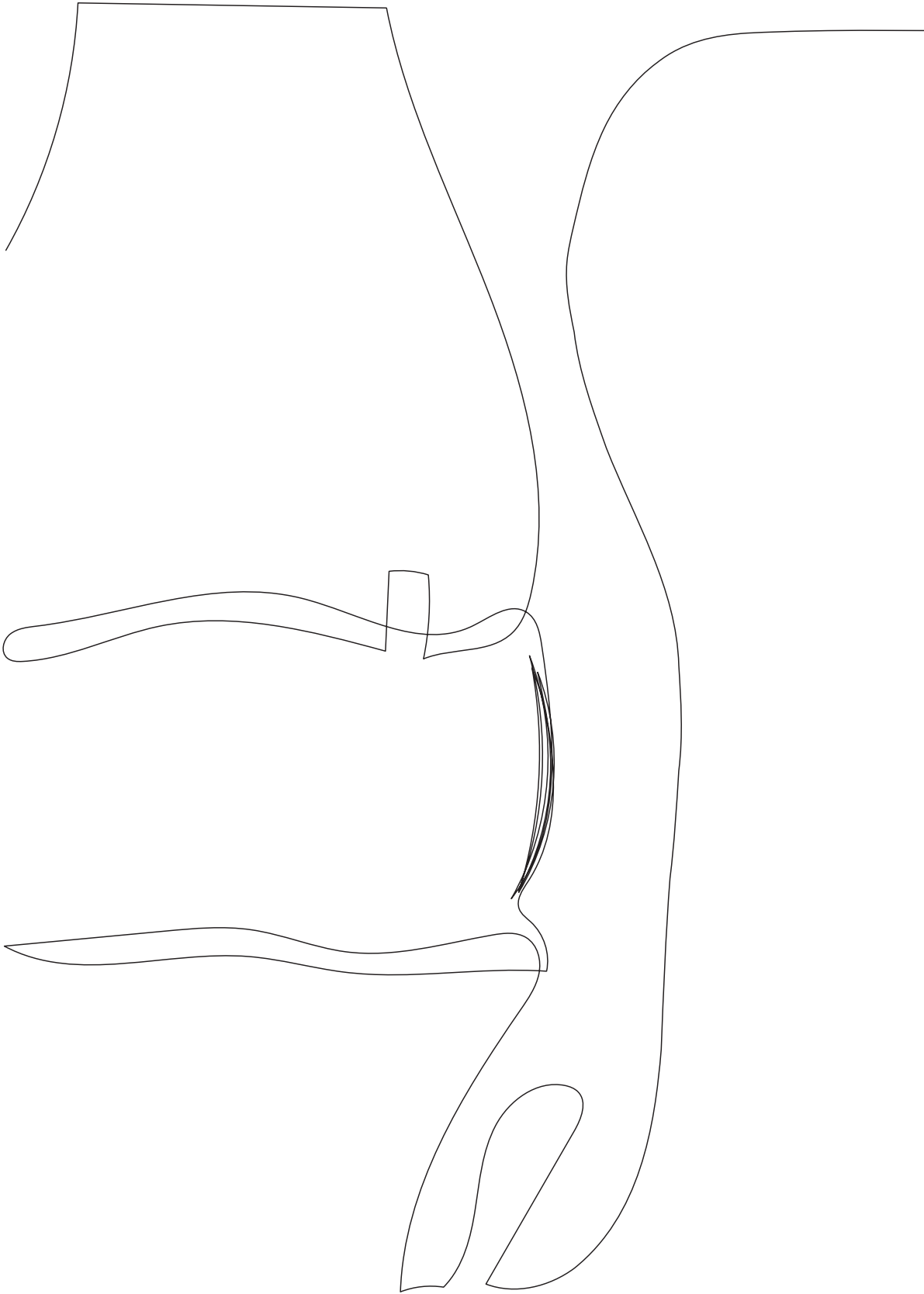


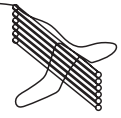
Supplementary Figure S1. Effect of instrument parameters on the span of stabilizing fibres. A) Effect of the amplitude. B) Effect of the wavelength. C) Effect of the collector velocity. * = $p < 0.05$ and for A, all differences were found significant. $n = 3$, 10 measurements per sample.



Supplementary Figure S2. Effect of process parameters on efficiency of the stabilizing fibres. The efficiency is calculated as the length of fibre that is out-of-plane compared to the deposited length. A) Effect of amplitude. B). Effect of Wavelength. C). Effect of collector velocity. D). Effect of Height.







Chapter 3

3

Combining multi-scale 3D printing technologies to engineer reinforced hydrogel-ceramic interfaces

Paweena Diloksumpan¹

Mylène de Ruijter^{2,3}

Miguel Castilho^{2,3,4}

Uwe Gbureck⁵

Tina Vermonden⁶

P. René van Weeren¹

Jos Malda^{1,2,3}

Riccardo Levato^{1,2,3}

Published in *Biofabrication* (2020)

DOI 10.1088/1758-5090/ab69d9

¹ Department of Clinical Sciences, Faculty of Veterinary Medicine, Utrecht University, The Netherlands

² Department of Orthopaedics, University Medical Center Utrecht, Utrecht University, Utrecht, The Netherlands

³ Regenerative Medicine Center, Utrecht, Utrecht University, Utrecht, The Netherlands

⁴ Department of Biomedical Engineering, Faculty of Engineering, Technical University of Eindhoven, The Netherlands

⁵ Department for Functional Materials in Medicine and Dentistry, University Hospital of Würzburg, Würzburg, Germany

⁶ Department of Pharmaceutics, Utrecht Institute for Pharmaceutical Sciences (UIPS), Faculty of Science, Utrecht University, The Netherlands

Abstract

Multi-material 3D printing technologies that resolve features at different lengths down to the microscale open new avenues for regenerative medicine, particularly in the engineering of tissue interfaces. Herein, extrusion printing of a bone-biomimetic ceramic ink and melt electrowriting (MEW) of spatially organized polymeric microfibrils are integrated for the biofabrication of an osteochondral plug, with a mechanically reinforced bone-to-cartilage interface. A printable physiological temperature-setting bioceramic, based on α -tricalcium phosphate, nanohydroxyapatite and a custom-synthesized biodegradable and crosslinkable poloxamer, was developed as bone support. The mild setting reaction of the bone ink enabled us to print directly within melt electrowritten polycaprolactone meshes, preserving their micro-architecture. Ceramic-integrated MEW meshes protruded into the cartilage region of the composite plug and were embedded with mechanically soft gelatin-based hydrogels, laden with articular cartilage chondroprogenitor cells. Such interlocking design enhanced the hydrogel-to-ceramic adhesion strength > 6.5-fold, compared with non-interlocking fibre architectures, enabling structural stability during handling and surgical implantation in osteochondral defects *ex vivo*. Furthermore, the MEW meshes endowed the chondral compartment with compressive properties approaching those of native cartilage (20-fold reinforcement versus pristine hydrogel). The osteal and chondral compartment supported osteogenesis and cartilage matrix deposition *in vitro*, and the neo-synthesized cartilage matrix further contributed to the mechanical reinforcement at the ceramic-hydrogel interface. This multi-material, multi-scale 3D printing approach provides a promising strategy for engineering advanced composite constructs for the regeneration of musculoskeletal and connective tissue interfaces.



Introduction

Establishing a secure integration between mechanically dissimilar materials is a major challenge in engineering interfaces between biological tissues. In musculoskeletal tissues, hard, mineralized materials are naturally integrated with soft tissues, for example, the cartilage-to-bone boundary. This interface plays a pivotal role in the regulation of inter-cellular communication, through the diffusion of bioactive molecules between the articular surface and the subchondral bone.¹²⁷ Such filter function, together with the transmission of mechanical loads,^{79,128} contributes to maintaining homeostasis and hence functionality of the articulating joint. Traumatic injuries to the articular cartilage and degenerative processes can lead to osteoarthritis, which is a prevalent and debilitating condition in our aging population. This disorder may result in the disruption of the integrity of the subchondral bone, cartilage and their interface, urging the development of approaches that can functionally restore the affected tissue. Thus far, principally, the use of soft materials has been investigated for cartilage restoration, in particular those based on biocompatible hydrogels that can provide a highly hydrated environment aiding the encapsulation and differentiation of cells. However, these materials are difficult to integrate with stiff materials that constitute successful supports as regenerative scaffolds or prosthetic replacements for mineralized tissues, such as bone.¹²⁹ Nevertheless, specific classes of double-network hydrogel formulations have been designed to feature outstanding toughness and adhesion strength to ceramics and metals.¹³⁰ However, these gels are very stiff or composed of dense polymer networks that have not been proven as suitable to support homogenous neo-tissue matrix deposition from encapsulated cells.^{131,132} Several strategies for integrating soft hydrogels with stiff bone substitute have been developed^{129,133–136}, including binding with adhesive glues¹³⁷, coupling through covalent chemical bonds¹³⁸, or forming compositional gradients using the same based material via casting¹³⁹. A major drawback of these strategies is that the majority offer little to no control over the architecture of the engineered interface.


The recent advances in 3D printing and biofabrication technologies open new avenues for the creation of multi-material architectures that can mimic or replace biological interfaces. Medical imaging, such as computed tomography, can be used as blueprints to replicate anatomical features of the native osteochondral boundary.¹⁴⁰ The layer-by-layer fabrication approach, typical of additive manufacturing techniques, enables us to freely design different pore geometries across the depth of the bone and cartilage compartments¹⁴¹, as well as to introduce gradients of bioactive cues and inorganic particles.^{142–147} Additionally, even low-viscosity hydrogels with low ability to retain their shape post-printing have been precisely deposited into biphasic structures reminiscent of osteochondral units, for instance with the aid of sacrificial supporting baths¹⁴⁸, extending

the array of cell-friendly materials usable in bone and cartilage bioprinting. Importantly, cell-laden hydrogels can be mechanically reinforced when printed in coordination with thermoplastic polymers^{82,149–152} and even ceramics that set under cell-friendly conditions.¹⁵³

However, such co-printing methods result in the shielding of the soft hydrogels from mechanical loads and do not necessarily improve their binding ability to an osteal anchor. Moreover, most of these methods suffer from limited spatial resolution (typically ~100 μm) and thus cannot mimic micro- and submicron- scale features of the osteochondral interfaces. A new solution for the generation of fully biofabricated osteochondral boundaries can come from combining printing technologies able to resolve details at different length-scales.¹⁵⁴ MEW has recently emerged as a high-resolution 3D printing method to create highly-ordered, thermoplastic microfibre meshes⁹¹ in the micron and sub-micron range⁸⁸, allowing for multimodal scaffold fabrication.¹⁵⁵ These MEW meshes, when infused with cell-friendly hydrogels, create composite materials with improved shear properties and outstanding compressive properties approaching those of native cartilage.⁸⁴ Despite this potential, the development of material-based strategies to create bioinspired, reinforced interfaces using such microfibre deposition methods has not been reported yet.

Biomaterials like α -tricalcium phosphate (α -TCP) have been used as injectable bone regenerative materials due to their biocompatibility and osteoconductivity.^{156,157} The self-setting capacity of α -TCP through hydrolysis also results in products that have a structure comparable with the inorganic components of native bone.¹⁵⁸ These properties allow us to process α -TCP for making customized scaffolds, for instance as recently shown for developing printable bone cements.¹⁵⁹ However, there is a limitation to using α -TCP due to its high solubility which leads to fast degradation. Incorporation of other inorganic phases, for instance, nanohydroxyapatite, FDA approved in several biomedical products^{160,161}, has been well-described to improve the osteogenic potential of the ceramic, both in terms of osteoinduction and osteoconduction.¹⁶² Given these promising biological properties and the low-temperature setting reactivity, this system offers a unique opportunity for direct printing with low melting polymers, as explored in this work.

In this present study, we introduce a novel approach that combines different 3D printing technologies, with the aim to directly form a secure integration at the interface between two mechanically distinct materials, particularly between cell-laden hydrogels and biologically relevant ceramics and polymers. To achieve that, a bioceramic ink that sets at physiological conditions, was developed based on a calcium phosphate (CaP) formulation that mimics the mineral phase of bone and shaped as subchondral bone substitute using a pneumatic-driven extrusion-based printer. Next, microfibrinous polymeric meshes



obtained by MEW were directly anchored into the ceramic ink and were embedded in a cell-laden soft hydrogel based on methacryloyl-modified gelatin (gelMA), to represent the cartilage component. Several microfibre structures were studied in their capacity as the interlocking agent to enhance the interfacial adhesion of the hydrogel-ceramic interface and as mechanical reinforcement to enhance the compressive properties of the hydrogel. This technology has been used to create fully biofabricated osteochondral plugs for the treatment of bone and cartilage defects.

Materials and methods

Preparation of the calcium phosphate-based paste

The printable calcium phosphate (pCaP)-based ink, consisting of a particle and a liquid phase, was prepared in-house (**Figure 1**). For 1 g of printable phase, 660 mg of milled alpha-tricalcium phosphate microparticles (α -TCP, average size 3.83 μm , Cambioceramics, Leiden, the Netherlands) were mixed with 40 mg of nanohydroxyapatite (nano-HA, particle size <200 nm, $\text{Ca}_5(\text{OH})(\text{PO}_4)_3$, Sigma Aldrich). The liquid phase was composed of a 40% w/v hydrogel precursor solution, consisting of either unmodified poloxamer (Pluronic[®] F-127, Sigma-Aldrich) or a custom-synthesized hydrolysable, crosslinkable poloxamer, whose terminal hydroxyl groups were modified by grafting caprolactone oligomers and methacryloyl groups (P-CL-MA, with 1 repeating unit for CL), as reported previously.¹⁶³ The unmodified (non-crosslinkable) and modified (crosslinkable) poloxamer were dissolved in PBS and PBS supplemented with 25 mM ammonium persulphate (APS, Sigma Aldrich), respectively. Prior to mixing, the particle and the liquid phases were stored at 4 °C for 30 min in order to prevent thermal gelation of the poloxamer component. Subsequently, either the non-crosslinkable (NC) or crosslinkable (C) poloxamer was added to particles and mixed manually by stirring for 3 min at 4 °C to ensure homogenous distribution of the particles. Subsequently, the prepared non-crosslinkable pCaP inks (NC-pCaP) and crosslinkable pCaP inks (C-pCaP) were loaded into a dispensing cartridge, closed with a retainer cap, and stored at 4 °C until used.

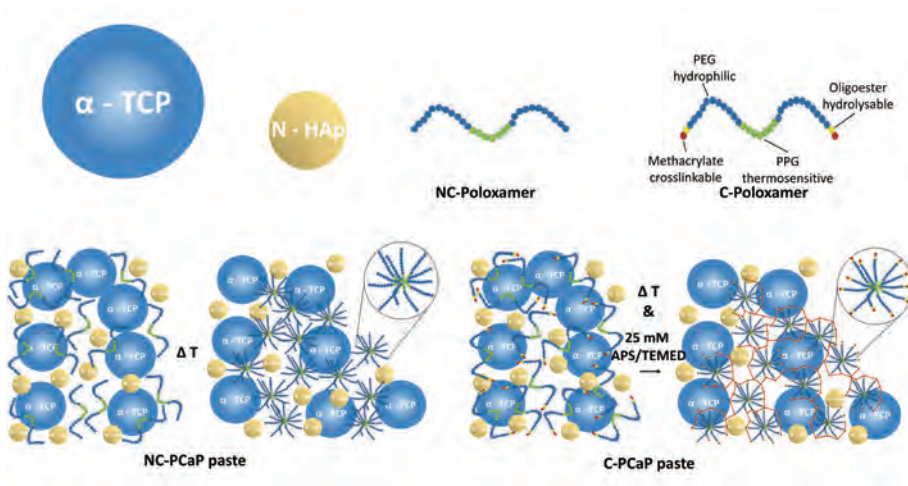


Figure 1. Material composition schematic pictures representing the compositions of the pCaP pastes.

Rheological characterization

Rheological characterization was performed on NC-pCaP, C-pCaP, NC-Poloxamer, C-Poloxamer and water-pCaP using a rheometer (Discovery Hybrid Rheometer (HR-2), TA instrument). The test was conducted on a Peltier plate with pre-set temperature of 20 °C. The test geometry was a 20 mm diameter parallel plate. All measurements were performed while covering each sample with a solvent trap to prevent water evaporation from the composite material. The geometry gap was set to 300 μm . Reactivity of the pCaP-based inks was assessed under oscillatory measurements at a frequency of 0.1 rad/s and 0.1% strain, which is within the linear viscoelastic range (LVR) for all samples. Shear recovery measurements were carried out under oscillatory conditions by applying low and high strain cyclically. A low strain of 0.05% was applied for 300 s and then increased to 150% (outside LVR) for 300 s at the same frequency of 0.1 rad/s. These steps were repeated three times. Finally, steady-state flow measurements were performed in order to assess flow behaviour of the materials while applying shear rates from 0.001–1000 S^{-1} . Consistency was ensured by repeating all measurements three times.

Printing of the bioceramic scaffolds

Bioceramic scaffolds were fabricated with pneumatic driven, extrusion-based 3D (bio) printing equipment (3DDiscovery, regenHU, Villaz-St-Pierre, Switzerland). To optimize printing parameters, two layers of meander infill in a circle was designed as a printing path and eventually generated g-code by using BioCAD software (regenHU, Villaz-St-

Pierre, Switzerland). The effects of extrusion pressure, translational speed of the collector plate and layer height on the diameter of printed strand were investigated, in order to optimize the printing resolution. The NC-pCaP ink was utilized initially for testing by extruding through a conical nozzle (inner diameter: 250 μm) at ambient temperature (while maintaining temperature between 20 and 25 $^{\circ}\text{C}$). The average diameter of printed strands from each printing setting was measured from stereomicroscopy pictures by using ImageJ software⁴³.

All printing settings for obtaining cylindrical filaments with precise alignment were selected. Additionally, the maximum designed strand-to-strand distance at which overhang filaments would retain their straightness without sagging to the lower layer was investigated. Based on the information, optimized porous cylindrical structures consisting of meandered infills in each layer were designed. After the printing process, the printed paste was allowed to set into a cement scaffold, through the hydrolytic conversion of the α -TCP microparticles into calcium deficient hydroxyapatite (CDHA)¹⁶⁴, via incubation in a saturated humidity environment at 37 $^{\circ}\text{C}$ for at least three days. Similar printing parameters and post-printing treatment was applied for the C-pCaP ink. Subsequently, C-pCaP scaffolds were immersed in 25 mM tetramethylethylenediamine (TEMED, Invitrogen) solution at 37 $^{\circ}\text{C}$ for one hour in order to polymerize the crosslinkable poloxamer. Finally, C-pCaP structures were rinsed in PBS twice, and air dried at ambient temperature. When required for cell culture, the scaffolds were disinfected by immersion in 70% v/v ethanol, followed by exposure to UV light for 2 h.

Macroporosity of pCaP scaffolds

Porous cylindrical pCaP scaffolds (diameter: 5.0 mm, height: 5.0 mm) were produced from either NC-pCaP paste or C-pCaP paste. Scaffolds were obtained by stacking meander pattern layers in a double alternated pattern (0° - 0° - 90° - 90°), to ensure a consistent lateral pore size of 500 μm . By varying the designed strand to-strand distance from 600 to 800 μm , NC and C scaffolds with four different macroporosity ranges were prepared: 20%–30%, 30%–40%, 40%–50%, and 50%–60% (N= 3–17). Porosity of printed pCaP scaffolds was determined by gravimetry analysis (equation (1)).¹⁶⁵

$$\text{Total porosity} = 1 - \frac{\rho_{\text{scaffold}}}{\rho_{\text{material}}} \quad (\text{equation (1)})$$

Relative density of the used material (ρ_{material}) was quantified as reported previously.¹⁶⁶ Actual dry weight of dense scaffolds, regardless of micro-porosity, was measured using mass scales. Average diameter and height of the scaffolds were measured by using digital

Vernier calipers. Relative density of fabricated scaffolds (ρ scaffold) was calculated from actual dry weight and volume of porous scaffolds.

Mechanical characterization of the bioceramic scaffolds


Unconfined uniaxial compression tests were conducted on scaffolds with different ranges of macroporosity (20%–30%, 30%–40%, 40%–50%, and 50%–60% ($n = 3-17$)), using a system (MTS Criterion® Electromechanical universal Test Systems, Model 42) equipped with a 500 N load cell. Samples were measured after equilibration in PBS for at least 30 min and subjected to a displacement ramp (0.5 mm/min) until failure. Raw data was used to calculate the compressive tangent modulus by measuring the slope of the linear region found in the range 0%-5% strain in the stress-strain curve, as well as ultimate strength and energy to failure using Matlab (R2018, MathWorks®).

Cell isolation and culture

Primary cells were obtained from healthy tissues (bone marrow and articular cartilage) of a deceased, skeletally mature equine donor (aged 6 years old; $n = 1$), donated for research by their owner, according to the guidelines of the Institutional Animal Ethical Committee of the veterinary clinic of Utrecht University. Mesenchymal stromal cells (MSCs) were harvested from bone marrow aspirated from the sternum, while articular cartilage-derived chondroprogenitor cells (ACPCs) were obtained from enzymatic digests of cartilage from the metacarpophalangeal joint, following previously reported protocols and following the ethical regulations of the host institution.¹⁶⁷ MSCs were expanded in minimum essential medium alpha (α -MEM, 22561 Gibco, The Netherlands) supplemented with 0.2 mM L-ascorbic acid 2-phosphate (ASAP, Sigma), 10% fetal calf serum (FCS, Lonza, The Netherlands), 100 U/ml penicillin with 100 mg/ml streptomycin (Life Technologies, The Netherlands) and 1 ng/ml basic fibroblast growth factor (bFGF, Peprotech, UK). ACPCs were expanded in Dulbecco's modified Eagle medium (DMEM, 31966, Gibco, The Netherlands), supplemented with 10% v/v FCS, 0.2 mM L-ascorbic acid-2-phosphate, 100 U/ml penicillin, 100 mg/ml streptomycin and 5 ng/ml (bFGF, Peprotech, UK)). Cells were used between passage 3 and 5.

***In vitro* cytocompatibility and osteogenic potential**

The indirect cytotoxicity of the bioceramic ink was determined to evaluate the potential release of harmful compounds from the CDHA and from the hydrogel component of the cement scaffolds. Four formulations of pCaP were prepared by mixing the particle phase with different liquid compositions: distilled water, NC-poloxamer, C-poloxamer and 10% gelatin-methacryloyl (gelMA). GelMA synthesis was performed as previously reported.¹⁶⁸ Cast pCaP discs (diameter: 5.0 mm, height: 2.0 mm) were incubated in MSC expansion medium for 48 h before using. MSCs (10^4 cells/well) were seeded on tissue-culture treated



polystyrene and cultured with eluates of the pCaP scaffolds. The pCaP-exposed medium was exchanged every two days. Cells exposed to MSCs expansion medium supplemented with 0.1% v/v Tween-20 were used as negative control. Cell metabolic activity was assessed with a resazurin assay (AlamarBlue™ Cell Viability, Invitrogen). Next, proliferation and osteogenic differentiation of cells that were in direct contact with the pCaP scaffold were assessed. To enhance the number of seeded cells on the scaffold, porous cylindrical C-pCaP scaffolds (diameter: 13.0 mm, height: 1.0 mm) were printed with single alternated pattern (0°-30°-60°-90°) and a designed strand-to-strand distance of 750 μm.

Firstly, MSCs were seeded onto the scaffolds (5 x 10⁴ cells/scaffold, n = 4 per time point) and cultured in the expansion medium, supplemented with 10 mM N-2-hydroxyethylpiperazine-N-2-ethane sulfonic acid (HEPES, Gibco) to assess cell proliferation. At day 1, 3, 7 and 14 the cell-laden scaffolds were collected, and cell lysates were obtained by the addition of the protein extraction buffer M-PER (Thermo Scientific). The number of cells at each time point was quantified by measuring lactate dehydrogenase activity in the lysate (LDH- kit, Roche diagnostic GmbH). Additionally, cell-laden scaffolds at each time point were washed in PBS, fixed with phosphate buffered formalin (pH 7.2), and stained for actin with phalloidin conjugates FTIC (Sigma) for 30 min to observe cell morphology. Nuclei were counterstained with 4',6'-diamidino-2-phenylindole (DAPI, 100 ng/ml, Sigma) for 1 min. Secondly, MSCs were seeded on bioceramic constructs (10⁵ cells/ scaffold, n = 4 per analysis) and cultured in the expansion medium, supplemented with 20 mM β-glycerol phosphate, 100 nM dexamethasone and 10 mM HEPES to assess osteogenic differentiation. The medium was refreshed every two days. At day 1, 7, 14, and 21 cell-laden scaffolds were lysated in M-PER and alkaline phosphate (ALP) activity was measured performing a p-nitrophenyl phosphate assay (SIGMAFAST™, Sigma Aldrich), together with DNA content, determined using the Quan-iT-Picogreen-dsDNA kit (Molecular Probes, Invitrogen, Carlsbad, USA). Formalin-fixed constructs were also labelled with DAPI and immunostained for the osteoblastic marker osteonectin (primary antibody, secondary antibody, Alexafluor 546 (goat anti-mouse, 1752107 Life technologies)). Fluorescently stained constructs were imaged with a confocal laser scanning microscope (TCS SP8, Leica, Netherlands).

Fabrication of multiphasic hydrogel thermoplastic-bioceramic composite scaffolds mimicking an osteochondral plug

Polycaprolactone (PCL) microfibre meshes were fabricated from medical-grade polycaprolactone (Purasorb® PC 12 Corbion PURAC, The Netherlands) using a custom-made melt electrowriting device as previously described.¹⁶⁹ MEW printing parameters were: printing temperature of 90 °C, collector velocity of 50 mm/s, voltage of 10 kV, and pressure of 1.5 bar. Printing was performed at room temperature (22–24 °C) with a

humidity between 30%–50%. By using these settings, microfibre meshes organized in orthogonal square box patterns (fibre diameter = 10 μm , fibre spacing = 300 μm , total height = 1.3 mm) were obtained, which were later cored to obtain 8 mm diameter cylinders using a biopsy punch. These cylindrical meshes were then fixed on a glass slide using a custom-made holder and placed onto the collecting platform of the extrusion-based printer. C-pCaP paste was directly printed over the MEW-printed microfibre mesh, to form a 6.3-mm diameter bioceramic scaffold. The initial height for depositing the C-pCaP paste was optimized thoroughly to ensure printing without damaging the architecture of the PCL microfibrils. The first two layers were generated without macroporosity to mimic the subchondral bone plate. The following layers were deposited with a designed strand-to-strand distance of 700 μm , forming a bone-mimetic osteal anchor. After letting the ceramic component set at 37 $^{\circ}\text{C}$, the MEW mesh was infused with a 10% w/v gelMA solution¹⁷⁰ in PBS, supplemented with 25 mM APS/TEMED to allow chemical crosslinking of the hydrogel, thus completing the cartilage mimetic-region of the engineered osteochondral plug (**Figure 2**). Finally, the overall construct was removed from the mold and transferred into 25 mM APS/TEMED supplemented PBS at 37 $^{\circ}\text{C}$ for one hour to allow completion of crosslinking of both the C-poloxamer in C-pCaP and gelMA hydrogel.

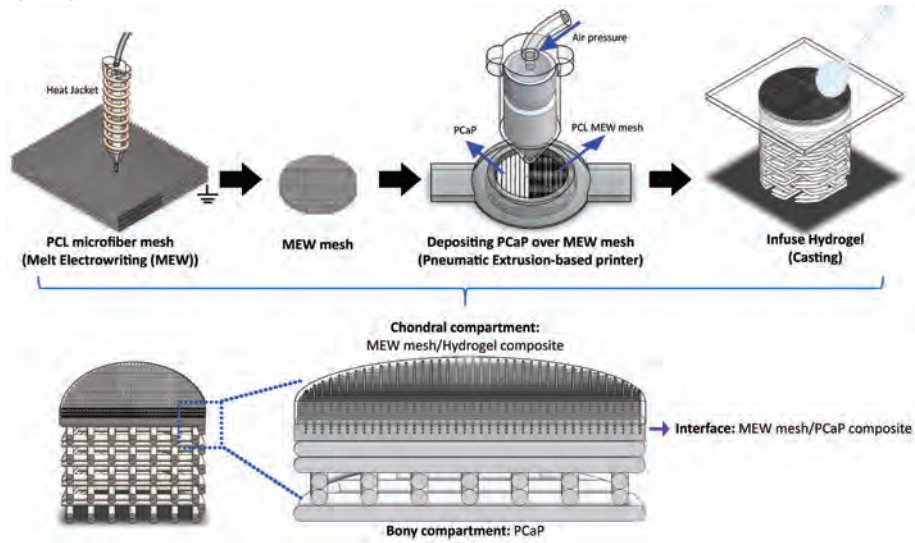



Figure 2. Fabrication process of the osteochondral construct by using a combination of different 3D printing techniques

Interfacial hydrogel-ceramic adhesion strength



The strength of the interconnection at the interface between microfibre-reinforced hydrogel and the bioceramic scaffold was determined using a Dynamic Mechanical Analyser (DMA Q800, TA Instrument), modified with ring-shaped custom-made sample holders. Additively manufactured samples were mounted so that the C-pCaP and hydrogel compartments were lodged each into the circular cavity of a holder. These holders were then displaced in the direction parallel to the ceramic-hydrogel interface applying a force ramp, until the two parts were completely separated. Shear stress and energy at failure were calculated respectively. Experimental groups consisted of gelMA: (i) cast onto C-pCaP scaffolds with a flat surface, (ii) cast onto C-pCaP scaffolds with grooved surface, which were obtained by adding one layer of parallel C-pCaP struts (spacing = 1.4 mm.), (iii) a microfibre composite that was cast onto the C-pCaP bone-mimetic scaffold (un-anchored microfibres), (iv) a microfibre composite that was cast onto the C-pCaP bone-mimetic scaffold (anchored microfibres). The latter were obtained with the combined MEW and ceramic extrusion printing approach. As additional control, a cylinder made of only gelMA was also tested, to analyse the mechanical strength under shear of a monolithic hydrogel. For each experimental group $n = 3-9$ samples were analysed.

Scanning electron microscopy (SEM) imaging of the engineered ceramic-hydrogel interface

The morphology of the interface between the microfibre meshes and the C-pCaP, as established in the combined printing approach, was visualised via SEM (Phenom PRO SEM, Thermo Fisher scientific; accelerating voltage of 10 kV). All structures were kept at $-80\text{ }^{\circ}\text{C}$ overnight and freeze-dried to remove water from the cartilaginous compartment, and all samples were cut in half in liquid nitrogen, in order to visualize the longitudinal cross-section of the composite scaffold.

Mechanical characterization of reinforced gelMA (cartilaginous compartment) of osteochondral construct


The compressive properties of the microfibre-reinforced gelMA linked to the C-pCaP scaffold, were measured in unconfined uniaxial compression. A 0.1 N/min ramp force was applied with a DMA device with mounted compression clamps, until reaching a 50% deformation of the disc-shaped hydrogel-microfibre composite compartment (height 1 mm diameter 6 mm). Experimental groups consisted of gelMA: (i) pristine, (ii) a microfibre composite, (iii) cast onto a C-pCaP bone-mimetic scaffold, (iv) a microfibre composite cast onto a C-pCaP bone-mimetic scaffold (un-anchored microfibres), (v) a microfibre composite cast onto a C-pCaP bone-mimetic scaffold (anchored microfibres). For each group, $n = 5-10$ structures were tested. The compressive modulus was derived from curve fitting between 12% - 17% strain rate.

Cartilage deposition in vitro in the engineered osteochondral plug **Engineered osteochondral plug preparation and culture**

In this part, osteochondral scaffolds consisted of a cell-free bone and an ACPC-laden cartilage compartment. The bone-mimetic region was composed of a porous C-pCaP structure, (designed strand-to-strand distance = 0.7 mm, diameter = 6.3 mm, height of C-pCaP = 3 mm), capped with a non-macroporous layer of C-pCaP struts, with an anchored microfibre mesh, prepared as described previously via combined printing. For the cartilage region, a 10% w/v gelMA hydrogel precursor solution in PBS was loaded with 2×10^7 ACPCs/ml and infused in the reinforcing microfibres linked to the C-pCaP structure. Cells were encapsulated at passage 4. To permit rapid crosslinking, the precursor solution was supplemented with a previously described visible-light responsive photoinitiator^{171,172}, composed of 0.5 mM tris (2,2'- bipyridyl) dichloro-ruthenium (II) hexahydrate (Sigma - Aldrich) and 5 mM sodium persulfate (Sigma Aldrich), and exposed to a 1300 lumen white light lamp for 8 min. Samples were cultured in a chondrogenic medium, consisting of DMEM (Gibco, Life Technologies), supplemented with 1% v/v ITS + premix (BD biosciences), 0.2 mM ASAP (Sigma Aldrich), 0.1 μ M dexamethasone (Sigma Aldrich), 1% v/v HEPES, 100 U/ml penicillin, 100 μ g/ml streptomycin (Gibco, Life Technologies) and 10 ng/ml of recombinant human transforming growth factor- β 1 (TGF- β 1, Peprotech). Samples were cultured for 6 weeks and harvested at two time points (day 1 and day 42) for subsequent analysis. Medium was refreshed every two days. Neo-cartilage formation in the cartilage-region of the engineered plugs, compared to the constructs composed of cell-laden reinforced gelMA only, was evaluated via immunohistochemistry and biochemical analysis. The effect of the neo-synthesized matrix over the culture time on the mechanical strength of the interface between the bone and cartilage compartment was also assessed.

Biochemical and histological evaluation of neocartilage formation

For biochemical evaluation, samples at week 1 (n = 3–6) and 6 (n = 5–14) of culture were harvested, and the chondral compartment was removed and with a razor blade and digested in papain (Papain from papaya latex, Sigma Aldrich) at 60 °C overnight. Sulphated glycosaminoglycan and DNA contents of the constructs were quantified performing a dimethylmethylene blue (DMMB, Sigma-Aldrich, The Netherlands) colorimetric assay and with a Quan-iTPicogreen-dsDNA-kit assay (Molecular Probes, Invitrogen, Carlsbad, USA). For histological analysis, samples at day 42 (n = 3) were fixated in 4% buffered formalin. For paraffin embedding, samples were decalcified with 0.5 M EDTA disodium salt for 1 day. Dehydration was performed through a graded ethanol series, followed by clearing in xylene, embedding in paraffin, and slicing into 5 μ m thin sections with a microtome. Sections were stained with safranin-O and Fast Green to visualize GAGs and collagens. Immunohistochemistry was performed to visualize type I collagen (primary antibody



EPR7785, 0.0022 mg./ml., Abcam) and type II collagen (primary antibody Col2A1 II-II6313, 0.6 mg./ml., DSHB). Endogenous peroxidases were blocked via incubation with 0.3% v/v hydrogen peroxide. Antigen retrieval was performed with pronase and hyaluronidase for type II collagen and type I collagen, respectively, at 37 °C. Subsequently, sections were blocked with bovine serum albumin (BSA, 5% w/v in PBS) for 1 h at room temperature, and the primary antibody was incubated overnight at 4 °C. IgGs were used as negative controls. Horseradish peroxidase-labelled secondary antibodies were added for 1 h at room temperature, and the staining was developed using 3,3-diaminobenzidine. Nuclei were counterstained with haematoxylin and sections were mounted in DPX (Millipore). For the osteochondral constructs, in order to visualize structure without removing the pCaP scaffold due to de-calcification steps, one formalin-fixed sample was dehydrated through a graded ethanol series and embedded in a methyl methacrylate (MMA) resin. Sections (300 µm thick) were obtained with a saw microtome (Leica SP 1600). Thereafter, all sections were stained with basic fuchsin to assess scaffold morphology. Histological slides were imaged using a light microscope (Olympus BX51, Olympus Nederland B.V.) equipped with a digital camera (Olympus DP73, Olympus Nederland B.V.).

Interfacial adhesion strength at the engineered osteochondral interface after culture

At day 1 ($n = 3$) and 42 ($n = 9$), osteochondral structures were harvested and kept in medium to ensure hydration. To determine the strength of the connection at the interface between the cartilaginous compartment and the pCaP-based bone compartment, the same settings that were performed for cell-free structures were applied.

Statistical analysis

Results were reported as mean \pm standard deviation. Statistical analyses were performed using Matlab (R2018a, The MathWorks, Inc.). Two-sample independent t-tests were performed to compare the diameter of strands that were printed from different pCaP formulations (NC-pCaP and C-pCaP), biochemical production of ACPCs from different structures (chondral and osteochondral constructs), and interfacial shear stress after cultivation with ACPCs for 1 and 42 days. The Wilcoxon rank sum test was performed to investigate the differences of the mechanical properties of pCaP scaffolds having different porosity and material composition (non-crosslinkable and crosslinkable). One-way ANOVA, with the Bonferroni post hoc test was performed to investigate the mechanical properties of produced osteochondral constructs in terms of interfacial shear stress and compressive modulus of the cartilaginous compartment. Additionally, this method was also applied to compare *in vitro* biological activity of cells with pCaP scaffolds (indirect and direct methods). Statistical significance was considered for $p < 0.05$.

Results and Discussion

Optimization printing parameters of printable calcium phosphate (pCaP) paste

First, a ceramic ink was developed to achieve high-resolution patterning and with a setting chemistry compatible with labile polymers and biological compounds. To reach this objective, α -TPC was selected as a main material, due to its mild setting reaction.¹⁵⁹ Two formulations of pCaP that could be hardened at physiological temperature were evaluated: one containing a non-crosslinkable poloxamer component (NC-pCaP) and one containing a modified, crosslinkable poloxamer component (C-pCaP). The solid particle to liquid (P/L) ratio of both ink formulations ensured the extruded ink retained its shape and could bear weight after placement, allowing for the formation of multilayer constructs without additional support. These were assessed through rheological characterization, to analyse the flow behaviour of the inks when shear forces are applied during printing (**Figure 3, Supplementary Figure S1**). When applying shear rates from 0.001 to 1000 S^{-1} , viscosity decreases over this range of shear rate. This flow profile shows a comparable shear-thinning behaviour for both the NC-pCaP and C-pCaP (**Figure 3A**). Additionally, both NC-pCaP and C-pCaP could rapidly recover from applied shears, a condition beneficial to produce high shape fidelity prints (**Figure 3B**). For printing, to ensure shape fidelity and uniformity of the printed filaments, printing parameters (extrusion pressure, translational speed) for deposition of the paste were established using the NC-pCaP formulation (**Figure 3D**). The optimal printing parameters: 0.2 MPa, 2 mm/s and 250 μm were selected for the pneumatic pressure, translational speed and layer thickness, respectively. With these parameters, the average diameter of the obtained C-pCaP filaments ($230.20 \pm 31.24 \mu m$) was close to the inner diameter of the used nozzle (250 μm), indicating a higher printing resolution than was found for NC-pCaP filaments ($349.22 \pm 33.56 \mu m$) (**Figure 3E**). Besides printing parameters, shape fidelity in the axial direction is also a prerequisite for the formation of multi-layered constructs; this factor depends also on the ability of an ink not to undergo deformation when overhanging filaments are stacked without sacrificial supporting material.¹⁷³ Maximum designed strand-to-strand distance for overhanging 90-degree filaments on top of each other without sagging was 800 μm (**Figure 3F**). Overall, high shape fidelity was achieved post-printing and upon cement setting, with open and interconnected pores, as well exemplified via μCT (Supplementary video SV1). Post-printing, the pCaP ink, which was composed of nanohydroxyapatite (N-HAp) and α -tricalcium phosphate microparticles (α -TCP), sets into a cement at physiological temperature, thanks to the hydrolytic conversion of α -TCP into calcium deficient hydroxyapatite (CDHA) (**Supplementary Figure S2, Supplementary Table 2**), and by further crosslinking of the methacryloyl groups in the C-pCaP formulation. While this stabilizes the fabricated construct, the α -TCP reactivity and setting initiation could



influence the rheology and printability of the ink over time (**Figure 3C**). This potential risk can be overcome through tight control of the temperature during the printing process.

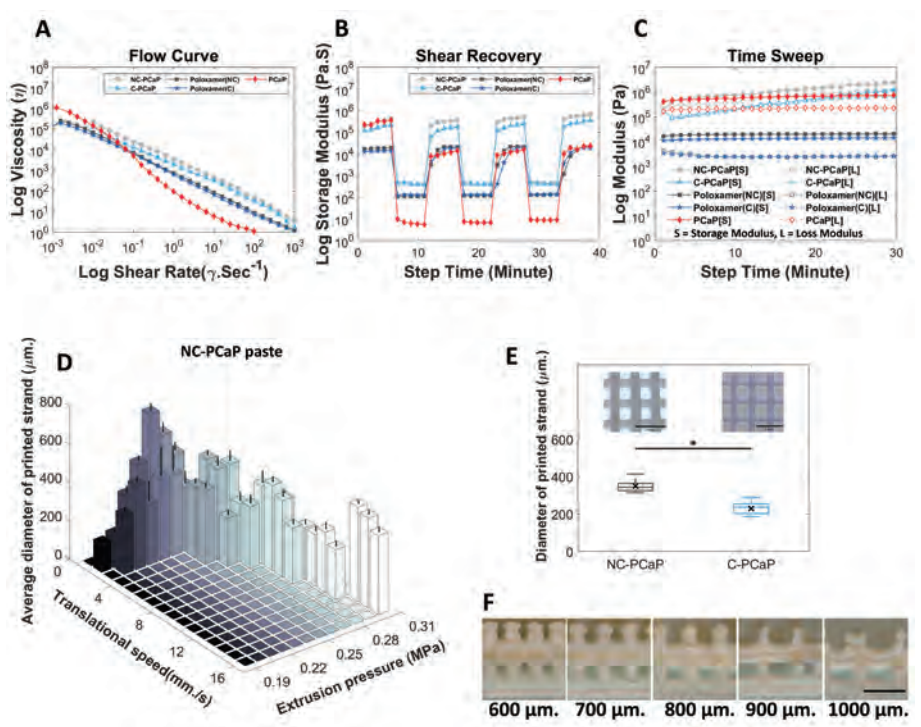


Figure 3. Rheometry and optimization of printing parameters. Rheological analysis highlighting (A) the shear-thinning and (B) shear recovery behaviour of all the inks, and (C) the storage modulus over the printing time, showing no distinctly different behaviour between cements based on the C or NC polymeric carriers. (D) Average diameter of printed strands obtained from two main setting parameters (translational speed and extrusion pressure), (E) comparison between diameter of printed strands fabricated from NC-pCaP paste and C-pCaP paste at the same settings and, (F) the strand-to-strand distance of printable calcium phosphate paste (pCaP). (Scale bar = 1 mm).

Mechanical properties of the biomimetic pCaP scaffolds

After obtaining optimal parameters for printing, mechanical properties of the printed structure (**Figure 4A**) are crucial especially for using it as a bone replacement. First of all, the presence of nanohydroxyapatite in the bioprintable paste was not found to significantly alter the mechanical properties of the cement after setting (**Supplementary Figure S3**). Next, scaffolds with different ranges of porosity were obtained after printing NC-pCaP and C-pCaP biomaterial inks following hardening and hardening-crosslinking, respectively. Tangent modulus, ultimate strength and energy to failure were characterized by performing unconfined compression tests and calculated from the stress-strain curves (**Figure 4B, Supplementary Figure S4A,B**). Importantly, all formulations and pore

designs exhibited compressive properties in the range of cancellous bone.^{174,175} Tangent modulus, ultimate strength and energy to failure of scaffolds made from both NC-pCaP and C-pCaP gradually decreased with increasing porosity, as expected (**Figure 4B,D, Supplementary Figure S4C**). Interestingly, there were no obvious differences in the compressive modulus of scaffolds produced from NC-pCaP and C-pCaP inks, with the only exception of the samples displaying 30%–40% designed porosity.

It has been mentioned in the literature that mechanical properties of self-setting ceramics are lower than high-temperature sintering ceramics.¹⁷⁶ Nevertheless, the scaffolds from this study still showed values in the physiological range reported for trabecular bone.^{174,175} While sintering may further improve the mechanical strength of the constructs, this would prevent the direct incorporation and anchoring of low-melting point thermoplastic polymers as presented in this study as a strategy to improve bone-to-soft tissue interfaces. As such, the high ratio selected for this study (70% w/w of particle content), while giving optimal shape fidelity post-printing, may hinder the formation of a densely crosslinked polymer network, hampering an increase in fracture toughness of the constituent ceramics that could come from the hydrogel covalent crosslink. Nevertheless, considering the overall promising compressive properties and the higher printed filament resolution, C-pCaP was used for the remaining part of this study.

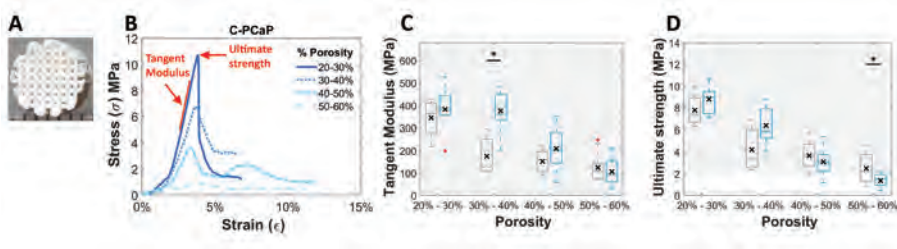


Figure 4. Mechanical properties: (A) representative pCaP scaffold, (B) representative engineered stress-strain curves of C-pCaP scaffolds, (C) tangent modulus, (D) ultimate strength of NC-pCaP paste (grey) and C-pCaP paste (blue) scaffolds with different porosities. (Greyish-filled area showing range of tangent modulus of cancellous bone [10–5000 MPa¹⁷⁴] (B) and ultimate strength [2–45 MPa¹⁷⁵] (C)).

***In vitro* evaluation of bioactivity using mesenchymal stromal cells (MSCs)**

Cytocompatibility and osteogenic potential of the bone constructs (**Figure 5**) was assessed *in vitro*, using equine bone marrow-derived cells, which were selected in the perspective of future *in vivo* analysis, as the horse is a well-accepted-respected model



for evaluating cartilage and osteochondral repair therapies.^{27,177,178} The effects of the release of potentially harmful components was investigated through the culture of MSCs in pCaP conditioned medium, using formulations of the cements that feature different polymeric carriers in the liquid phase. Although free poloxamer above a certain concentration can be harmful¹⁷⁹, our data indicates no negative effect, suggesting no release of detrimental degradation products from the crosslinked poloxamer network or uncontrolled pH changes due to ions released by an incomplete setting reaction of the α -TCP microparticles. There was an increase in number of viable cells from day 1 to day 7 in all experimental groups (**Figure 5A**) and there were no statistically significant differences after 7 days between the poloxamer-CaP conditioned medium, the positive control (fresh culture medium), and a CaP control with an embedded well-known biocompatible polymer (gelMA). Importantly, MSCs were able to proliferate when seeded directly onto the C-pCaP scaffolds, as indicated by lactate dehydrogenase (LDH) activity (**Supplementary Table 1**). Moreover, osteogenic differentiation of equine MSCs cultured on C-pCaP scaffolds was observed after 21 days of culture. The expression of alkaline phosphatase (ALP), an early marker of osteogenic differentiation¹⁸⁰, increased upon MSC culture directly on scaffolds, with higher values and characteristic early peak detection at 7 days in medium supplemented with osteogenic factors (**Figure 5B**). Cell proliferation was confirmed via immunofluorescence, observing confluent cell layers on the printed struts that displayed an elongated morphology and developed actin stress filaments after 14 days of culture (**Figure 5C**). This is in line with previous studies involving scaffolds using comparable ceramic base components.¹⁵⁹ Importantly, upregulation of osteonectin, a marker of maturing osteoblasts and a hallmark of bone deposition, was detected starting from day 14 in samples with osteogenic medium (**Figure 5D, Supplementary Figure S4 D,E**). Overall, the data confirms that the selected pCaP formulation and scaffold have the potential for osteo-regeneration, in line with results reported on other bioceramic materials with similar chemical composition.

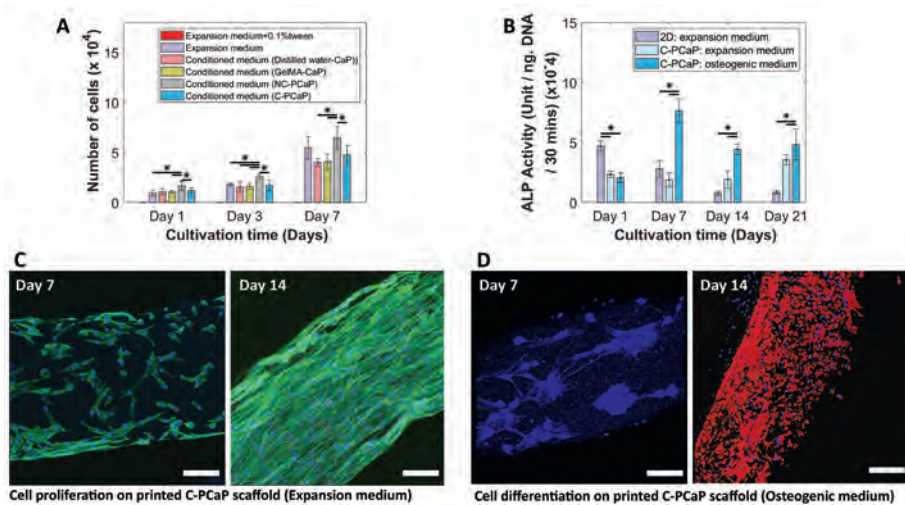


Figure 5. *In vitro* evaluation of bioactivity of the pCaP scaffold. (A) The effect of possible harmful release from composite CaP-based material contained different polymeric carriers on the number of viable cells, (B) the potential of osteogenic differentiation of equine MSCs was investigated through ALP activity, (C) cell proliferation on the C-pCaP filament after cultivation for 7 and 14 days (nucleus (dapi: blue) and F-actin (phalloidin: green)), and (D) cell differentiation on the C-pCaP filament toward an osteogenic lineage after cultivation for 7 and 14 days in an osteogenic medium (nucleus (dapi: blue) and osteonectin protein (osteonectin: red)) (scale bar = 100 μ m).

Fabrication and mechanical properties of the engineered cartilage-bone interface

For proper integration, it is crucial that the deposition of C-pCaP ink does not alter the organized structure of PCL-microfibre mesh (**Figure 6**). Additionally, preservation of the MEW-printed architecture and microfibre alignment is fundamental to control the mechanical reinforcing effect against compression provided by the PCL mesh when soft hydrogels are embedded in it.⁹³ Therefore, the initial height for the deposition of the first layer of C-pCaP was set to 80% of total mesh height. Thanks to the fluid paste-like rheological behaviour of the ceramic ink before setting, the material is able to form an interpenetrated structure with the PCL mesh, without altering the microfibre organization and with no detectable effect on the shape fidelity of the extruded ceramic filaments. After the setting of the C-pCaP, the PCL-ceramic ordered composite is formed, with the microfibrils anchored into the cement phase and protruding in an ordered fashion into the cartilage region of the osteochondral plug, in which the gelMA hydrogel is lodged by

a simple injection (**Figure 7A**). The strength of the interconnection (**Figure 7B**) at the engineered ceramic-hydrogel interface and the compressive modulus of the chondral compartment (**Figure 7C**) were evaluated by using the systems in (**Figure 7D**), and analysing the yield point under interfacial shear stress (**Figure 7E**) and the compressive modulus (**Figure 7F**), respectively. The interfacial strength of the structures was significantly improved compared to conditions in which the hydrogel was either cast on a smooth or grooved pristine pCaP osteal part, or when the reinforcing microfibrils were laid on top of but not anchored into the pCaP (**Figure 7E**). The embedding of the MEW reinforcing microfibrils within the bioceramic resulted in an approximately 6.5-fold increase, from 2.7 ± 0.5 kPa for the gelMA casted on top of the ceramic, without microfibril interlocked within ceramic, to 17.7 ± 2.0 kPa for the condition in which the fibres were embedded within the ceramic scaffold. Evaluation of the interfacial toughness showed a similar trend as the interfacial strength (**Supplementary Figure S5**). Interestingly, upon mechanical failure of the interface, the microfibrils remained well organized and anchored within the bioceramic material, as found by microstructural observation via scanning electron microscopy (SEM) (**Figures 7G,H**). Collapse upon shear occurred due to loss of adhesion integrity and delamination of the sole hydrogel component.

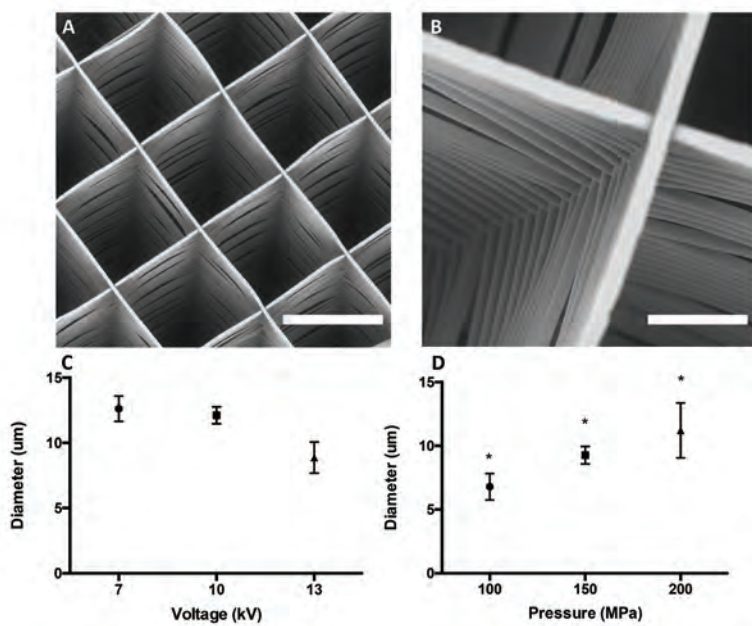


Figure 6. Micro-structure and printing parameters of the MEW fibrous scaffold. (A) and (B) SEM micrographs showing the architecture of the microfibril mesh produced by MEW (A: scale bar = 300 µm, B: scale bar = 50 µm), (C) Relationship between voltage and diameter of PCL microfibril for printing the MEW microfibril mesh. (D) Relationship between pressure and diameter of PCL microfibril for printing MEW microfibril mesh.

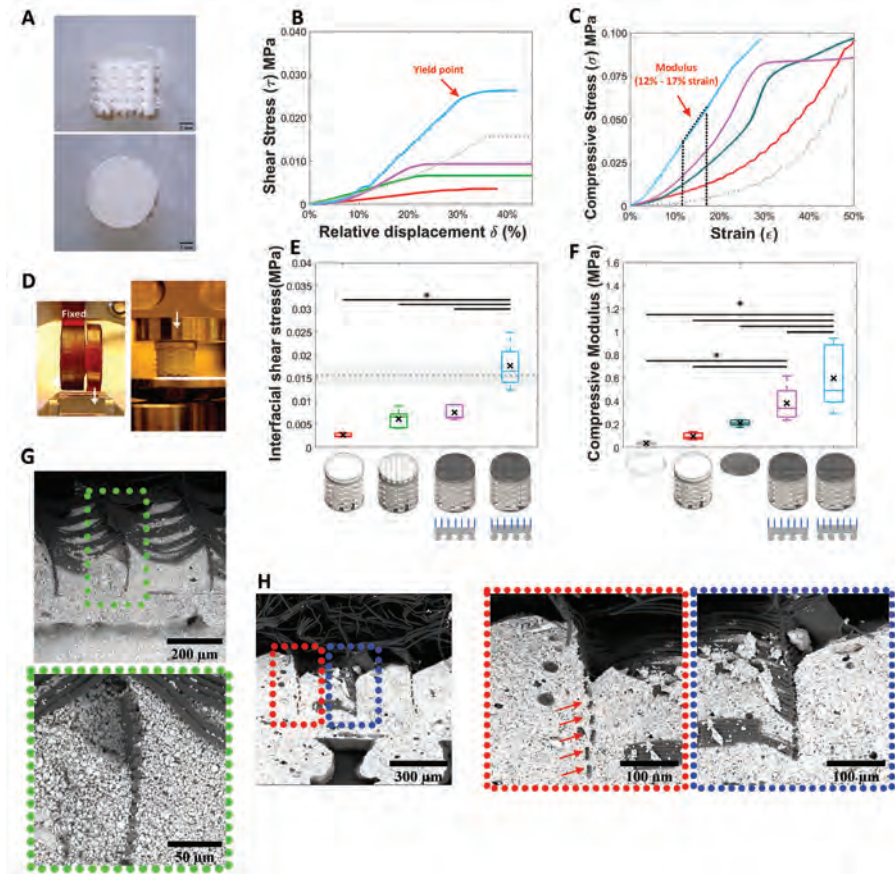



Figure 7. Mechanical properties of the osteochondral unit. (A) Osteochondral unit (scale bar = 1 mm.), (B) representative stress-displacement curves from interfacial shear stress assessment at the interface between the chondral and bone compartment, (C) representative stress-strain curves from compression assessment of chondral compartment, (D) mechanical testing (interfacial shear stress: left, and compressive modulus (right)), (E) interfacial shear stress of an engineered osteochondral unit showing alterations due to differences in either interfacial architecture or compositions (gelMA on ceramic (unmodified surface; red), gelMA on ceramic (modified surface; bright green), microfibre reinforced gelMA on ceramic (non-anchor fibre; pink), microfibre reinforced gelMA on ceramic (anchor fibre; blue) and monolithic gelMA hydrogel (mean (grey dotted line) \pm SD (grey filled area))), (F) compressive modulus of chondral compartment showing alterations due to difference in composition (gelMA alone (grey), gelMA over flat interfacial surface of pCaP (red), microfibre reinforced gelMA alone (dark green), microfibre reinforced gelMA on ceramic (non-anchor fibre; pink), microfibre-reinforced gelMA on ceramic (anchor fibre; blue)), (G) SEM micrographs of cross sections of an osteochondral unit revealing embedded microfibres within non-macro porous layer of the bone compartment of newly fabricated structure and (H) after interfacial shear stress assessment.



The observed yield shear stresses were slightly above that of gelMA itself (15.6 ± 2.4 kPa), as measured by submitting a monolithic gelMA hydrogel to the shear test. In contrast, for the biphasic hydrogel-bioceramic the fracture was propagated along the interface between hydrogel and bioceramic. Taken together, these results suggest that the MEW microfibrinous mesh acts as a bridge between the bony and cartilage compartment in the engineered plug, and that the stability of the interconnection could be further improved employing hydrogels with higher shear strength than gelMA, as well as with strategies to covalently graft the hydrogel component to the thermoplastic microfibrines.¹⁸¹ An important implication of using MEW-microfibrines is their ability as reinforcing elements, to remarkably improve the mechanical properties of otherwise soft hydrogels. Previous work demonstrated the ability to enhance the stiffness of gelMA-based constructs, reaching compressive properties mimicking those of native cartilage⁹⁴, while computational modelling unravels the mechanisms beyond this behaviour.⁹³ In line, in the present study, an increment in compressive modulus was observed for the microfibre-reinforced gelMA structures (**Figure 7F**), with the orthogonal boxes structure architecture selected for the MEW-printed meshes. Importantly, properties were even further improved when the microfibrines were embedded within the bioceramic scaffold (3.2-fold versus reinforced hydrogels alone) (**Figure 7F**), approaching the values of healthy human knee cartilage.¹⁸² This was likely achieved through the stabilisation of the base of the MEW-printed structure and facilitated load transfer to the pCaP scaffold. Such stabilization could prevent early bucking of the stacked layers of microfibrines, which has been identified as the main cause of failure of MEW box-shaped meshes under compressive loads.⁹³ Also, the stabilization of the MEW fibres within the ceramic scaffold allows a more effective lateral confinement of the gelMA hydrogel upon axial compression, thus resulting in a stiffer response. Although interfacial strength is still lower than those found in the native, mature bone-cartilage boundary¹⁸³, this mechanical stabilization and reinforcing effect greatly facilitates the surgical handling of the engineered cartilage construct, as well as its implantation *in situ* by press-fitting into an osteochondral defect in a tissue explant model (**Figure 8A**).

To further investigate the potential of the multi-scale composite osteochondral plugs for the formation of cartilage-like matrix *in vitro*, the chondral reinforcing meshes were infused with articular cartilage derived progenitor cells (ACPC)-containing gelMA and constructs were cultured for 6 weeks. Constructs with (**Figure 8B**) and without the osteal C-pCaP anchor were tested, to evaluate the possibility to obtain neo-cartilage in the presence of a bone-supporting material. ACPCs remained viable within the microfibre reinforced gelMA and the deposition of the cartilage-like extracellular matrix was observed in both structures after 6 weeks of culture (**Figure 8C**).

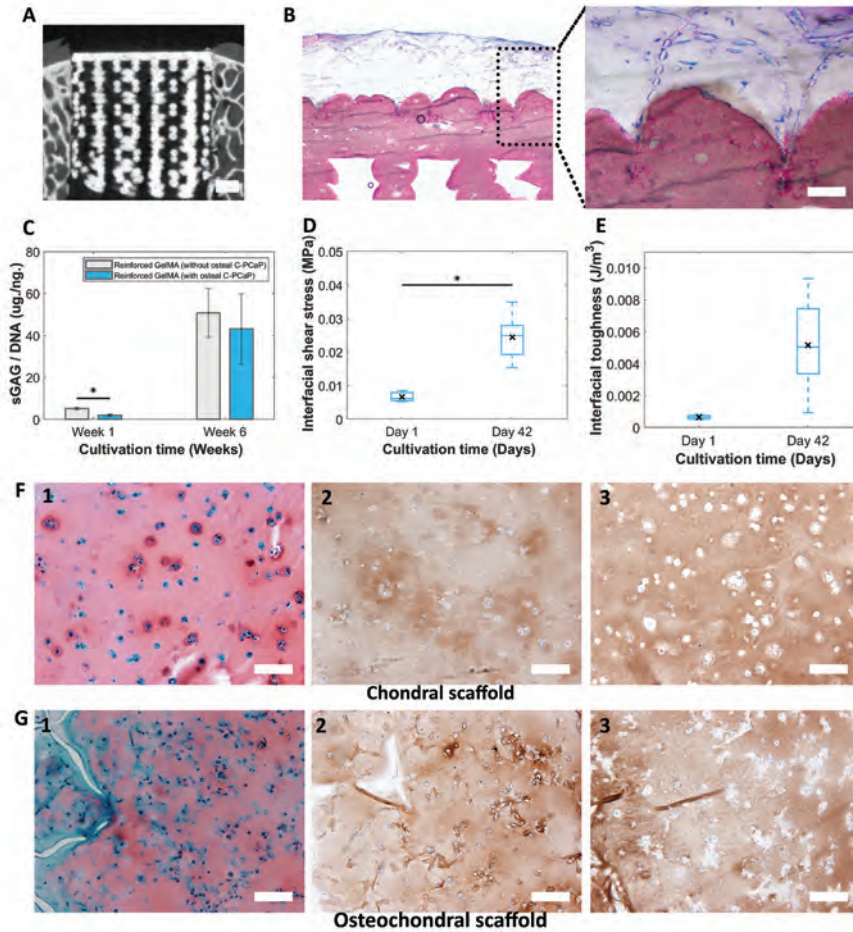


Figure 8. Cartilage deposition *in vitro* in the engineered osteochondral plug. (A) Micrograph obtained from micro-CT scanning showing a biomimetic pCaP scaffold that could be placed press-fit inside an *ex vivo* osteochondral defect. (Scale Bar = 1 mm), (B) basic fuchsin and methylene blue staining reveal pattern of embedded PCL microfibres inside the non-porous layer of the C-pCaP scaffold of the constructs with osteal C-pCaP anchor. (Scale Bar = 100 μ m), (C) quantification of sGAG in hydrogel per DNA content. (D) Interfacial adhesion strength and (E) interfacial toughness (day 1 and day 42) while applying shear force at the interface between equine ACPCs encapsulated in gelMA and C-pCaP-based bone compartment. (F1), (G1) Safranin-O staining, (F2), (G2) type II collagen immunostaining and (F3), (G3) type I collagen immunostaining of paraffin embedded microfibre reinforced gelMA without osteal C-pCaP (F) and with osteal C-pCaP (G), respectively, after cultivation for 42 days. (Scale Bar = 100 μ m).



Additionally, the neo-synthesized matrix influenced the strength of the interconnection at the bone-cartilage interface of the cell-laden grafts, which improved approximately 3.7-fold from 6.6 ± 1.7 kPa at day 1 to 24.4 ± 6.5 kPa at day 42 (**Figure 8D**). Interfacial toughness showed a similar trend (**Figure 8E**). Histological evaluation by means of safranin-O staining revealed sGAG deposition (**Figures 8F1, G1**). Type II collagen (Col II) production was also detected in both chondral (**Figure 8F2**) and osteochondral constructs (**Figure 8G2**), respectively. Type I collagen (Col I) deposition was also detected via histological analysis (**Figures 8F3, G3**). Col I is often present as an immature marker in gelMA-based constructs^{158,184} and can be reduced by incorporation of hyaluronan into the hydrogel matrix.¹⁸⁵ These results underscore that the differentiation of ACPCs towards the chondrogenic lineage is not hampered by the calcium phosphate-based scaffold, suggesting that the construct can be safely used for testing of osteochondral repair techniques.

Overall, a dual reinforcing effect (compression stiffness and interfacial shear strength) was achieved using the combination of ceramic extrusion printing and microfibre electrowriting. Moreover, the coordinated fabrication of such organized, multi-scale composite structures offers new possibilities for functional restoration of damaged osteochondral units. This approach can be further refined by tuning both biological and mechanical properties of the constructs, taking advantage of the physiological setting kinetics of the pCaP ink. Besides facilitating the formation of a tight engineered cartilage-to-subchondral bone connection and supporting osteogenesis *in vitro*, low-temperature setting cements hold the potential to incorporate growth factors (i.e. to enhance osteoinductive and angiogenic properties¹⁸⁶, or even the simultaneous printing of ceramic and hydrogel embedded living cells¹⁵⁰). With this in mind, the co-printing in a single biofabrication process of cell-friendly ceramics, cell-laden hydrogels and electrowritten microfibres, can be envisioned to comprehensively capture the architecture of native tissue interfaces. In fact, although in this study gelMA was infused in the chondral compartment of the construct, MEW and extrusion-based bioprinting can already be converged in a single biofabrication process, for instance to mimic phenotypic gradients within tissues, such as the zonal cell distribution in articular cartilage.¹⁵¹ Likewise, as more convoluted microfibre reinforcement geometries can be produced in the hydrogel compartment, specifically designed microfibre motifs could be incorporated to further enhance shear resistance¹⁸⁷, or even to improve tensile behaviour¹⁸⁸, the latter with potential application towards the regeneration of tendon and ligament-to-bone interfaces.

Conclusions

In this study, we demonstrate a novel approach to mechanically integrate hydrogel-based soft tissues to a stiff, bone-like material with potential application for the regeneration hard-to-soft tissue interfaces, in particular in case of osteochondral plugs. To achieve this, a multi-scale printing approach, combining ceramic extrusion 3D plotting and the electrowriting of thermoplastic microfibrils, was developed. Importantly, the mechanical properties of each compartment (bone, cartilage, interface) can be controlled through the internal architecture of both the reinforcing microfibre mesh and porous bioceramic by means of printing. Additionally, such an approach relying on low stiffness, electrowritten meshes, provides hydrogel strengthening and compressive properties comparable to native cartilage, without shielding cells from beneficial mechanical loads. Owing to the compatibility of the operating physiological temperatures and environmental conditions used for the printing and setting of the pCaP ink, direct anchoring of electrowritten PCL structures in the cement material could be achieved. All materials used, as well as the composite structure, had no impact on cell survival and hence permitted bone and cartilage engineering *in vitro*. This approach offers a promising opportunity for designing interfaces and composite materials with multiple applications in connective tissue regenerative medicine. Overall, these results provide important cues for the biofabrication of a next generation of multi-material, composite tissues and interfaces, which could integrate 3D printed elements mimicking living tissues down to the micron range.

Acknowledgements

The authors would like to thank Anneloes Mensinga and Mattie van Rijen for the assistance with cell culture and the histological analysis. The authors also wish to acknowledge the funding support from the Royal Thai government scholarship (Thailand, PD), the Dutch Arthritis Association (LLP-12 and LLP22) and the European Research Council under grant agreement 647426 (3D-JOINT). The primary antibodies against type II collagen (II-II6B3) developed by T F Linsenmayer and E S Engvall, respectively, were obtained from the DSHB developed under the auspices of the NICHD and maintained by the University of Iowa, Department of Biology, Iowa City, IA, USA.



Supplementary data

Supplementary methods

X-ray diffraction pattern

X-ray diffraction patterns were recorded with a Bruker D8 Advance system (Bruker, Karlsruhe, Germany) in a 2Theta range from 20-40° with Cu K α radiation (40 KV/ 40 mA) with a step size of 0.02° and a total measurement time of 1 s/step. Quantification was performed by Rietveld refinement analysis using Topas software (Bruker, Germany). The amorphous content of the samples was calculated using the G-factor method with a crystalline corundum reference according to Hurlé *et al.*¹⁸⁹

3

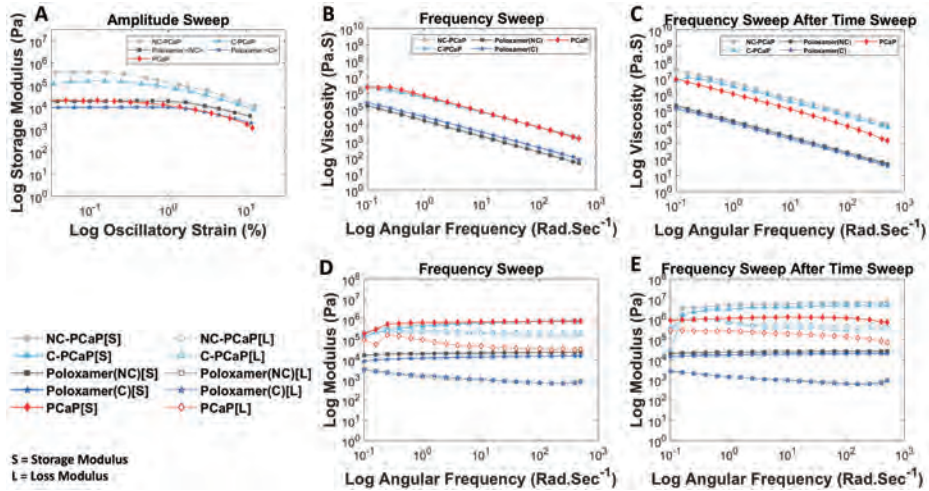
Supplementary data

Amount of cells	Day 3	Day 7	Day 14
Mean	1602.62	6568.07	10201.17
Standard Deviation	± 570.00	± 3256.64	± 5992.86

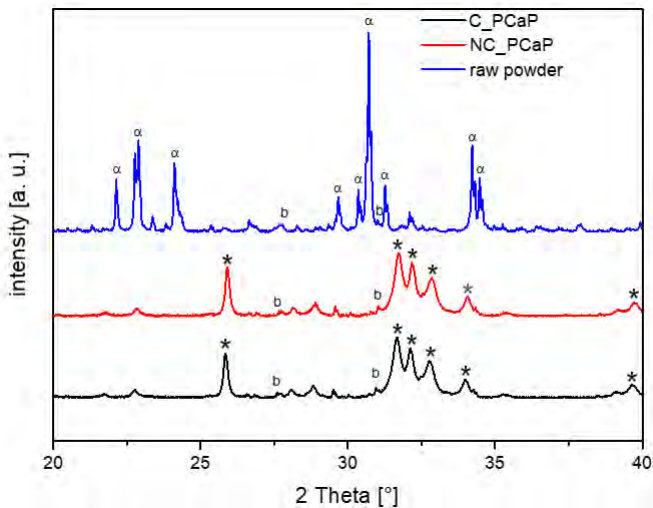
Supplementary Table 1. Proliferation of equine MSCs on C-pCaP scaffolds during cultivation for 14 days

Sample	α -TCP [%]	Hydroxyapatite [%]	β -TCP [%]	Amorph [%]
Powder	94.2	1.5	4.3	15
C-pCaP	2.1	95.8	2.1	35
NC-pCaP	1.8	95.2	3.0	32

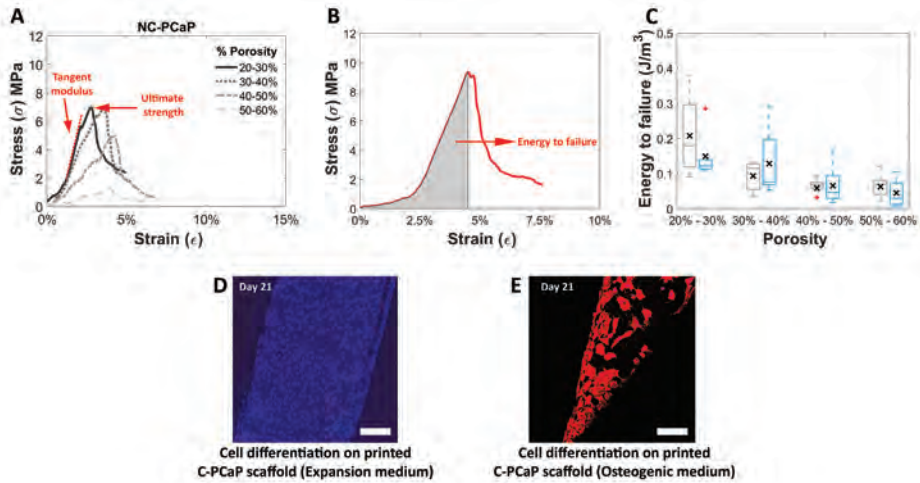
Supplementary Table 2. Quantification of the XRD patterns by Rietveld refinement (TOPAS software, Bruker, USA), showing the conversion of α -TCP to an apatite phase.



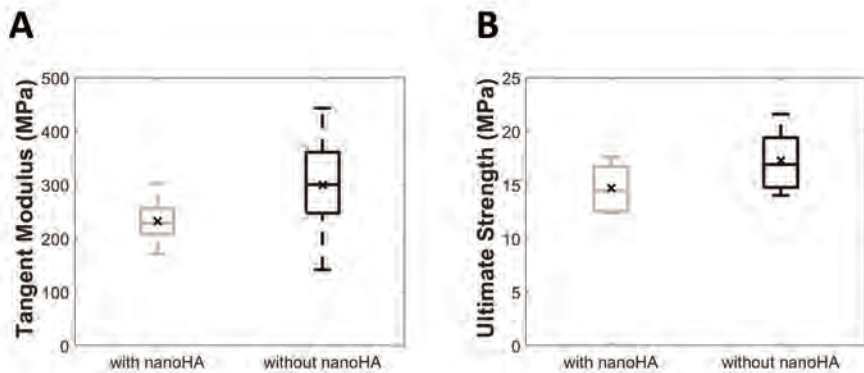
Supplementary Figure S1. A; Amplitude sweep representing LVR, B; Frequency sweep (relationship between angular frequency and complex viscosity), C; Frequency sweep (relationship between angular frequency and complex viscosity, obtained by using same material after performing time sweep test), D; Frequency sweep (relationship between angular frequency and modulus), E; Frequency sweep (relationship between angular frequency and modulus, obtained by using same material after performing time sweep test).



Supplementary Figure S2. X-ray diffraction patterns of raw powder and scaffolds. Diffraction peaks in the raw powder can be assigned to crystalline α -tricalcium phosphate (PDF-No.: 09-0438) with a minor fraction of β -tricalcium phosphate (PDFNo.: 09-0169, marked with "b"), possibly present as minor impurity in the α -TCP particle formulation. The fabricated scaffolds consisted of low crystalline hydroxyapatite (PDF-No.: 09-0432) from hydrolysis of α -TCP, as shown by the typical broad peaks peculiar of CDHA formation¹⁹⁰, while the β -TCP fraction remained unreacted. (α = α -TCP, b = β -TCP, * = CDHA).



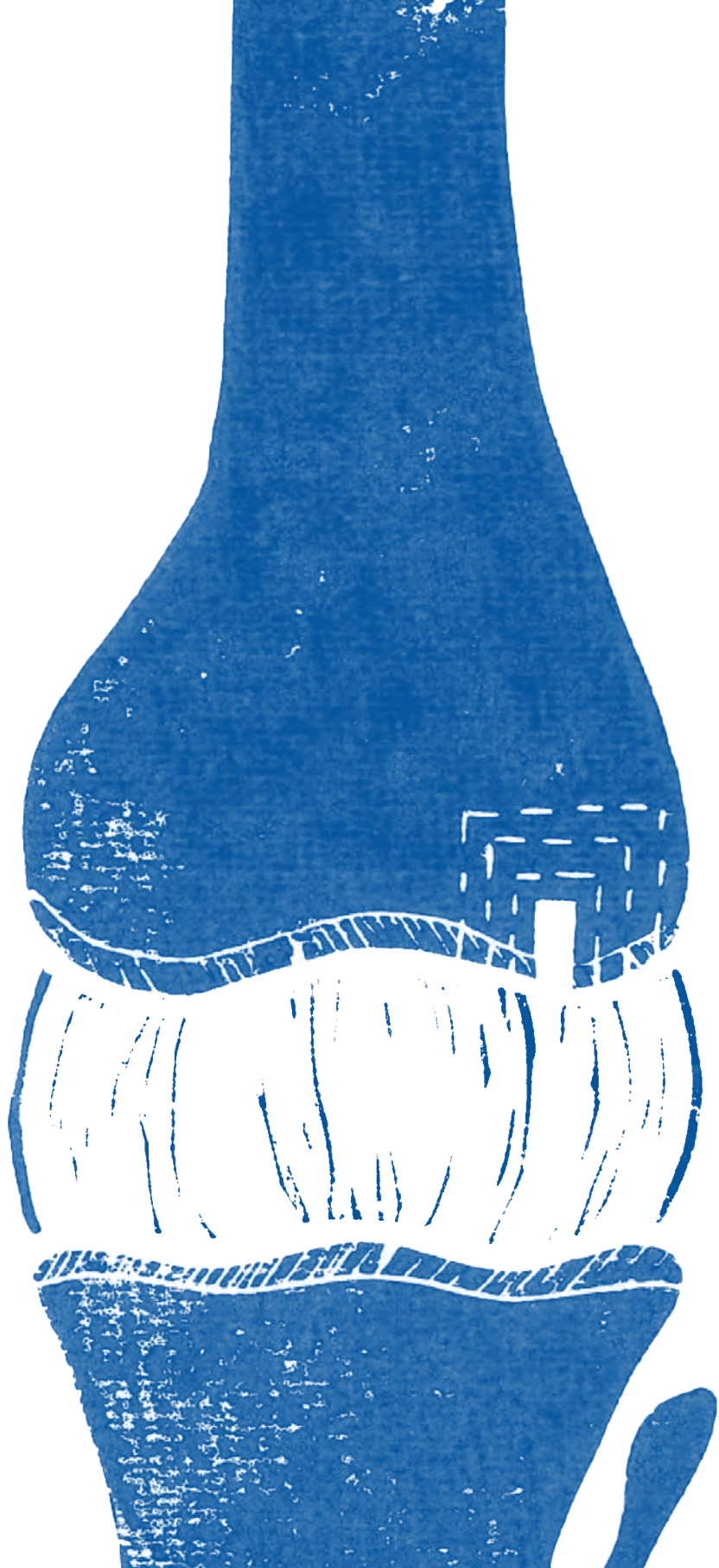
Supplementary Figure S3. A; Tangent Modulus of hardened cement structure produced from composition of α -TCP with and without nano-hydroxyapatite; B; Ultimate strength of hardened structure produced from composition of α -TCP with and without nano-hydroxyapatite. No significant differences were found between the two groups, suggesting that the added nanoHA does not have a relevant impact on the compressive properties of the produced cement. (n = 6 for each group).



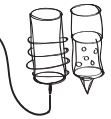
Supplementary Figure S4. A; Representative stress-strain curves of NC-PCaP scaffolds at different porosities showing how to calculate tangent modulus and ultimate strength. B; Representative stress-strain curve showing how to calculate energy to failure. C; Energy to failure of NC-PCaP paste (grey) and C-PCaP paste (blue) scaffolds with different porosities. D; Merged image between fluorescence staining of nucleus (dapi: blue) and osteonectin protein (osteonectin: red) of equine MSCs that were cultured on a C-PCaP scaffold for 21 days in an expansion medium showed no sign of osteogenic upregulation. (Scale Bar = 100 μ m.). E; Merged image between fluorescence staining of nucleus (dapi: blue) and osteonectin protein (osteonectin: red) of equine MSCs that were cultured on a C-PCaP scaffold for 21 days in an osteogenic supplement medium showed signs of osteogenic upregulation. (Scale Bar = 100 μ m.).

Supplementary video SV1

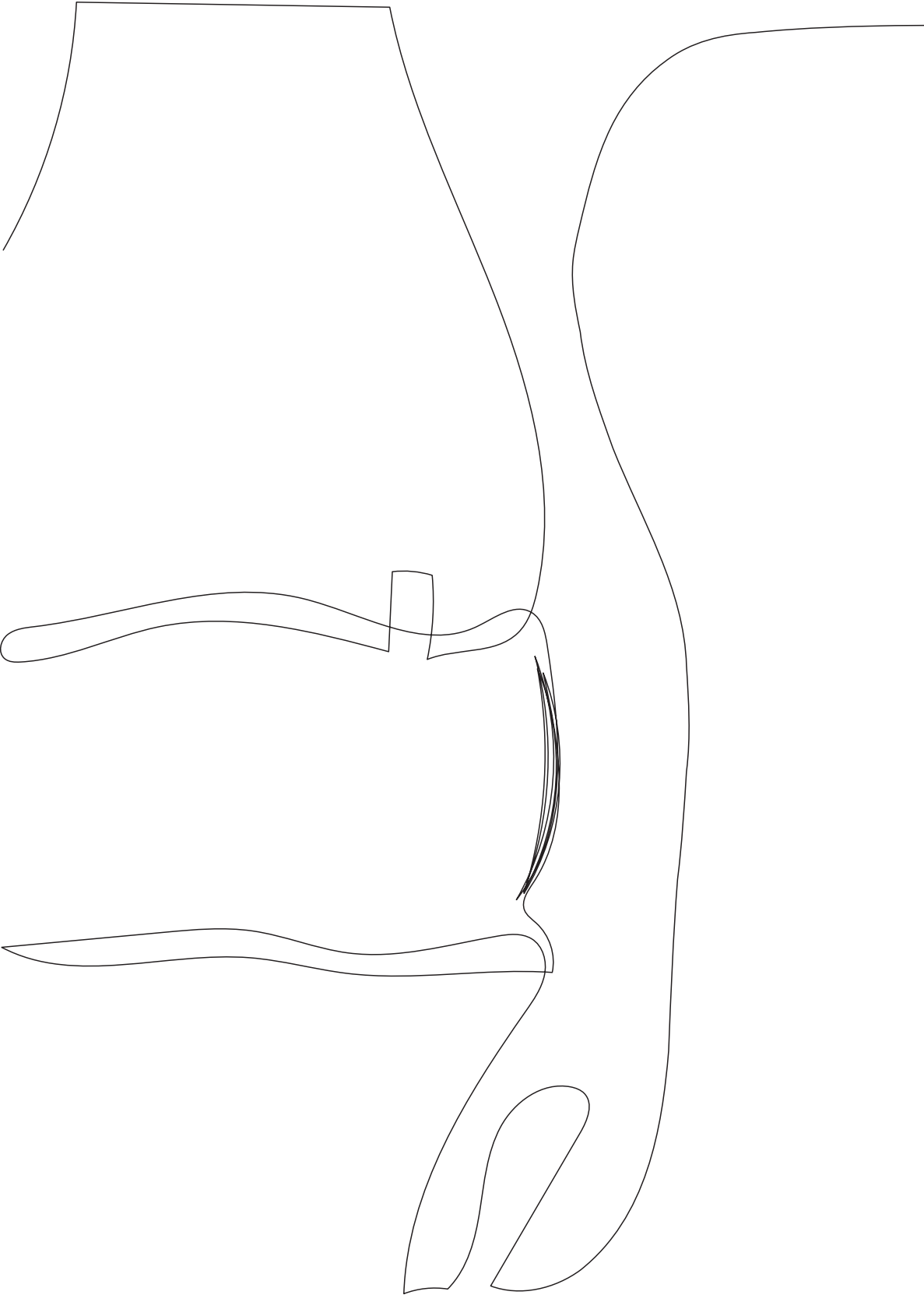
Video showing the open and interconnected porosity within the inner structure of the porous 3D printed scaffolds, as shown through a series of μ -CT sections of the constructs. (This can be accessed through: <https://iopscience.iop.org/article/10.1088/1758-5090/ab69d9#supplementarydata>)



Part II



Incorporating melt electrowriting in
the bioprinting process for multi-scale
biofabrication





Chapter 4

4

Multi-technology biofabrication: a new standard for manufacturing of functional tissues

Miguel Castilho^{1,2,3*}

Mylène de Ruijter^{1,3}

Stephen Beirne⁴

Claire C. Villette⁵

Keita Ito^{1,2,3}

Gordon G. Wallace⁴

Jos Malda^{1,3,6}

Published in Trends in Biotechnology (2020)

DOI: 10.1016/j.tibtech.2020.04.014

¹ Department of Orthopaedics, University Medical Center Utrecht, Utrecht, The Netherlands

² Orthopaedic Biomechanics, Department of Biomedical Engineering, Eindhoven University of Technology, Eindhoven, The Netherlands

³ Regenerative Medicine Center Utrecht, Utrecht, The Netherlands

⁴ Intelligent Polymer Research Institute, and ARC Centre of Excellence for Electromaterials Science, University of Wollongong, Wollongong, Australia

⁵ Structural Biomechanics, Department of Civil and Environmental Engineering, Imperial College London, London, United Kingdom

⁶ Department of Clinical Sciences, Faculty of Veterinary Sciences Utrecht University, Utrecht, The Netherlands

Abstract

Most available 3D biofabrication technologies rely on single-component deposition methods, such as inkjet, extrusion, or light-assisted printing. It is unlikely that any of these technologies used individually would be able to replicate the complexity and functionality of living tissues. Recently, new biofabrication approaches have emerged that integrate multiple manufacturing technologies into a single biofabrication platform. This has led to fabricated structures with improved functionality. In this review, we provide a comprehensive overview of recent advances in the integration of different manufacturing technologies with the aim to fabricate more functional tissue structures. We provide our vision on the future of additive manufacturing (AM) technology, digital design, and the use of artificial intelligence (AI) in the field of biofabrication.



From Cell Therapy to the Biofabrication of Tissues and Organs

Every day, ~18 people die in Europe alone due to the shortage of human donor organs. In 2017, it was estimated that only 19% of 34 000 patients on waiting lists for organs would receive an organ transplant.¹⁹¹ To overcome this, great efforts have been devoted to regenerative medicine (RM) strategies that could restore damaged tissues and organs. Since first appearing during the early 1960s, regenerative strategies have come a long way from the first stem-cell transplantation¹⁹² to the 3D biofabrication (see Glossary) of artificial tissue-like structures of today.¹⁹³

Stem-cell therapies have proved successful when applied to diseased or injured tissues in small animal models, such as rodents.¹⁹⁴ Unfortunately, clinical trials in large animal models and humans have rendered conflicting results, with the best scenarios supporting only minor benefits mostly regarded as nonregenerative and limited to paracrine effects.¹⁹⁴ This situation has not been improved significantly by the use of 3D cellular aggregates with improved cell–cell interactions and a protective self-secreted extracellular matrix (ECM) layer.¹⁹⁵ More recently, developmental biologists have shown that cultured pluripotent stem cells can differentiate into organ-specific cells and further self-organize into small 3D organ-like structures, such as intestinal or kidney organoids.^{196,197} However, none of these strategies or *in vitro* organ developmental approaches have yet shown the ability to recreate biological structures with the functional richness, multi-scale structure, and size of a living tissue.^{195–197}

It is known that living tissues comprise some of the most complex and hierarchically functional materials and are composed of different cell types and ECM components, including bioactive molecules and structural elements. The complex interplay between the components of native tissue suggests that, to recreate tissue equivalents that result in a functional *in vivo* outcome, the tissue equivalent should be as similar to the native tissue organization and composition as possible. Bioprinting, one of the main emergent biofabrication approaches, allows the *in vitro* fabrication of biological constructs with precise combinations of cells and biomaterials, while complimentary digital manufacturing processes enable biological structures to be shaped into the geometry of the target tissue or organ.¹⁹³ Biofabrication comprises a growing toolbox of a range of fabrication strategies, of which the most established are droplet, extrusion, light- and laser-assisted bioprinting. Each of these strategies has a different working principle, which has its own associated advantages and drawbacks with regards to cell processing, resolution and material selection (**Box 1 and Figure 1 A**). So far, researchers have predominantly adopted a single fabrication strategy based on the target tissue composition and/or size. However, similar

challenges as for cell-based therapies and *in vitro* organ developmental approaches have been observed (i.e., limited ECM deposition and organization, and absence of required functionality).⁸⁰ These challenges are mainly due to insufficient synergy between material composition and organization, because the self-organization capacity of cells was not sufficient enough to recreate tissue functionality and single fabrication approaches are not mature enough to recreate the tissue mimicking environment to guide those cells.

Box 1

Single Deposition Biofabrication Methods Mimic Shape but Compromise Function

The cornerstone of bioprinting lies in sequential layer-by-layer material deposition, which allows the manufacturing of anatomically inspired tissue equivalents potentially from patients' own cells. Since their first description during the early 21st century, the focus has been on four bioprinting technologies: droplet⁴³⁵, extrusion²⁶⁰, light^{172,373} and laser⁴³⁶ based bioprinting. Until now, the majority of these technologies have relied on a single deposition method, which cannot fully replicate the complexity and composition of living tissues.

Droplet-based bioprinting, which involves selective deposition of cell-containing material droplets, can produce 3D structures from more than one cell suspension with micron resolution, but cannot achieve biologically relevant cell densities (achieved cell density <10⁶ cells/ml)⁴³⁵ or large tissue sizes (achieved size <3 cm thickness).^{437,438}

Extrusion-based printing, which encompasses the selective dispensing of a material through an extrusion nozzle, allows for the deposition of more physiologically relevant cell densities, yet compromises on printing resolution (achieved resolution >100 μm), and prevention of cell damage during extrusion remains challenging.^{372,439} Further research showed that

electrohydrodynamic biofabrication technologies, which combine extrusion-assisted printing within an electrical field, can increase resolution down to the submicron range and, therefore, potentially resemble the complex ECM microenvironments of biological tissues; however, cell compatibility and low reproducibility are still of concern.⁴⁴⁰

Light-based bioprinting, which comprises the selective solidification of a cell-containing hydrogel layer by applying a light energy source (e.g., UV or visible light), is not limited by shear stresses and typically allows for the manufacture of volumetric constructs (cm scale)³⁷³ with considerably higher resolutions (>50 μm).¹⁷² Important disadvantages are related to the limited flexibility regarding the use of multicell types and material combinations. By contrast,

laser-based bioprinting involves the selective application of a pulsed laser to an absorbing layer, containing a cell-laden hydrogel ink, which induces the transfer of a cell-hydrogel droplet to a receiver substrate.⁴³⁶ The innovative contactless material deposition involved in this bioprinting strategy allows for higher cell densities than the previously discussed bioprinting technologies. However, its potential to print large, volumetric structures and incorporate multiple biological components requires further attention. One limitation that is common to all the described manufacturing technologies is the low mechanical resistance of the bioprinted constructs. To date,

most bioprinting technologies use intrinsically weak hydrogels that can provide the right conditions for cell survival, yet fail to withstand the harsh mechanical environment observed *in vivo*.^{336,381}

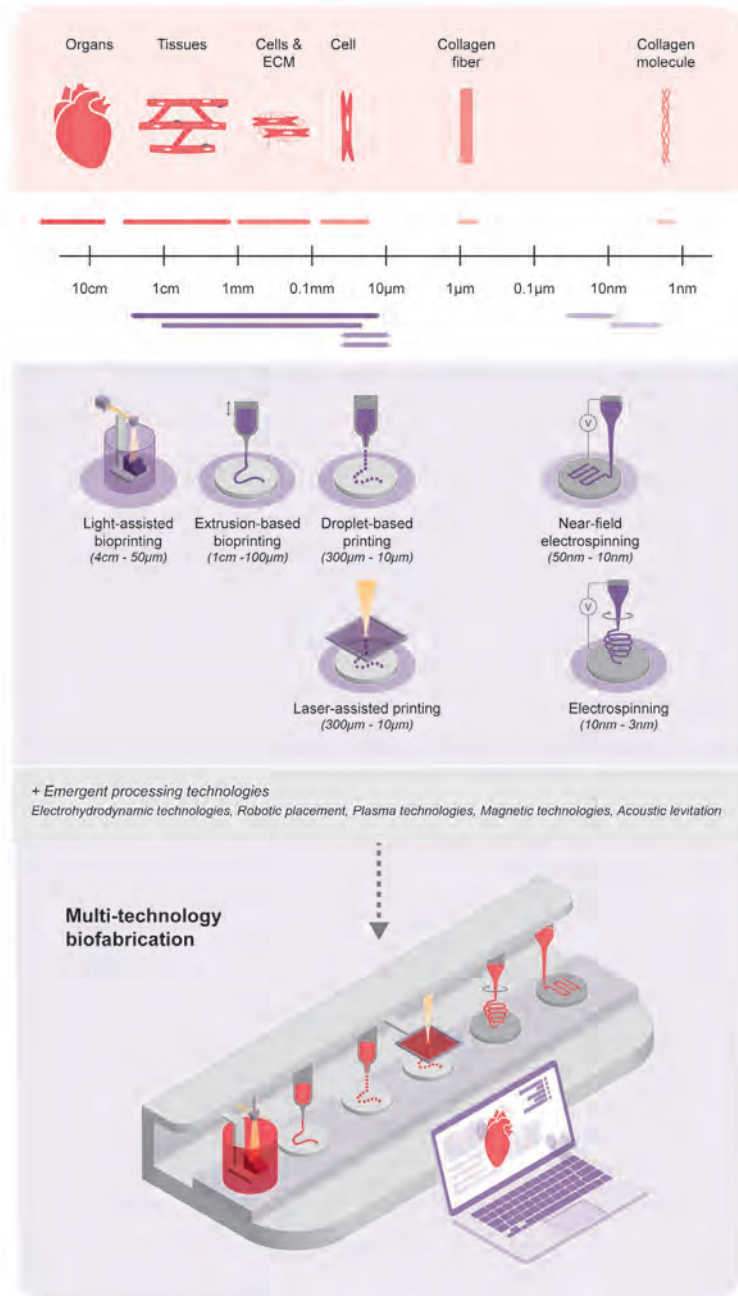


Figure 1. Schematic Illustration of Multitechnology Biofabrication. (A) Comparison of the typical operation length of single deposition biofabrication technologies with the size and hierarchical structure of tissues and organs. (B) In-process variation of printing length scales and simultaneous material processing potential when complementary biofabrication technologies are combined in a single-printing platform. Abbreviation: ECM, extracellular matrix.

We believe that an important current development in the evolution of manufacturing functional tissue and organ structures is the potential to combine different manufacturing processes into a single biofabrication platform (**Figure 1B**). Recent evidence suggests that the simultaneous use of complementary fabrication processes allows for the strategic arrangement of multiple cells and ECM components at different length scales, taking us closer to the heterogeneous composition and complex multi-scale organization of living tissues.¹⁹³ Additionally, recent advances in information technologies enable user-friendly access to **AI** systems that provide help for optimal design and decision making, and with that accelerate progress in manufacturing of tissue mimicking equivalents.

Here, we provide an overview of the current advances on combining biofabrication technologies and discuss opportunities and challenges for converging existent and emerging processing technologies towards functional tissue manufacturing. Furthermore, we identify future directions, in particular how **digital design** can be synergized with multitechnology biofabrication platforms. In a decade of exponential growth of information technologies, particularly machine learning and AI, we believe that numerical technologies when coupled to advanced bioprinting systems will have a key role in realizing high-throughput fabrication of **functional living tissues**.

Convergence of Biofabrication Technologies

What Is Multitechnology Biofabrication?

Multitechnology bioprinting can be defined as the integration of complementary fabrication technologies into a single biofabrication platform, wherein they operate in a synergistic manner to deliver living, functional constructs. Complementary processes can include different, but compatible, component deposition methods, such as the primary bioprinting classes reviewed in Box 1, but also other emergent manufacturing technologies, such as fibre deposition methods, magnetic technologies, acoustic levitation, or plasma technologies.

The foreseen integration of complementary technologies in a single-printing platform is not a trivial challenge, but would allow in-process variation of printing length scales, materials, and deposition methods, which is a clear deviation from trends in the conventional 3D (bio-)printing space. True convergence can only occur where the interchange between different manufacturing techniques occurs automatically without the need for operator intervention, thus moving away from existing multistep assembly methods. Furthermore, while most bioprinting techniques have inherent commonality in the use of three-axis positioning systems, there are distinct differences in the resolution



and positional accuracy of these systems, as well as the software used to manage them. Convergence will lead to hardware design compromises, where higher resolution (and more expensive) positioning systems necessary for high-resolution deposition techniques have to be used for low-resolution systems. Additionally, in process characterization technologies (e.g., optical or ultrasound) and appropriate software to enable the detection of cell damage and print errors, and subsequent adaptation, will be required. These adaptive software tools will potentially need to determine whether a printing process has 'failed' or if it can be 'recovered' by adapting printing parameters or trajectories, so that machine efficiency as well as efficient use of cell-laden bioinks is maximized. It is here that the use of AI will become fundamental for accounting for all printing scenarios and parameters selection. In addition, these digital tools will help in determining the optimal shaping of bioprinted constructs to guide matrix deposition for functional tissue formation.

In our opinion, multitechnology biofabrication represents a paradigm shift in tissue manufacturing because it allows the combination and spatial organization of different cell types and biological or artificial components, which is not possible with single-process printing methods or conventional manufacturing processes. This current trend in the fabrication of living tissues is observed in the most recent scientific literature, as reviewed later.

Converged Biofabrication Technologies and Increased Functionality of Manufactured Tissues

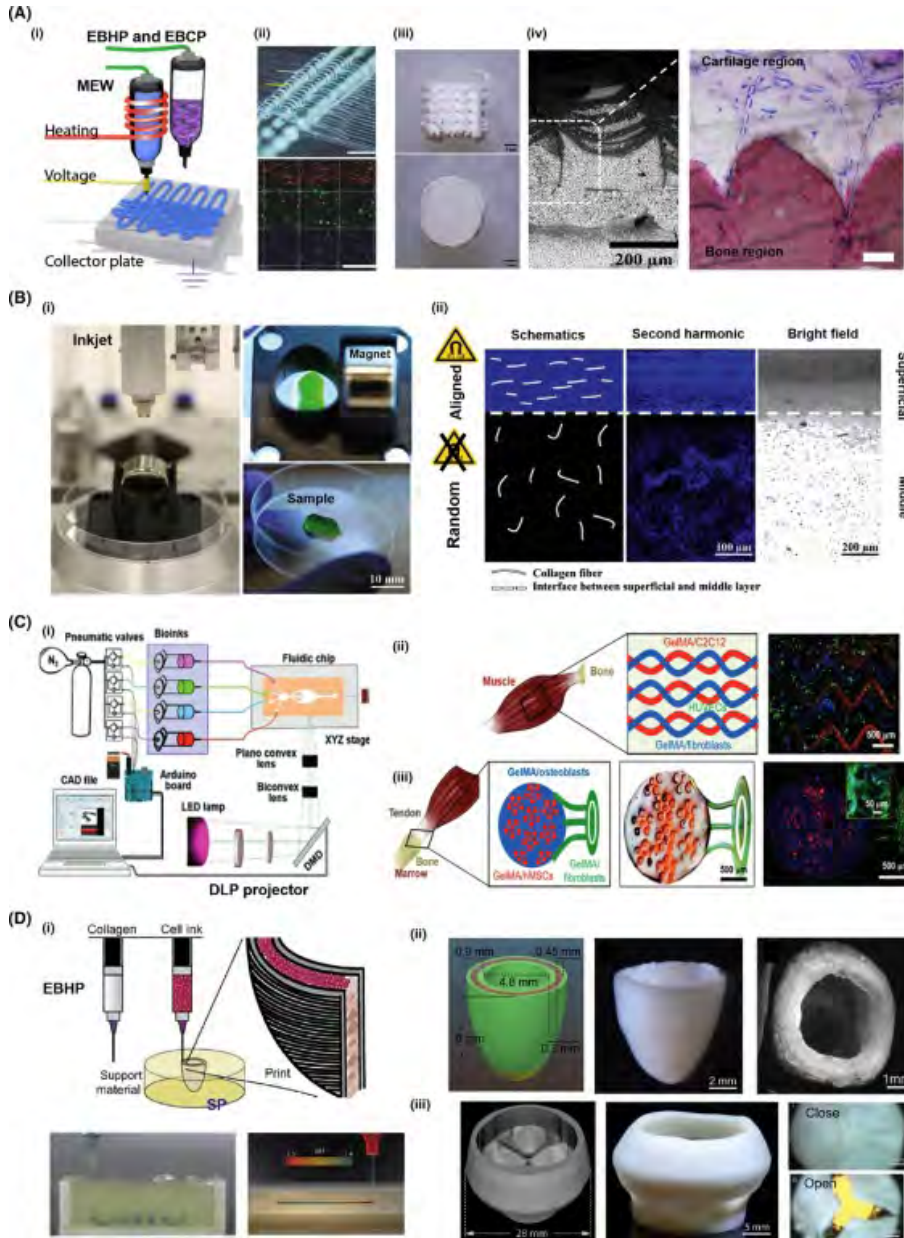
While the first report on leveraging functionality of biomedical devices by combining 3D printing technologies with traditional manufacturing methods dates back to the 1990s¹⁹⁸, only very recently have researchers focused on integrating the working principles of different biofabrication technologies to enhance the functionality of artificially generated tissues. One of the earliest reports presented the combination of electro-driven fabrication technologies with bioprinting strategies, in particular, the combination of melt spinning technologies with extrusion^{199,200} or light-assisted bioprinting²⁰¹. For example, melt electrowriting (MEW) and extrusion-based bioprinting have been successfully integrated in a single biofabrication platform, allowing for the fabrication of constructs with a spatial distribution of different cell types and improved mechanical functionality without compromising cell viability and differentiation (e.g., cartilage¹⁹⁹ and osteochondral tissue repair²⁰²) (**Figure 2A**). This combination of technologies provided the groundwork to solve one of the current biofabrication conundrums, namely the lack of biomechanical properties of the bioprinted constructs. From a scale-up perspective, the lengthy

fabrication time of the fibre technologies (e.g., >1 h for MEW constructs with 600 mm³)¹⁹⁹ remains a challenge and negatively impacts cell viability due to hydrogel drying. We anticipate that future hybrid fibre-cell printing apparatus will move from the conventional multinozzle approach towards gradually implementing needleless printheads. A similar strategy is already used for industrial-scale production of fibre yarns.²⁰³ Alongside this strategy, we foresee that the collector platform could be implemented on a climatized, fluid nebulizer system that could prevent hydrogel drying and maintain cell survival during extended manufacturing times. This will require further decoupling of the high-voltage components from the main components of the climatization platform, and the design of low-conductivity fluids that experience minimal effects within electrical fields.

An alternate combinatorial approach that can precisely control the local material composition and orientation on printed structures is the combination of magnetic fields with droplet-²⁰⁴ or light-based printing technologies²⁰⁷. For example, Betsch and coworkers incorporated a magnetic field into a droplet-based bioprinter to align chondrocyte-loaded collagen fibres during bioprinting (**Figure 2B**), while Martin and colleagues proposed a hybrid system that integrates magnetic control with digital light processing (DLP) to fabricate graded composite structures, including an 'osteon-like' microstructure.²⁰⁷ A major limitation of present set-ups is the low intensity and the bidirectionality of the magnetic field generated (in the milli-tesla range, and along collector plate plane). To overcome this, we anticipate that the next generation of droplet- or light-based bioprinter could be placed inside large magnetic coils, preferably covering the three cartesian coordinate axes (X, Y, and Z), which could generate higher intensity magnetic fields (in the tesla range)

Figure 2. Examples of Multitechnology Biofabricated Tissues with Improved Material Combinations and Hierarchical Structures.

(A) (i) Osteochondral implant obtained by extrusion-based thermoplastic printing (EBHP) and melt electrowriting (MEW); (ii) MEW fibres of polycaprolactone (PCL) guided over a pluronics hydrogel strand; (iii) osteochondral unit comprising a GelMA hydrogel reinforced with a MEW printed fibre scaffold at the chondral region and a printed calcium phosphate (CaP) at the bone layer. (iv) SEM image and histology section of cross-section of the osteochondral unit revealing embedded MEW fibres within the (CaP) region and new cartilage and bone tissue being formed at the chondral and osteo regions, respectively. Scale bars: 500 μm (ii) and 100 μm (iv). (B) (i) Chondrocyte-laden constructs with a zonal collagen organization obtained by combining inkjet bioprinting with a magnetic field; (ii) collagen bioinks with aligned collagen fibres in a superficial layer increase the compressive properties of printed structures. (C) (i) Skeletal muscle strip and tendon to bone interphase obtained by combining an extrusion-assisted microfluidic chamber with digital light processing. (ii) Muscle strip comprising interwoven GelMA containing C2C12 cells (red) and gelMA containing fibroblast (blue) filaments; (iii) tendon-to bone insertion containing patterned gelMA with osteoblasts (blue), human mesenchymal stem cell (hMSC; red), and fibroblasts (green) filaments. (D) (i) Human-scale ventricle model and trileaflet heart valve printed by extrusion-based hydrogel printing inside a suspended bath; (ii) ventricle model comprising cardiac cells (pink) and supporting collagen shells (green); (iii) trileaflet heart valve supporting pulsatile flow. Reproduced under a Creative Commons Attribution Non-Commercial License CC BY-NC from ¹⁹⁹ (A2) ; reproduced with permission from²⁰⁴ (B), ²⁰⁵(C), and ²⁰⁶(D).



and control the direction of the field throughout a spherical volume. Special attention will have to be paid to ensure that the magnetic forces do not interfere with the operation of the dispensing systems being used.

Other emerging approaches comprise extrusion-based printing with light-based bioprinting²⁰⁵ or sacrificial support materials²⁰⁸. Such strategies have the potential to process biologically relevant materials that were previously marked as 'unprintable', while maintaining high cell viability and allowing for the fabrication of tissue-like constructs with biologically relevant structures and sizes. For example, Miri and co-workers integrated an automated extrusion-based microfluidic chamber with DLP in a single bioprinting device (**Figure 2C**). By combining multiple cell-laden hydrogels at high cell densities and with refined spatial resolution, sophisticated biological structures, such as a skeletal muscle strip and a tendon-to-bone insertion on a millimetre size scale, were achieved.²⁰⁵

The groups of Feinberg, Miller, and Grover developed a suspended layer bioprinting process that has been shown to allow the fabrication of complex biological systems on a centimeter scale.^{148,208,209} A microgel suspension (fluid gel) was used to structure a secondary extrusion-based printed cell-laden solution, which was cured post printing and subsequently removed as a separate construct. This allowed a range of different living tissue structures to be printed, from an osteochondral unit of 2 mm in height¹⁴⁸ to a trileaflet heart valve of ~3 cm in diameter (**Figure 2D**).²⁰⁶ Although this approach deviates from the combination of two or more technologies into a single device, it is, in our opinion, also a form of multitechnology biofabrication because it merges the principles of in-liquid printing, initially introduced by the stereolithographic systems, with conventional extrusion-based printing. Moreover, this approach shows great promise towards tackling organ fabrication upscaling and vascularization challenges, and might become one of the most impactful technologies in the biofabrication field if converged with other emerging fabrication technologies, such as acoustophoresis.^{210,211} We foresee that, by manipulating acoustic waves in bulk fluid gels, or even directly in cell-suspended media, it will be feasible to improve cellular organization and further introduce an extra level of control over the cellular nano and microenvironment. The first hybrid apparatus of this configuration will potentially implement low-frequency sound generators positioned around the suspended bath container. Focus should lie on preventing interference of resonant frequencies with the bioprinter hardware. Additionally, acoustic field propagations and forces in cell-laden biological fluid gels should be controlled.

Furthermore, promising results on improving cell–material interactions and in directing stem cell behaviour have been reported by combining extrusion-based bioprinting with plasma technologies²¹² or droplet-based printing.²¹³ The combination of atmospheric



plasma and extrusion-based printing allowed the selective introduction of biological cues (e.g., different growth factors) on extruded polymer filaments, which can potentially guide and accelerate tissue renewal.²¹² Alternatively, Liu and coworkers combined extrusion-based printing with inertial force jetting, a derivative of droplet-based bioprinting that uses alternated viscous and inertial force jetting. This integrated method allowed the precise deposition of cells on designated locations, thereby inducing cell interactions at a distance of <math><100\ \mu\text{m}</math>.²¹³ In this process, fine control of cell distribution was achieved through imaging of an extrusion-based printed cell-laden material to manually determine the ideal locations for single cell depositions. We envision that the next progressive steps will be incorporating the co-extrusion of materials to achieve a gradient in cell densities in the bulk substrate and automation of the required secondary cell location, in short, adaptive gradient control. An overview of current efforts towards multitechnology biofabrication and their main characteristics is summarized in **Table 1**.

Table 1. Representative Examples of Converged 3D (Bio)fabrication Technologies³

Converged technologies		Cell printing	Main characteristics	Refs
AVIF	EBHP	Yes	Structuring cell/biomaterials with 100- μm precision	213
DLP	EBHP	Yes	Control over cell and biological gradients; flexibility over multi-material deposition	205
EBCP	MEW	Yes	Improved soft–hard interface tissue regeneration and interfacial strength	202
	MEW	Yes	Improved mechanical properties of soft cell-laden hydrogels; control over reinforcing architectures	199
EBHP	A	Yes	Control over macro and microarchitectural characteristics of living tissues; contact-less cell organization	211
	SP	Yes	Tissue upscaling; incorporation of large cell densities and viable vasculature networks	214
	MES	No	Fabrication at larger length scale (macro and micro)	200
EBTP	AP	No	Guided new cell and new tissue formation by biomaterials functionalization with biologics	212
	EBHP	Yes	Anatomically shaped constructs; improved mechanical properties of soft microtissues	215
IJ	M	Yes	Optimal for anisotropic living tissue fabrication; contact-less control of micro and nano-sized bioinks	204
	SE	Yes	Tissue upscaling; improved mechanical properties of soft microtissues	216
SL	SE	Yes	Guided new tissue formation and improved mechanical properties of soft microtissues	201

³ Abbreviations: A, acoustophoresis; AP, atmospheric plasma; AVIF, alternating viscous and force jetting; DLP, digital light processing; EBCP, extrusion-based cement printing; EBHP, extrusion-based hydrogel printing; EBTP, extrusion-based thermoplastic printing; IJ, inkjet; M, magnetophoresis; MEW, melt electrowriting; MES, melt electrospinning; SE, solution electrospinning; SL, stereolithography; SP, suspended printing.

From Digital Design to ‘Semiautonomous’ High-Throughput Devices

The idea of engineering living tissues by digitally controlling the organization of tissue equivalents based on model predictions is both intriguing and potent and, in our opinion, will have a key role in the development of high-throughput biofabrication of functional tissues. The boost in computational power, big data collection, and AI techniques have the potential to enable systematization, automation, and control of design and biofabrication. Together with rational digital design technologies grounded on formalized scientific experience and mechanistic understanding, supervised and unsupervised machine learning should be harnessed to support semiautonomous biofabrication solutions to complex design problems.

Digital Design Technologies for Instructed Bioprinting

Typically, the flexibility of bioprinting draws from numerous design parameters, including multi-scale architecture, material composition, and dynamic cell–cell and cell–material interactions.^{217,218} Understanding and predicting the effect of multiple interacting design features involves different disciplines and creates a challenge in developing design principles and strategies for functional 3D bioprinting. Various tissue-engineering (TE) design parameters are interdependent, and conflicting objectives need to be addressed in the design, such as the necessity for both significant scaffold stiffness and high porosity, in the case of bone TE.²¹⁷ Interdependent and conflicting design parameters and objectives require comprehensive methodical optimization techniques^{219,220}, which can only realistically be solved using computing.

Optimization techniques involve building numerical models of the multiphysics processes at play in a bioprinted construct to predict the influence of design parameter changes on the construct properties. ‘Parametric design’ is well suited to these aims, and refers to a design methodology that is built on algorithmic thinking and relies on the definition of a family of initial parameters and the relationships they keep with each other and with the final design. Parametric design naturally enables systematic parameter space exploration and subsequent selection of optimal design parameter set.²²¹ Another powerful digital design approach that is well established in structural/mechanical engineering is topology optimization, where the best distribution of material within a selected design space is numerically derived to comply with a set of constraints.²²² 3D fabrication appears to synergize with topology optimization because it allows for practical production of the resulting organic shaped structures that are often incompatible with conventional fabrication techniques. Promising attempts have been made at implementing topology



optimization for TE construct designs, in particular to jointly meet both stiffness and permeability criteria.^{219,220,223}

Despite these computational advances, bioprinting designs still rely on arbitrary parameter selection and decisions are made based on a trial and error approach. This suboptimal design methodology incurs substantial costs in both time and expenses related to *in vitro* or *in vivo* experiments.²¹⁷ Computational efficiency is one of the greatest current obstacles to the large-scale use of digital design optimization for bioprinting constructs. Microscale continuum models are used to predict the mechanical behaviour of the scaffold with a resolution relevant to cellular processes. In addition, inclusion of multi-scale, multiphysics, time-dependent phenomena, such as fluid–solid interactions and mechanobiology processes, dramatically increases the number of variables to solve.^{224,225} A common solution to overcome computational complexity is to reduce the scope of the simulation to a smaller number of structural elements^{224,226} although the direct implication is the necessity to use homogeneous cellular structures. We envision that implementing ‘soft computing’ techniques, such as metamodels, to integrate empirical evidence and human-like ‘vagueness’ in computational modeling will significantly increase the design flexibility and leverage design-centered biofabrication for better biomimicry.^{227–229} AI techniques, including regression models and neural networks²³⁰, are ideal candidates for such fast-running metamodels, with only limited reduction in accuracy compared with complex multiphysics mechanistic models. Empirical knowledge that is not directly or homogeneously interpretable by humans can be harnessed via unsupervised machine learning.²³¹

Flexible and ‘Semiautonomous’ Bioprinting Platforms for Functional Tissue Fabrication

We envision that the next generation of bioprinters will become more practical, user-independent, ‘semiautonomous’ systems. Advances such as process parameter selection and real-time monitoring of cell function and material properties during bioprinting will become commonplace. Given that functional tissue fabrication also includes complexity in anatomical design, it is conceivable that collaborative robotic systems (robotic arms) will work in unison to create functionally heterogeneous structures; however, this will not be viable if the positional accuracy and software control of these robotic arms cannot at least match the accuracy of more established three-axis platforms. Up to now, conventional approaches to biofabrication have relied on deposition technologies integrated with three-axis positioning systems. In most cases, this means that structures are deposited onto planar substrates. This inherent requirement is a limitation that is not representative of the natural anatomical relevant structures that the biofabrication field aims to recreate. Several groups have taken inspiration from established computer numerical control (CNC)

machining techniques to include additional axes, such as a fourth rotary axis beneath the deposition head to produce structures of increasing complexity on cylindrical mandrels, including radial stents²³² and valve structures²³³.

Moreover, as a means to work outside of the restrictions of automated positioning systems, there are a growing number of examples of handheld, freeform biofabrication^{234,235} devices with the intent to rapidly translate advances in biomaterials research into the clinical environment. Operation of these devices is reliant on the surgeon's expertise and fine motor control to directly deposit biomaterials to the *in vivo* point of need. To mimic the surgeon's motion in an automated platform, it is necessary to begin using six-axis robotic arms. Multi-axis robotic arms will not only facilitate handheld biofabrication, but also significantly improve the process flexibility of multitechnology bioprinting platforms, allowing cell and/or biomaterial deposition onto clinically relevant geometries and facilitating the interchange between printing technologies. However, adopting these systems will present challenges to the biofabrication research community due to the need for significantly more sophisticated control programming and user interface development. Current digital design tools, slicing algorithms, and tool path generation software, typically outputting G-code instructions, are not compatible with robotic system language. Therefore, we envision that the already interdisciplinary biofabrication field will need an influx of advanced robotics engineers and computer engineers as the use of systems with increased degrees of freedom becomes more common. In addition, we foresee that AI will be fundamental for linking digital design tools with control instructions for positioning systems. Due to the fabrication constraints of some bioprinting technologies, specific AI algorithms will have to be developed to automatically remove unnecessary geometrical features from digitally design models and adequately position objects within the building substrate. For example, bioprinting technologies, such as EHD, operate in the base of a single, continuous filament deposition, while light-based technologies require homogeneous light penetration, which will significantly limit tool path direction and cell distribution on a converged set-up.

The next generation of multitechnology bioprinters will also encompass real-time inline monitoring of the printing process through combinations of machine vision, inspection sensors, and feedback control systems so that deviation from preplanned designed structures can be detected and the printing process automatically adjusted to compensate for the error. We believe that a profound impact will be seen from the area of machine vision, extending the application of AI to monitor and control the bioprinting process. To make this feasible, three main challenges must be solved. First, optical- and laser-profiling technologies will have to be integrated into the multitechnology bioprinting platforms to allow for screening of biofabricated constructs within different length scales (i.e., at



both the cellular and tissue/organ scale). Here, the use of lens-free microscopes should be attractive due to their small form factor, only a few cm³, and their potential to monitor dynamic biological processes without the need for cell labels.²³⁶ An alternative ‘machine vision’ strategy was shown by Ruland *et al.* with a quantitative ultrasound imaging system that allows for cell growth and new tissue formation monitoring within bioprinted constructs.²³⁷ Second, different inspection sensors, such as speed, material reservoir volume, temperature, CO₂ and O₂, humidity, and pH, will have to be integrated in the printing platform to monitor key instrument parameters and environmental conditions. The first imperative steps to integrating sensors for motion/vibration, temperature, and humidity within standard 3D printers have already been taken.²³⁸ Third, specific AI software for bioprinting will have to be developed to analyse the large data sets that are collected from machine vision and inspection sensors. Based on the information gathered, AI will have to produce real-time predictions on how printing parameters (e.g., dispensing rate, light intensity, fabrication temperature, collection speed, and/or printing chamber environment conditions) should be adapted to correct identified flaws on bioprinted constructs. AI will also be essential to identify crossover points between multiple fabrication technologies and incompatible printing parameters. However, reliable AI algorithms will have to be trained based on test cases and first be proven with simple technology and material combinations before full technology convergency. Here, deep neural networks is perhaps the most promising AI method due to the large data set that can be processed and recent experience with the specificities of each technology.²³⁹

Concluding Remarks and Future Perspectives

We are now at the crossroads where biofabrication technologies have opened exciting perspectives to restore or replace damaged tissues and organs, although each technology individually has not yet been able to deliver functional tissue structures of biologically relevant size. The integration of complementary fabrication technologies in a single-printing platform has recently given rise to what we believe is a new biofabrication era (see Outstanding Questions). The in-process variation of printing length scale and different material processing capabilities of multitechnology biofabrication platforms is a clear deviation from conventional 3D (bio-)printing, which is opening new perspectives for the fabrication of hierarchical structures with relevant sizes and combinations of different cell types and ECM components. Examples of functional multitechnology bioprinted constructs are diverse, ranging from mechanical robust articular cartilage constructs that are manufactured by melt-spinning technologies and extrusion-based bioprinting, to skeletal muscle strips obtained by extrusion-assisted microfluidic chamber combined with digital light processing, and human-sized trileaflet heart valves manufactured by merging extrusion-based printing with suspended manufacturing. Further evidence of the impact and potential of multitechnology bioprinting in the RM field are the different

commercially available multitechnology bioprinters recently introduced by bioprinting companies.

However, one of the current challenges is that the complexity of the equipment is increasing exponentially, making multitechnology printers more viable in a laboratory environment than for clinical use. Alternatively, the realization of less complex systems customized for particular applications is beginning. For example, handheld devices are gaining more attention for *in situ* fabrication of 'outer tissues', such as skin, cornea, and cartilage. In addition, we believe the recent advancements in multiaxis robotic systems will allow printing onto surfaces that more closely resemble the contours of natural structures in our body, while inspection sensors and real-time monitoring of the printing process will improve process reproducibility. In parallel, we believe that AI will have an important role in this new biofabrication era. Given that humans can only analyse limited information simultaneously, new multitechnology biofabrication hardware will be powered by AI tools to aid simultaneous monitoring of printing parameters and printed parts. To help in organizing our view, we have developed a conceptual model that illustrates how multitechnology bioprinters could be used in a future patient treatment process chain (**Figure 3**)

Finally, another important challenge that remains is the synergistic potential of the combination of digital design and biofabrication. Integrated computer models of biosystems, as well as numerical optimization techniques, are key for the fast and reliable design and manufacture of advanced functional biological and biomedical constructs. Smart and flexible computing will be pivotal to enable on-demand tailored and cost-effective biofabrication solutions to complex design problems. In our opinion, the next-generation biofabrication systems should transcend native tissue structural replication and actively direct promote the development of functional tissue structures.

Outstanding Questions

- Can we further recapitulate the functionality of native tissue by combining complementary manufacturing technologies into a single biofabrication platform?
- Which biofabrication technologies can successfully be combined and which combinatorial approaches can achieve the required resolution and material combinations to further mimic tissue structure, composition, and function?
- How can we achieve high-throughput biofabrication?

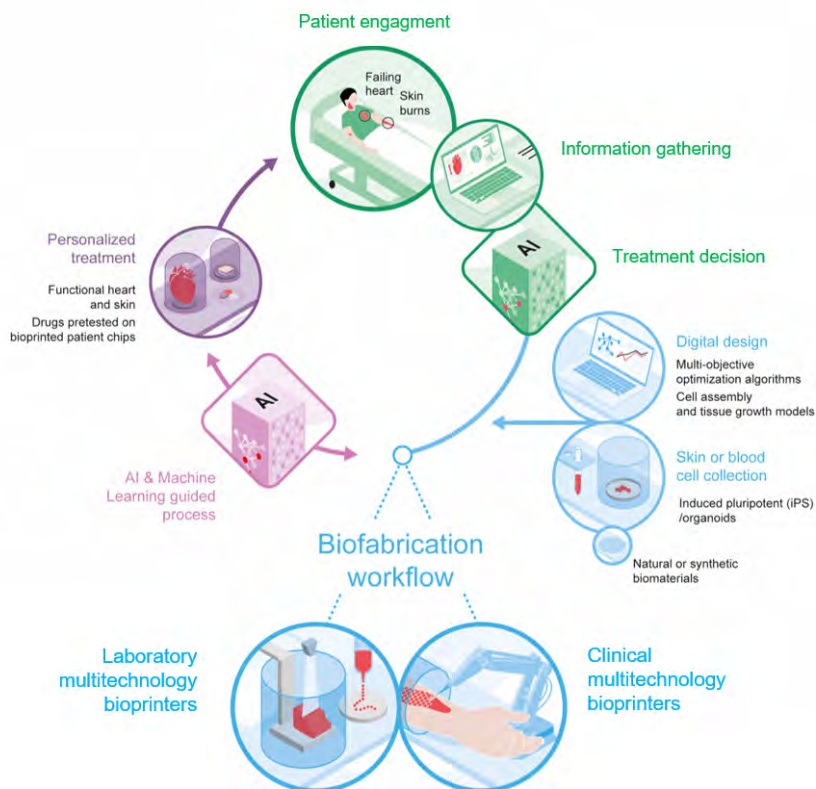


Figure 3. How Will Multitechnology Bioprinters Improve Patient Care? Example of a future patient treatment process chain where multitechnology bioprinters will support artificial tissue and organ fabrication. The process chain starts with a patient engaging with the healthcare system after experienced health problems, such as a failing heart and skin burns (Step 1. Patient engagement). Then, the gathering of patient clinical information begins based on physical examinations and diagnostic tests (Step 2. Information gathering). Subsequently, a treatment decision is taken by clinicians with the support of artificial intelligence (AI) algorithms to facilitate the integration and classification of lesions or affected organs (Step 3. Treatment decision). Depending on the affected tissue, two biofabrication routes will be followed: *in situ* tissue bioprinting for outer tissue fabrication using simple multitechnology bioprinters (clinical multitechnology bioprinters) and laboratory tissue bioprinting for solid organs and personalized organ-on-a-chip fabrication using a more complex combination of bioprinting technologies (laboratory multitechnology bioprinters) (Step 4. Biofabrication workflow). Biofabricated tissues will be developed from the patient's own cells [induced pluripotent stem cells (iPSCs) or organoids] and combined with natural or synthetic materials. Tissue organ design will be conducted by using a digital design tool and the biofabrication process will be assisted by AI algorithms. The personalized heart, skin, and drug (tested on patient chips) are then delivered to the patient (Step 5. Personalized treatment).

Acknowledgments

The authors would like to acknowledge support from the strategic alliance University Medical Center Utrecht–Utrecht University–Eindhoven University of Technology and funding from the partners of Regenerative Medicine Crossing Borders powered by Health~Holland, Top Sector Life Sciences & Health, ReumaNederland (LLP-12 and LLP22), the European Research Council (Grant Agreement No. 647426, 3D-JOINT), and the Netherlands Organization for Scientific Research (Materials Driven Regeneration, 024.003.013). Funding from the Australian Research Council Centre of Excellence Scheme (CE 140100012) and ARC Industrial Transformation Training Centre Scheme (IC160100026) is also gratefully acknowledged. The authors would also like to thank the Australian National Fabrication Facility-Materials Node (ANFF).

Glossary

Acoustophoresis (AP) and magnetophoresis (MP)

arranging microparticles and/or cells by applying a controlled acoustic or magnetic field, respectively, to a material.

Artificial intelligence (AI)

set of numerical algorithms able to make decisions without being explicitly programmed.

Biofabrication

automated generation of biologically functional products with structural organization from living cells, bioactive molecules, biomaterials, and cell aggregates through bioprinting or bioassembly and subsequent tissue maturation processes.

Digital design

process of generating 3D models with a computer-based software followed by evaluation of their performance (e.g., structural, mechanical or biological) using numerical simulation tools.

Digital light processing (DLP)

process of generating a 3D structure by light- or laser-assisted resin curing.

Droplet-based

process of accurate droplet deposition by generating pulses in the nozzle with acoustics (piezoelectric or ultrasound) or fluctuations in air pressure (microfluidic systems).



Electrohydrodynamic processing

generation of nanometre to micrometre-scale fibres by establishing an electrical field between the deposition material and collecting surface; includes solution electrospinning, melt electro-spinning, and writing

Extrusion-based printing

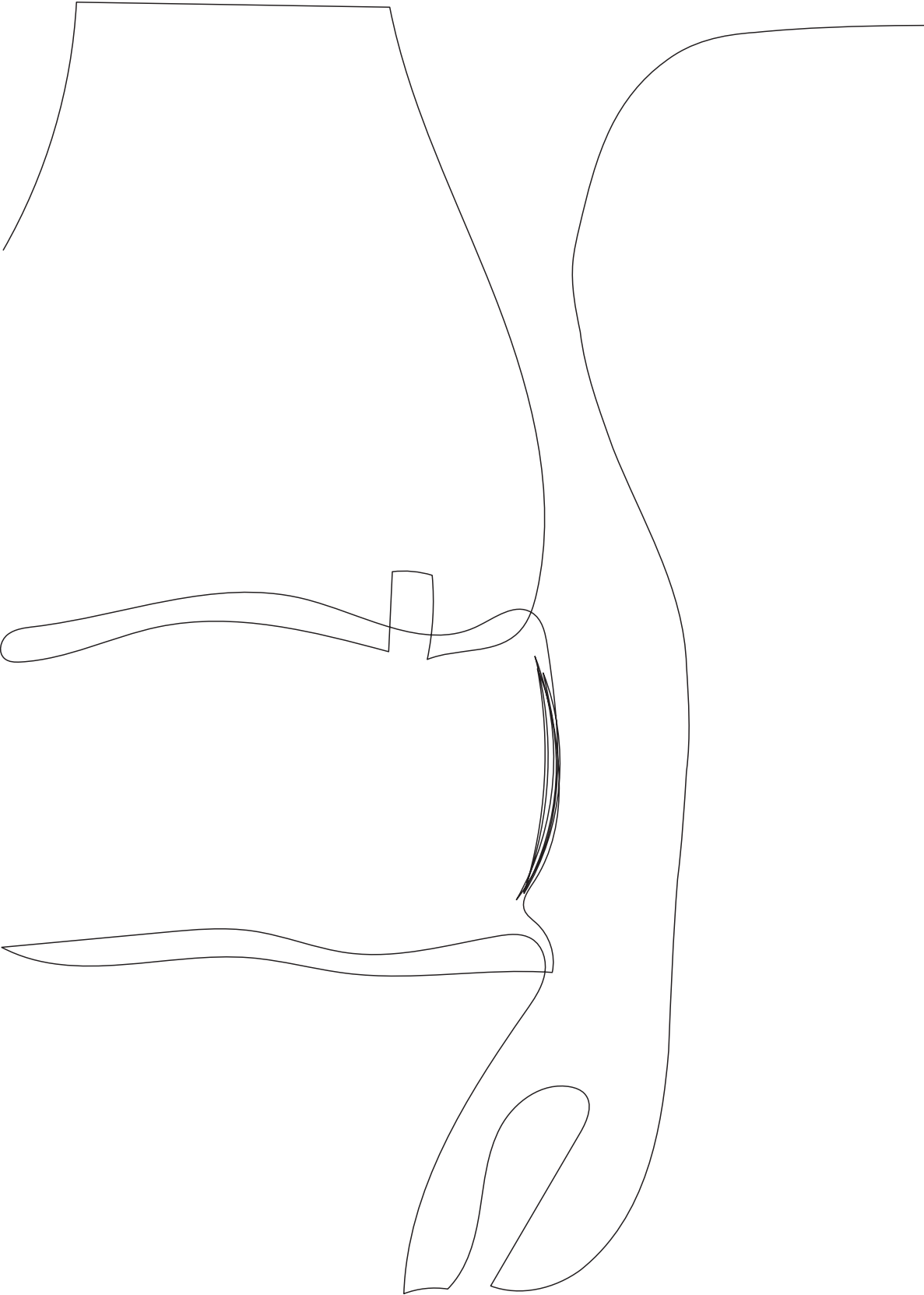
(micro)-extrusion of a material through a nozzle to allow fibre deposition in a layer-by-layer fashion. Extrusion can be regulated pneumatically, or by use of a mechanical piston or screw system.

Inline printing process monitoring

access fidelity of cell/biomaterial deposition during the printing process using machine vision and inspection sensor systems of key printing parameters and printing environment conditions.

Multitechnology biofabrication

automated process that integrates complementary manufacturing technologies into a single biofabrication platform to produce biological structures. Integrated technologies operate in a collaborative way and allow in-process variation of printing length scale and simultaneous processing of different materials.





Chapter 5

Simultaneous Micro-Patterning of Fibrous Meshes and Bioinks for the Fabrication of Living Tissue Constructs

5

Mylène de Ruijter¹

Alexandre Ribeiro¹

Inge Dokter¹

Miguel Castilho^{1,2}

Jos Malda^{1,3}

Published in *Advanced Healthcare Materials* (2018)

DOI: 10.1002/adhm.201800418

Front cover 2019, special issue: Building Blocks for Biofabricated Models

¹ Department of Orthopaedics, RMCU Utrecht, UMC Utrecht, University of Utrecht, The Netherlands

² Department of Biomedical Engineering, Eindhoven University of Technology, The Netherlands

³ Department of Clinical Sciences, Faculty of Veterinary Medicine, Utrecht University, The Netherlands

Abstract

Fabrication of biomimetic tissues holds much promise for the regeneration of cells or organs that are lost or damaged due to injury or disease. To enable the generation of complex, multicellular tissues on demand, the ability to design and incorporate different materials and cell types needs to be improved. Two techniques are combined: extrusion-based bioprinting, which enables printing of cell-encapsulated hydrogels; and melt electrowriting (MEW), which enables fabrication of aligned (sub)-micrometer fibres into a single-step biofabrication process. Composite structures generated by infusion of MEW fibre structures with hydrogels have resulted in mechanically and biologically competent constructs; however, their preparation involves a two-step fabrication procedure that limits freedom of design of microfibre architectures and the use of multiple materials and cell types. How convergence of MEW and extrusion-based bioprinting allows fabrication of mechanically stable constructs with the spatial distributions of different cell types without compromising cell viability and chondrogenic differentiation of mesenchymal stromal cells is demonstrated for the first time. Moreover, this converged printing approach improves freedom of design of the MEW fibres, enabling 3D fibre deposition. This is an important step toward biofabrication of voluminous and complex hierarchical structures that can better resemble the characteristics of functional biological tissues.



Introduction

Biofabrication is a rapidly advancing field that uses bioprinting or bioassembly to create organized 3D structures that are biologically functional.²⁴⁰ These engineered biological constructs can be used for drug discovery and screening, for the development of *in vitro* models of human disease or ultimately, as implants to restore or replace damaged tissue.^{241–243} In order to successfully engineer a biologically functional construct, it is essential to stimulate neo-tissue formation and improve spatial organization and mechanical integrity as seen in native tissues.^{38,244,245} Extrusion-based bioprinting techniques are already used to generate hydrogel constructs that replicate some native tissue features, such as zonal organization of articular cartilage tissue, and can generate vascularized tissue structures, bone tissue gradients, and the air– blood barrier by using different materials, cell types, and cell densities.^{167,246–249} However, hydrogels that support extensive cellular differentiation are intrinsically soft and thus mechanically unstable.¹¹³ This challenge can potentially be resolved with fibre reinforcing strategies, including adaptation of textile techniques that enable fabrication of 3D-woven networks.^{250–252} However, these techniques are limited in control over material or cell deposition. Fused deposition modeling (FDM) does allow for hydrogel reinforcement and control over cell deposition. Unfortunately, the relatively low printing resolution ($\approx 200 \mu\text{m}$) of the reinforcing material with FDM limits space for tissue maturation^{82,102,150,181,253,254} and this reinforcing strategy usually fails to provide an adequate micromechanical environment for tissue differentiation.²⁵⁵ An alternative strategy to reinforce hydrogels involves the incorporation of sub-micron scale, organized fibre scaffolds generated by melt electrowriting (MEW).^{84,88,108,187,256} This electrohydrodynamic fibre writing uses a high voltage electrical field to form sub-micrometre fibres from polymer melts. Previous studies show that MEW fibres used to fabricate 3D screening devices to test cellular response to microstructures can facilitate the specific alignment of cells.^{169,257} However, this fabrication procedure requires a two- step approach—the fabrication of the fibre scaffold, followed by embedding a cell-laden hydrogel inside—which severely limits control over accurate deposition of multi-materials and cells, and subsequently the creation of hierarchical structures.

The aim of this study was to generate biologically functional constructs with more complex architecture and composition by converging MEW and extrusion-based bioprinting into a single- step manufacturing procedure. Here, we demonstrate that this combination increases freedom of design, while maintaining the specific advantages associated with each of the individual techniques.

Materials and Methods

Materials

The bioink for the cell experiments was 10% (w/v) gelatin methacryloyl (gelMA) (80% DoF, synthesized as previously described²⁵⁸) because of its high chondrogenic differentiation capacity²⁵⁹ and the crosslinker Irgacure 2959 (BASF, Ludwigshafen, Germany) was dissolved in phosphate-buffered saline (PBS) at 0.1% w/v. Pluronic F127 hydrogel (40% w/v in PBS) was used as a model-ink to study the ability to guide MEW fibres with a hydrogel template because of its high shape fidelity. Medical-grade polycaprolactone (PCL) (PURASORB PC 12, Lot# 1412000249, 03/2015, Corbion Inc., Gorinchem, The Netherlands) was used as MEW material.

Cells

Equine-derived mesenchymal stromal cells (eMSCs) were harvested at passage 3, embedded in 10% (w/v) gelMA at 20×10^6 cells mL⁻¹, and subsequently cultured in chondrogenic differentiation medium consisting of DMEM 41965 (Gibco) supplemented with penicillin/streptomycin (1%, Gibco), l-ascorbic acid-2-phosphate (0.2×10^{-3} m, Sigma Aldrich), ITS + Premix Universal Culture Supplement (1%, Corning), dexamethasone (0.1×10^{-6} m, Sigma Aldrich) and recombinant human TGF- β 1 (10 ng mL⁻¹) for 28 d, medium was refreshed twice per week. To show control over cell deposition, eMSCs were labeled with a Vybrant cell labeling kit (Thermo Fischer Scientific), according to manufacturer's protocol prior to encapsulation in gelMA. Confocal imaging was used to analyse cell distribution (Leica SP8X). To assess the effect of the fabrication conditions on the constructs, eMSC-laden 10% gelMA discs were cast, crosslinked for 15 min (UVP CL-1000 Ultraviolet Crosslinker), incubated for 0, 15, 30, 45, or 60 min, and cultured for 28 d. Metabolic activity was measured with an Alamar Blue staining (Resazurin sodium salt, Alfa Aesar) and cartilage-like matrix formation was quantified with a GAG/DNA analysis [Dimethylmethylene blue (DMMB, Sigma Aldrich, Picogreen, Quant-iT, Thermo Fischer Scientific)]. To evaluate if the cells were affected by the converged printing process, alternating layers of PCL fibres and gelMA (10% w/v; encapsulated with eMSCs) were fabricated. PCL fibres were deposited at 85 °C, with a collector velocity of 80 mm/s, pressure of 1.0 bar, collector distance of 6.0 mm, and with a voltage of 5, 10, or 15 kV. After printing, all samples were cultured for 28 d in chondrogenic differentiation medium and analysed for viability, metabolic activity, and chondrogenic differentiation with a LIVE/DEAD assay (Calcein, Ethidium homodimer, Thermo Fischer Scientific), GAG/DNA, Safranin-O, and collagen type II staining, respectively. An eMSC-laden cast disc was used as a control.



Scaffold Fabrication - Cast Scaffolds

Ten percent (cell-laden) gelMA samples were cast in discs using a Teflon mold at 15–18 °C and UV crosslinked for 15 min (UVP CL-1000 Ultraviolet Crosslinker).

Scaffold Fabrication - Converged Printed Scaffolds

Converged printing was performed in a single-step approach (3DDiscovery Evolution, regenHU). Scaffold design was either layer-by-layer deposition of MEW fibres and extrusion-based bioprinted (cell-laden) hydrogel, or deposition of gel inside the MEW squared structures (boxes). PCL fibres were deposited at 85 °C, with a collector velocity of 80 mm/s, 5.0 kV, 1.0 bar, and at a collector distance of 6.0 mm. Ten percent w/v gelMA was extruded with a pressure of 0.5 bar, at 15–18 °C, and a collector velocity of 25 mm/s. To investigate the possibilities of using a hydrogel to guide 3D MEW fibre deposition, different layers of hydrogel (Pluronic, 40% w/v, extruded with a pressure of 1.0 bar and a collector velocity of 22 mm/s, at room temperature) were printed in the x-axis direction, after which the MEW fibre was deposited in y-axis direction.

Mechanical Analysis

To analyse the mechanical properties of converged printed scaffolds, alternating layers of MEW PCL and 10% gelMA without cells were deposited. The MEW boxes had a line spacing of 400 µm and total scaffold height was 1.8 mm. The elastic peak and equilibrium moduli were assessed by unconfined compression using dynamical mechanical analysis (Q800, TA Instruments). Samples were prestrained at 20% strain followed by isostrain of 15 min. As a control, cast 10% gelMA discs (height = 2 mm, diameter = 6 mm) with and without MEW reinforcement were analysed.

Statistics

For samples that were used for mechanical analysis, an $n = 5$ was applicable; for samples including cells, an $n = 3$ was used. For the quantitative data, a one-way ANOVA, post hoc Bonferroni was performed to test differences between groups. Differences were found to be significant when $p < 0.05$.

Results and Discussion

To illustrate generation of organized cellular structures, equine-derived mesenchymal stromal cells (eMSCs) were labelled with fluorescent dyes, embedded in 10% gelatin-metacryloyl (gelMA) and simultaneously printed with polycaprolactone (PCL) MEW fibres (**Figure 1A**). Precise arrangement of cells and materials in 3D was demonstrated by filling the pores of micro fibre scaffolds with extruded *Tetris*-like shapes of eMSC-laden gels

(**Figure 1B**). Fine control over cell deposition was shown in both in-plane (x- and y-axis) printing (**Figure 1C,D**) and out-of-plane (z-axis) printing (**Figure 1E**). The 13 μm diameter of the MEW fibres (PCL), compared with the 200–400 μm diameter of the extruded bioink (gelMA), emphasizes the low volume of PCL in this multi-scale fabrication process. The resolution of converged printing is currently limited by the resolution of hydrogel deposition. Nonetheless, the MEW boxes contribute to the shape fidelity of the printed hydrogel. Therefore, the 200–400 μm diameter of the extruded gelMA was relatively smaller compared with previously reported diameters of $>500 \mu\text{m}$.^{248,260} Precise control over the deposition of the cell-containing bioink also provides the opportunity to control porosity and pore shape in the composite constructs(**Figure 1D**), which is essential when considering oxygen and nutrient supply in larger tissue constructs.^{261,262} To our knowledge, we are the first to demonstrate this more refined level of controlled 3D spatial organization when combining both micrometre-scale fibres and cell-laden hydrogels.

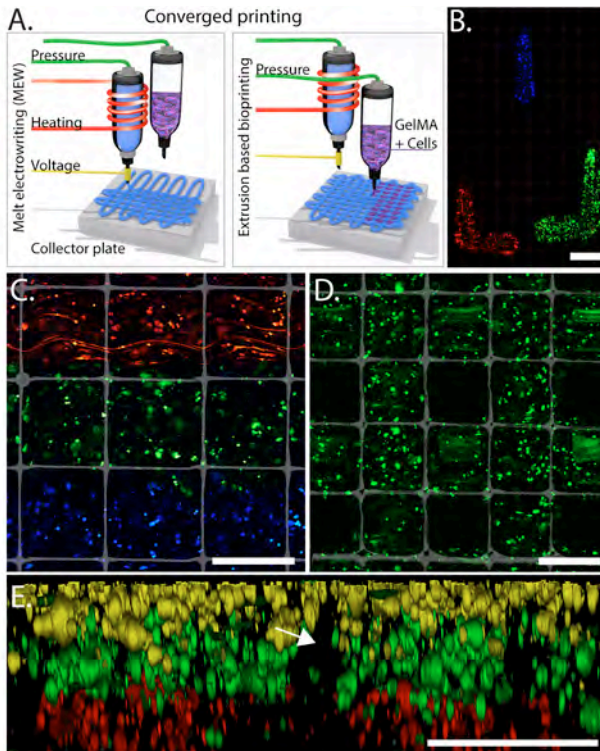


Figure 1. Convergence of MEW (PCL) and extrusion-based bioprinting (gelMA) into a single-step approach A) allows for control over spatial placement of cells. Control over positioning of cells (membrane-labeled eMSCs) while using MEW and extrusion-based bioprinting B) (top view) results in hierarchical structures C) (top view), and the ability to fabricate porous constructs while including MEW D) (top view) and layered distribution in z-direction E) (cross section; arrow indicates where MEW mesh was positioned). eMSCs stained with DiI (red), DiO (blue/yellow), and DiD (green). Scale bars = 400 μm .



Improvements in organization of tissue architecture are an important step toward recapitulating the complex architecture of tissues. Clearly, fibres in native tissue possess specific alignment that goes beyond the square, rectangular, or triangular structures that are typically fabricated with MEW.^{108,188} We demonstrated that during the converged printing of MEW and extrusion-based hydrogel printing, the hydrogel (here 40% w/v Pluronic F127) guides the spatial 3D architecture of the PCL fibres, and that this can be in the form of a single hydrogel strand (**Figure 2A**), interlocking the hydrogel (**Figure 2B**), or more complex shapes such as prisms (**Figure 2C**). The guiding of the MEW fibre by the hydrogel can even result in MEW fibres that have an out-of-plane character (**Figure 2D**). Although precise control over the spatial formation of fibrous structures remains challenging, the converged printing approach improves this control over fibre deposition, which is imperative in order to more closely mimic the fibrous component of the extracellular matrix architecture of the native tissue.

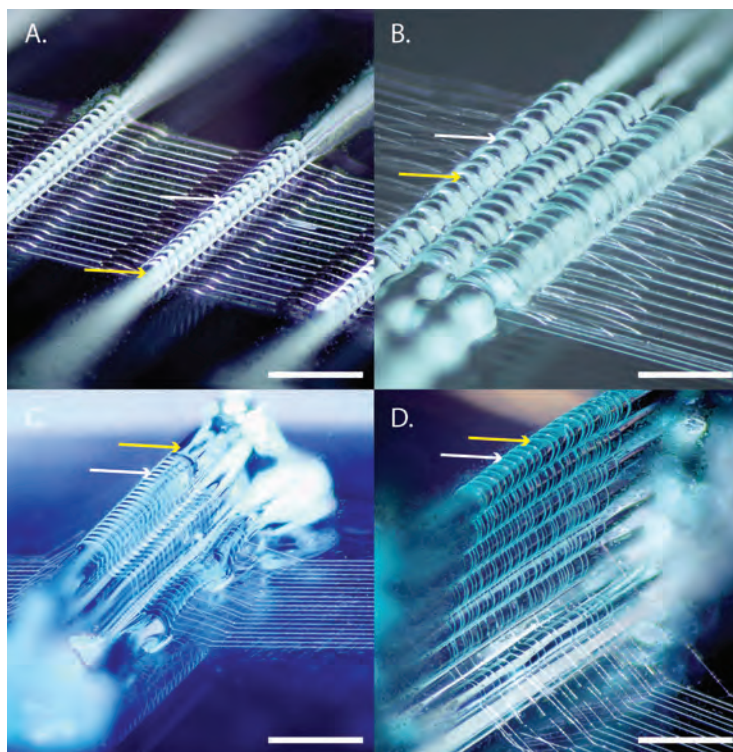


Figure 2. Toward more complex tissue architectures: using hydrogel (Pluronic, 40% w/v) to guide the direction of MEW (PCL) fibres. MEW fibres are guided over a single strand of hydrogel (A), interlocked with hydrogel (B). This enables more complex fibre architectures (C) and out-of-plane fibre deposition (D). Yellow arrows depict the hydrogel whereas the white arrows depict the PCL fibre. Scale bar = 500 μm .

In addition to structural organization, the generation of mechanically competent constructs is crucial for the clinical application of the bioprinted constructs. We investigated the mechanical behaviour of composite constructs fabricated with the proposed single-step converged printing method, compared with similar constructs obtained by the two-step cast method. Both peak and equilibrium moduli under uniaxial compression loading conditions were assessed (**Figure 3A**). The compressive peak modulus of converged printed constructs increased from 19.85 ± 7.51 kPa for gel alone to 246.84 ± 66.42 kPa for fibre-reinforced gel, whereas the compressive peak modulus of the cast constructs increased from 49.48 ± 7.81 kPa for gel alone to 278.13 ± 56.72 kPa for fibre-reinforced gel. This increase in compressive peak modulus for the cast samples is comparable to previous studies where a volume fraction of 6% was used with the same materials (PCL and 10% gelMA).⁸⁴ Additionally, the reinforcement effect remains at equilibrium where the compressive equilibrium modulus of samples increased from 11.90 ± 4.09 (printing, gel alone) to 53.02 ± 8.73 kPa (converged printing, reinforced gel), and from 17.02 ± 6.79 (cast, gel alone) to 64.17 ± 13.41 kPa (cast, reinforced gel) (**Figure 3B**). The compressive moduli of the converged printed samples did not significantly differ from the cast samples, meaning that the reinforcing effect is not affected by the converged printing approach. However, it is essential to establish a scaffold design that decreases the amount of gel between the stacking of the MEW fibres to ensure fusion of the MEW fibres in the z-direction, since this fusion is essential for the mechanical stability of the hydrogel–thermoplastic composites.²⁵³ Since both the equilibrium as peak moduli of the converged printed scaffolds increased compared with printed gel only scaffolds, and no differences were found compared with the cast samples, the converged printing approach is able to increase the mechanical stability of the gelMA–PCL composites.

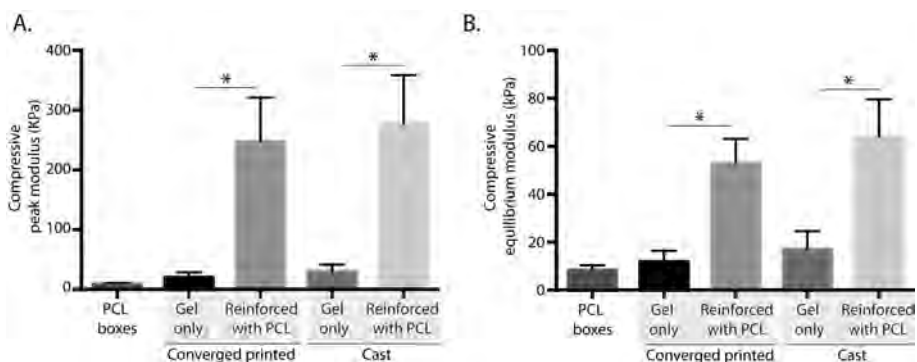


Figure 3. Convergence in a single-step approach does not affect the reinforcing effect of the MEW fibres. An increase in the compressive peak A) and equilibrium B) modulus was found when combining MEW (PCL) printing and extrusion-based hydrogel printing (10% gelMA). No differences were found between the converged printed and the cast samples. * = $p < 0.05$.



Combining MEW and hydrogel printing introduces parameters that are potentially harmful for cells embedded on extruded hydrogel structures. Thus, we demonstrated that the converged fabrication process does not affect cell survival or differentiation. First, since fibre diameters in sub-micrometer scale need to be generated, fabrication time, defined as the time needed to print the construct prior to crosslinking, is considerably higher compared with hydrogel extrusion-based bioprinting approaches. Construct fabrication time is based on a collector velocity of 80 mm s⁻¹, a fibre diameter of 13 μm, the line spacing between the MEW fibres, and the required scaffold volume (**Figure 4A**). Second, due to the increase of fabrication time, we assessed the effect of exposure time to environmental conditions during converged printing on the metabolic activity of the embedded cells (**Figure 4B**). For this, eMSCs (20 × 10⁶/ mL) were encapsulated in 10% gelMA and exposed to fabrication conditions by placement into an active fabrication chamber for 0–60 min; constructs were subsequently cultured in chondrogenic differentiation medium for four weeks. Metabolic activity, compared with cast constructs not subjected to the fabrication conditions, was found to be decreased by 12%, 33%, 63%, and 80% after 15, 30, 45, and 60 min, respectively. Third, the high voltage (typically 5–15 kV) required for MEW to acquire the jet may impact cell survival.

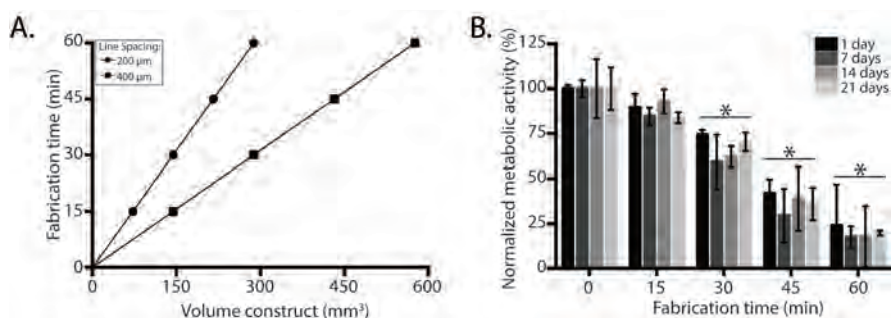


Figure 4. Effect of environmental conditions on cells. Converged printing increases printing time of constructs, which is related to the volume and line spacing of the prints A). Converged printed constructs with a volume of 100 mm³ and a line spacing of 400 μm, resulted in 10 min of printing time per construct. Incubating the hydrogel after crosslinking decreased metabolic activity of the cells B). Metabolic activity was normalized against cast control sample without incubation time. * = significant difference from an incubation time of 0 min, $p < 0.05$.

To assess the effect of the high voltage on cell behaviour, eMSCs were embedded in 10% gelMA and constantly subjected to 0, 5, 10, or 15 kV. After 14 d, eMSC viability was 92% ± 3%, 93% ± 3%, 91% ± 2%, and 90% ± 2% for 0, 5, 10, and 15 kV, respectively (**Figure 5A** and **Figure S1A** in the Supporting Information). Furthermore, metabolic activity of the constructs that were subjected to such voltage did not decrease,

compared with the control samples that were not subjected to a voltage difference (**Figure S1B** in the Supporting Information). In addition, as MSCs have the ability to differentiate toward multiple lineages, including bone, fat, tendon, myoblasts, neural-like cells, and cartilage tissue, this converged printing method has potential application in multiple tissue types.^{263–265} As a proof of concept that the converged printing process was not harmful for eMSCs, we specifically demonstrated the potential to form cartilage-like tissue. We first measured glycosaminoglycan's (GAGs), one of the main extracellular matrix components of cartilage, with a GAG/DNA assay over 28 d of culture. All samples showed an increase in GAG/DNA to an average of $11 \pm 1 \mu\text{g}/\mu\text{g}$ and $22 \pm 2 \mu\text{g}/\mu\text{g}$ after 14 and 28 d of culture, respectively. This finding was irrespective of the application of high voltage applied (**Figure 5B**). We confirmed this observation by safranin-O staining, which revealed that GAGs are evenly distributed throughout the samples (**Figure 5C**). For collagen type II, another main component of the extracellular matrix of cartilage, production was found to be increased over time in all samples, irrespective of the voltage applied (**Figure 5C**). No significant differences were observed for cell viability, metabolic activity, or cartilage-like matrix production between the cast and converged printed scaffolds. Hence, converged printing did not affect cell (MSC) behaviour in terms of viability, metabolic activity, and chondrogenic differentiation, and is therefore a promising biofabrication technique to fabricate hierarchical multi-material, or multicellular structures with the potential to differentiate toward a mature tissue structure.

Conclusion

To our knowledge, this study demonstrates, for the first time, the successful convergence of MEW and extrusion-based hydrogel printing into a single-step manufacturing approach, improving our control over structure design and fibre writing. Our biofabrication technique allows us to grow living cells in a microenvironment with precisely controlled 3D spatial organization that more faithfully recapitulates the complex architecture of native tissues. This greatly increases the ability to fabricate clinically relevant constructs without compromising mechanical integrity, cell viability, or (chondrogenic) differentiation.

Acknowledgements

The authors thank Sarah L. Opitz for proofreading this manuscript. The help of Kylee Marie Schaffer during this project was highly appreciated. This work was financially supported by the European Research Council under grant agreement 647426 (3D-JOINT), the Dutch Arthritis Foundation (LLP-12), and the European Community's Seventh Framework Programme (FP7/2007–2013) under grant agreement 309962 (HydroZONES). The converged 3D printing technology used in this work is a novel biomanufacturing process under development as part of the EU funded—E11312 BioArchitect project together with regenHU.

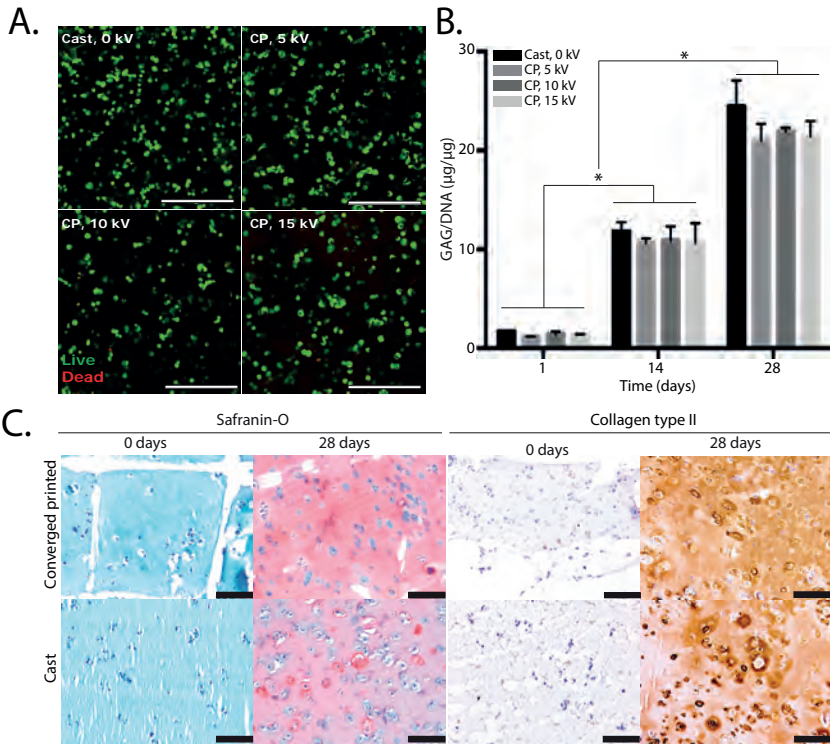


Figure 5. MSC behaviour after converged printing process. Cell viability ($t = 14$ d) in converged printing (CP) approach was comparable to cast control sample for all voltages used A). Chondrogenic differentiation was not compromised by the converged printing (CP) approach, showing no statistical differences in GAG/DNA compared with cast samples, for 5, 10, and 15 kV B). Safranin-O and collagen type II staining shows good proteoglycan and collagen type II distribution throughout the entire construct C). Scale bar = 100 μ m, * = $p < 0.05$.

Supplementary data

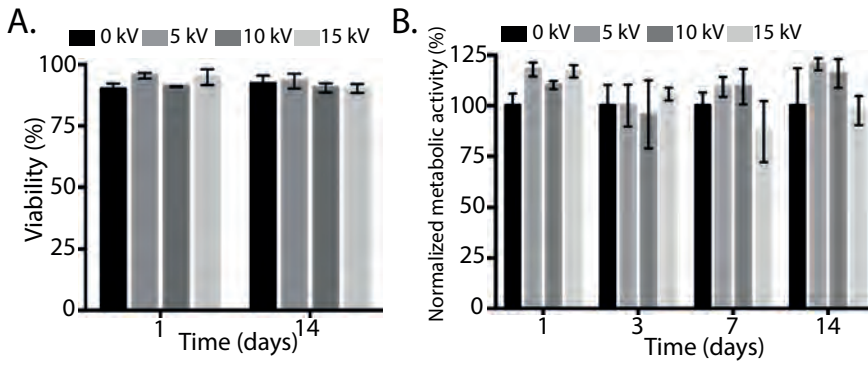
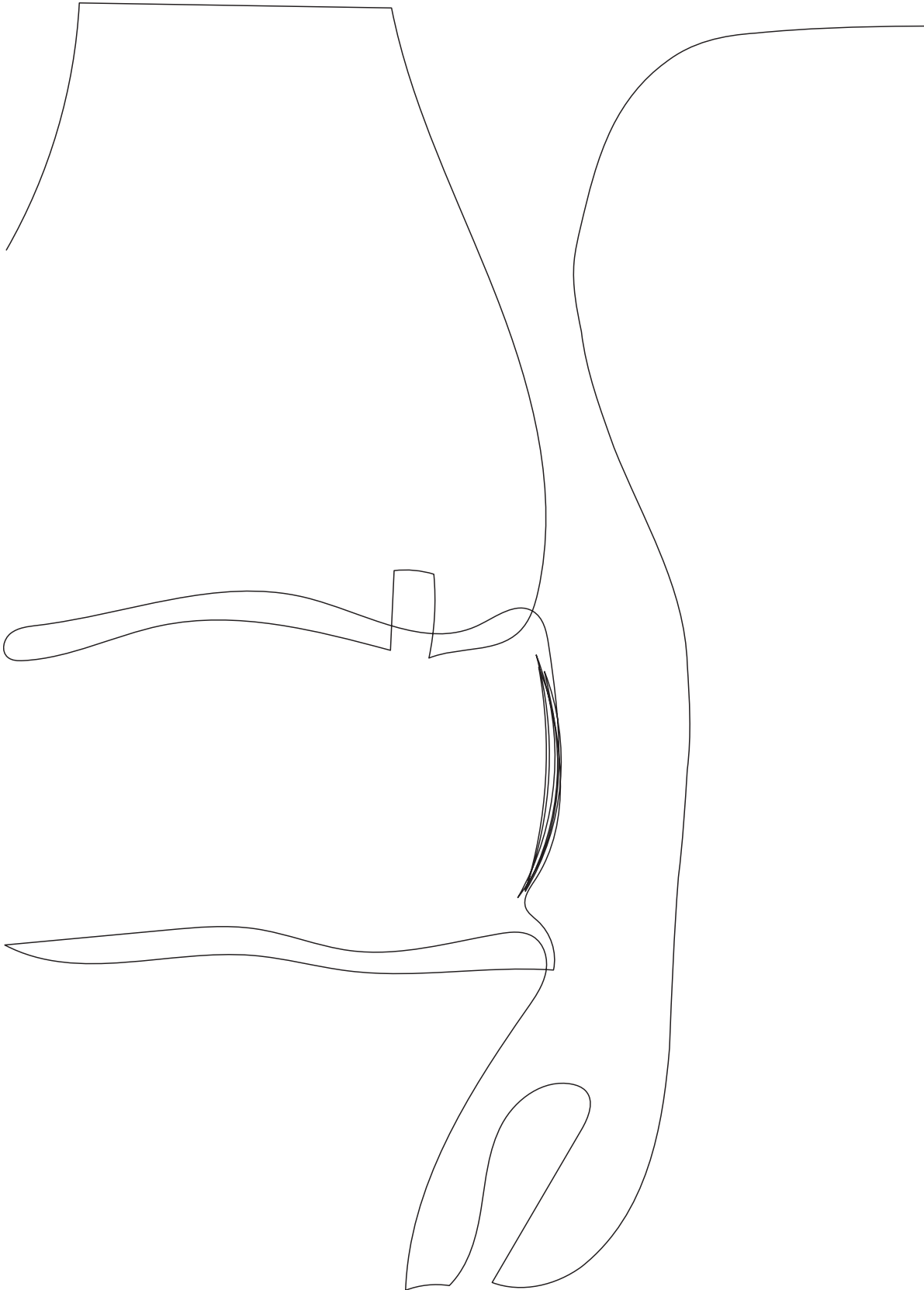


Figure S1 Viability and metabolic activity of eMSCs in 10% gelMA after 0 – 15 kV, over the course of 21 days. No difference in viability (A) between different high voltages and the control sample where no voltage was applied. Metabolic activity in % compared to 0 kV control sample (B). Metabolic activity of samples that were subjected to high voltage was not affected.







Chapter 6

Melt electrowriting onto anatomically relevant substrates: Resurfacing a diarthrodial joint geometry

6

Mylène de Ruijter^{1*}

Quentin C. Peiffer^{1*}

Joost van Duijn¹

Denis Crotte²

Dominic Ernst²

Jos Malda^{1,3}

Miguel Castilho^{1,4}

* = Authors contributed equally

Published in Materials & Design (2020)

DOI: 10.1016/j.matdes.2020.109025

¹ Department of Orthopaedics, RMCU Utrecht, UMC Utrecht, University of Utrecht, The Netherlands

² RegenHU Ltd, Villaz-St-Pierre, Switzerland

³ Department of Clinical Sciences, faculty of Veterinary Medicine, Utrecht University, The Netherlands

⁴ Department of Biomedical Engineering, Eindhoven University of Technology, The Netherlands

Abstract

Three-dimensional printed hydrogel constructs with well-organized melt electrowritten (MEW) fibre-reinforcing scaffolds have been demonstrated as a promising regenerative approach to treat small cartilage defects. Here, we investigate how to translate the fabrication of small fibre-reinforced structures on flat surfaces to more anatomically relevant structures. In particular, the accurate deposition of MEW-fibres onto curved surfaces of different conductive and non-conductive regenerative biomaterials is studied. This study reveals that clinically relevant materials with low conductivities are compatible to resurface with MEW fibres in a single-step printing approach. Moreover, accurate patterning on non-flat surfaces was successfully shown, provided that a constant electrical field strength and an electrical force normal to the substrate material is maintained. The application of potentially resurfacing the geometry of the medial human femoral condyle is confirmed by the fabrication of a personalised osteochondral implant. The implant composed of an articular cartilage-resident chondroprogenitor cells (ACPCs)-laden hydrogel reinforced with a well organized MEW mesh retained its personalized shape, and improved compressive properties when compared to hydrogels alone, as well as supported neo-cartilage formation after 28 days *in vitro* culture. This study establishes the groundwork for translating MEW from planar to anatomically relevant geometries that the regenerative medicine field aims to recreate.



Introduction

Articular cartilage in diarthrodial joints functions as a load-bearing tissue with a nearly frictionless surface. This unique characteristic is attributed to the composition of cartilage tissue where its (structurally) important components, type II collagen fibrils and glycosaminoglycans (GAGs), as well as cells are hierarchically distributed throughout the tissue.^{266,267,268} However, damage to the knee joint can cause pain and immobility, and if left untreated, can potentially lead to osteoarthritis (OA).^{18,269} Surgical treatment options for osteochondral defects, such as bone marrow stimulation (for small defects $\leq 2 \text{ cm}^2$)²⁷⁰ and osteochondral grafting⁵⁵, or for chondral defects such as cell-based therapies, including autologous chondrocyte implantation (for medium size defects, 2 cm^2 to 4 cm^2)²⁷¹, are sub-optimal as these typically result in the formation of mechanically weak fibrocartilage tissue.²⁷⁰ As a last resort option to reduce clinical symptoms and improve patient's mobility, total knee replacement (TKR) surgery, with the use of metallic implants, is used.⁵⁸ As the metallic TKR have a limited life-span, this last resort option has to be postponed or even eliminated.^{58,58}

Regenerative approaches based on biofabrication²⁴⁰ technologies are a potential alternative to repair damaged articular cartilage tissue.¹⁵² Advances in (micro) fibre formation and deposition technologies, such as melt electrowriting (MEW)^{84,90,93,272} and extrusion-based deposition of bioinks²⁷³, have recently enabled the fabrication of mechanically stable, fibre reinforced cartilage implants.^{85,188,274} Recent developments in the convergence of MEW and extrusion-based technologies within a single manufacturing process allowed the fabrication of constructs with regional compositional variations in both the cellular and fibre components, inspired by what is observed in healthy native articular cartilage.^{273,275,276} In particular, this technology-convergence has shown promising results for the fabrication of implants to treat small cartilage defects with coplanar surfaces.^{274,273} However, generating human-scale constructs with anatomical relevant shapes still remains a major challenge. The underlying limitation is predominantly related to the electrohydrodynamic working principle of MEW. While MEW relies on the use of a constant electrostatic force to deposit micrometer size fibres in well-organized three dimensional (3D) patterns^{155,277}, MEW structures are generally deposited onto flat substrates as to not interfere with this electrostatic force.

It is known that the electrical field (EF), and its resulting electrical force, the main fibre pulling force in the MEW process, is affected by the collector design in both shape, dimension,²⁷⁸ and material properties,²⁷⁹ as well as by the instrument configuration and process parameters.^{280–282} In particular, the electrical conductive properties of the collecting material, together with the processing parameters, *i.e.* applied voltage,

collector-to-spinneret distance, collector velocity, and environmental conditions, are important parameters that can influence accurate MEW fibre deposition^{282–284}. While using glass-slides to easily collect fibers⁸⁸, only more traditional metallic substrates, such as copper, stainless steel or aluminium, with planar surfaces, have shown to ensure uniform fibre diameters and accurate fabrication of ordered three-dimensional (3D) fibrous microstructures. Unfortunately, most biologically degradable materials used in regenerative medicine are intrinsically nonconductive and native living tissue structures are generally non-flat. For example, materials used for (osteo)chondral repair, such as degradable thermoplastics²⁸⁵, hydrogels^{286,287}, or bioceramics²⁸⁸, are expected to interfere with the EF of the MEW process, while complete diarthrodial joint resurfacing requires accurate patterning, following the anatomical curvature of this joint. To exploit MEW as a technique to produce reinforcing fibres in/onto anatomical relevant shapes and onto clinically relevant materials, it is fundamental to further understand the effects of the electrical properties of the collecting material and its respective geometry on accurate fibre deposition.

Therefore, in this study, we investigate how to translate the fabrication of fibre reinforced structures from flat to more anatomically relevant, non-flat surfaces with the convergence of MEW and extrusion-based printing technologies. In particular, the accurate deposition of MEW-fibres onto anatomically relevant shapes (wedges and curved domes) and biomaterials, *i.e.* bioceramics, magnesium phosphate cement (MgP); thermoplastics, polycaprolactone (PCL); and hydrogels, gelatin methacryloyl (gelMA), is studied (**Figure 1**). Through computational modelling, the effect of collecting substrate electrical properties and geometry on the underlying EF distribution and electrical force is investigated. Lastly, the feasibility of fabricating a mechanically reinforced condyle-shaped construct, with biodegradable materials, through the combination of MEW and the extrusion of a cell-laden hydrogel is assessed.

Materials and Methods

Materials

Gelatin methacryloyl (gelMA) was synthesized as previously described²⁵⁸. Briefly, gelatin (type A, derived from porcine skin, 175 Bloom, Sigma Aldrich) was dissolved at 10% w/v in phosphate-buffered-saline (PBS) at 60 °C after which 0.6 g methacrylic anhydride (Sigma Aldrich) was added per g of gelatin to achieve an 80% degree of functionalisation. Freeze-dried gelMA was diluted with PBS to obtain a final gelMA concentration of 10% w/v. To initiate the cross-linking reaction, a combination of 5mM sodium persulfate (Sigma Aldrich) and 0.5mM Tris(2,2'-bipyridyl) dichlororuthenium (II) hexahydrate (Sigma Aldrich)

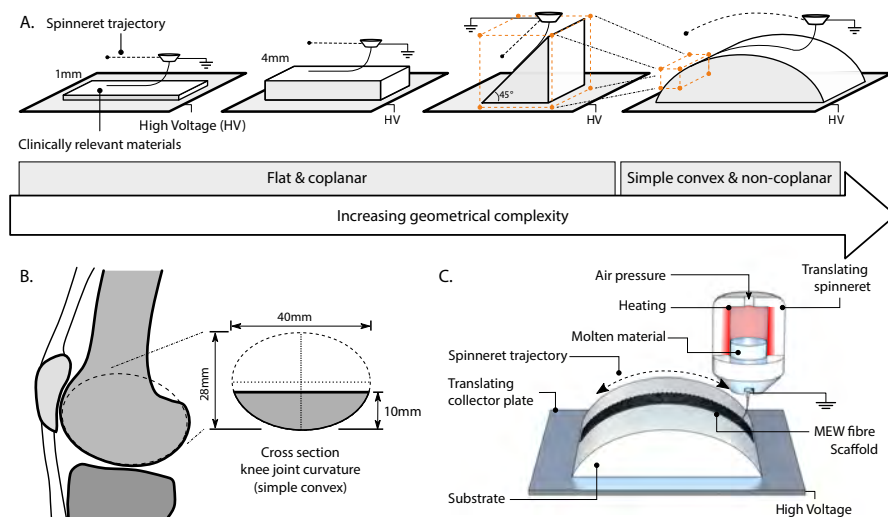


Figure 1. Deposition of melt electrospun (MEW) fibres on clinically relevant shapes and materials. A) Schematic representation of the different collecting geometries ranging from flat (with a thickness of 1 and 4 mm) to a 45°-wedge and curved dome-shaped structures. B) Curved shape structures were designed to approach the geometry of an average human femoral condyle surface. C) Schematic representation of the MEW process, where PCL micro-fibres are patterned on a substrate with the geometry that mimics the contour of an articulating joint.

was added to the gelMA solution and subsequently cast in custom-made PDMS molds with different shapes (flat/wedge/dome) and cross-linked for 10 min under led light (20W LED, Jobmate). Magnesium ceramic (MgP) was prepared by mixing an $Mg_3(PO_4)_2$ and MgO powder to a 4:1 weight ratio, after which a 3.5% w/v polyethylene oxide solution (Mw 600,000 to 1,000,000) (Acros Organics) was added. The solution was cast in above mentioned PDMS moulds and dried at 37°C for 4 hours. Finally, the MgP was hardened with a 3.5M solution of di-Ammonium hydrogen phosphate (Merck) overnight at 37°C. Polycaprolactone (PCL, Purasorb PC12, Corbion) was molten at 80°C and cast in PDMS moulds, while Aluminium (Aluminium 51 ST, Salomon's Metalen B.V) wedge/dome-shaped substrates were directly manufactured by a conventional CNC milling device.

Impedance spectroscopy measurements

Dielectric properties of substrate materials were measured with an impedance/gain-phase analyser (1260 Impedance Analyser, Solartron Analytical) with a dielectric interface (1296A Dielectric Interface System, Solartron Analytical, 12962A Sample Holders, Solartron Analytical). Cylinders ($r = 20$ mm) of 1 mm and 4 mm thicknesses of each material (gelMA,

MgP, PCL) were tested at room temperature. An alternating current (AC) level of 100 mV was set, and the impedance of each substrate was measured with a frequency sweep (1 MHz – 1 Hz, 5 points/decade). The capacitance (C) in Farad of each material composition was obtained and the relative permittivity (ϵ_r) was calculated according to,

$$\epsilon_r = \frac{C}{C_0} \quad (1)$$

where C_0 is the capacity of the empty capacitor. In addition, electrical conductivity (σ) in siemens per metre was obtained indirectly by determining first the material resistance (R) with a digital multimeter, and then obtained by,

$$\sigma = \frac{l}{RA} \quad (2)$$

where l terms represent length and A the cross-sectional area of the measured material specimen.

Surface roughness measurements

Surface roughness of substrate materials was measured using a surface roughness tester (SJ-400, Mitutoyo Corp.) as detailed in Supplementary Methods.

Melt electrowriting (MEW)

MEW was performed with polycaprolactone (PCL, Purasorb PC12, Corbion) molten in a metallic cartridge at 80°C with an air pressure of 110-125 kPa, 24G nozzle, voltage of 7-11 kV (3D Discovery Evolution, RegenHU). The printhead was either kept at a constant Z-coordinate of 6 mm, or was varied following the surface curvature of the collecting substrate (Z-correction) in which the distance between the printinghead and the collecting substrate was always 6 mm. For all experiments, the MEW jet was stabilized prior to printing by printing 40 lines which were analysed for deviations in fiber diameter and/or pulsing.¹⁰⁷

Fibre evaluation

Fibre morphology and fibre stacking was evaluated by scanning electronic microscopy (SEM) (Phenom Pro desktop, ThermoFischer Scientific) (Supplementary Figure 2A). Samples were coated with 6 nm gold using a rotary pumped coater (Q150R, Quorum Technologies). Prior to SEM, each multi-layered construct was cut in liquid nitrogen with a scalpel.



Printing accuracy quantification

Fibre scaffolds were imaged with an upright microscope (Olympus BX430) and subsequently processed with Fiji (version 2.0.0-rc-54/1.51h). A selection of pores in the central region of the scaffold were selected (Supplementary Figure 2B) after which the pore ration was measured (Supplementary methods).

Finite element analysis

Numerical simulation of the electric field strength and distribution were performed (COMSOL Multiphysics Simulation Software, Version 5.1 COMSOL Inc.). The MEW printhead and collecting substrate geometries (flat, wedge and curved) were designed according to the printer and substrates used. The electric conductivity of the stainless-steel printhead and collector was set to $1.45 \times 10^6 \text{ S m}^{-1}$, and of the air volume to $1 \times 10^{-15} \text{ S m}^{-1}$. Relative permittivity of 2.3 and 2.7 were defined for substrate materials PLC and MgP, respectively. GelMA and Al were defined as conductive materials (electrical conductivities of $1.25 \times 10^{-3} \text{ S m}^{-1}$ and $3.20 \times 10^7 \text{ S m}^{-1}$, respectively). The electric field strength and distribution was simulated by applying a negative potential to the collector 9 kV, while the spinneret was kept at 0 kV (grounded) at a distance of 6 mm for flat substrates; 6 mm and 31 mm for the wedge substrates; and 6 mm and 11 mm for curved substrates. For simplicity, no charge dissipation was considered.

Fabrication and matrix formation of clinically relevant surfaces

A polycaprolactone (PCL) dome structure was resurfaced with MEW fibres and gelatin methacryloyl (gelMA) hydrogel, encapsulated with articular cartilage progenitor cells (ACPCs). A screw driven extrusion-based PCL printing (3D Discovery Evolution, RegenHU) was used to fabricate the dome structure. PCL was heated to 90°C and extruded with a extrusion rate of 3 rev/min and a translational speed of 4mm/s, with 40% porosity. Subsequently, 50 layers of MEW PCL fibres were deposited on top of this dome structure with a collector distance of 6 mm, collector velocity of 20 mm/s, pressure of 110 kPa, and a voltage of 9 kV. During MEW, the spinneret followed the contour of the dome structure, keeping z-distance constant.

Cell culture

Equine derived articular cartilage-resident progenitor cells (ACPCs) were isolated from the metacarpophalangeal joints of skeletally mature equine donors and expanded as previously described.¹⁶⁷ These donors have been donated to science by their owners and procedures were followed according to the guidelines of the Ethical and Animal Welfare body of Utrecht University.^{34,167} After expanding, cells were embedded in 10% gelMA (cell density = $20 \times 10^6 / \text{ml}$), supplemented with tris-bipyridyl- ruthenium (II) hexahydrate (Ru, 0.2 mM, Sigma Aldrich)/sodium persulfate (SPS, 2mM, Sigma Aldrich), which was either

deposited on top of the MEW structure of the PCL dome with a pipet, or perfused in a Teflon mold to fabricate cell-laden cast 3D discs (height = 2mm, diameter = 6 mm) that was used a control group. Crosslinking occurred under visible light conditions for 10 minutes after which the constructs were cultured in chondrogenic differentiation medium (Supplementary methods) for 28 days. All cultures were performed under sterile and normoxic culture conditions at a temperature of 37°C and 5% CO₂.

***In vitro* evaluation of (bio) fabricated implants**

During culture, metabolic activity was measured using a resazurin assay (Sigma Aldrich) at day 1,7,14, 28. After 28 days, matrix formation was quantified by biochemical assessment of GAG (dimethylmethylene Blue (DMMB), Sigma Aldrich) per DNA (Quant-iT-Picogreen-dsDNA-kit, Invitrogen) according to manufacture protocols. Additionally, samples were embedded in MMA, polymerized, and saw, or paraffin embedded and cut, to visualize the cell distribution (haematoxylin staining (Sigma Aldrich)) and matrix distribution, respectively. Matrix distribution was visualized with a safranin O (Sigma Aldrich), combined with fast green to stain fibrous tissue (Sigma Aldrich). Immunohistochemistry was performed to visualize type II collagen (II-II6B3, DSHB).

Mechanical analysis of fibre reinforced gelMA scaffolds

Uniaxial compression tests were performed on a universal testing machine (Zwick Z010, Germany) equipped with a 20 N load cell. Tests were conducted at a rate of 1 mm/min at room temperature, with all samples immersed in PBS to approximate physiological conditions. Cylindrical samples with a diameter of 5mm and a height of 1 mm were used. For each engineered stress-strain curve, the elastic modulus, defined as the slope of the linear region from 0.15 to 0.20 mm/mm. was determined.

Statistical analysis

Data is represented as mean ± standard deviation. For surface roughness measurements, impedance spectroscopy, fibre diameter measurements, scaffold thickness, pore ratio, and in vitro studies, at least 3 samples per group were used. For the mechanical tests, at least 4 samples were analyzed per group. An unpaired t-test (GAG/DNA) and a two-way ANOVA, post hoc Tukey test (metabolic activity) were used to test the difference between the cultured disc and dome structures. A one-way ANOVA with Tukey's post hoc test was used to compare the means of the different groups for the mechanical data, fibre diameter, scaffold thickness, and pore ratio measurements. Test differences were considered significant at a probability error (p) of $p < 0.05$. Normality and homogeneity were checked with Shapiro-Wilks and Levene's tests, using GraphPad Prism version 6 (San Diego, USA)



Results

Material properties: Surface roughness and electrical conductive properties

Magnesium phosphate (MgP) and gelMA substrates presented higher surface roughness values (R_a and R_q between 3.61 and 5.21 μm) than PCL and Aluminium substrates (R_a and R_q between 0.07 and 0.32 μm) (**Supplementary Table 1**).

Impedance spectroscopy confirmed the electrical conductivity and relative permittivity of PCL, MgP, gelMA, and aluminium (Al) collecting substrates of 1 and 4 mm (**Table 1**). PCL and MgP behaved as non-conductive materials with relative permittivity values of 2.11 and 4.32, respectively. GelMA was confirmed partly conductive with a relative permittivity of 5×10^7 . Aluminium confirmed its conductive properties as measured relative permittivity was out of the measurement range.

Table 1. Relative permittivity (ϵ_r) and electrical conductivity (σ) of investigated materials.

Substrate biomaterial	Relative permittivity (ϵ_r , at 1Hz)	Electrical conductivity (σ , S/m)
Polycaprolactone (PCL)	2.11	/
Magnesium phosphate based cement (MgP)	4.32	/
Gelatine methacryloyl (gelMA)	5×10^7	$4.17 \times 10^{-3} - 1.25 \times 10^{-2}$
Aluminium (Al, control)	/	3.20×10^7

Effect of collecting material conductivity on fibre deposition

The effect of the conductivity of the collecting materials on fibre deposition was studied using substrates with thicknesses of 1 and 4 mm (**Figure 2A, B**). A significant smaller fibre diameter was observed when depositing onto non-conductive substrates (8 μm for PCL and MgP) as compared to collecting onto conductive substrates ($> 11 \mu\text{m}$ for gelMA and aluminium) (**Figure 2C**). This phenomenon was confirmed for different collector velocities (**Figure 2C**) and different voltages (**Supplementary Figure 1A**). Morphologically, fibres deposited onto PCL and MgP maintained a cylindrical shape (**supplementary Figure 1B**) whereas fibres deposited on aluminium and gelMA were more flattened (ellipsoidal) for the first layer (**Supplementary Figure 1C**) this morphology was not directly related to material surface roughness. Collecting material thickness did not affect fibre diameters. Computational simulation confirmed that the EF strength along the Z-axis (i.e. out-of-collector plane direction) was slightly higher for conductive collecting materials as compared to the non-conductive collecting materials. The profile of the EF along the z-axis was independent of substrate thickness (**Figure 2 E,F**). Additionally, the

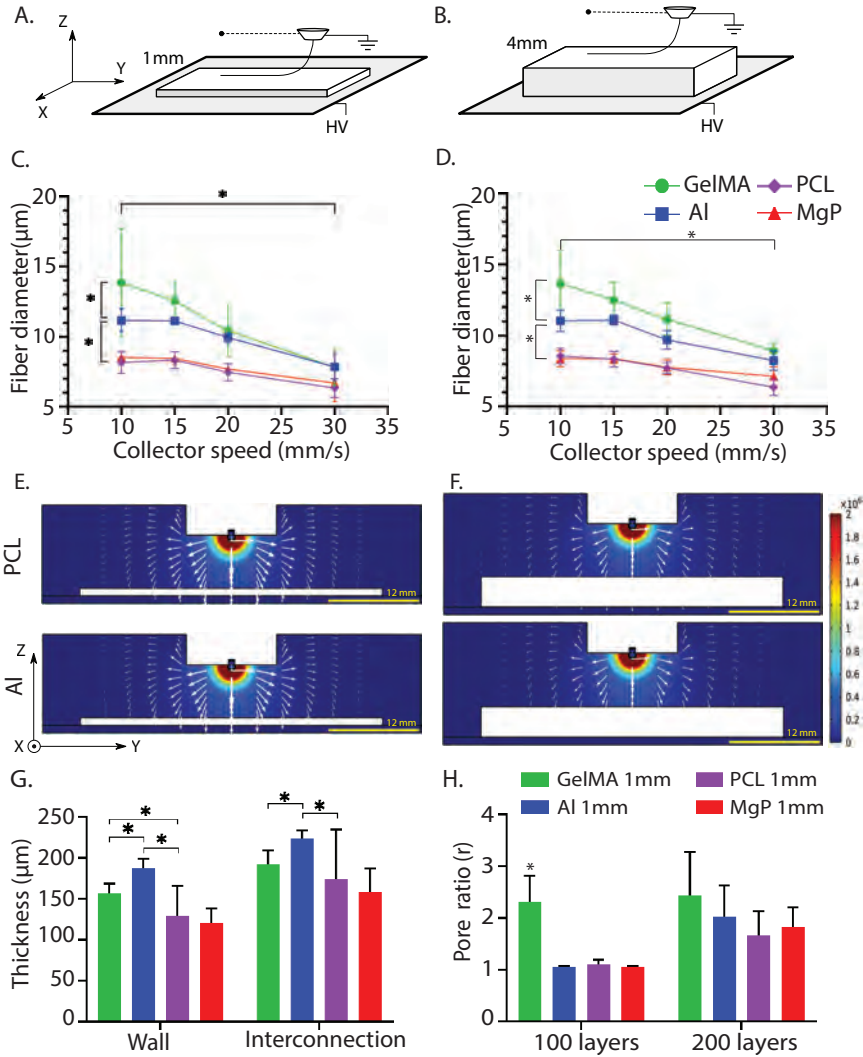


Figure 2. Fibre collection on flat-shaped collecting materials (PCL, MgP, gelMA, and Al). A, B) collecting materials of 1 mm and 4 mm high were investigated. C) Effect of collector velocity on fibre diameter of fibres deposited on 1 mm thick collectors. D) Effect of collector velocity on fibre diameter of fibres deposited on 4 mm thick collectors. E) Computational simulation of EF strength (V/m) and distribution (white arrows in logarithmic scale) for non-conductive (PCL) and conductive (Al) collecting material of E) 1 mm and F) 4 mm thick. G) Final scaffold thickness as a reflection of fibre stacking accuracy. Collector velocity = 15 mm/s. H) Pore ratio of scaffolds deposited on 1 mm thick collectors ($r = 1$ indicates a printed scaffold that conforms to the planned design, while values $r > 1$ indicates imperfect fibre stacking). * = $p < 0.05$.



global EF distribution was similar for the different substrate materials, and concentrated predominantly around the spinneret.

Scaffolds fabricated onto non-conductive materials (PCL, MgP) were $\sim 50 \mu\text{m}$ less high as compared to scaffolds fabricated onto conductive materials (gelMA, aluminium) (**Figure 2G, supplementary Figure 2A**). Scaffolds printed on gelMA showed more (2 – fold) deviation from design than the scaffolds printed onto PCL, MgP, or aluminium (**Figure 2H, supplementary Figure 2B**). Overall, an increase in the amount of layers from 100 to 200 resulted in higher pore ratios, which demonstrated a decrease in fibre stacking accuracy upon increasing the amount of layers. The thickness (1 mm or 4 mm) of the collecting material did not affect accurate fibre stacking (**Supplementary Figure 2C**).

Effect of collector geometry on fibre deposition –non-flat, wedge and curved

Printing onto a 45° wedge substrates showed similar trends as printing onto dome-structures. In general, printing without z-correction in the printing trajectory (**Supplementary Figure 3A**), resulted in poor fibre placement (inconsistency in fibre diameter and consequently distorted scaffold architectures) (**Supplementary Figure 3B**).

Z-correction in the printhead trajectory also improved the accuracy of fibre deposition when printing onto dome-structures (**Figure 3A, B**). Computational simulation confirmed that the EF strength was constant and normal to the curved surface when printing with z-correction in the printhead trajectory (**Figure 3C**). Although scaffold thickness was relatively unaffected by the collecting material used, scaffold printed on Al and MgP substrates did show a significant difference between the thickness of fibres deposited on top of the dome (centre) or more at the edges (lateral) (**Figure 3D**). Additionally, gelMA showed a higher pore ratio compared to PCL, MgP, and aluminium (**Figure 3E**). No significant differences were found between the lateral and the central parts of the scaffolds fabricated on the curved-shaped PCL or gelMA, when using a z-correction in the printhead trajectory (**Supplementary Figure 4**).

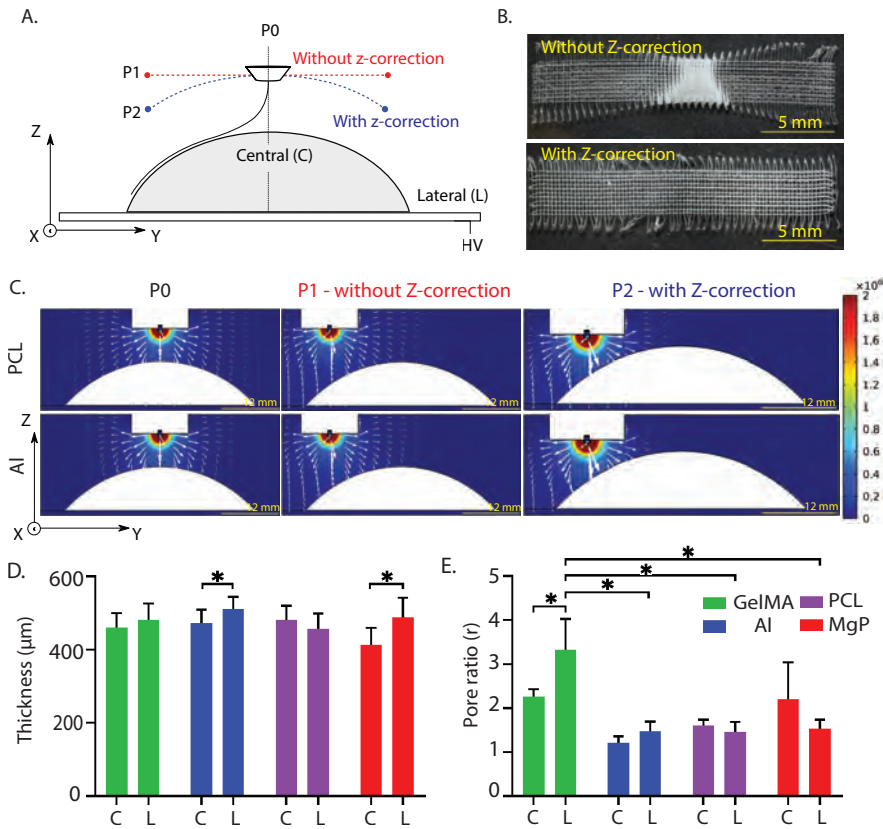


Figure 3: Fibre collection on curved collecting materials (PCL, MgP, gelMA, and Al). A) Schematic representation of the evaluated printhead trajectories with and without z-correction. B) Representative stereoscopic images of scaffolds printed on aluminium dome-shaped structures with and without z-correction of the printhead trajectory. C) Computational simulation of EF strength (V/m) and distribution (white arrows in logarithmic scale) for a non-conductive (PCL) and conductive (aluminium) curved-shaped collecting materials. Quantification of D) the final scaffold thickness and E) the pore ratio of scaffolds deposited on curved-shaped collecting materials with z-correction in the printhead trajectory. C and L represent central and lateral parts of the dome structures, respectively. * = $p < 0.05$

Resurfacing the entire joint surface – Simple convex surfaces

A PCL scaffold, approximating the native curvature of an average human femur, was successfully resurfaced with a boxed-microfibre architecture and filled with a cell-laden gelMA hydrogel (**Figure 4A**). The interfibre spacing (400 μm) that was used in this study to mechanically reinforce the cell-laden hydrogel, indeed showed a significant increase in the compressive modulus as compared to hydrogel only and scaffold only groups (**Supplementary Figure 5**). During the 28 days of culture, the fibre reinforced hydrogel on top of the femur structure retained its shape (**Figure 4B**) and embedded cells showed comparable metabolic activity to those in cast disc controls (**Figure 4C**). Histological evaluation of the constructs revealed abundant positive staining for safranin O and type II collagen (**Figure 4D**). No significant differences in cartilage-like matrix deposition was observed between the condyle-shaped constructs and the cast disc controls (**Figure 4E**).

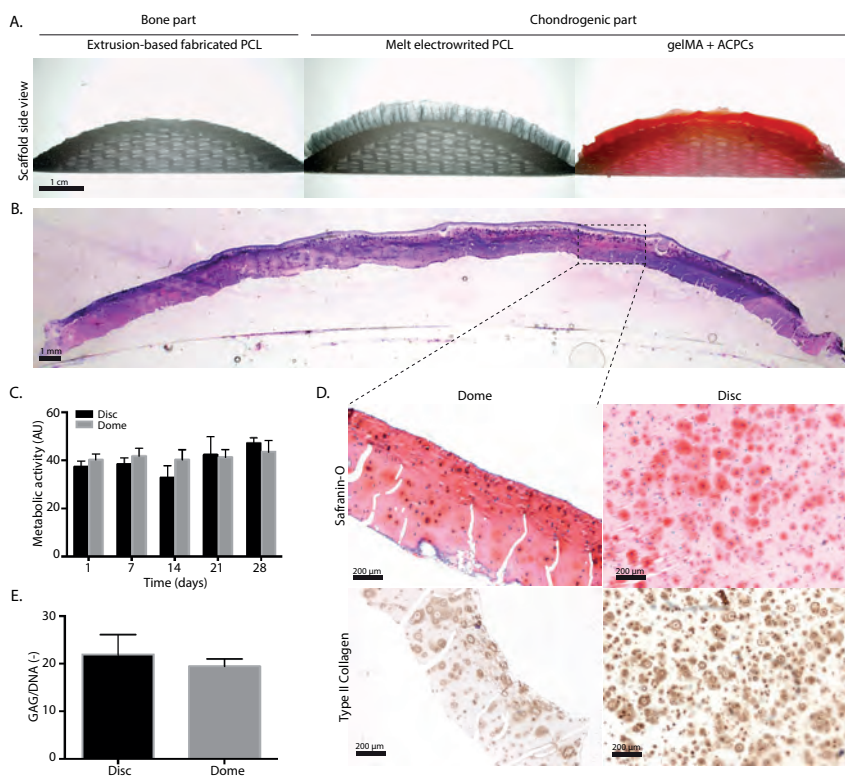


Figure 4: Resurfacing a fully resorbable PCL mimicking contour of a human femoral condyle surface and cartilage-like tissue formation after 28 days of *in vitro* culture. A) Macroscopic cross section of MEW fibre-reinforced gelMA hydrogel with encapsulated articular chondrocyte progenitor cells onto an extruded PCL substrate that approximates native human femur curvature. B) H&E staining of the manufactured implant after culture. C) Metabolic activity of cast discs and printed femoral structures. D) Safranin-O and type II collagen staining of printed femoral structures sections after culture. E) Proteoglycan content normalized to DNA.

Discussion

This study demonstrates the challenges of translating the fabrication of microfibre reinforcing scaffolding structures from flat to curved, anatomically relevant geometries and clinically relevant material with multi-scale bioprinting technologies. Although MEW fibre stacking on gelMA was less accurate as compared to MEW fibre stacking on PCL, MgP, and aluminium, accurate deposition of MEW-fibres onto clinically relevant material and anatomically relevant shapes was achieved. Furthermore, a converged printed, resurfaced human condyle-shaped construct was fabricated and supported cartilage-tissue formation after 28 days of *in vitro* culture.

It was shown that MEW fibre diameters are strongly affected by the materials they are printed on. Printing on conductive materials (gelMA, aluminium) resulted in larger fibre diameters as compared to printing on non-conductive materials (PCL, MgP). This observation can be explained by the fact that dielectric materials modifying the overall EF strength, which consequently disturbs the orientation and pulling force exerted on the molten jet.^{283,279,289} Fibres collected on the PCL substrates had a more cylindrical morphology compared to those collected on gelMA. This could be attributed to the more homogeneous fibre-cooling prior the deposition of the fibres as a result of the EF-induced jet-lag. Interestingly, fibre diameter was not affected by the thickness of the collecting materials used, which confirmed that electrical conductive properties are not significantly affected by the dimensions, within the range of the present experiment, of the material.

In addition, we observed that the effect of the material composition of the collecting substrates on the deposition of the fibres was less than would be expected based on the previously observed disturbance of the EF by dielectric materials.^{283,284,289} However, the scaffolds fabricated on PCL and MgP structures had a high deposition accuracy, as demonstrated by the high pore ratio, and was comparable to the accuracy obtained on aluminium substrates. The permittivity of both PCL and MgP was not high enough to generate significant disturbance of the EF and consequently, affect the accuracy of the fibre deposition process. Our computational simulations confirm this hypothesis, as only small differences in the EF strength magnitude were determined when using PCL and MgP as collecting materials in comparison to the more conductive collecting materials.

Interestingly, accurate fibre deposition on non-flat, *i.e.* wedge- and curve-shaped, collecting materials was significantly improved when the distance between the printhead and the collecting substrate material remained constant (*i.e.* when applying a z-correction to the printhead trajectory). It has been shown that an increase in collector distance leads to a drop in the overall EF strength if the voltage is not increased accordingly.²⁹⁰



Consistent with literature that shows the effect of substrate geometry on jet deflection,²⁹¹ our computational simulations showed a significant change in the global EF distribution when z-correction is employed. This data demonstrates that when applying z-correction to the printhead trajectory, the geometry of the substrate is not a limiting element in accurate fibre deposition on non-flat substrates.

Although we have shown that accurate deposition of MEW fibres is possible on different collecting materials and on anatomically relevant geometries, some deposition inaccuracies were still observed. In general, fibre deposition was less accurate on gelMA as a collecting surface compared to deposition on PCL, MgP, and aluminium substrates. This could possibly be due to the high-water content of gelMA, as evaporation of water due to the proximity of the heated MEW spinneret affects the electrical properties of gelMA during the fabrication process. Additionally, we hypothesized that evaporation of water could potentially result in an increase of the local humidity and, therefore, cause disturbance the EF. Moreover, as gelMA is a mechanically soft material (compressive modulus for 10% gelMA (80% DoF, 175 bloom) = 20 kPa), the gelMA wedge and dome collecting structures were more prone to movements upon the vibrations that were induced by fast machine displacement (due to the fast collecting velocities used), increasing the instabilities during fibre deposition on these substrates. The observed decreased accuracy of fibre deposition with increasing fibre scaffold thickness is consistent with recent literature and described as possibly due to remnant charges trapped in already deposited fibres.²⁹⁰

As a potential application to treat full-thickness cartilage or osteochondral defects, we demonstrated the fabrication of structures with a fibre-reinforced osteochondral construct that anatomically reflects the curvature of the native femoral condyle surface. Notably, these constructs presented high shape fidelity and remained shape during the 28-day of *in vitro* culture period. Moreover, homogenous and abundant cartilage-like tissue formation throughout the cartilage compartment of the constructs was observed. This demonstrates that reinforcing strategies could be translated from frequently fabricated small, osteochondral plugs with flat, coplanar surfaces²⁰², towards anatomically relevant structures with patient-specific geometries. Although resurfacing anatomically relevant surfaces has previously been shown with a dense fibre matrix, those scaffolds did not allow for cell deposition and homogeneous extra cellular matrix.²⁹² To the best of our knowledge, this is the first study to report the fabrication of a larger, microfibre reinforced, low fibre density, hydrogel-based construct that follow the articulating surface. Ultimately, to investigate the effect of different anatomically relevant geometries and biological applicable material combinations, future studies should consider to evaluate microfibre patterning onto convex and irregular shaped geometries composed of more than one material combination, and with included porosity for the bone-reflecting component.

Conclusion

Taken together, this study successfully demonstrates the printing of well-organized microfibre scaffolds on clinically relevant collecting materials with non-flat geometries. The electrical properties of the substrate materials revealed a greater impact on accurate fibre deposition than the substrate thickness. Notably, deposition of MEW fibres was possible not only on conductive resorbable materials, like hydrogels, but also on less conductive materials, including bioceramics and thermoplasts. Accurate fibre deposition on non-flat geometries (wedge- and curved-shape structures) was shown to be successful, yet, maintaining the electrostatic force constant and normal to the collecting surface was fundamental for the successful deposition of micro sized fibres. This further understanding of the underlying physical principles of the MEW process allowed the fabrication of a complete condyle-shaped biological construct, for which abundant cartilage-like matrix formation after 28 days of *in vitro* culture was shown. This finding establishes the groundwork for further translation of the convergence of MEW and bioprinting, from flat to more anatomically relevant geometries that regenerative medicine intends to create.

Acknowledgements

This research was supported by EU funded—E11312 BioArchitect project together with regenHU, the Dutch Arthritis Foundation (LLP-12), and the European Research Council (ERC) consolidator grant 3D-JOINT (#647426). MC also acknowledges the strategic alliance University Medical Center Utrecht—Technical University Eindhoven and the partners of Regenerative Medicine Crossing Borders (www.regmedxb.com) and powered by Health~Holland, Top Sector Life Sciences & Health.

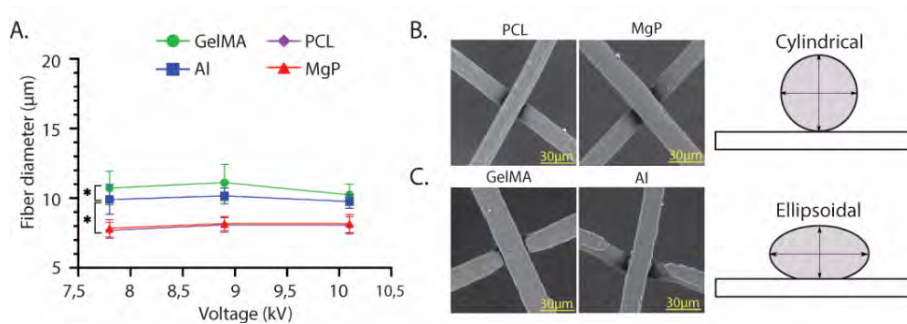
The authors gratefully thank Jacopo Bani, Alexandre Ribeiro and Michael Kuster for their help with the experimental part of this manuscript. In addition, the authors are very grateful to Marco Viveen Department of Microbiology, Utrecht Medical Center, for assistance with SEM analysis, and to Dr. Colin Peach from the faculty of Geosciences of the Utrecht University for the support with impedance spectroscopy measurements and analysis. The primary antibody against type II collagen (II-II6B3), developed by T. F. Linsenmayer, was obtained from the DSHB developed under the auspices of the NICHD and maintained by the University of Iowa, Department of Biology, Iowa City, IA, USA.



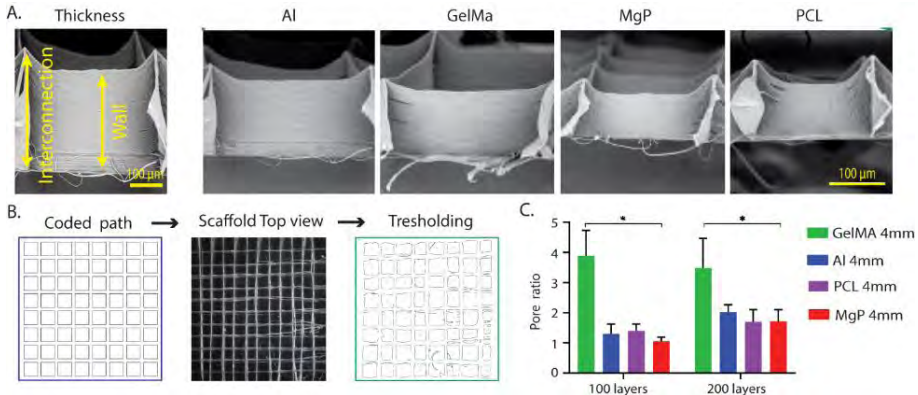
Supplementary data

Supplementary Table 1. Surface roughness of investigated materials

Substrate biomaterial	Average roughness (R_a , μm)	Route mean square roughness (R_q , μm)
Polycaprolactone (PCL)	0.21	0.32
Magnesium phosphate-based cement (MgP)	4.41	5.21
Gelatine methacryloyl (gelMA)	3.64	4.50
Aluminium (Al, control)	0.07	0.09



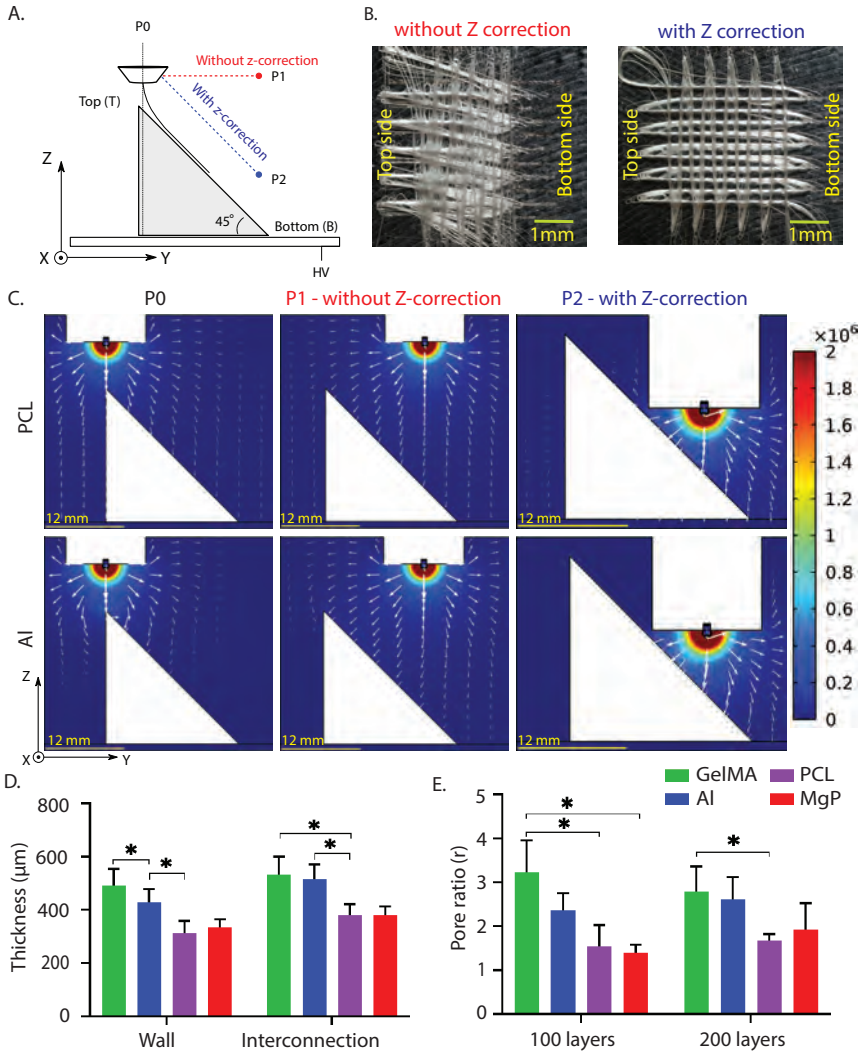
Supplementary Figure 1. A) Effect of applied voltage on fibre diameter. * = $p < 0.05$. Representative SEM images and schematic illustration of B) cylindrical fibres collected onto PCL and MgP substrates and C) ellipsoidal fibres collected onto gelMA and Al.



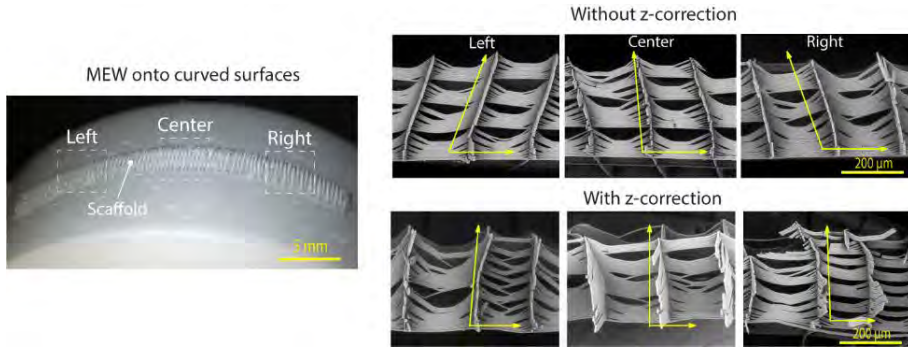
Supplementary Figure 2. A) Representation of measured differences between interconnection and wall thickness and representative SEM images of MEW scaffolds cross section collected onto different substrate materials. B) Imaging methodology used to quantify pore ratio. Top view images of coded path, printed scaffold and respective thresholding. C) Variation of pore ratio of scaffolds deposited on 4 mm thick collectors ($r = 1$ indicates a printed scaffold that conforms to the planned design, while values $r > 1$ indicates imperfect fibre stacking). * = $p < 0.05$.

Effect of collector geometry on fibre deposition –non-flat, wedge

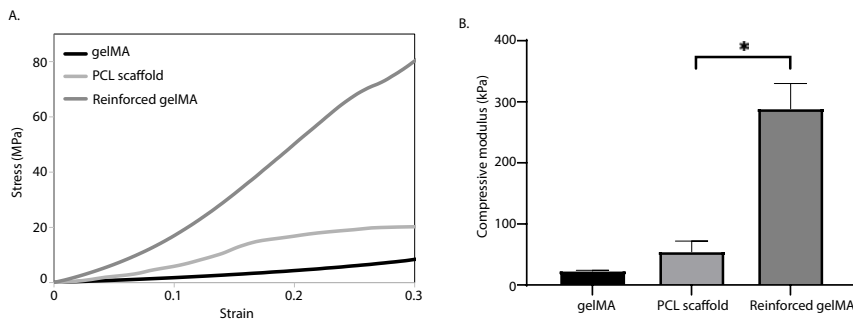
Once z-correction was applied to the printing trajectory, fibre placement accuracy was increased with only small fluctuations in fibre diameter between ascending ($\varnothing = 12.3 \pm 1.4 \mu\text{m}$) and descending ($\varnothing = 11.5 \pm 0.7 \mu\text{m}$) movements. Computational simulations showed that the EF strength at the surface of the wedge decreased when printing without a z-correction in printing trajectory (Supplementary Figure 3C). For prints with a z-corrected trajectory, the EF strength remained constant and the electrical force is normal to wedge surface (Supplementary Figure 3C). These observations were slightly more pronounced for less conductive materials (PCL and MgP). Scaffolds fabricated (using z-trajectory correction) onto non-conductive wedges (PCL, MgP) were 100 to 200 μm smaller than scaffolds fabricated onto conductive wedges (gelMA, aluminium) (Supplementary Figure 3D). Additionally, scaffolds fabricated on PCL and MgP wedges featured two-fold lower pore ratio than scaffolds fabricated onto the gelMA wedge (Supplementary Figure 3E).



Supplementary Figure 3: Fibre collection on wedge-shaped collecting materials (PCL, MgP, gelMA, and Al). A) Schematic representation of the evaluated printhead trajectories with and without z-correction. B) Representative stereoscopic images of scaffolds printed on aluminium wedge-shaped structures with and without z-correction of the printhead trajectory. C) Computational simulation of EF strength (V/m) and distribution (white arrows in logarithmic scale) for a non-conductive (PCL) and conductive (aluminium) wedge-shaped collecting materials. E) Quantification of final scaffold thickness at the walls and interconnections of the deposited fibres and of the pore ratio of scaffolds with 100 and 200 mm fibre spacing deposited on wedge-shaped collecting materials with z-correction in the printhead trajectory. * = $p < 0.05$



Supplementary Figure 4. Representation stereoscopic image of melt electrowritten PCL scaffolds onto a curved PCL substrate with and without z-correction. Representative SEM detailing the microstructure deformation at center, left and right (lateral) part of a PCL curved substrate. Yellow arrows highlight out-of-plane scaffold deformation.



Supplementary Figure 5. Reinforcement effect of cast melt electrowritten PCL scaffolds incorporated in gelMA hydrogel. These PCL scaffolds show the same inter fibre spacing ($400\ \mu\text{m}$) as compared to the ones that are used in the proof-of-principle in vitro study. A) representative stress-strain curves. B) compressive modulus of gelMA only, fibre reinforcing PCL scaffold only, and reinforced gelMA.

Supplementary Movie 1: Melt electrowriting onto ceramic non-flat, wedge substrate

Supplementary Movie 2: Melt electrowriting onto hydrogel non-flat, curved substrate



Supplementary methods

Surface roughness measurements

Surface roughness of substrate materials was measured using a surface roughness tester (SJ-400, Mitutoyo Corp.). Tests were carried out at 0.5 mm/s scanning speed and covered a specimen length of approximately 4 mm. For each substrate material, the average surface roughness (R_a) and the route mean square route roughness (R_q) was evaluated. R_a was calculated as,

$$R_a = \frac{1}{L} \sum_{x=1}^L |Z_x| \quad (3)$$

where L is the evaluation length of the substrate material and Z_x is the measured profile height. R_q was obtained by,

$$R_q = \sqrt{\frac{1}{L} \sum_{x=1}^L Z_x^2} \quad (4)$$

All measurements were repeated at least three times and in two different locations of each substrate material.

Printing accuracy quantification

Fibre scaffolds were imaged with an upright microscope (Olympus BX430) and subsequently processed with Fiji (version 2.0.0-rc-54/1.51h). A selection of pores in the central region of the scaffold were selected (Supplementary Figure 2B) and background signal was isolated from the scaffold with a thresholding step. Then, a particle analysis was run to count the number of “pores” (n_{measured}) and measure their area ($A_{\text{measured}}(i)$), where i indicates a specific pore in the range of [$i = 1 \dots n_{\text{measured}}$]. The pore ratio (r) was determined by,

$$r = \frac{n_{\text{measured}}}{n_{\text{design}}} \quad (5)$$

where n_{design} indicates the number of pores and $A_{\text{design}}(i)$ their respective area, that were designed. The pore ratio was validated against a second quality measure “open surface” (Q) determined as,

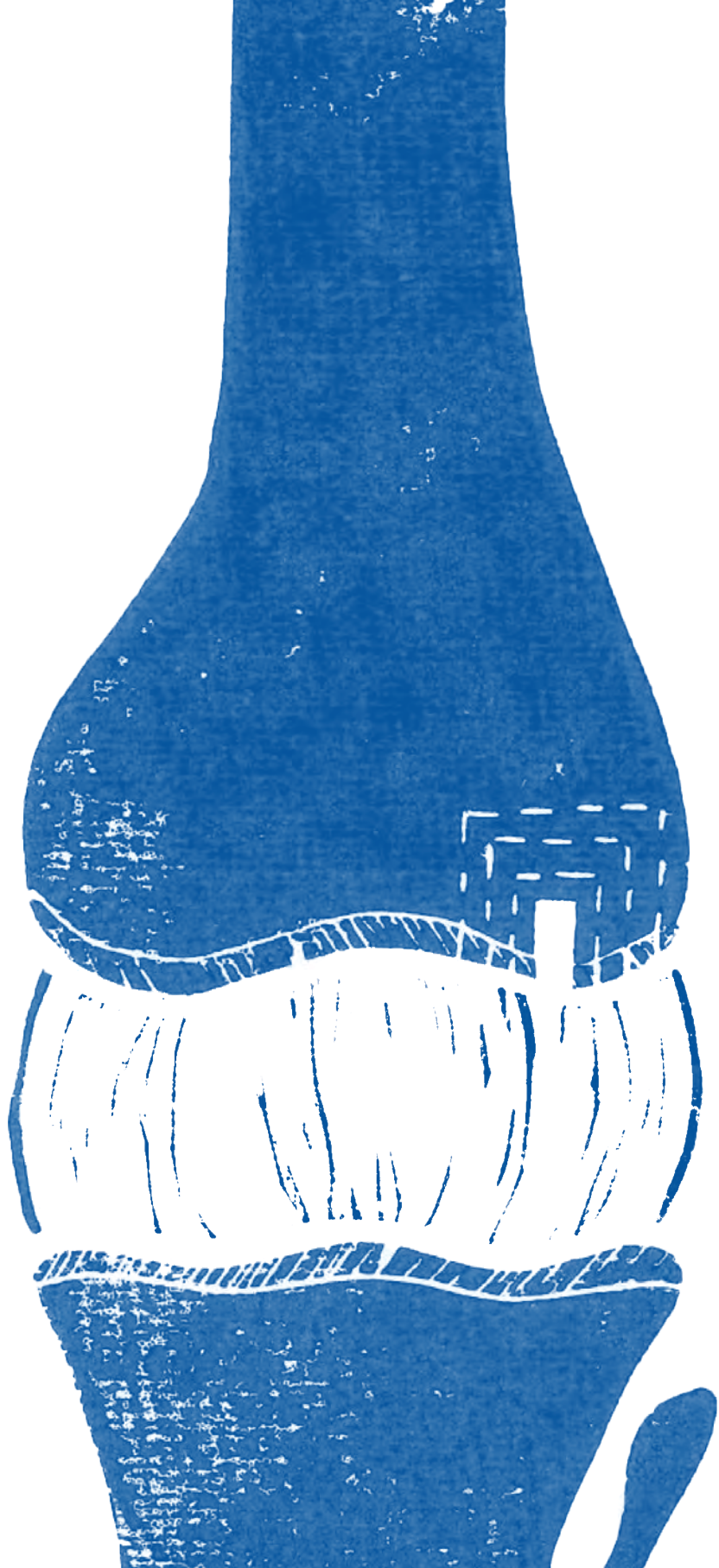
$$Q = \frac{\sum_{i=1}^{n_{\text{measured}}} A_{\text{measured}}(i)}{\sum_{i=1}^{n_{\text{design}}} A_{\text{design}}(i)} \cdot 100 \quad (6)$$

A value of $Q = 100\%$ corresponds to a printed scaffold that conforms to the theoretical design (no fibre misalignment), while values lower than 100% indicate a shift in fibre stacking. Values $Q = 0\%$ indicate that the fibres are randomly distributed covering the entire open surface. Since no significant differences between pore ratio and open surface were found, only results for pore ratio were presented.

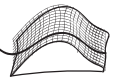
Chondrogenic differentiation medium

Chondrogenic differentiation medium consisted of Dulbecco's modified eagle medium (31966, Thermo Fisher Scientific, USA) supplemented with 1% penicillin/streptomycin, 1% l-ascorbic acid-2-phosphate, 1% ITS + Premix Universal culture supplement (Corning, USA), 2.5% HEPES (1M, Gibco, Thermo Fisher Scientific, USA), 0.4% dexamethasone (0.1×10^{-6} M, Sigma Aldrich, USA) and 0.1% recombinant human transforming growth factor- β 1 (TGF- β 1) (10 ng/mL, Preprotech, UK). Medium was refreshed three times per week.

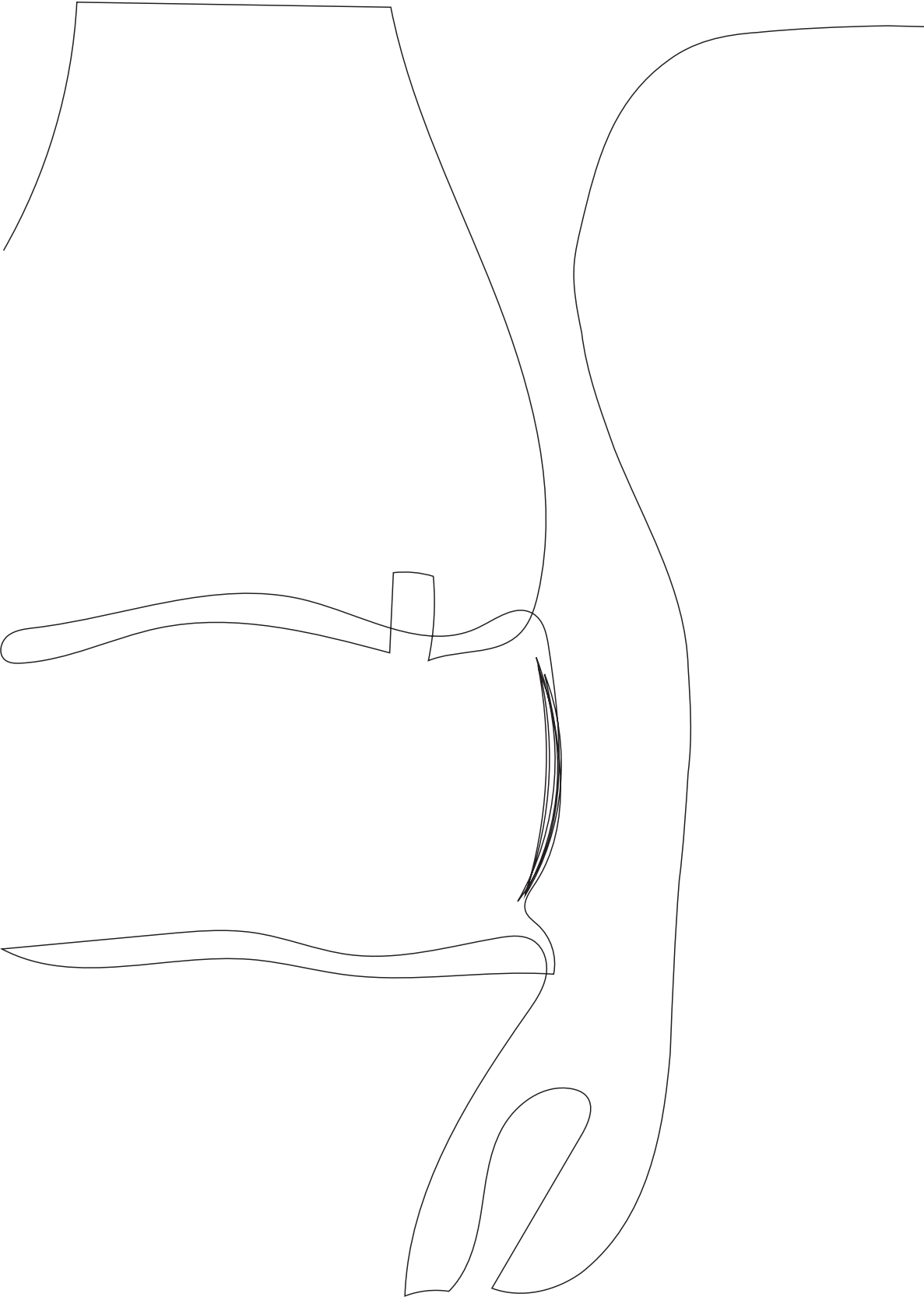


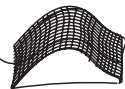


Part III



Application and *in vivo* translation of multi-scale biofabrication approaches





Chapter 7

Bone morphogenic protein 9 stimulates efficient cartilage-like matrix production by articular cartilage-resident chondroprogenitor cells onto 3D melt electrowritten scaffolds

7

Florencia Abinzano¹
Mylène de Ruijter¹
Anneloes Mensinga¹
Miguel Castillo^{1,2}
I. M. Khan³
P. René van Weeren⁴
Riccardo Levato^{1,4}
Jos Malda^{1,4}

Manuscript in preparation

¹ Department of Orthopaedics, Regenerative Medicine Utrecht, UMC Utrecht, University of Utrecht, The Netherlands

² Department of Biomedical Engineering, Eindhoven University of Technology, The Netherlands

³ Centre for NanoHealth, Swansea University Medical School, Swansea, UK

⁴ Department of Clinical Sciences, Faculty of Veterinary Medicine, Utrecht University, The Netherlands

Abstract

In search for a regenerative approach to treat cartilage defects, three dimensional (3D) *in vitro* cultured constructs are being explored. These constructs typically contain high cell densities to stimulate abundant neocartilage formation through enhanced cell-cell communication. For the translation of such 3D cell-laden constructs towards the treatment of larger defects, significant amounts of cells will be needed. Given the fact that chondrocytes lose their chondrogenic potential after multiple proliferative cycles, it is challenging to achieve such large cell quantities, especially when considering an autologous approach. The successful use of mesenchymal stromal cells (MSCs) as an alternative cell source is hampered as these cells tend to undergo hypertrophic differentiation. Articular cartilage-resident chondroprogenitor cells (ACPCs), on the other hand, are a promising candidate for cell-based therapies as these can efficiently be expanded while preserving their chondrogenic phenotype. To further increase neocartilage formation, growth factors are also used during *in vitro* culture. In this study, ACPCs were stimulated with bone morphogenic protein 9 (BMP-9) which resulted in more efficient cartilage-like matrix production. The stimulated ACPCs were combined with melt electrowritten (MEW) micro-fibre meshes, to support shape retainment. Furthermore, the organized MEW fibres induced a mechanically reinforcing effect once cartilage-like matrix formation was achieved. This combination of efficient cartilage-like matrix production and mechanical reinforcement holds promise for generating large cartilage tissue equivalents while maintaining control over the required shape.



Introduction

Articular cartilage defects can lead to pain and disability for patients and the prevalence is high. Indeed, 60% of patients that are investigated arthroscopically are diagnosed with focal cartilage defects.^{25,26} Cartilage exhibits limited regenerative capacity and damage to this tissue can therefore lead to the development of osteoarthritis (OA), which eventually can result in the need for a knee replacement at a relatively young age.²⁹³ Current treatment options are still sub-optimal as these generally result in the formation of type I collagen rich, fibrous cartilage with weaker mechanical properties.²⁹⁴ Regenerative approaches to treat cartilage defects, such as autologous chondrocyte implantation (ACI) have shown promising results.²⁹⁵ However, cell-based therapies still show a high variation between outcomes, depending on factors including age, size of defect and level of physical activity.²⁹⁶ Furthermore, cell availability and selection of the most effective cell source remains a challenge, even when a co-culture approach of different cell types is used.²⁹⁶

Although, the use of autologous cell sources, such as chondrocytes and mesenchymal stromal cells (MSCs) is preferred to avoid adverse immune responses, the use of these cells poses its own limitations. Chondrocytes generate cartilage matrix components, yet, they also tend to de-differentiate and lose their ability to produce chondrogenic matrix when expanded *in vitro*, posing a limit on the number of regenerative cells that can be obtained from an autologous source.^{167,295} Additionally, as autologous chondrocytes are acquired via a biopsy from a non-load bearing cartilage area, donor site morbidity can occur. Autologous MSCs on the other hand, are widely available and can easily be obtained from the patient's bone marrow. MSCs can be expanded *in vitro* to high cell numbers and can differentiate towards the chondrogenic lineage when exposed to specific culture conditions.²⁹⁷ However, MSCs tend to go into hypertrophic growth and subsequent endochondral pathway.²⁹⁸ Articular cartilage-derived chondroprogenitor cells (ACPCs) are precursor cells that reside within the superficial layer of articular cartilage and are a promising alternative to MSCs and chondrocytes. ACPCs exhibit stem-like characteristics as they show trilineage differentiation potential and maintain their chondrogenic capacity after multiple proliferation cycles.^{33,299} ACPCs present similar surface markers as MSCs and have been found to express the SOX9 gene while retaining telomerase activity.^{34,300} Interestingly, unlike MSCs, ACPCs do not undergo hypertrophic differentiation.³⁰¹

The majority of research on ACPCs has been performed using the standard chondrogenic TGF- β 1-supplemented media that were originally developed for the chondrogenic differentiation of MSCs.¹⁶⁷ Recently, multiple additional chondrogenic factors were tested on bovine ACPCs and specifically bone morphogenic protein 9 (BMP-9), also

known as growth differentiation factor 2 (GDF-2), was found to significantly improve chondrogenesis.³⁰² Thus, BMP-9 seems a promising chondrogenic stimulant for ACPCs.

Tissues in the knee joint are subjected to tremendous loading conditions. Clinical application of cell-based therapies, therefore, requires therapeutic solutions that are mechanically stable enough to withstand such environment and maintain their shape. Strategies to achieve mechanical stability and shape retainment include the use of mechanically reinforced biomaterials.^{82,84,184,188} Although biomaterials (e.g hydrogels) aid to keep the regenerative cells in place, they can also limit cell-cell interactions, which are vital for cartilage-like tissue formation.^{95,303–306} An alternative, hydrogel-free, approach to facilitate cell-cell communication while still providing a 3D structure that can guide the architecture of newly forming tissue is the use of fibre meshes fabricated with melt electrowriting (MEW). MEW is a (sub)micro-fibre fabrication technique that produces scaffolds that are used as 3D culture systems.^{88–90} For example, MEW meshes have been used to guide cell adhesion and alignment,^{169,307} but also to generate tissue-sheets made from organoids.³⁰⁸ Because of the micro-meter scale fibres, the MEW fibre meshes allow ample matrix formation. Additionally, MEW meshes significantly increase the mechanical properties of hydrogels as of the stable fibre intersections, combined with limited buckling of the MEW fibres by the surrounding hydrogel.^{84,92,93,187,274} Hence, MEW offers a unique capacity to harbor high cell densities and provide a 3D environment for the development neo-cartilage.

The aim of this study was to create durable, cartilage constructs by maximizing cartilage matrix production by ACPCs and incorporating the cells within reinforcing MEW microfibre meshes to aid in shape preservation.

Materials and Methods

Cell isolation and expansion

Cells for this study were obtained from equine donors following previously described protocols.¹⁶⁷ The horses died from causes unrelated to joint issues and their bodies were donated to research by their owners, following the Ethical Guidelines of the University Medical Center Utrecht and the Faculty of Veterinary Medicine of Utrecht University.

Briefly, to isolate ACPCs, articular cartilage was acquired from the knee joints under sterile conditions, minced and digested overnight. ACPCs were then selected using a fibronectin adhesion protocol and tested for trilineage differentiation.^{34,167} Cells were then expanded to passage 3 in Dulbecco's modified Eagle medium with GlutaMAX (DMEM, 31966, Gibco,



The Netherlands) supplemented with 10% v/v heat inactivated FBS, 1% v/v penicillin and 1% v/v streptomycin (Life Technologies, The Netherlands), 1% non-essential amino acids solution (NEAA, Gibco, The Netherlands), and 5 ng/ml basic fibroblast growth factor (bFGF, Peprotech, UK). MSCs were obtained from bone marrow aspirates from 3 different donors and expanded until passage 3 using α MEM (22561, Gibco, The Netherlands) supplemented with 10% v/v heat inactivated FBS, 1% v/v penicillin and 1% v/v streptomycin, 1 ng/ml bFGF and 0.2 mM ascorbic acid-2-phosphate (ASAP, Sigma, The Netherlands). After expansion, cells were frozen and stored in liquid nitrogen until further use.

3D culture

Pellets of 250.000 ACPCs or MSCs were formed using ultra-low attachment plates (Corning Costar, Sigma, The Netherlands). The resulting pellets were then cultured in either BMP-9 medium (DMEM/F12 GlutaMAX (31331-028, Gibco, The Netherlands) supplemented with 10mM HEPES (Gibco, The Netherlands), 1% ASAP, 1% ITS premix (Corning, Sigma, The Netherlands), 1% Pen/Strep and 100 ng/ml fresh recombinant human BMP-9 (PeproTech, The Netherlands) or TGF- β 1 medium consisting of DMEM/F12 GlutaMAX, 1% Pen/Strep, 1% ITS premix, 1% ASAP, 100 nM dexamethasone (Sigma-Aldrich, The Netherlands) and 10 ug/ml fresh TGF- β 1 (PeproTech, The Netherlands) for 28 days. An extra group (switch group) was added to assess if using BMP-9 for only 10 days was enough to stimulate growth and then change the cells to regular TGF- β 1 media (**Figure 1A**). Medium was refreshed 3 times per week.

Fabrication of 3D fibre meshes

Melt electrowriting (MEW) was used to fabricate scaffolds of medical grade polycaprolactone (PCL, PURASORB PC 12, Corbion PURAC, The Netherlands) with a closed surface followed by a uniform box-pattern with an inter fibre distance of 400 μ m. The closed surface was achieved by depositing MEW fibres with an inter fibre distance of 100 μ m in a box-pattern in an alternating 0°- 45°- 90°- 135° direction. MEW was performed at room temperature (20 - 24°C) and at 30 - 45% humidity, with a custom built device as previously described.¹⁶⁹ Using a 25G nozzle, at a printing temperature of 90°C, air pressure of 2.0 bar, collector distance of 3 mm, voltage of 5 kV, and collector velocity of 9 mm/s, the average fibre diameter was $10.6 \pm 0.4 \mu$ m and total height of the scaffolds was 1 mm. To increase hydrophilicity, the meshes were hydrolyzed by submerging them 30 minutes in 1M sodium hydroxide solution, followed by rising 4 times for 10 minutes in milliQ water. Meshes were then sterilized by submerging them in 70% ethanol for 20 minutes and air-dried in a sterile environment.

Fabrication of reinforced 3D tissue constructs

For the fabrication of reinforced 3D tissue constructs, cylindrical samples of 6 mm in diameter were punched out of sterile MEW meshes and placed flat at the bottom of in-house developed silicone well, which were in turn placed into 6-well plates. ACPCs were expanded and resuspended in BMP-9 medium. Cell-containing medium (150 μ l; 5×10^6 cells) was gently placed on top of the meshes, or straight into the bottom of the silicon wells for the mesh-free controls. Cells were allowed to settle for 30 minutes. After that, 1 ml of medium was gently added to each well.

Analysis of cartilage-like matrix formation

Pellets and constructs were harvested for analysis of cartilage-like tissue formation after 10 and 28 days of culture. For histology, samples were placed in formalin overnight, dehydrated, encased in paraffin and sectioned into 5 μ m slices. Safranin-O, type I collagen, and type II collagen stainings were performed according to established protocols (n = 3).¹⁶⁷

To perform biochemical analysis, pellets (n = 3) and constructs (n = 5) were lyophilized and subsequently digested using a papain solution. A dimethylmethylene blue assay (DMMB, Sigma Aldrich, The Netherlands) was performed to quantify the amount of glycosaminoglycans (GAGs) and a PicoGreen assay was done to quantify DNA (Quant-iT PicoGreen, Life Technologies, The Netherlands). For the pellets, the measurement of alkaline phosphatase (ALP) was also performed. For that, additional samples (n = 3) were placed into M-PER Mammalian Protein Extraction Reagent, freeze-thawed and ALP was measured using the p-nitrophenyl phosphate assay (SIGMAFAST, Sigma-Aldrich). DNA was also quantified for these samples as described above. Gene expression was evaluated using quantitative polymerase chain reaction (qPCR) (n = 3). mRNA was isolated with an RNeasy Mini kit (Qiagen, Germany). cDNA was then amplified and synthesized using the Superscript III Platinum SYBR Green One-Step qRT-PCR Kit (Life Technologies, The Netherlands). Relative gene expression was calculated by comparing the Ct value of type X collagen (COLX) to the housekeeping gene hypoxanthine phosphoribosyltransferase-1 (HPRT1), using primers that have been previously described.¹⁶⁷ All calculations were done using the PCR Miner algorithm.

Mechanical analysis

To test the compressive strength of the fabricated reinforced and control constructs, samples were washed with phosphate-buffered saline (PBS) and an unconfined uniaxial compression test was performed with a dynamic mechanical analyser (DMA Q800, TA Instruments, The Netherlands) (n = 5). A strain rate of 20%/min was applied and the compressive modulus was calculated as the slope of the stress/strain curve within 10



to 15% strain. Samples used for mechanical analysis were then frozen and processed for biochemical analysis.

Statistical analysis

Results were expressed as mean \pm standard deviation. GraphPad Prism 8.0 (GraphPad Software, USA) was used to perform 2-way ANOVA analyses, including multiple comparisons using a post-hoc Bonferroni test. Results were considered significant when $p < 0.05$.

Results

Induced chondrogenesis on 3D aggregates

ACPCs that were stimulated with BMP-9 showed an increase in pellet size (> 2 mm) as compared to ACPCs that were stimulated with standard chondrogenic TGF- β 1 media (~ 1 mm) (**Figure 1A, B**). Additionally, BMP-9 stimulation negatively affected the growth of MSC pellets, which showed smaller sizes as compared to MSCs that were stimulated with standard chondrogenic TGF- β 1 media. Overall, the ACPCs outperformed MSCs for cartilage-like tissue formation in all conditions (**Figure 1C**). After 28 days of culture, a significant increase in the production of GAGs/DNA was found for ACPCs stimulated with BMP-9 ($135.5 \mu\text{g}/\mu\text{g}$) as compared ACPCs stimulated with standard TGF- β 1 medium ($9.8 \mu\text{g}/\mu\text{g}$) (**Figure 1C**). Remarkably, in the BMP-9 group, abundant cartilage-like tissue formation was already present after 10 days in culture, and significant differences in GAGs/DNA were found for BMP-9 stimulated ACPCs ($19.1 \mu\text{g}/\mu\text{g}$), as compared to the BMP-9 stimulated MSCs ($2.8 \mu\text{g}/\mu\text{g}$) and the TGF- β 1 stimulated ACPCs ($5.9 \mu\text{g}/\mu\text{g}$) (**Figure 1C**). Furthermore, after 28 days of culture GAGs/DNA was higher for BMP-9 stimulated ACPCs ($135.5 \mu\text{g}/\mu\text{g}$) as compared to the switch group ($69.01 \mu\text{g}/\mu\text{g}$). Although TGF- β 1 stimulation resulted in an increase in GAGs/DNA for both MSCs and ACPCs, after 10 and 28 days of culture, no significant difference was found for GAGs/DNA between TGF- β 1 stimulated MSCs (10 days: $3.9 \mu\text{g}/\mu\text{g}$, 28 days: $10.2 \mu\text{g}/\mu\text{g}$) and TGF- β 1 stimulated ACPCs (10 days: $5.9 \mu\text{g}/\mu\text{g}$, 28 days: $9.8 \mu\text{g}/\mu\text{g}$). DNA quantification showed no significant difference between stimulation methods for the ACPCs after 28 days (**Figure 1D**). For MSCs, an increase in DNA for the TGF- β 1 group ($1466 \mu\text{g}$) was found as compared to BMP-9 ($372.9 \mu\text{g}$) and the switch group ($561.6 \mu\text{g}$) after 28 days. No significant difference in DNA was found for the ACPCs that were stimulated with BMP-9 ($1914.9 \mu\text{g}$), TGF- β 1 ($2027.9 \mu\text{g}$), or switched from BMP-9 to TGF- β 1 after 10 days ($1918.9 \mu\text{g}$). Histologically, all ACPC pellets presented a high content of GAGs (**Figure 1E**), as well as type II collagen (**Figure 1F**). For ACPCs, the safranin-O staining showed a higher intensity of staining for the BMP-9 stimulated pellets as compared to the pellets that were stimulated with the standard TGF- β 1 protocol. Additionally, the pellets stimulated with BMP-9 show more lacunae around the cells as compared to the pellets that were stimulated with the standard TGF- β 1 protocol.

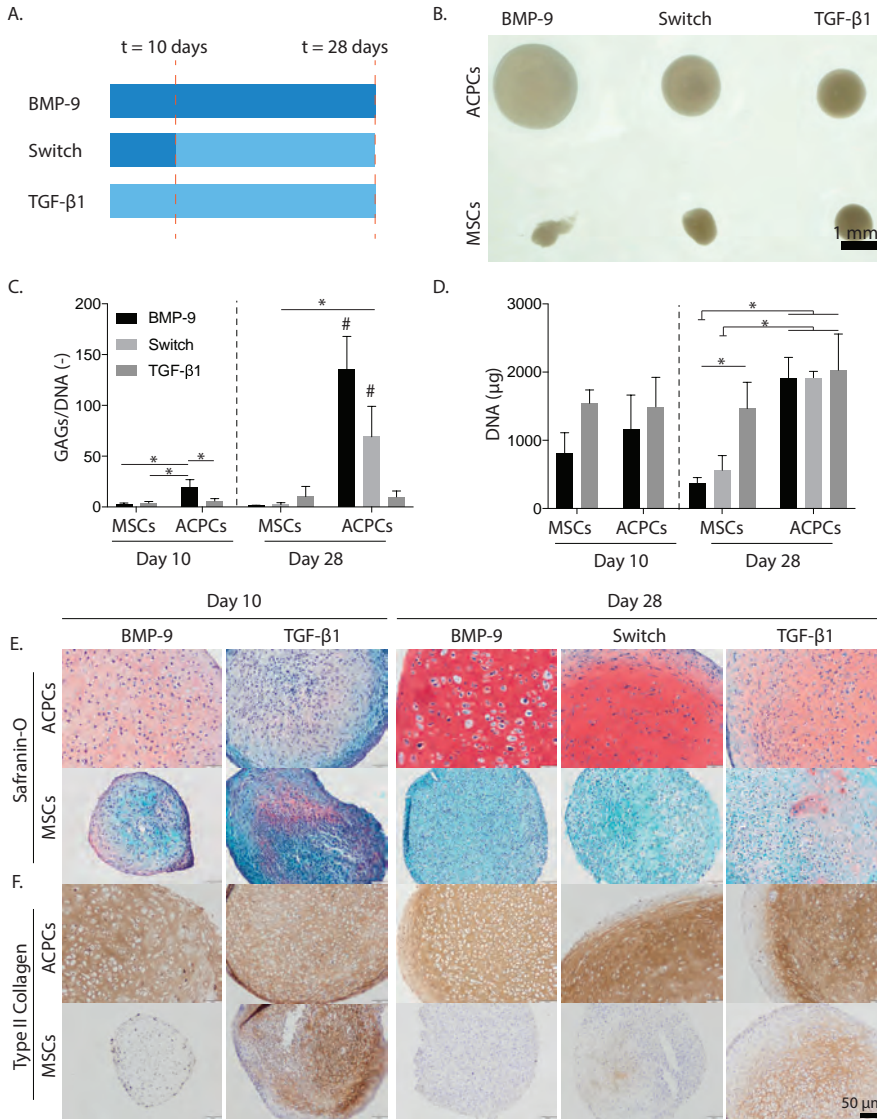


Figure 1. Effect of BMP-9, TGF-β1, and switching from BMP-9 to TGF-β1 stimulation on pellets made from ACPCs and MSCs. A) Representation of the growth factor supplementation groups and timing of switching from BMP-9 to TGF-β1. B) Effect of different groups on morphology and size of pellets of ACPCs and MSCs after 28 days of culture. Scale bar = 1 mm. C) Quantification of GAGs/DNA after 10 and 28 days of culture. D). Quantification of DNA after 10 and 28 days of culture. E) Safranin-O staining representing cartilage-like matrix formation (red) after 10 and 28 days of culture. F) Type II collagen staining depicting type II collagen in brown after 10 and 28 days of culture. Scale bar = 50 μm. * = Statistically different ($p < 0.05$ ANOVA post hoc Bonferroni). # = Statistically different from all other groups ($p < 0.05$ ANOVA post hoc Bonferroni).



Absence of osteogenic markers in 3D aggregates

No difference in relative gene expression of type X collagen was found between the TGF- β 1 group as compared to the BMP-9 group for both MSCs and ACPCs (**Figure 2A**). Furthermore, the production of ALP/DNA was consistently low for most samples (**Figure 2B**). None of the ACPC or MSC samples stained positive for type I collagen (**Figure 2C**).

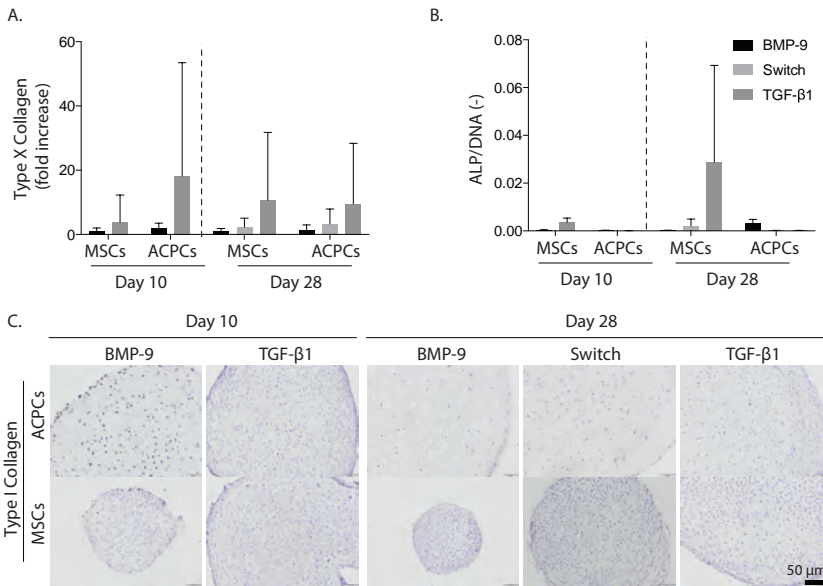


Figure 2. Effect of BMP-9, TGF- β 1, and switching from BMP-9 to TGF- β 1 stimulation on de-differentiation of pellets made from ACPCs and MSCs. A) Type X Collagen gene expression as compared to housekeeping gene by ACPC and MSC pellets after 10 and 28 days of culture. B) Quantification of ALP formation per DNA by ACPC and MSC pellets after 10 and 28 days of culture. C) Type I collagen staining depicting type I collagen in brown after 10 and 28 days of culture. Scale bar = 50 μ m.

3D cell culture onto reinforcing MEW microfibre meshes

MEW meshes with a dense bottom architecture were successfully fabricated (**Figure 3A**). The smaller pore size combined with the differently aligned fibres offered a foundation for the internal (400 μ m x 400 μ m) boxed-structure, which retained its shape and pore size, therefore allowing successful 3D culture of ACPCs onto these meshes. Although some lateral tissue growth was found (**Figure 3B**, black arrow), the ACPCs cultured on these meshes retained the required disc shape and did not turn into the typical pellet shape

(Figure 3B). After 10 days of culture, no difference in compressive modulus was found between the ACPCs (12.6 kPa) and the ACPCs reinforced with MEW meshes (22.2 kPa). After 28 days of culture, the combination of the ACPCs within the MEW mesh resulted in a significantly higher compressive modulus, with the reinforced construct (199.0 kPa) presenting more than 3.5 times the compressive modulus as compared to the cell-only samples (53.2 kPa) (**Figure 3C**). Biochemical analysis showed no significant differences in the amount of GAGs/DNA between the cell-group and the reinforced-group (**Figure 3D**).

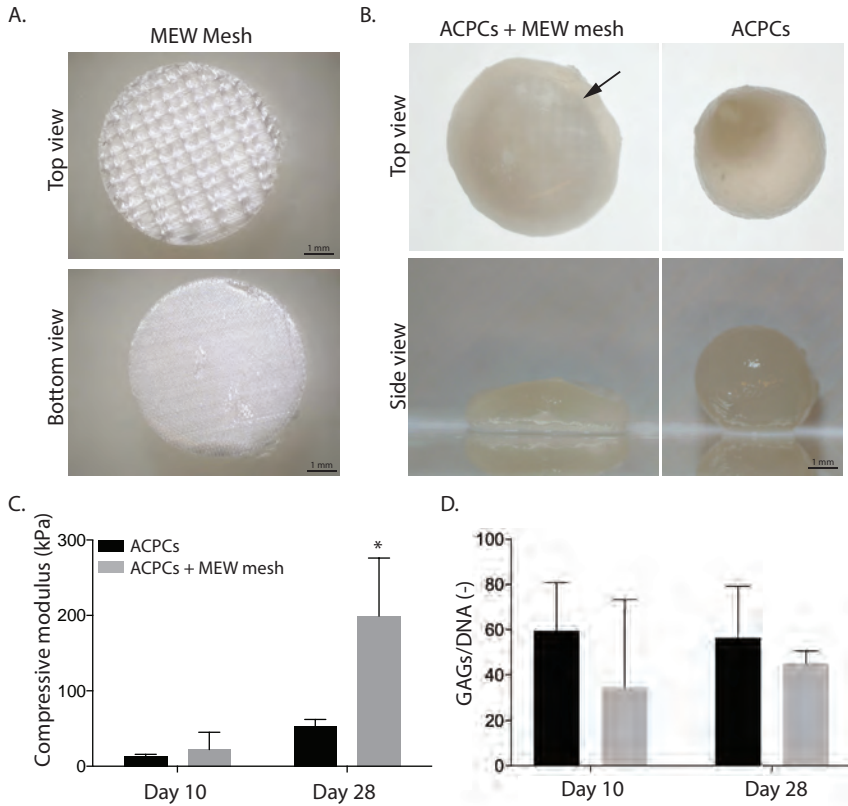


Figure 3. *In vitro* 3D culture of ACPCs within MEW fibre meshes. A) Top and bottom view of the used MEW mesh. B) Top and side view of ACPCs cultured in the MEW mesh as compared to normal culture after 28 days of culture. Black arrow indicating lateral tissue growth. C) Compressive modulus of ACPCs cultured within the MEW mesh as compared to cell-only culture after 10 and 28 days. D) Quantification of GAGs per DNA after 10 and 28 days for ACPCs cultured within the MEW mesh and cell-only culture.



Discussion

The results from this study show that BMP-9 significantly improved the performance of ACPCs in terms cartilage-like matrix production. These findings are in line with those previously reported by Morgan *et al.*, where BMP-9 was found to be a potent chondrogenic factor for bovine ACPCs.³⁰² When the growth factor supplementation of ACPCs was switched from BMP-9 to TGF- β 1 after 10 days, the matrix deposition slowed down, limiting the overall growth of tissue aggregates. Despite the increase in pellet size, the DNA content of ACPCs cultures was not significantly affected by the growth factors used. This suggests that pellet growth resulted from matrix deposition. On the other hand, BMP-9 stimulation showed a negative effect on DNA content and chondrogenesis of MSCs as compared to TGF- β 1 stimulation. After switching from BMP-9 to TGF- β 1 after 10 days of culture, similar GAG/DNA levels as the TGF- β 1 cultured group were not achieved.

While Morgan *et al.* and Hill *et al.*^{302,309} both observed stimulatory effects of BMP-9 in cultures of cells derived from immature specimens, this study confirmed these effects for cultures of progenitor cells obtained from the joints of mature animals. Critically, this expands the possibilities of BMP-9 as an effective chondrogenic factor, irrespective of donor-age. This is supported by the fact that adult cartilage cells have been found to lose their receptors for TGF- β 1 signalling, yet not the BMP-9 receptor ALK-1, which has been shown to be unaffected by aging.³¹⁰ In this study, ALK-1 expression was found after 10 days in both MSCs and ACPCs when exposed to BMP-9.

Interestingly, this study showed significant cartilage-like matrix formation after only 10 days of BMP-9 stimulation, with GAGs and type II collagen already present. This efficient method of tissue formation yields promise for shorter pre-culture times, as well as faster *in vitro* testing systems and thus also reduces costs.

Hypertrophic growth of MSCs is a significant problem in articular cartilage regeneration as this generally results in eventual osteogenic differentiation.²⁹⁸ Previous studies by Levato *et al.*, and McCarthy *et al.* found no signs of hypertrophy of ACPCs when stimulating with TGF- β 1.^{167,301} However, van Caam *et al.* and Blunk *et al.* found that exposing chondrocytes to BMP-9 can lead to hypertrophy.^{311,312} Furthermore, this particular growth factor was shown to have conflicting effects when added to MSC cultures. While Majumdar *et al.* showed that 100 ng/ml BMP-9 can induce chondrogenesis on MSCs and even help overcome the negative effects of inflammatory proteins,³¹³ Yan *et al.* and Lamplot *et al.* found that BMP-9 can also be used to induce osteogenesis on MSCs.^{314,315} Nonetheless, this study found no signs of hypertrophy in the MSC or ACPC pellets when combined with BMP-9, as shown by low gene expression of type X collagen when ACPCs were stimulated with

BMP-9. Additionally, the production of ALP and lack of type I collagen upon histological evaluation confirms that both the ACPCs and MSCs are not differentiating towards the osteogenic lineage.

The use of BMP-9 in combination with ACPCs is particularly interesting as both have been shown to play a role in joint development.³⁰² For example, a study by Yu *et al.* described the importance of BMP-9 on regenerating a synovial joint after digit amputation.³¹⁶ BMPs in general have been linked to early chondrogenesis, guiding the development on the early phases.³¹⁷ Similarly, a study by Longobardi *et al.* described how the progenitor cells are involved in joint development, undergoing an early phase of cell condensation where direct cell-to-cell interaction is key in the commitment to cartilage development.³¹⁸ The number of cells then remain stable, while the growth of the tissue is linked to matrix deposition. In the current study, the BMP-9 stimulated ACPC pellets, also showed no significant increase on the number of cells and high matrix deposition to generate the overall growth.

MEW fibre meshes have been used as a base structure for 3D cell culture and to guide cartilage-like matrix formation. Directing cartilage-like matrix formation with inert PCL fibres has been shown to induce collagen alignment upon the dynamic culture of spheroids for tibial resurfacing.³¹⁹ Although Daly *et al.* used thick (150 µm) FDM PCL fibres, the directional potential of inert PCL fibres might be true for the thinner MEW fibres as well.

A similar use of MEW fibre meshes showed that these constructs can be used to culture spheroids of adipose-derived stromal cells and guide them towards the formation of tissue-sheets that can be used as tissue culture models or for implantation.³⁰⁸ Where McMaster *et al.* used precultured spheroids, the cells used in this study were directly deposited on the MEW fibre mesh, which was successful as the design of the MEW fibre meshes included a bottom layer with a high density of fibres that prevented the cells from getting out of the mesh. This high-density fibre layer also prevented collapsing of the mesh upon culture, resulting in a more reproducible and successful culture method.

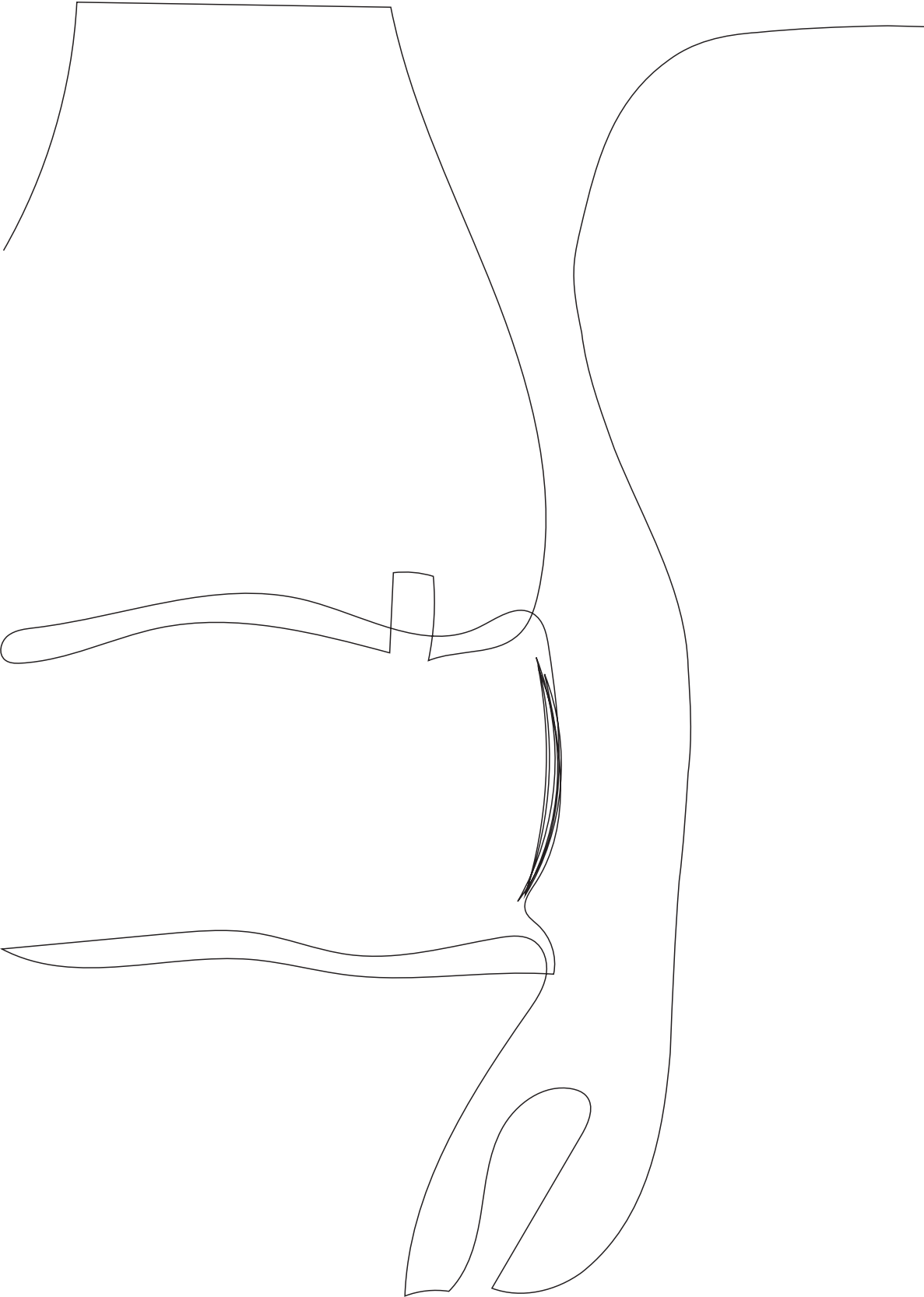
The additional reinforcing effect of the MEW fibre meshes, that was previously seen when combined with hydrogels^{84,92,187,274}, was only evident after cartilage-like matrix formation occurred. Initial mechanical stability was not provided by the MEW fibre meshes. As fast and efficient matrix formation by use of BMP-9 was demonstrated, and the reinforcing effect was shown after matrix formation was observed, including only a short pre-culture period would be sufficient to induce the reinforcing effect and aid in creating a mechanically stable construct. In the case that direct implantation after cell

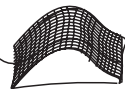


seeding is required, a rapidly degrading hydrogel, such as fibrin glue, may well pose a solution as a fast degrading hydrogel does not limit cell-cell interaction as slow degrading hydrogels do.^{320,321} By occupying minimal volume, the microfibre meshes allow the ACPCs to experience the direct cell-to-cell interaction that is crucial to recreate cartilage development.⁹⁵ Importantly, the MEW fibre meshes also guided the matrix formation of the cells into a disc shaped construct. The ability of MEW fibre meshes to control the shape of neo formed cartilage-like tissue yields promise for personalized larger cartilage implants. Upon fabrication of such implants, the anatomically convex shape of the condyle needs to be considered and control over tissue growth will result in a smooth articulating surface, which is vital for proper joint function. To achieve this, MEW onto anatomically relevant structures and materials, such as demonstrated in **Chapter 6** is needed.

Conclusion

Taken together, this study showed the efficient production of large quantities of cartilage-like matrix without inducing hypertrophic growth of ACPCs by stimulating ACPCs with BMP-9. The MEW fibre meshes used in this study were shown to aid the maintenance of the required shape of cartilage-like tissue, without limiting the efficient and homogeneous cartilage-like matrix deposition. These MEW fibre meshes additionally increased the compressive properties after matrix formation. The impact of these results for cartilage tissue engineering specifically lie in the efficient and spatially-controlled production of large quantities of cartilage-like tissue matrix that is key for the fabrication of larger, clinically relevant, implants.





Chapter 8

Pivotal importance of reinforcement of cartilage implants confirmed in challenging large animal model; presence of transplanted cells probably secondary

8

Mylène de Ruijter¹,
Paweena Diloksumpan²,
Inge Dokter¹,
Harold Brommer²,
Ineke H. Smit²,
Riccardo Levato^{1,2},
P. René van Weeren^{2*},
Miguel Castilho^{1,3},
Jos Malda^{1,2*}

Manuscript under review

¹ Department of Orthopaedics, RMCU Utrecht, UMC Utrecht, University of Utrecht, The Netherlands

² Department of Clinical Sciences, faculty of Veterinary Medicine, Utrecht University, The Netherlands

³ Department of Biomedical Engineering, Eindhoven University of Technology, The Netherlands

Abstract

In articular cartilage, the collagen arcades provide the tissue with its extraordinary mechanical properties. As these structures cannot be restored once damaged, functional restoration of articular cartilage defects remains a major challenge. We report that the use of a reinforced osteochondral implant, based on a gelatin methacryloyl cartilage phase, reinforced with precisely patterned melt electrowritten polycaprolactone micrometer-scale fibres in a zonal, cartilage-mimicking fashion, can provide long-term mechanically stable neo-tissue in an orthotopic large animal model. Interestingly, the cell-free implants, used as a control in this study, showed abundant cell ingrowth and similar favourable results as the cell-containing implants. Our findings underscore the hypothesis that mechanical stability is more determining for the success of the implant than the presence of cells and pre-cultured extracellular matrix. This observation is of great translational importance and highlights the aptness of advanced 3D (bio)fabrication technologies for functional tissue restoration in the harsh articular joint mechanical environment.



Introduction

The biomechanical function of the tissues within the skeletal system is pivotal to provide structure and strength to the body. Articular cartilage sustains similar forces as the skeletal bones, but also mitigates these by its shock-absorbing character. This tissue is mechanically characterized by a combination of resilience and high resistance against compression and shear forces. This mechanical performance is permitted by the composition and structure of the extracellular matrix (ECM) of this relatively homogeneous, avascular and aneural tissue, combined with the strong interconnection of cartilage and bone into a cohesive functional structure (the osteochondral unit), that ensures load transmission and provides frictionless movement. The ECM of articular cartilage is a strong combination of a type II collagen network that is under intrinsic tension from highly hydrophilic proteoglycan aggregates.^{322,323} The tissue is sparsely populated with cells (1-12%) that only have a limited capacity of restoration of the tissue structure when skeletal growth has ceased, as the turnover of the main structural element, the collagen, is virtually nil in mature individuals.^{27,38,268} The calcified cartilage connects the articular cartilage with the mechanically widely different, much more rigid, subchondral bone. The resulting osteochondral unit allows, when in good health, proper joint function and nearly frictionless movement between opposing long bones.

In the quest for a regenerative solution for the unmet clinical need for the treatment of articular cartilage damage^{42,43} several biomaterial-based approaches have been explored, many of which involve the use of hydrogels for the cell-friendly environment they can provide.^{216,324-327} Despite promising *in vitro* results and in small animal models³²⁸, these attempts did thus far not succeed to create a mechanically stable tissue that repeatably has stood the test of *in vivo* testing in a large animal model.³²⁹⁻³³¹ Therefore, calls have been made to take a different approach in this area - from one that is primarily focused on optimizing the cell environment, towards that of recreating - more closely - the structural and mechanical features that define cartilage.¹⁰⁰

With the goal of restoring a biomechanically competent environment, this study (**Figure 1**) presents a function-driven strategy by which an osteochondral implant was engineered based on the convergence of melt electrowriting (MEW)^{89,90} with extrusion-based 3D bioprinting within a single-fabrication platform.^{199,276} The implant was composed of a 3D-printed calcium phosphate-based (pCaP) bone phase, which was anchored with the cartilage phase through embedded polycaprolactone (PCL) fibres generated with MEW to securely connect the cartilage and bone components of the osteochondral unit.²⁰² In addition, reinforcement of hydrogel structures with highly organized structures of these (sub)micrometer-scale fibres increases the compressive and shear properties of

hydrogel-thermoplastic composites to values approaching those of the native cartilage tissue.^{84,187,188,274} Moreover, the choice of relatively slowly degrading polycaprolactone (PCL) as structure-giving material may well guarantee the long-term retention of the mechanical properties of the implant. Given the fact that the ECM is a major determinant of the biomechanical functionality and in view of the significant economic and regulatory challenges associated with the clinical translation of cell-based regenerative techniques, we chose to compare a cell-seeded with a cell-free implant. For this, the most challenging large animal model³³², the horse, was used.

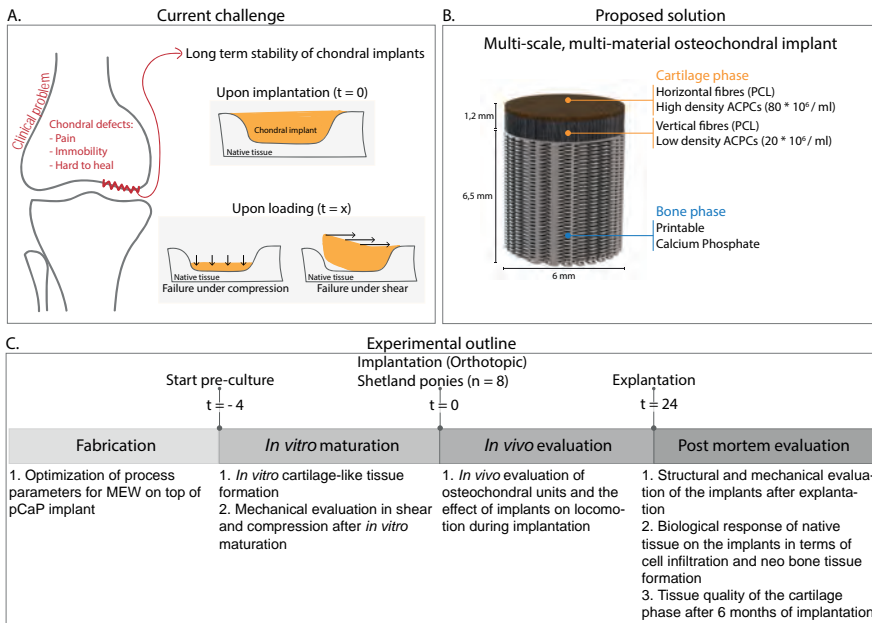


Figure 1. Schematic overview of this study. A) Current regenerative implants for cartilage defects are not satisfactory, as these implants are not stable upon loading after orthotopic implantation. B) Design details of the proposed multi-scale, multi-material osteochondral implant with details in the bi-layered cartilage phase and regenerative pCaP bone phase. ACPCs = Articular Cartilage-resident chondroProgenitor Cells. PCL = Polycaprolactone. C) Experimental outline of the performed study (t in weeks).

Methods

Cell isolation, expansion, and differentiation

Equine Articular Cartilage-resident Chondroprogenitor Cells (ACPCs) were isolated from healthy metacarpophalangeal joints of skeletally mature equine donors, as previously described.^{34,167} These donors had been donated to science by their owners and



procedures were followed according to the guidelines of the Ethical and Animal Welfare body of Utrecht University. ACPCs were cultured in expansion medium until passage 5, after which they were cultured in chondrogenic differentiation medium (1ml per implant) for 28 days. Expansion medium consisted of Dulbecco's modified eagle medium (31966, Thermo Fisher Scientific, USA) supplemented with 10% fetal bovine serum (Gibco, Thermo Fisher Scientific, USA), 1% penicillin-streptomycin (Gibco, Thermo Fisher Scientific, USA), 1% l-ascorbic acid-2-phosphate (0.2×10^{-3} M, Sigma Aldrich, USA), 1% non-essential amino acids (100X, Gibco, Thermo Fisher Scientific, USA), and 5 ng/mL bFGF (Preprotech, UK), and medium was refreshed twice per week. Chondrogenic differentiation medium consisted of Dulbecco's modified eagle medium (31966, Thermo Fisher Scientific, USA) supplemented with 1% penicillin/streptomycin, 1% l-ascorbic acid-2-phosphate, 1% ITS + Premix Universal culture supplement (Corning, USA), 2.5% HEPES (1M, Gibco, Thermo Fisher Scientific, USA), 0.4% dexamethasone (0.1×10^{-6} M, Sigma Aldrich, USA) and 0.1% recombinant human transforming growth factor- β 1 (TGF- β 1) (10 ng/mL, Preprotech, UK). Medium was refreshed three times per week. All cultures were performed under sterile and normoxic culture conditions at a temperature of 37°C and 5% CO₂.

Materials

Bioink: Gelatin methacryloyl (gelMA, degree of functionalization = 80%) was synthesized from low endotoxin gelatin (beMatrix gelatin LS-H, type B, porcine skin, 300 Bloom, Nitta Gelatin, USA) as previously described.^{168,258} Dialysis was performed for 4 days at 4°C, after which gelMA was lyophilized, and stored at -20°C until further use. Upon use, freeze-dried gelMA was dissolved in PBS at 8% w/v. 2-hydroxy-1-[4-(2-hydroxyethoxy)phenyl]-2-methyl-1-propanone (Irgacure 2959, BASF, Germany) was used as a crosslinking agent at 0.1 % w/v and UV-crosslinked for 15 minutes (UVP CL-1000 Ultraviolet Crosslinker, 120 000 microjoules per cm²). Gels were prepared at 8% w/v to match the same compressive properties observed in previous studies when using gelatin from different sources (**Supplementary Figure 4**).

Printable calcium phosphate (pCaP): The paste was prepared as a mixture of 2.2 g/ml of alpha-tricalcium phosphate (α -TCP) (average particle size = 3.83 μ m, Cambioceramics, The Netherlands), 0.13 g/ml of nano-hydroxyapatite (nano-HA, particle size < 200 nm, Ca₅(OH)(PO₄)₃, Sigma-Aldrich, USA) in a 40% w/v poloxamer-solution (Pluronic® F-127, Sigma-Aldrich, USA). After scaffold fabrication, pCaP-scaffolds were allowed to set for 4 days at 37°C under saturated humidity.

Polycaprolactone (PCL): Medical-grade PCL (PURASORB PC 12, Corbion, The Netherlands) was used as received for the MEW process.

Scaffold design and fabrication

An osteochondral implant (**Figure 1B**, total height = 7.7 mm, diameter = 6 mm), consisting of three different layers, was fabricated by combining extrusion-based printing with MEW and 3D bioprinting (3DDiscovery Evolution, regenHU, Switzerland). The bone compartment (height = 6.5 mm) of the implant consisted of printable calcium phosphate. This biomimetic bone compartment was fabricated from pCaP paste, by using pneumatic extrusion-based 3D printing (3DDiscovery, regenHU, Switzerland). PCaP was printed on top of 50 layers (total height = 400 μm) of PCL MEW fibres to increase the interfacial strength between the bone and cartilage layer. PCaP cylindrical structures (diameter = 6 mm) were printed consisting of 2 non-macropored layers where PCaP integrated with PCL micro-fibres. Subsequently, macro-pored layers were added by depositing PCaP strands (diameter = 250 μm) with a designed strand-to-strand distance of 700 μm in a double alternating pattern (orientation = 0°- 0°- 90°- 90°). PCaP scaffold fabrication was performed at room temperature (20 – 25°C) with an extrusion pressure of 0.2 MPa and a translational speed of 2 mm/s. The cartilage compartment of the implant was bi-layered with a distinction between the middle and deep zone and the superficial tangential zone. The middle and deep zone (height = 1 mm) consisted of box-like (laydown pattern 0°- 90°- 0°- 90°) MEW PCL fibres (inter-fibre distance = 300 μm), infused with 8% gelMA and ACPCs (20 * 10⁶ / ml). The superficial tangential zone (height = 200 μm) consisted of MEW fibres (inter fibre distance = 100 μm) that were deposited in laydown pattern 0°-45°-90°- 135°, with a slight offset to induce a higher density of tangentially aligned fibres. These fibre-meshes were infused with 8% gelMA and ACPCs (80 * 10⁶ / ml).

MEW fibre deposition optimization

The driving force behind MEW fibre deposition is the strong electrical field between the spinneret and the collector plate. By introducing a structure into this field, the electrical field is altered and therewith the fibre deposition is different. To decrease alteration of the fibre deposition on the implant due to this effect, a more stable electrical field around the edges of the implants was established by using an aluminium block to surround the pCaP bone phase (**Supplementary Figure 3**). To optimize MEW printing parameters, the measured distance between the MEW fibres (inter-fibre distance) was compared with the programmed inter fibre distance, while using voltages ranging from 5-10 kV and relative collector distances ranging from 5 – 9 mm. Additionally, the inter fibre distance on top of the pCaP implant was compared with the inter-fibre distance onto the aluminium block. Pressure and collector velocity remained at 1.25 bar and 15 mm/s, respectively. Light microscopy (Olympus BX51, Olympus Nederland B.V., The Netherlands) was used to assess



the fibre deposition quality, images were taken (Olympus DP73, Olympus Nederland B.V., The Netherlands) and measurements were performed with ImageJ (version 2.0.0-rc-54/1.51h).

SEM imaging

Scanning electron microscopy (SEM) (Phenom Pro Desktop SEM, Thermo Fischer Scientific, USA) was performed with an accelerating voltage of 10 kV to image the MEW fibres on top of the pCaP implant. Prior to imaging, samples were coated with 2 nm of gold to improve imaging quality.

Biochemical evaluation of 3D fabricated implants

To quantify the amount of sulphated glycosaminoglycans (GAGs) and correct them for DNA content, colorimetric dimethylmethylene blue (DMMB, Sigma Aldrich, USA) and fluorometric Picogreen (Quant-iT-Picogreen-dsDNA-kit, Invitrogen, USA) assays were performed, respectively. Prior to these assays, implants were enzymatically digested overnight at 60°C using a papain digestion solution.

(Immuno)histological evaluation

Histological evaluation of the pre-cultured constructs was performed to assess the distribution of cartilage-like matrix components. The constructs were formalin-fixed and embedded in paraffin. The *in vivo* explants were decalcified with EDTA for 6 months, prior to embedding in paraffin. EDTA was refreshed weekly and decalcification progress was checked weekly with micro-CT imaging. Tissue sections (thickness = 5 µm) were deparaffinized with xylene and were rehydrated by gradual ethanol steps (100% - 70%) prior to staining. Safranin-O staining was used to visualize GAG distribution, combined with fast green (Sigma Aldrich, USA) to stain fibrous tissue, and haematoxylin (Sigma Aldrich, USA) to stain cell nuclei. A haematoxylin/eosin (H&E) staining was performed to provide an overview of matrix formation and implant stability.

Immunohistochemistry was performed to visualize type II collagen deposition. First, pronase (1 mg/mL, Roche, USA) and hyaluronidase (10 mg/ml, H2126, Sigma Aldrich, USA) were used for antigen retrieval, and sections were blocked with bovine serum albumin prior to primary antibody incubation II-II6B3 (DSHB, USA). IgG was used as negative control staining. Samples were incubated over night at 4°C, washed, incubated with matching secondary antibody (1:100, IgG HRP, P0447) for 1 hour at room temperature, and washed again. Subsequently, 3,3-diaminobenzidine-horseradish peroxidase (DAB, Sigma Aldrich, USA) was used to visualize the staining. After staining the cell nuclei with haematoxylin, pictures of histologically stained sections were made with a light microscope (Olympus BX51, The Netherlands).

Mechanical analysis

The compressive modulus and complex shear modulus of gel only constructs were compared with constructs that contained boxed reinforcement and with constructs that contained bi-layered reinforcement. The compressive modulus was evaluated at $t = 0$ days, after 14 days, and after 28 days. Compressive tests were performed on a Dynamical mechanical analysis (DMA, Q800, force range = 0,0001N – 18 N, TA instruments, USA). Compression modes included unconfined tests for engineered constructs before implantation and indentation for engineered constructs after explantation. Unconfined compression was performed by first applying a preload of 0.001N to test samples and then strained to 30% at 20% strain/min. Indentation was performed on the engineered implant and adjacent native cartilage tissue by first applying a preload of 0.001 N, to ensure initial contact between the test samples and the flat indenter, followed by a ramp force of 0.250 N/min up to 2.0 N . During indentation, the cartilage was kept hydrated by continuously pipetting PBS over the surface of the implant. Engineered stress was calculated based on the force and specimen's unloaded cross-sectional area, while engineered strain was based on ratio between unloaded specimen cartilage thickness (measured with calliper) and displacement of either unconfined compression platen or the indenter. For the indentation test, the loaded area was approximated as the transverse cross-sectional area of a flat ended cylindrical indenter ($\varnothing = 2$ mm). The compressive modulus was calculated from the elastic region of the engineered stress-strain curves (linear regression applied between 10% and 12% strain).

The complex shear modulus was evaluated after 28 days of culture and measured with a rheometer (Discovery HR-2, TA instruments, USA). An oscillatory rheometric protocol with plate-plate (diameter = 25 mm) configuration was employed. After determining the viscoelastic (LVE) range with an amplitude sweep, a frequency sweep within this LVE range (0.05 – 500 rad/s, 0.01% strain) was performed under a 5% strain preload to prevent sliding of the sample. The complex shear modulus was calculated at 10 rad/s by dividing stress over strain.

***In vivo* evaluation of implants: the animal model**

Equus caballus ferus (Shetland ponies, female, weight = 150 - 200 kg, $n = 8$, **Table 1**) was used as an animal model to evaluate the mechanical stability and regenerative capacity of the hierarchically structured osteochondral implants. As an internal control, a cell-free osteochondral scaffold was used with the same architecture as the cell-laden implants. Implants were inserted in defects in the medial femoral ridge of the equine knee or stifle joint under randomization of implant placement in the left or right joint.



The ponies arrived at the animal facility 4 weeks before starting the procedure to get acclimatized and were housed as a group at pasture. Prior to surgery they were moved to individual boxes and were fed a limited ration of concentrates with hay for maintenance and had free access to fresh water.

For surgery, ponies were premedicated with detomidine (intravenous (IV), 10 µg/kg) and morphine (IV, 0.1 mg/kg) and anesthesia was induced with midazolam (IV, 0.06 mg/kg) and ketamine (IV, 2.2 mg/kg). Anesthesia was maintained with isoflurane in oxygen together with continuous rate infusion of detomidine (IV, 10 µg/kg/h) and ketamine (IV, 0.5 mg/kg/h). Meloxicam (IV, 0.6 mg/kg), morphine (Epidural injection, 0.1 – 0.2 mg/kg) and ampicillin (IV, 10 – 15 mg/kg) were administered pre-operatively as analgesic medication and antibacterial preventative therapy, respectively.

The medial femoral ridge of the stifle joint was exposed by arthrotomy and an osteochondral lesion (diameter = 6 mm, depth = 7.2 mm) was surgically created using a power drill. The surgical area was flushed by saline for cooling and removal of debris. Cell-laden constructs were implanted press-fit in a randomly chosen hind limb, with the cell-free control being implanted in the contralateral limb. After closing the arthrotomy wound in 4 layers in routine fashion, procaine penicillin was administered (Procopen, intramuscular (IM), 20 mg/kg). Post-operatively, nonsteroidal anti-inflammatory medication (meloxicam per os (PO), SID, 0.6 mg/kg) was administered for 5 days and opioids (tramadol, PO, BID, 5mg/kg) was administered for 2 days.

Post-operatively, the animals were kept stabled for 6 weeks with daily monitoring of vital signs, lameness checks at walk and examination of the operated joints for swelling or other signs of inflammation. In weeks 5 and 6, they were hand-walked for 10 minutes twice daily and from week 7 they were kept at pasture. Quantitative gait analysis and radiographic exams were performed at 3 weeks, 3 months, and 6 months post-operatively. After 6 months, the animals were humanely euthanized by intravenous injection of an overdose of pentobarbital (IV, 1400 mg·kg⁻¹ body weight), following sedation (detomidine IV, 10 µg/kg) and induction (Midazolam (IV, 0.06mg·kg⁻¹ body weight) and ketamine IV, (2.2 mg·kg⁻¹ body weight)). All procedures had been approved by the ethical and animal welfare body of Utrecht University (Approval nr. AVD108002015307 WP23).

Table 1. Age and gender of experimental animals used for this study

Animal	Age (years)	Gender
1	6	female
2	8	female
3	12	female
4	11	female
5	6	female
6	7	female
7	5	female
8	14	female

Gait analysis during *in vivo* testing period

During the acclimatization period, the ponies were trained on a treadmill (Mustang, Fahrwangen, Switzerland) using a standard protocol for treadmill habituation. Twenty-eight spherical reflective markers (diameter = 24 mm (topline) and 19 mm (elsewhere)) were attached with double-sided tape and second glue to anatomical landmarks (**Supplementary Figure 2B**). Kinematic data were collected at trot using six infrared optical motion capture cameras (ProReflex, Qualisys, Gothenburg, Sweden) recording for 30 seconds (frame rate = 200 Hz) at each session to obtain a sufficient number of strides.

To process the data, the reconstruction of three-dimensional coordinates of each marker was automatically calculated by Q-Track software (Qtrack, Qualisys, Gothenburg, Sweden). Each marker was identified and labelled using an automated model (AIM model) and manual tracking and raw data were exported to Matlab (version 2018a, Niantics, California) for further analysis. Using custom written scripts, two symmetry parameters were calculated using the vertical displacement of the head and pelvis (tubera sacrale) markers, for each stride. Additionally, the differences between the two vertical displacement minima of the head ($\text{MinDiff}_{\text{head}}$) and pelvis ($\text{MinDiff}_{\text{pelvis}}$) were calculated. Using the markers, limb-segments were formed and angles between these limb-segments were calculated. The difference between the maximal and minimal angle was defined as the range of motion (ROM) of a joint. For each timepoint, the mean value of all strides for each parameter was calculated.

Evaluation of *in vivo* neo bone tissue formation (μ -CT)

Microcomputed tomography (μ -CT) was employed for the quantitative analysis of the bone compartments from the harvested osteochondral lesions (N=8 for cell-laden constructs, N=8 for cell-free constructs). Six freshly made osteochondral grafts were scanned in a μ -CT scanner (Quantum FX-Perkin Elmer) to quantify the initial volume of



pCaP material, pre-operatively. The post-mortem harvested tissue containing the defect area and the surrounding native tissue were similarly scanned (voltage = 90 kV, current = 200 μ A, voxel size = 30 μ m³ and total scanning time = 3 minutes). Subsequently, the 3D-reconstructed images were processed and analysed using image J.³³³ and Bone J.³³⁴ software. Two-dimensional regions of interest (ROIs) were selected in an axial plane at the boundary between the defect and the surrounding native tissue and interpolated to form 3D-volumes of interest (VOI). Thresholding was performed to separately selected area of ceramics and newly formed bone for further calculation. Thresholding values were selected based on the image histogram where different intensity of ceramic and newly formed bone can be identified. After thresholding, processed images were compared with original images. Then, the percentages of mineralized newly formed bone, of non-mineralized tissue and of remaining ceramics, including the percentage of ceramics volume loss, were quantified.

Evaluation of *in vivo* cartilage formation

After explantation, the implants were macroscopically evaluated and pictures were taken with a stereomicroscope (Olympus stereomicroscope (Olympus Soft Imaging Solutions GmbH, The Netherlands). Biopsies (diameter = 1 mm) of the newly formed tissue and adjacent native tissue were taken for biochemistry. The rest of the explant was further processed for immuno(histological) evaluation.

Statistics

Data is presented as mean \pm standard deviation. All *in vitro* studies were performed in triplicate, and mechanical analysis was performed with $n = 5$. To test the differences between groups, either an unpaired t-test, or a one-way ANOVA with post hoc Bonferroni test was performed. Difference between groups was considered statistically significant if $p < 0.05$. For the *in vivo* study, randomization was done to decide which construct (cell-seeded or not) was implanted in which stifle joint and post-explantation evaluation was performed blindly by making use of a key.

Results

Multi-scale 3D biofabrication of the osteochondral implant

Hierarchy in fibre orientation and cell density was successfully achieved by converging extrusion-based bioprinting and MEW processes. Patterning of MEW fibres onto the non-conductive CaP bone phase was obtained by ensuring a constant electrical field strength and an electrical force perpendicular to the substrate; an aluminium block surrounded the pCaP plug during fabrication as to prevent fibres piling up at the edges of the pCaP

plug. Control over fibre deposition on top of the pCaP plug allowed for fabrication of a bi-layered cartilage phase representing the middle/deep and superficial tangential zones of the native tissue (**Figure 2A**). While MEW a uniform box-structure, an increase in voltage resulted in a decrease in the distance between the deposited MEW fibres (inter-fibre distance) on top of the pCaP bone phase of the osteochondral implant (**Figure 2B**). Furthermore, an increase in relative collector distance (CD) resulted in additional decrease in the measured inter-fibre distance (**Figure 2C**). A voltage of 7 kV and a relative CD of 5 mm resulted in more accurate inter-fibre distance ($409.1 \pm 49.0 \mu\text{m}$) as compared to the programmed value ($400 \mu\text{m}$). Additionally, this combination of parameters led to the most homogeneous fibre deposition, as no fibres were piling up at the edges of the pCaP scaffold since the difference between the inter-fibre distance on top of the pCaP plug and onto the aluminium block was neglectable (**Figure 2D-F**).

Using a voltage of 7 kV and a relative CD of 5 mm a bi-layered cartilage phase (**Figure 2A**) with a clearly distinct pattern in the layer representing the middle and deep zones compared to the layer representing the superficial tangential zone was obtained. The middle and deep zones demonstrated a uniform box structure and 'z-directional' stacking (according to local coordinate axis in **Figure 2**), whereas the superficial tangential zone featured primarily tangentially oriented fibres with little z-directional stacking. For this superficial tangential layer, programmed inter-fibre distances of $100 \mu\text{m}$, $200 \mu\text{m}$, and $400 \mu\text{m}$ in a laydown pattern of 0° – 45° – 135° – 180° corresponded with interconnected pores that showed an average inter-fibre distance of $49.2 \pm 6.2 \mu\text{m}$, $110.1 \pm 17.4 \mu\text{m}$ and $359.2 \pm 29.6 \mu\text{m}$, respectively (**Supplementary Figure 1A, B**). Cells were able to penetrate into all meshes, irrespective of pore size (**Supplementary Figure 1C**); however, most cells were caught by meshes that were fabricated with an inter-fibre distance of $100 \mu\text{m}$ (**Supplementary Figure 1D**). Therefore, $100 \mu\text{m}$ inter-fibre distance, which was the smallest that resulted in the creation of a smooth surface, was selected for the superficial tangential zone of the osteochondral implants.

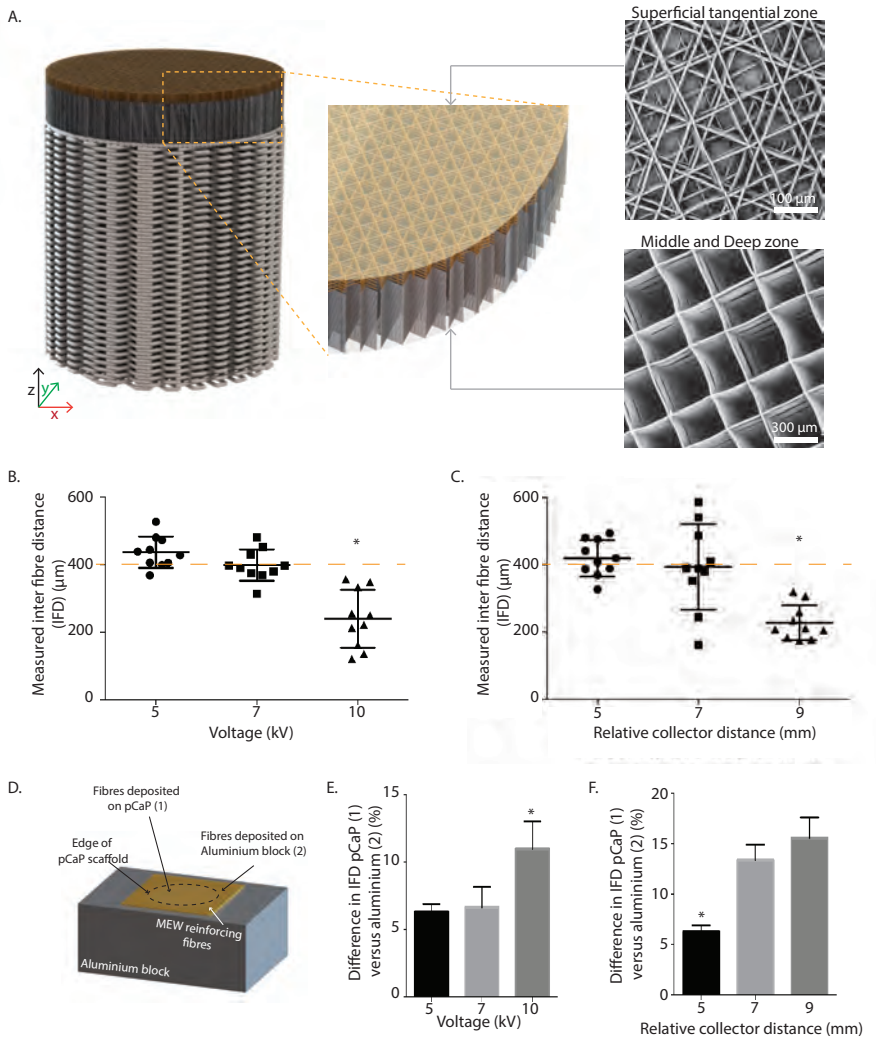


Figure 2. Optimization of process parameters for deposition of reinforcing microfibres on top of the pCaP implant. A) Illustration of bi-layered cartilage phase, including SEM images that confirm the directionality of the fibrous component of the superficial tangential zone, and the middle and deep zone. B,C) Measured inter-fibre distance is affected by both voltage and relative collector distance. D) Schematic indication of measurements taken E,F) Effect of voltage and relative collector distance on difference of inter-fibre distance on top of the pCaP bone phase as compared to on top of the aluminium block. Higher % reflects more piling up of reinforcing fibres at the edges of the pCaP bone phase. Error bars represent standard deviation, * = Statistically different from all other groups ($p < 0.05$).

Mechanical and *in vitro* evaluation of osteochondral implants

After 28 days of *in vitro* culture, the compressive modulus of the bi-layered reinforced constructs was significantly higher (603.2 ± 205.4 kPa) than those of the boxed-reinforced (294.2 ± 147.5 kPa) and non-reinforced cell-laden hydrogels (19.6 ± 5.8 kPa). For all cell-laden groups these values were higher as compared to the compressive modulus prior to *in vitro* culture when the compressive modulus of the cell-laden hydrogel was 13.9 ± 0.2 kPa, improved by the uniform boxed-reinforcing fibre structure to 192.3 ± 54.6 kPa and even further improved with the bi-layered fibre structures to 222.6 ± 30.7 kPa (**Figure 3A**). Notably, the inclusion of the bi-layered reinforcing structure resulted in a higher complex shear modulus (87.8 ± 21.7 kPa) after the *in vitro* culture compared to the non-reinforced cell-laden hydrogel (10.3 ± 3.0 kPa) and the boxed-reinforced constructs (30.5 ± 11.8 kPa) (**Figure 3B**).

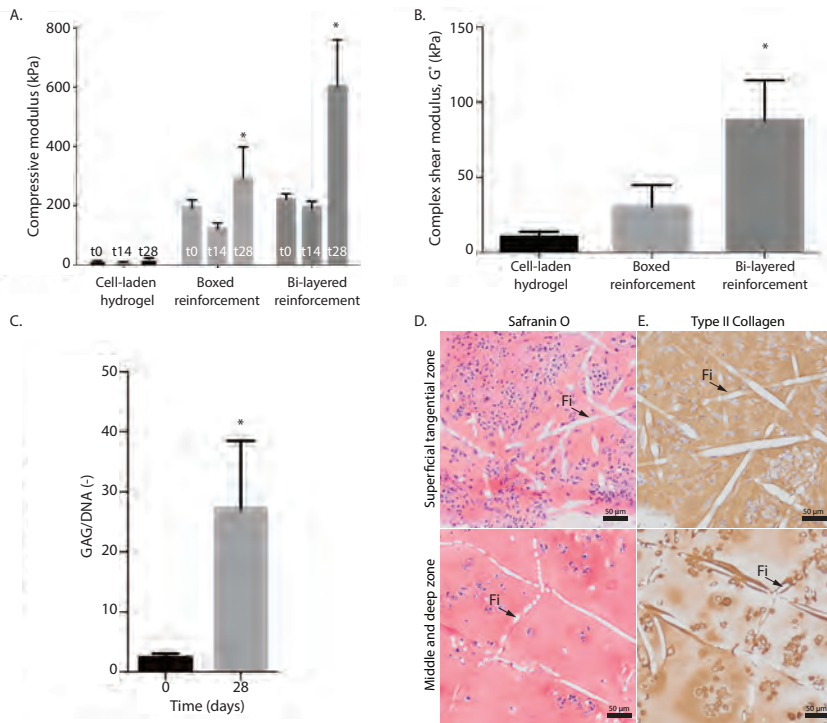


Figure 3. Mechanical analysis and *in vitro* cartilage-like tissue formation of the osteochondral implants. A) A general increase in compressive modulus over time was found and bi-layered reinforcement has increased the compressive modulus after 0, 14 and 28 days of culture. B) Bi-layered reinforcement has increased the complex shear modulus after 28 days of culture. C) 28 days of *in vitro* culture resulted in an increase in quantitative GAG deposition, normalized per DNA. D) Homogeneous distribution of safranin-O and type II collagen staining was found in both the superficial tangential, and middle and deep zone after 28 days of *in vitro* culture, top view (Fi = MEW fibre). Error bars represent standard deviation, * = $p < 0.05$, one-way ANOVA, *post hoc* Bonferroni (A,B), unpaired t-test (C).



The *in vitro* pre-culture period resulted in an overall glycosaminoglycan (GAG) content of $27.2 \pm 9.8 \mu\text{g GAG}/\mu\text{g DNA}$ (**Figure 3C**), which was, together with type II collagen, homogeneously distributed throughout the middle/deep, and the superficial tangential zones of the cartilage component of the implant (**Figure 3D**). Further, the reinforcing MEW fibres, which appeared in the stained histological sections as white, were shown to preserve the original designed orientation established during the printing process (**Figure 2A**).

***In vivo* evaluation of osteochondral implants:**

No complications occurred during surgery or during post-surgery recovery. Radiographic examination (X-rays) confirmed the correct implant orientation of the implants after 3 and 6 months of implantation (**Supplementary Figure 2A**).

Gait analysis during the implantation period revealed that symmetry parameters were not affected by the type of implant, as no difference was found between the cell-laden and cell-free group at any time point (**Supplementary Figure 2B-K**). Symmetry parameters (MinDiff Head and MinDiff Pelvis) show a slight deviation after 3 months of implantation, yet these values were back to base level after 6 months of implantation (**Supplementary Figure 2C,D**). Both pelvis roll range of motion (ROM) and pelvis yaw ROM significantly increased within 3 months of implantation (**Supplementary Figure 2E, F**) and pelvis yaw showed a further increase until 6 months of implantation (**Supplementary Figure 2F**). Pelvis pitch ROM slightly decreased within the first 3 months of implantation (**Supplementary Figure 2G**). No differences in limb parameters (fetlock extension, limb height, protraction, and retraction) were found between the cell-laden and cell-free implants. (**Supplementary Figure 2H-K**).

Post-mortem evaluation

Structural and mechanical evaluation of the implants after 6 months of implantation:

Pre-cultured osteochondral constructs were implanted in the medial femoral ridge of stifle joint, slightly below the articulating surface ($0.5 \pm 0.4 \text{ mm}$). After 6 months, within the majority of the implants repair tissue was observed macroscopically (**Figure 4A-C**). At most of the sites that had received a cell-free implant the defect was partially filled with repair tissue with a transparent to whitish colour (**Figure 4B**). The repair tissue in the defects treated with cell-laden implants had a more whitish and less transparent character (**Figure 4A-C**).

Cross-sections of the implants, stained with Haematoxylin & Eosin (H&E), revealed lateral bone ingrowth into the osteal anchor of the implant (**Figure 4D**). Additionally, these tissue sections confirmed that the cartilage compartments of the implants still remained intact and provided a good filling of the original defect after 6 months of implantation (**Figure 4D, E**). Moreover, the reinforcing MEW fibres ("Fi" in **Figure 4E**) remained visible throughout the entire cartilage compartment of the implant.

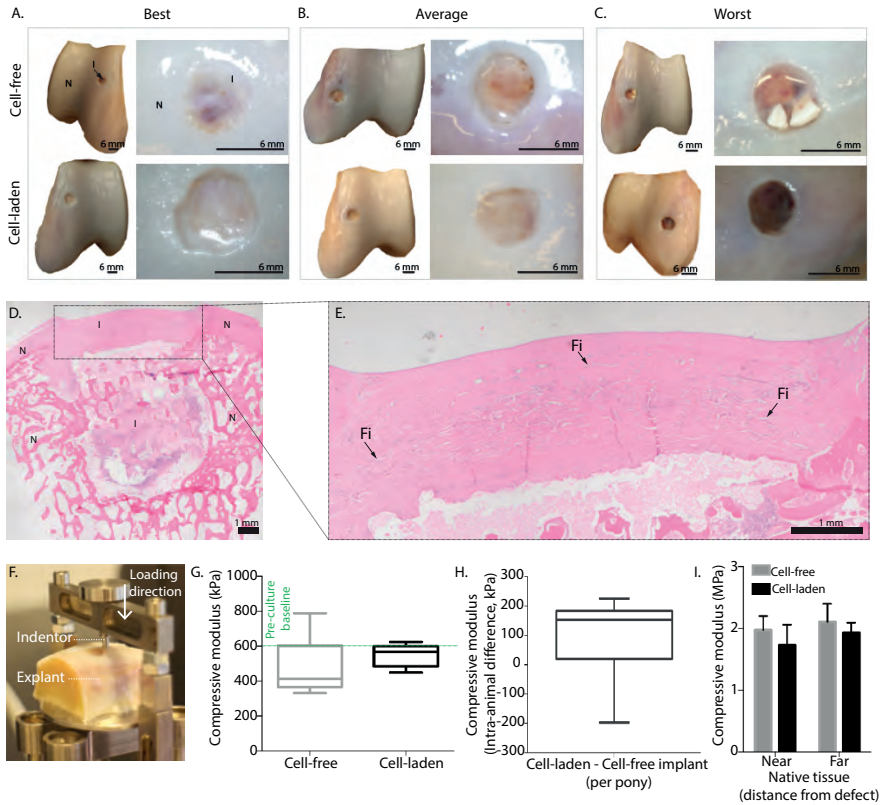


Figure 4. Structural and mechanical evaluation of the implants. A-C) Macroscopic evaluation of the explants showing the best (A), average (B), and worst (C) samples for the cell-free and cell-laden implants. D, E) H&E staining of a cell-laden implant, highlighting the presence of the reinforcing fibres throughout the cartilage phase (N = native tissue, I = implant, Fi = MEW fibre). F) Compressive mechanical testing of the implants and native tissue after explantation. G) After 6 months of implantation, a similar compressive modulus was found for the implants, as compared to the pre-implantation timepoint. H) Internal difference per pony between the cell-laden and cell-free implants. I). Compressive modulus of native tissue measured near the defect site and far from the defect site. Error bars represent standard deviation, * = $p < 0.05$, one-way ANOVA, post hoc Bonferroni.



Mechanical analysis under indentation loading (**Figure 4F**) showed no significant difference ($p = 0.073$) in compressive modulus between the cell-free (0.5 ± 0.2 MPa) and cell-laden implants (0.6 ± 0.1 MPa) (**Figure 4F, G**). Comparing the compressive properties after 6 months of implantation with those prior to implantation revealed that the compressive properties of the cell-laden implants were conserved and no significant decrease in compressive modulus was found after 6 months implantation. Importantly, at the time of explantation, the cell-free implants had gained significant additional compressive properties and comparison with internal controls revealed that there was no significant difference with the compressive modulus of the cell-laden implants (**Figure 4H**). Additionally, composition of the native tissue near (<2 mm) and further away (>10 mm) from the treated defect site was independent of the presence or absence of cells in the implanted construct (**Figure 4I**).

Haematoxylin and eosin (H&E) staining of tissue sections showed abundant infiltration of cells in the cartilage compartment of the cell-free implants (**Figure 5A**). Cells in the cartilage compartment of both the initially cell-free and cell-laden implants showed a mixed morphology of fibrous/spindle-shaped and rounded cells (**Figure 5A**). Furthermore, the bone compartment of all implants, based on osteoconductive ceramics³³⁵, showed considerable cell infiltration, and all implants additionally showed neo-bone tissue formation (**Figure 5B**).

Micro-CT imaging revealed degradation of the pCaP bone anchor. The pCaP volume decreased significantly from 129.2 ± 8.5 mm³ to 31.7 ± 14.2 mm³ and 31.6 ± 21.5 mm³ for the cell-free and cell-laden implants, respectively (**Figure 5C**). No significant difference in percentage of pCaP degradation was found between the cell-free (75.5 ± 11.0 %) and cell-laden (75.6 ± 16.6 %) groups (**Figure 5D**). Although all implants showed bone infiltration into the pCaP part, some bone resorption around the pCaP part was also found. Neo-bone tissue formation was found in both the cell-free and cell-laden implants (**Figure 5E**). Interestingly, this neo-bone tissue formation was irrespective of the cartilage component, as there was no significant difference in volume of neo-bone tissue formation between the cell-free (28.3 ± 30.8 mm³) and cell-laden (21.48 ± 19.5 mm³) implants (**Figure 5E**). Additionally, no significant difference was found for non-mineralized tissue between the cell-free (123.4 ± 30.0 mm³) and cell-laden (137.1 ± 35.2 mm³) implants (**Figure 5F**).

The implants showed an increased GAG/DNA content after 6 months of implantation compared to the pre-culture (t28) timepoint (**Figure 6A**). Interestingly, within the initially GAG-deprived cell-free implants, a significant increase in GAG/DNA was found up to the level of the pre-cultured cell-laden samples, after 6 months of implantation. Additionally, no significant difference in GAG/DNA was found ($p = 0.1813$) between these cell-free (41.5

$\pm 9.0 \mu\text{g}/\mu\text{g}$) and the cell-laden implants ($45.4 \pm 16.3 \mu\text{g}/\mu\text{g}$) (**Figure 6A**). Nevertheless, both implants showed significantly less GAG/DNA content in comparison to the surrounding native tissue ($117.5 \pm 74.4 \mu\text{g}/\mu\text{g}$). A similar trend was observed for the overall GAG content of the implants normalized per dry weight. A significant increase in GAGs was shown for the initially GAG deprived cell-free implants, and no significant differences were found between the cell-free ($8.7 \pm 4.2 \mu\text{g}/\text{mg}$) and cell-laden implants ($8.8 \pm 6.8 \mu\text{g}/\text{mg}$) (**Figure 6B**). Interestingly, also no difference in DNA content, normalized per dry weight, was found between the cell-free ($176.0 \pm 104.5 \mu\text{g}/\text{mg}$) and cell-laden implants ($202.5 \pm 127.9 \mu\text{g}/\text{mg}$) (**Figure 6C**).

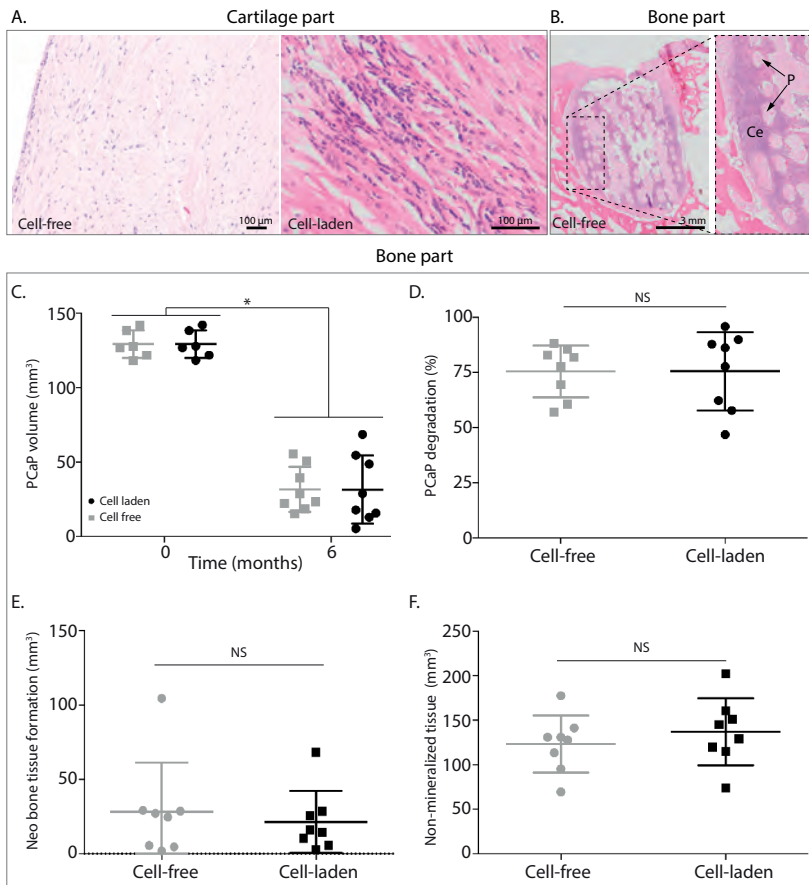


Figure 5. Interaction of native tissue and implants. Haematoxylin and eosin staining to assess cell infiltration in the cartilage and bone part and cell morphology in the cartilage part. A) Cell infiltration in cartilage part of the cell-free implant and cell morphology (mixture of spindle/fibrous and rounded chondrogenic morphology) in the cartilage part of the cell-laden implant. B) Cell infiltration and bone formation bone part of cell-free implants. (P = pCaP voids, Ce = cells). C-F) Quantification of micro-CT data after 6 months of implantation. C) Total volume of pCaP over 6 months. D) pCaP degradation over 6 months in percentages. E) Volume of neo-bone tissue formation. F) Volume of non-mineralized tissue. Error bars represent standard deviation, * = $p < 0.05$, NS = no significant difference, unpaired t-test.

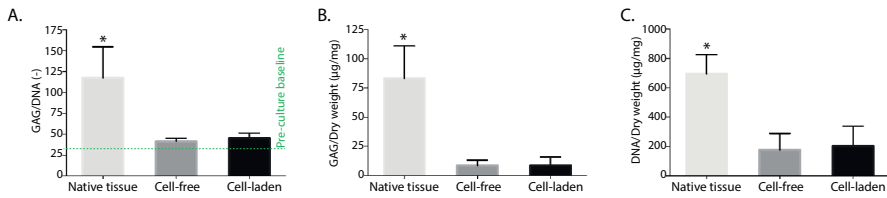


Figure 6. Tissue quality of the cartilage phase of the implants after 6 months of implantation. A) Quantitative biochemistry shows no difference between the cell-laden and cell-free implants in average GAG/DNA. Green dotted line represents the level of GAG/DNA prior to implantation for cell-laden implants. B) Average GAG/Dry weight compared with native tissue. C) Average DNA/Dry weight compared with native tissue. Error bars represent standard deviation, * = $p < 0.05$, one-way ANOVA, post hoc Bonferroni.

Discussion

The potential of biofabrication technologies for the regeneration of musculoskeletal tissues has been postulated for over a decade, but long-term functionality and mechanical stability had not yet been reported within large animal models.^{79–81,152} This study is the first to demonstrate the mechanical stability and maintenance of resorbable osteochondral implants that include microfibre reinforcement for cartilage repair. These were fabricated via converging two (bio)printing technologies and through the precise control over fibre architecture, implants were generated that provided long-term mechanical stability.

Our mechanically stable design is inspired by the architecture of the native type II collagen network of the osteochondral tissue and was realized by reinforcing the hydrogel-cartilage phase with hierarchically oriented micro-scale fibres²⁷⁴, which were firmly integrated with a biodegradable bone anchor. The hierarchy in the fibre orientation, *i.e.* a uniform boxed structure representing the middle/deep zones and a zone with primarily tangentially-oriented fibres to represent the superficial tangential zone, resulted in increased compressive and shear properties, as well as improved load distribution.^{93,274} In fact, the inclusion of such a thin layer of tightly packed and tangentially oriented fibres at the implant surface, has recently been shown to enable the axial loads to be distributed over a larger volume of the underlying middle and deep reinforcing region, therefore more effectively transferring axial loads throughout the engineered construct.²⁷⁴

After 6 months of implantation, macroscopically all implants (cell-free and cell-laden) showed formation of a repair tissue. Biochemical assessment of the post-mortem retrieved implants showed a further increase in GAG/DNA for the cell-laden implants (45.4 µg/µg of GAG/DNA) compared to the pre-implantation timepoint (28.0 µg/µg of GAG/DNA),

providing evidence that additional ECM production occurred after *in vivo* implantation. This finding shows superior performance of these osteochondral plugs compared to earlier equine studies in which GAG content of precultured implants decreased, presumably due to leaking out of matrix components as a result of the exposure to loading.^{336,337}

An important observation is that the cell-free gel-fibre combination used as the cartilage phase of the implants attracted chondrogenic ECM producing cells in the *in vivo* situation and that GAG/DNA content of the neo-tissue formed in cell-free implants was equal to that seen in the cell-laden, pre-cultured implants. The osteochondral implants were inspired by native tissue, and specifically the type II collagen fibre structure. Fibre diameters obtained with the MEW process are already one to two orders of magnitude smaller than those produced with conventional extrusion-based techniques.⁸⁸ Nevertheless, they are still much thicker than the native collagen fibres, which not only function as the reinforcing fibrous component of articular cartilage, but also play a role in the entrapment of deposited GAGs and swelling restriction.³³⁸ We recently postulated that better understanding of the mechanisms of collagen structure development combined with evolving (bio)fabrication and printing approaches would lead to further functional mimicking of native articular cartilage tissue.¹³ The work reported here, is the first to underscore that hypothesis in a representative large animal model and suggests that the technical solution potentially lies in the convergence of (bio)printing technologies that enable creation of a mechanical environment that supports ECM production *in vivo*.^{276,339,340} The impact of this finding goes beyond the translation of (bio)fabricated implants, as it affects the fundamental ideas about using cells in regenerative therapies.

Conclusion

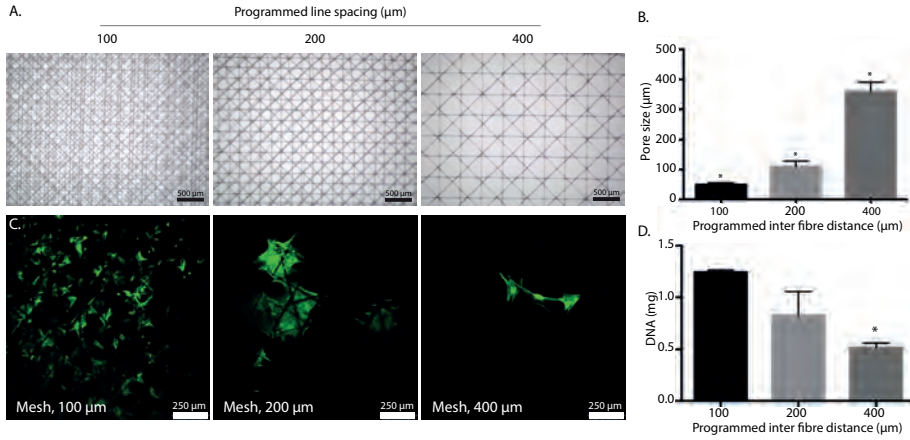
In conclusion, this study demonstrates that implants with a defined hierarchy in the cartilage compartment, produced using converged fabrication technologies, are able to withstand the challenging *in vivo* situation in a large animal model for a prolonged period of time. This convergence of biofabrication technologies allowed the manufacture of implants with multi-scale architectures, in which the bi-layered microfibrillar reinforcement in the chondral compartment and its integration with the bone anchor, substantially improved the compressive and shear properties. Importantly, this study suggests that the mechanical characteristics are a more important drive for the regenerative response than the presence of pre-cultured cells, as implants containing pre-cultured regenerative cells and abundant cartilage-like matrix at the time of implantation did not outperform cell-free implants with the same biomaterial composition and architecture. This observation is of great fundamental, as well as translational importance and supports the hypothesis that functional mimicking of the collagen architecture in the implants may be pivotal for optimal functionality and tissue restoration *in vivo*.



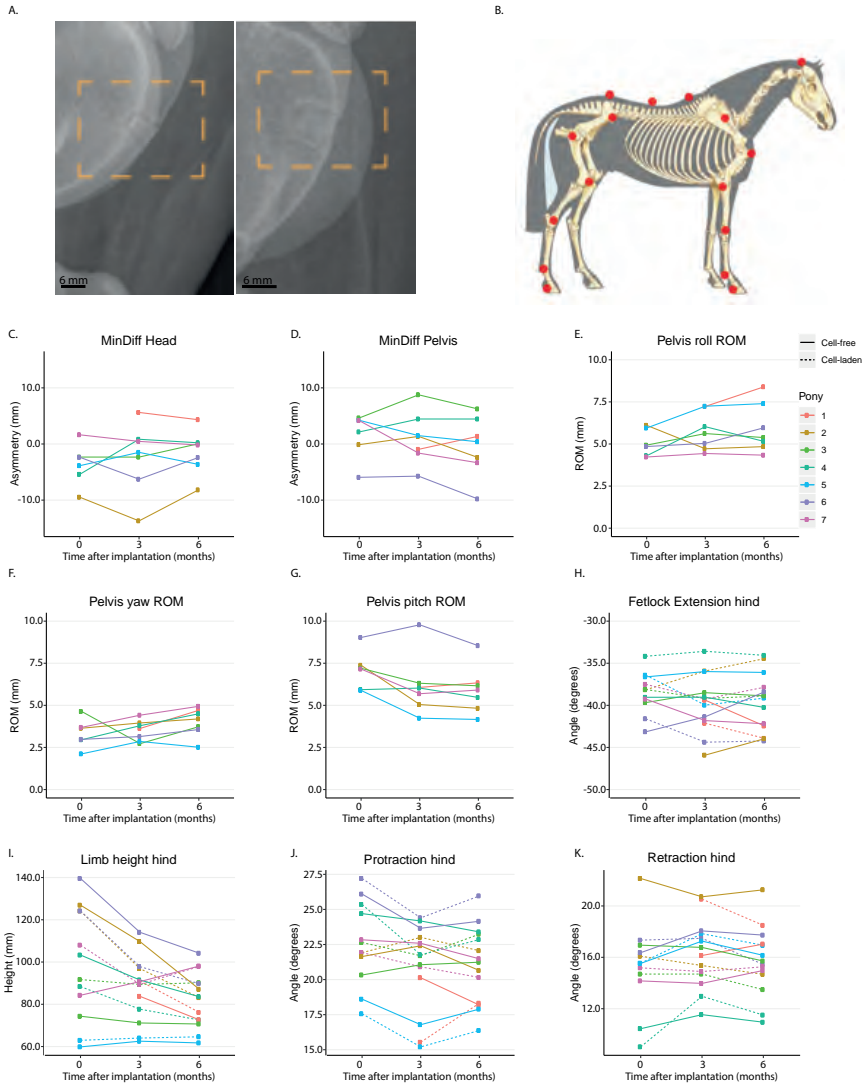
Acknowledgements

The primary antibodies against type II collagen type (II-II6B3) developed by T. F. Linsenmayer, was obtained from the DSHB, developed under the auspices of the NICHD and maintained by the University of Iowa, Department of Biology, Iowa City, IA, USA. Support with SEM imaging was kindly provided by Marco Viveen. This work was financially supported by the European Research Council under grant agreement 647426 (3D-JOINT), EU funded E11312 BioArchitect project and by Dutch Arthritis Society (grants CO-14-1-001, LLP-12 and LLP-22).

Supplementary Data



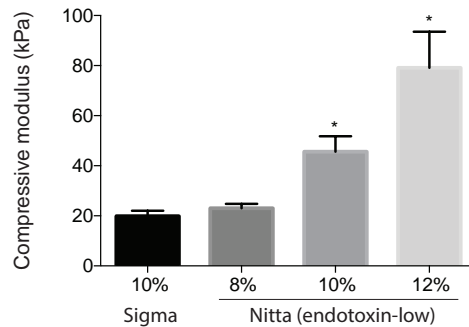
Supplementary Figure 1. Optimization of the superficial tangential MEW reinforcing layer for cell infiltration. A) Top view images of superficial tangential layers with differently programmed inter-fibre distances. B) Quantification of actual average pore size as a result of programmed inter-fibre distance. C) Fluorescently labelled ACPCs entrapped in meshes with different inter-fibre distances. (LIVE/DEAD staining) D) Quantification of DNA in the superficial layers with different inter-fibre distances. Error bars represent standard deviation * = $p < 0.05$, one-way ANOVA, *post hoc* Bonferroni.



Supplementary Figure 2. *In vivo* evaluation of osteochondral. A) Representative X-rays during the implantation period. B) Schematic representation of marker-locations based on anatomical landmarks for gait analysis. C-K) Gait analysis after 0, 3, and 6 months. Legend in E applicable for all graphs. C,D) Symmetry data of the head and pelvis. E) Pelvis roll range of motion (ROM). F) Pelvis Yaw range of motion. G) Pelvis pitch range of motion. H) Fetlock extension hind. I) Limb height hind. J) Protraction hind. K) Retraction hind. T0 = Prior to implantation.

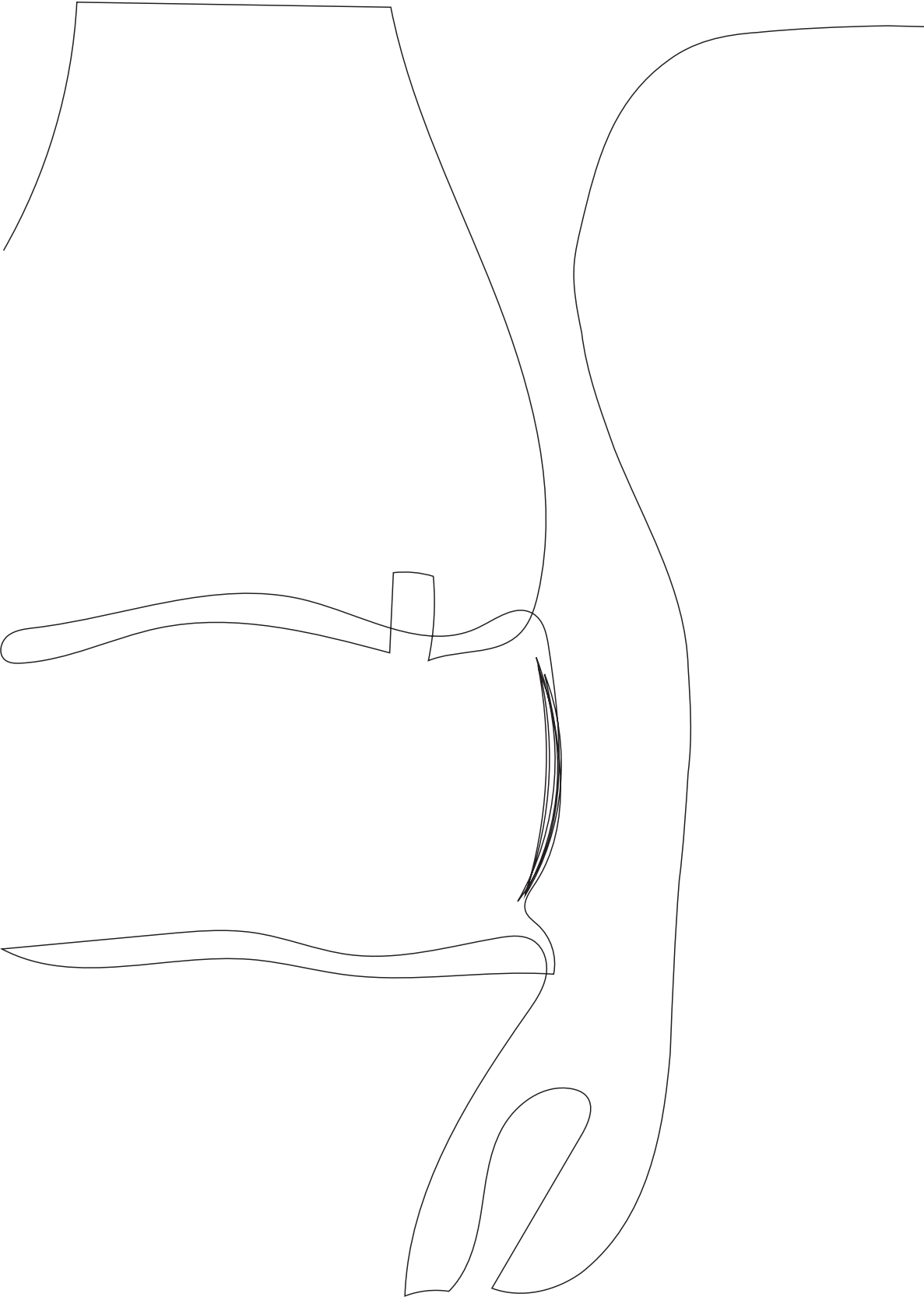


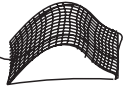
Supplementary Figure 3. Implant manufacturing to prevent piling up of the microfibrils at the edges of the implant. Aluminium block is used around the pCaP bone phase to achieve less piling up of the fibres.



Supplementary Figure 4. Comparing the compressive modulus of endotoxin-low (Nitta) gelatin-based gelMA with frequently used Sigma gelatin-based gelMA. 8% endotoxin-low gelMA shows comparative compressive modulus with 10% Sigma gelatin. Error bars represent standard deviation. * = $p < 0.05$, one-way ANOVA, post hoc Bonferroni.







Scaling up from osteochondral plug to patient-specific condyle resurfacing: fabrication, *in vitro* characterization, and mechanical characterization under physiological conditions of clinically relevant osteochondral implants.

Mylène de Ruijter¹
Nasim Golafshan¹
Inge Dokter¹
Ioanna Gkoni¹
Roderick Verberne²
Joao Garcia¹
Laura Creemers¹
P. René van Weeren³

Pieter. A.J. Brama⁴
Daniel J Kelly^{5,6,7,8}
Keita Ito^{1,9}
Paige Little²
Peter Pivonka²
Jos Malda^{1,3}
Miguel Castilho^{1,9}

Manuscript in preparation

¹ Department of Orthopaedics, Regenerative Medicine Utrecht, UMC Utrecht, University of Utrecht, The Netherlands.

² Science and Engineering Faculty, School of Mechanical Medical & Process Engineering, Queensland University of Technology, Brisbane, Australia

³ Department of Clinical Sciences, Utrecht University, The Netherlands.

⁴ School of Veterinary Medicine, University College Dublin, Dublin, Ireland

⁵ Trinity Centre for Biomedical Engineering, Trinity Biomedical Sciences Institute, Trinity College Dublin, Ireland

⁶ Department of Mechanical and Manufacturing Engineering, School of Engineering, Trinity College Dublin, Ireland

⁷ Department of Anatomy, Royal College of Surgeons in Ireland, Dublin, Ireland.

⁸ Advanced Materials and Bioengineering Research Centre (AMBER), Royal College of Surgeons in Ireland and Trinity College Dublin, Dublin, Ireland.

⁹ Department of Biomedical Engineering, Eindhoven University of Technology, The Netherlands

Abstract

Articular cartilage defects are common and current surgical treatments provide sub-optimal tissue repair. Multiple biofabrication approaches have tried to recreate the chondral architecture in biochemical and structural composition and this has frequently been combined with an osteal anchor in the form of an osteochondral plug. In this study, the translation from this relatively small plug to larger clinically-relevant and patient-specific implants is explored. Osteochondral patient-specific large (surface area = 469 mm²) implants consisted of a porous bone component, close cartilage-to-bone interface, and a microfibre reinforced cell-laden gelatin methacryloyl (gelMA) cartilage component. The effect of implant size (bone component only) on stress-strain distribution and cartilage-like tissue formation is studied by means of axial compression and compression under 50° and 60° flexion angles using a robotic arm system. The implant stiffness decreased with increased implant size. An increase in size of the cartilage component (from 6 mm diameter discs to 24 mm diameter discs) did not hamper cartilage-like tissue formation *in vitro*. As the larger implants include a patient-specific complex shaped geometry, a software tool has been developed and validated to automatically generate a numerical control programming language (*i.e.*, g-code) that resurfaces a bone structure with melt electrowritten (MEW) microfibrils based on a 3D-standard tessellation language (.STL) file. As a proof of principle, a large complex shaped implant was fabricated and cultured *in vitro* to assess 3D matrix distribution. This study shows the first steps in translating from osteochondral plugs to larger patient-specific implants.



Introduction

Articular cartilage (AC) defects generally result in progressive deterioration of the joint, causing pain and reducing mobility, significantly affecting the quality of life of patients.^{17,18} The problem is intensified by the fact that AC has limited regenerative capacity^{42,43} and current surgical approaches to repair focal defects show sub-optimal long-term outcomes due to the formation of fibrous tissue with inferior mechanical properties. Although allograft transplantation may result in the retainment of qualitatively better tissue, this application is restricted due to logistical constraints and difficulty in achieving a patient-specific fit.⁵⁶

Biofabrication²⁴⁰ seems a promising approach to fulfil the need to improve treatment of AC damage by fabrication of patient-specific implants. This field aims to restore tissue function by combining the regenerative capacity of the patient's own cells with biomaterials and/or bioactive cues using additive manufacturing techniques that allow spatial control over the deposition of such components. Implants generated with biofabrication strategies are very versatile as they can be tailored to the individual patient's specific AC defect(s), based on the translation of patient data retrieved from medical imaging techniques to machine-specific instructions. Up to now, evaluated implants for the restoration of AC defects are shaped as osteochondral plugs, where the osteal component acts as an anchor for the cartilage part upon implantation.^{81,336} Integration with the host tissue of the biodegradable osteal component is generally based on the recruitment and stimulation of endogenous cells from the bone marrow. PCL-magnesium-based 3D printable paste is a promising composite material explored for this osteal components due to its biodegradability and load-bearing properties.³⁴¹ Further, biofabrication approaches for the restoration of the chondral part have mainly focused on recreating the native zonal cartilage tissue architecture^{38,322} in terms of biochemical and structural components, including the distinct type II collagen "Benninghoff arcades"⁴⁰ architecture that are imperative for AC's mechanical function.³²³ To achieve 3D cartilage-like matrix deposition *in vitro*, chondrocytes¹⁸⁵, mesenchymal stromal cells (MSCs)³⁰⁵, or articular cartilage resident chondroprogenitor Cells (ACPCs)¹⁶⁷ are embedded in mechanically soft hydrogels. However, these soft hydrogels are not able to withstand the challenging mechanical environment of the joint and thus, fibre reinforcing technologies have been explored to achieve mechanical competent cell-laden biodegradable constructs.^{82,86,150,329} Melt electrowriting (MEW)^{89,90} is considered a promising fibre reinforcing technology for hydrogel-based cartilage implants as it uses only a small fraction of (sub)micro-fibres, yet still allows for a significant increase in the mechanical properties of these hydrogel-thermoplastic constructs due to the tight control over the network architecture.^{84,93,187,188} Recently, MEW has been combined with the extrusion-based 3D printing of bioinks in

a single-step fabrication approach²⁷³, which allowed for accurate deposition of both the fibrous and non-fibrous components and also created a mechanically secure interconnection between the cartilage-to-bone interface.²⁰² Osteochondral plugs that were fabricated with this converged printing approach showed to be mechanically stable enough to withstand the challenging *in vivo* environment in the stifle joint in the equine model for up to 6 months (**Chapter 8**). Yet, such plugs do not directly reflect the shape of the observed defects in patients as they are round, have a specific, relatively small diameter, and show a flat surface. Upscaling the size of implants results in individual challenges for the bone component (mechanical), the cartilage component (mechanical and biological), as well as challenges related to the combined osteochondral unit (fabrication of the patient-specific convex geometry).

Therefore, the aim of this study (**Figure 1**) was to scale-up the fabrication of from the relatively simple osteochondral plug to larger, more complex patient-specific implants, and subsequently demonstrate their load bearing properties under physiological loading conditions. We studied the effect of implant size (bone component only) on the mechanical properties of this bone component, but also the effect of implant size on cartilage-like tissue deposition. Additionally, to fabricate a patient-specific large osteochondral unit with a convex geometry, a semi-automatic software tool for resurfacing a complex-shaped bone-reflecting part of the joint structure has been achieved.

Materials and methods

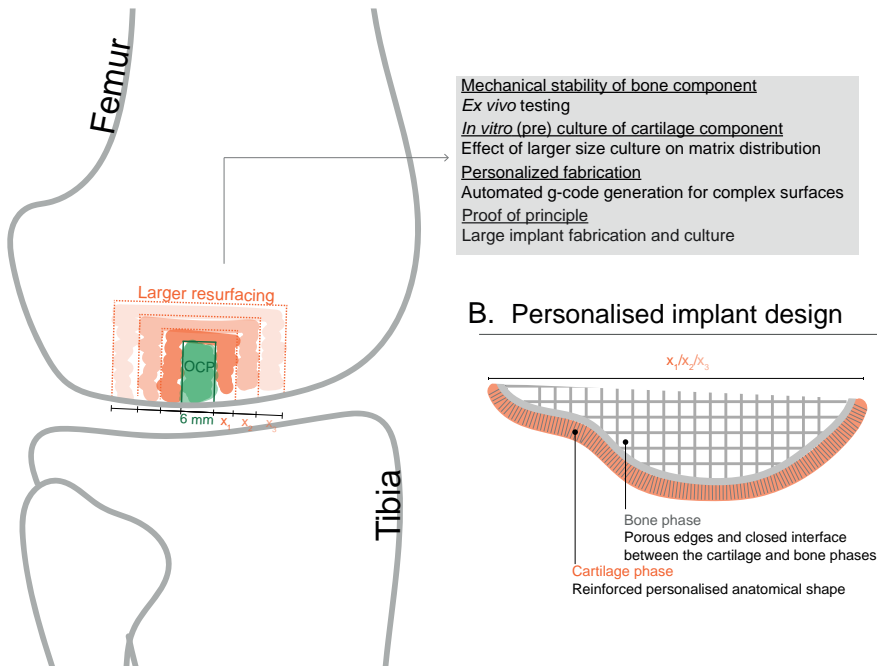
Cell harvest, expansion and culture conditions

Goat articular chondroprogenitor cells (ACPCs) were harvested from femur condyles, obtained from the local slaughterhouse, according to previously published protocols used for harvesting equine ACPCs.^{34,167} ACPCs were cultured in expansion medium until passage 5, after which they were embedded in the hydrogel and cultured in chondrogenic differentiation medium for 28 days. Expansion medium consisted of Dulbecco's modified eagle medium (31966, Thermo Fisher Scientific, USA) supplemented with 10% fetal bovine serum (Gibco, Thermo Fisher Scientific, USA), 1% penicillin-streptomycin (Gibco, Thermo Fisher Scientific, USA), 1% l-ascorbic acid-2-phosphate (0.2×10^{-3} M, Sigma Aldrich, USA), 1% non-essential amino acids (100X, Gibco, Thermo Fisher Scientific, USA), and 5 ng/mL bFGF (Preprotech, UK), and medium was refreshed twice per week. Chondrogenic differentiation medium consisted of Dulbecco's modified eagle medium (31966, Thermo Fisher Scientific, USA) supplemented with 1% penicillin/streptomycin, 1% l-ascorbic acid-2-phosphate, 1% ITS + Premix Universal culture supplement (Corning, USA), 2.5% HEPES (1M, Gibco, Thermo Fisher Scientific, USA), 0.4% dexamethasone (0.1×10^{-6} M, Sigma Aldrich, USA) and 0.1%



recombinant human transforming growth factor- β 1 (TGF- β 1) (10 ng/mL, Preprotech, UK). Medium was refreshed three times per week. All cultures were performed under sterile and normoxic culture conditions at a temperature of 37°C and 5% CO₂.

A. Study overview



B. Personalised implant design

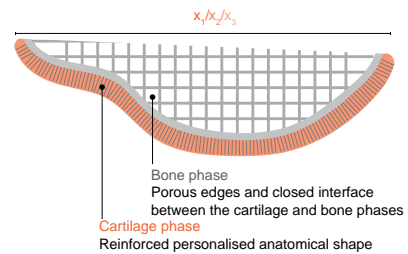


Figure 1. A) Study overview, highlighting the challenges that arise when transitioning from osteochondral plugs towards (partial) joint resurfacing. B) Personalised implant design highlighting side porosity in the bone phase and personalised anatomically-shaped reinforcement in the cartilage phase.

Implant fabrication

Bone component: Polycaprolactone (PCL, Purasorb PC12, Corbion, The Netherlands) was used as received. The PCL implants were printed via fused deposition modelling (FDM, 3D Discovery Evolution, regenHU, Switzerland). The cartridge temperature was set at 80°C, while the temperature of the nozzle was set at 90°C. The extrusion of the melted PCL was controlled by a screw-system at a constant feed rate of 2 revs/min with a collector velocity of 2mm/min.

MgP-PCL was prepared as previously described (Golafshan *et al. under review*). MgP-PCL implants were printed with a 3D-bioprinter (3DDiscovery Evolution, regenHU Ltd, Switzerland) using a conical shaped, 22G nozzle (Nordson EFD, USA) at a velocity of 5 mm/min and a pressure ranging from 0.060 to 0.220 MPa, based on the viscosity of the MgP-PCL paste. The infill density of each layer was set at 35%, the overlapping perimeter at 15%, and the layer height at 0.2 mm. After printing, the dimensions of the generated implants were measured to assess shape fidelity of the printed implants. To eliminate solvents, the implants were washed in 70% ethanol for 6 hours and subsequently submerged in Milli-Q water for 24 hours.

Cartilage component: Gelatin methacryloyl (gelMA) was synthesized as previously described^{168,258}. Briefly, gelatin (type A, derived from porcine skin, 175 Bloom, Sigma Aldrich, The Netherlands) was dissolved at 10% w/v in phosphate-buffered-saline (PBS) at 60 °C after which 0.6 g methacrylic anhydride (Sigma Aldrich) was added per g of gelatin to achieve an 80% degree of functionalisation. Freeze-dried gelMA was diluted with PBS to obtain a final gelMA concentration of 10% w/v and subsequently placed in a 37°C incubator to ensure a homogeneous solution. To initiate the cross-linking reaction, a combination of 5mM sodium persulfate (Sigma Aldrich) and 0.5mM Tris(2,2'-bipyridyl) dichlororuthenium (II) hexahydrate (Sigma Aldrich) was added to the gelMA solution. Implants were crosslinked for 10 min under led light (20W LED, Jobmate, China)

Fibre reinforcing component: MEW was performed with PCL which was molten in a metallic cartridge at 80°C. The MEW head was translating in z- and y-direction whereas the high voltage collector plate was translating in x-direction. An air pressure of 110-125 kPa, voltage of 7-11 kV, collector velocity of 20 mm/s, and a constant collector to implant distance of 6 mm were applied to extrude the PCL fibres through a 24G nozzle.

Anatomically shaped implants:

To acquire the precise anatomy of the ovine stifle, micro-CT data were acquired at the Medical Engineering Research Facility (MERF) of Queensland University of Technology (QUT). From reconstructed CT models the tibia and the femur were segmented and subsequently exported into the Standard Tessellation Language (.STL) format. On the medial femoral condyle, three different sized defects, and subsequent implants, were generated by forming a 55° inclination with the horizontal plane (Autodesk Netfabb Premium 2019, San Rafael, USA). The design of the implants was based on the principle of limiting cellular penetration from the bone compartment to the cartilage compartment and the knee-joint space, while allowing cell infiltration into the bone compartment.



Mechanical testing of printed implants under physiological loading:

Two loading conditions were applied based on body weight & gait analysis of ovine³⁴² that will be used for subsequent *in vivo* testing of the developed implants (average body weight 60kg, 2 years old). For the first loading condition (axial load), implants were fixed at a knee flexion angle of 55°, the angle at which maximum axial force is registered³⁴², and cyclic compressed (6x) up to a maximum force of 2000N at a rate of 400N/s. These tests were performed on a universal testing machine (Instron 5967, US). For the second loading condition (flexion and extension), gait was resembled by allowing extension-flexion of femur and tibia vary between 50° - 60° at 5°/sec. Here, the axial load was kept constant at 400N (scaled due to the limitations of the unit cell available). For this second loading condition, a 5 degrees of freedom (DoF) robotic arm system was used (QUT, Australia). For both loading condition, a pre-load of 100 N was applied to ensure contact between the test samples and the opposing tibia. Implants composed of PCL and MgP-PCL with different sizes (small (S): 5 x 17 mm, medium (M): 10 x 17 mm, large (L): 15 x 17 mm) were studied. As a model joint (*i.e.*, tibia and femur compartments), a digital light processing (DLP)-fabricated patient-specific ovine joint was used (Non-deformable R05 material, Envisiontec, Germany) with defects that corresponded with the implant measurements.

For the mechanical analysis, stress-strain curves were calculated from the applied force and displacement data from the axial loading experiment. Here, stress is defined as the applied force divided by the implants' loaded area. Loaded area between implant and opposing tibia, was determined by stained paper positioned between implant and tibia. Strain was defined as the ratio between the initial implants thickness and the displacement of compression head. Implant stiffness was calculated from the slope of the engineered stress-strain curve near the maximum value of stress for each loading cycle. The implants that were tested in the flexion and extension experiment only reflect the maximum force as the contact area could not be determined (work in progress). In addition, all tested implants were measured before and after loading to quantify implants permanent deformation.

Automation of MEW printing path based on .STL file

A python program was written to automatically generate numerical control programming language (*i.e.*, g-code) from .STL files for the resurfacing movement of the MEW head. A visual presentation of the printing trajectory was made with NC Viewer © 2018 Xander Luciano. Machine specific codes can be included in this program, or after extracting the g-code, to make this code more versatile for other machines. User input is only needed for parameters such as line spacing, collecting implant or printhead velocity, collector to implant distance and intended scaffold height. The python script runs through a series of events including importing the mesh and extracting coordinates of the .STL file, adjusting

z-coordinates based on collecting implant to printhead distance, finding x- and y- values for the required line spacing, finding and combining the x-, y-, and z-trajectories, including machine specific input, and exporting the resulting g-code into a .txt file (**Supplementary Figure 1**). As a control mechanism, midpoint checks are added to the code to generate x-y-, y-z-, and x-z-scatterplots and histograms of the x-, y-, z- coordinates. In this code, the accuracy of the amount of steps made in x-, y-, and z-direction can be altered by changing the programmed trajectory accuracy (PTA) and a low input value reflects a higher accuracy. The average steps in x- and y- direction based on a low, medium, and high PTA was calculated based on all point in all lines for that specific direction. The effect of the PTA on the fibre diameter was measured with light microscopy (Olympus DP73, Olympus Nederland B.V., The Netherlands) and Fiji software (version 2.0.0-rc-54/1.51h). To measure the percentage of resurfacing of the implant, the deviation between the deposited MEW mesh and the edge of the implant was measured from a topview perspective.

***In vitro* culture**

To analyse the effect of implant size on *in vitro* cartilage-matrix deposition different diameter discs (diameter = 6, 12, 24 mm) were cultured in chondrogenic differentiation medium. Additionally, as osteochondral plugs, depending on the material used, may hamper the influx of nutrients and efflux of waste components during *in vitro* culture, the effect of a flat plate system (reflecting the same number of nutrient and waste exchange directions as the osteochondral plugs) as compared to a transwell system (reflecting the highest number of nutrient and waste directions during bulk static culture conditions) has been evaluated.

Biochemical evaluation of cartilage-like tissue formation

To quantify the amount of sulphated glycosaminoglycans (sGAGs) and correct them for DNA content, colorimetric dimethylmethylene blue (DMMB, Sigma Aldrich, USA) and fluorometric Picogreen (Quant-iT-Picogreen-dsDNA-kit, Invitrogen, USA) assays were performed, respectively. Prior to these assays, implants were enzymatically digested overnight at 60°C using a papain digestion solution.

Histological evaluation of cartilage-like tissue formation

Histological evaluation of the *in vitro* cultured constructs was performed to assess the distribution of cartilage-like matrix components. The constructs were formalin-fixed and embedded in paraffin. Tissue sections (thickness = 5 µm) were deparaffinized with xylene and were rehydrated by gradual ethanol steps (100% - 70%) prior to staining. Safranin-O staining was used to visualize GAG distribution, combined with fast green (Sigma Aldrich, USA) to stain fibrous tissue, and haematoxylin (Sigma Aldrich, USA) to stain cell nuclei. Immunohistochemistry was performed to visualize type II collagen deposition. First,



pronase (1 mg/mL, Roche, USA) and hyaluronidase (10 mg/ml, H2126, Sigma Aldrich, USA) were used for antigen retrieval, and sections were blocked with bovine serum albumin prior to primary antibody incubation II-II6B3 (DSHB, USA). IgG was used as negative control staining. Samples were incubated over night at 4°C, washed, incubated with matching secondary antibody (1:100, IgG HRP, P0447) for 1 hour at room temperature, and washed again. Subsequently, 3,3-diaminobenzidine-horseradish peroxidase (DAB, Sigma Aldrich, USA) was used to visualize the staining. After staining the cell nuclei with haematoxylin, pictures of histologically stained sections were made with a light microscope (Olympus BX51, The Netherlands).

SEM imaging

Scanning electron microscopy (SEM) (Phenom Pro Desktop SEM, Thermo Fischer Scientific, USA) was performed with an accelerating voltage of 10. Prior to imaging, samples were coated with 2 nm of gold to improve imaging quality.

Statistics

Data is presented as mean \pm standard deviation. Fibre diameters, inter-fibre spacings, and resurfacing percentages were measured on 5 samples per group. All *in vitro* culture studies were performed in triplicate, and mechanical analysis was performed with $n = 3$. To test the differences between groups, either an unpaired t-test, or an ANOVA with post hoc Bonferroni test was performed. Difference between groups was considered statistically significant if $p < 0.05$.

Results

Fabrication

Based on CT scans of ovine joints, Standard Tessellation (.STL) files were generated. In these .STL files, defects of 5 mm (S), 10 mm (M), and 15 mm (L) were made in the medial femoral condyle. Implants that were based on these defects presented a contact surface area of 302, 459, and 469 mm² to fit into the 5 mm, 10 mm, and 15 mm defect, respectively (**Figure 2A**). The .STL files (**Figure 2B**) of the implants were used to design the bone component with a closed layer between the bone and cartilage interface and an open pore structure at the bottom and at the sides of the implant that will eventually interact with native tissues (**Figure 2C-D**). Printed implants showed a good fit in the DLP-fabricated model of the defect (**Figure 2E**).

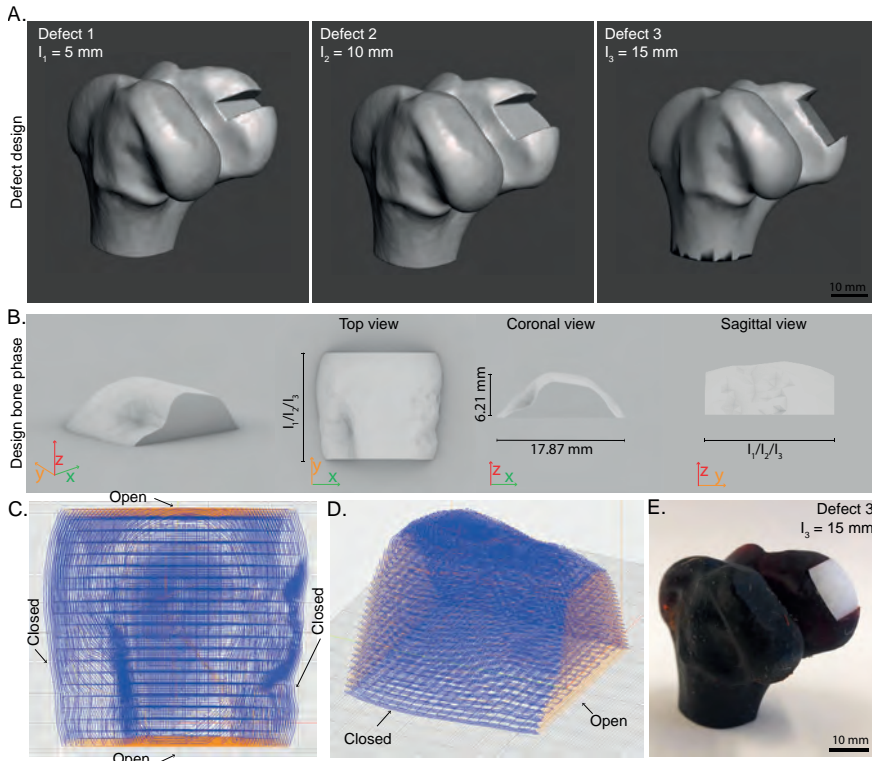


Figure 2. Implant design and printing trajectory of bone phase of the implant. A) Design of the defects with a difference in sagittal length (sagittal length $l_1 = 5$ mm (S), $l_2 = 10$ mm (M) and $l_3 = 15$ mm (L)). B) Rendering of implant reflecting complex shaped surface. C) Top view of the printing trajectory, with open pores (orange) on the connecting side and including 4 closing shells (blue) around the implant. D) Side view of printing trajectory. E) Digital Light Processing (DLP)-printed models that were used for digitally transferable *ex vivo* testing of implant, here filled with a PCL implant.

For the bone component, frequently used medical grade PCL was compared with magnesium phosphate enhanced PCL (MgP-PCL) implants. Both PCL and MgP-PCL showed a high shape fidelity after printing and successfully resolved the designed pore structure in the x-, y-, and z-direction (**Figure 3A**). MgP-PCL did show a higher fibre diameter (PCL: $208 \mu\text{m} \pm 14 \mu\text{m}$, MgP-PCL: $300 \mu\text{m} \pm 20 \mu\text{m}$) and a lower inter-fibre spacing (PCL: $593 \mu\text{m} \pm 25 \mu\text{m}$, MgP-PCL: $424 \mu\text{m} \pm 28 \mu\text{m}$) as compared to PCL (**Figure 3B, C**). The inner pore structure of the first 4.7 mm was successfully achieved (**Figure 3D-E**). Printing of MgP-PCL implants showed high dimensional accuracy and reflected the STL file well. (**Figure 3F-G**).

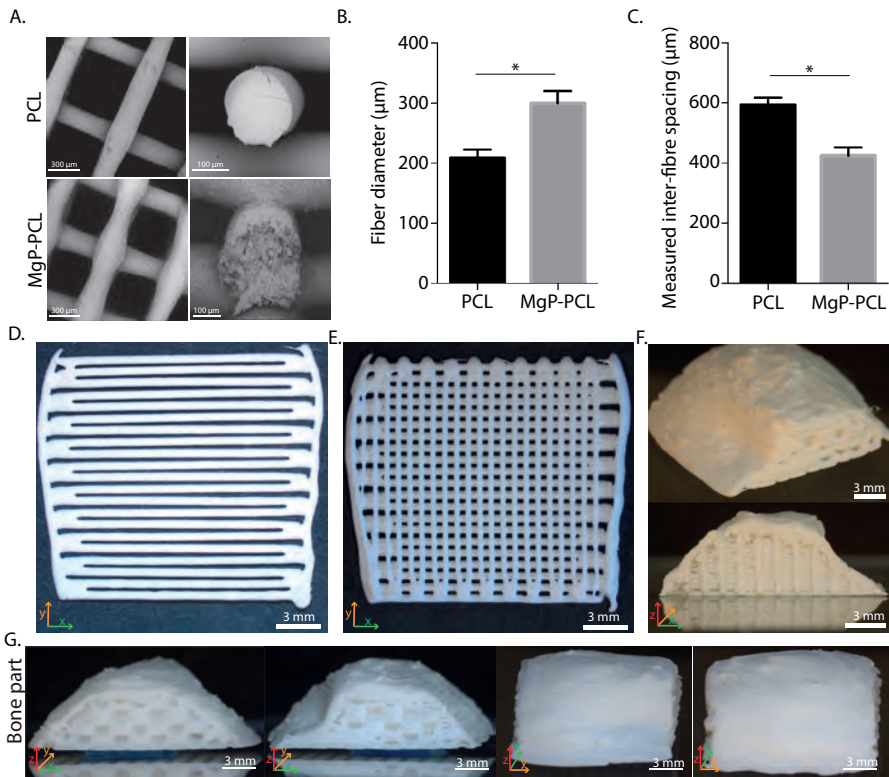


Figure 3. Details of PCL and MgP-PCL printed implants. A), Fibre morphology of PCL and MgP-PCL strands. B) Fibre diameter of PCL and MgP-PCL printed strands. C) Measured inter-fibre spacing of the PCL and MgP-PCL implants. D-E) Top view of the porous inner structure of the first 4.7 mm. F-G) MgP-PCL printed implant, representing the bone part from different angles. * = $p < 0.05$, t-test.

Mechanical testing

Uniaxial cyclic compression (Axial loading, **Figure 4A**) on the implants was performed with the opposing DLP fabricated tibia and yielded different stress strain curves for the small versus the large implant (**Supplementary Figure 2**). The implant stiffness of both small and large implants was increased per cycle (**Figure 4B**). The small implants yielded a significant higher stiffness compared to the large implants (**Figure 4B**). For the PCL implants, the implant thickness significantly decreased after compressive testing for the medium (11 %) and large samples (13 %) (**Figure 4C**). When varying extension-flexion rotation at a constant axial compression (**Figure 4D**) larger PCL implants showed a lower maximum force compared to smaller implants with 76 N and 187 N after 5 cycles of compression, respectively (**Figure 4E**). After compression under flexion and extension,

the medium (7 %) and large (10 %) implants showed a significant decrease in final implant thickness as compared to before compressive testing (**Figure 4F**).

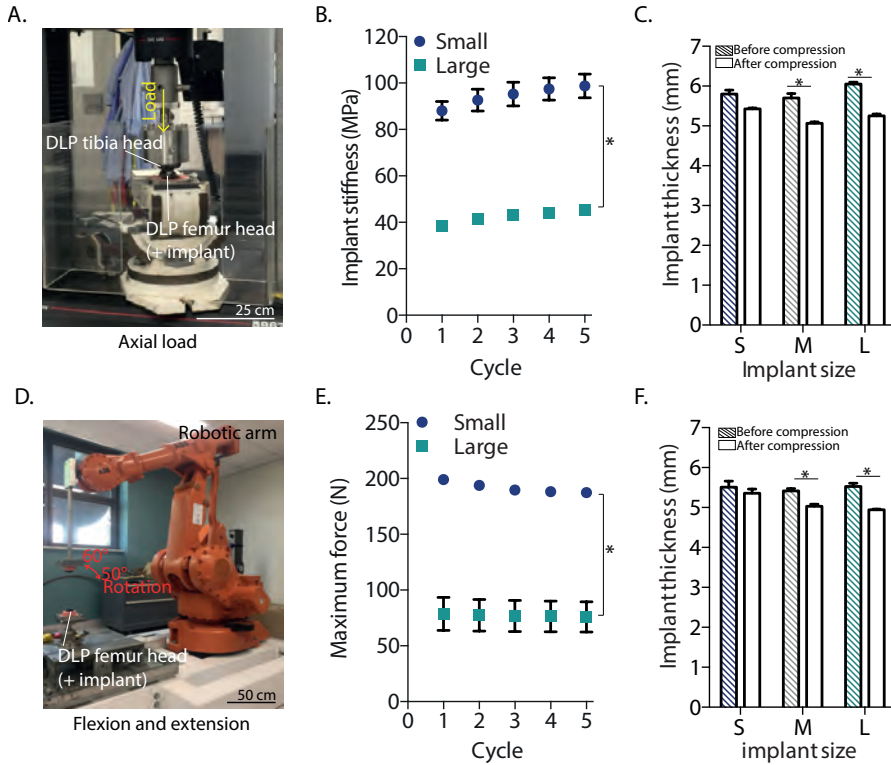


Figure 4. Mechanical evaluation of MgP-PCL and PCL implants under physiological loading. A) Axial loading condition. B) Stiffness of small and large PCL implants per cycle. C) Final implant thickness of different sized implants of PCL before and after 5 cycles of compression as a reflection of permanent deformation. D) Flexion and extension testing with a robotic arm system. E) Maximum force of small and large implants (Surface area was not determined, work in progress). F) Final implant thickness of different sized PCL implants before and after compression as a reflection of permanent deformation. * = $p < 0.05$, ANOVA post hoc Bonferroni.

In vitro culture

Caprine ACPCs showed slight positive staining for alizarin red, oil red O and safranin O staining (**Figure 5A**) after culture in adipogenic, osteogenic, and chondrogenic medium for 21, 28, and 28 days, respectively. Additionally, an increase in sGAGs per DNA was found for all donors during 28 days of *in vitro* culture in 3D cell-laden hydrogel discs, a typically



used 3D *in vitro* culture system for cartilage tissue engineering (**Figure 5B**). This increase was predominantly shown in the first 14 days of culture.

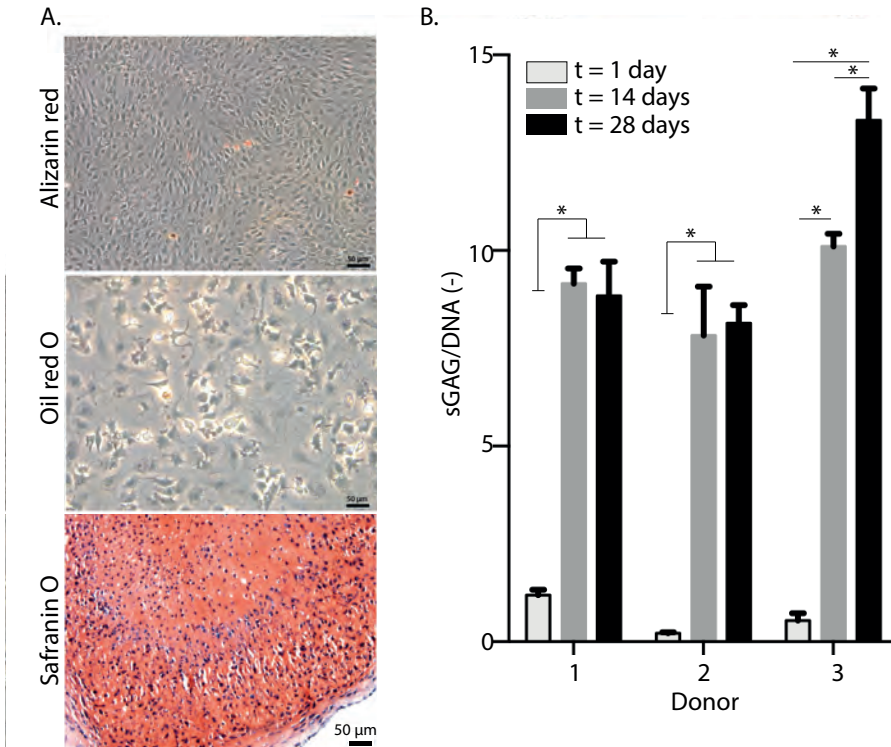


Figure 5. Caprine ACPCs. A) Tri-lineage assay shows that goat derived ACPCs are able to differentiate into the osteogenic, adipogenic, and chondrogenic lineage. B) Quantification of sGAG/DNA per donor over the course of 28 days of *in vitro* culture. * = $p < 0.05$, ANOVA, post hoc Bonferroni.

When assessing the effect of disc size (diameter = 6, 12, 24 mm, **Figure 6A**) on cartilage-like matrix distribution, all disc diameters showed an increase in sGAG/DNA after 14 and 28 days of culture (**Figure 6B**). After 28 days, a decrease in sGAG/DNA was observed with increasing disc diameters, with 81, 59, and 48 $\mu\text{g}/\mu\text{g}$ sGAG/DNA for discs with a diameter of 6, 12, and 24 mm, respectively. A transition from a flat plate system (to reflect the same number of nutrient and waste exchange directions as engineered cartilage on osteochondral implants) to a transwell system (that reflects the highest number of nutrient and waste exchange directions for bulk static culture) (**Figure 6C**) did not affect

sGAG/DNA, total sGAG or DNA content in the 6 or 24 mm diameter discs after 28 days of culture (**Figure 6D**).

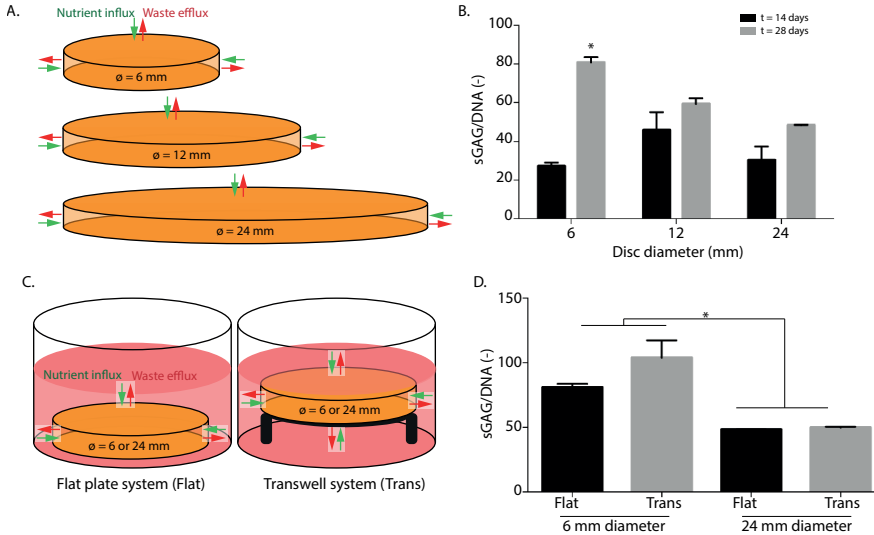


Figure 6. *In vitro* tissue culture. A-B) Effect of disc diameter (diameter = 6, 12, 24 mm, $h = 2$ mm) on cartilage like matrix formation in terms of sGAG/DNA. C-D) Effect of in vitro culture on a flat plate system as compared to on a transwell system with respect to cartilage-like matrix formation for 3D discs of 6 and 24 mm in diameter. * = $p < 0.05$, ANOVA, post hoc Bonferroni.

Automatic numerical control programming language (*i.e.*, g-code) generation

G-code generation to resurface the patient-specific .STL file, while keeping the distance between the collecting implant and the printing head equal by translating in z-direction, was successfully automated (**Figure 7A**). The number of steps along the length of a complete line in x-, or y- direction, depended on the difference in z-coordinates along this same x-, or y-trajectory and was determined as the Programmed Trajectory Accuracy (PTA) (**Figure 7B**). This PTA can be adjusted by the user and an increase in PTA included more steps in x-, and y- direction. Although a higher PTA involved an increased number of steps and therefore an increase in MEW jet disturbance by acceleration and deceleration in the motion pattern, only the high PTA printing condition showed a significant increase in fibre diameter as compared to the low and medium PTA (**Figure 7C**). Even though the lower PTA showed a lower resurfacing trajectory (**Figure 7B**), the measured resurfacing

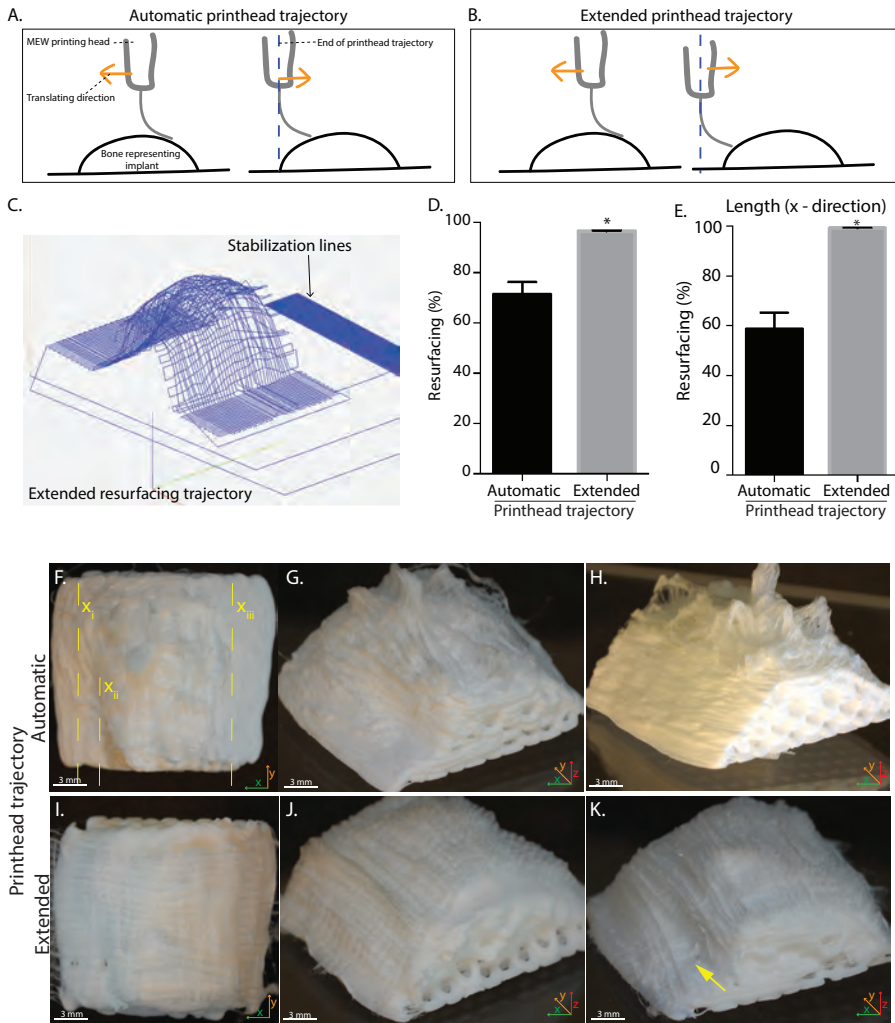


Figure 8. Extending the printhead trajectory. A). Automatically generated printhead trajectory stops resurfacing at the edge of the implants. B) Manually extended printhead trajectory moves beyond the edge of the implant. C). Simulation of the eventual printhead trajectory. D) Effect of manual extension of the printhead trajectory on the total measured % of resurfacing. E) Effect of manual extension of the printhead trajectory on the measured number of resurfacing in x-direction only. F-H) Macroscopic images of the implants that were resurfaced with the fully automated g-code. I-K) Macroscopic images of the implants that were resurfaced with the extended printhead trajectory. * = $p < 0.05$, unpaired t-test.



By adjusting the automatic printhead trajectory (**Figure 8A**) that followed the exact pattern of the .STL of the implant to an extended printhead trajectory (**Figure 8B, C**), where the printing trajectory is manually extended in the automatically generated g-code, the measured percentage of resurfacing was increased from 71% to 96% (**Figure 8D**). This increase was mainly found in the x-direction where the collecting implant showed more deviation in z-direction as compared to the y-direction (**Figure 8E**). The 71% of measured resurfacing for the automated printhead trajectory was affected by the geometry of the implant as the part where the geometry included the concave curvature ($x_{ii} - x_{iii}$) showed a lower percentage of resurfacing as compared to the part where the geometry only included the convex curvature ($x_i - x_{iii}$) (**Figure 8F**). Interestingly, incomplete resurfacing (71%) resulted in inaccurate fibre deposition and subsequent piling up of fibres at the top of the implant (**Figure 8F-H**). This effect was not found for the implants that were printed with the extended trajectory, where accurate fibre patterning was observed (**Figure 8I-K, Supplementary Figure 3**). Fibre deposition around the concave curvature (yellow arrow in **Figure 8K**) was less accurate as compared to fibre deposition at the convex curvatures.

***In vitro* culture of completely resurfaced implants**

As a proof-of-principle, the completely resurfaced implants (**Figure 9**) were cultured for 28 days. Directly after fabrication, macroscopic evaluation demonstrated that the implant showed a smooth surface and maintained integrity.

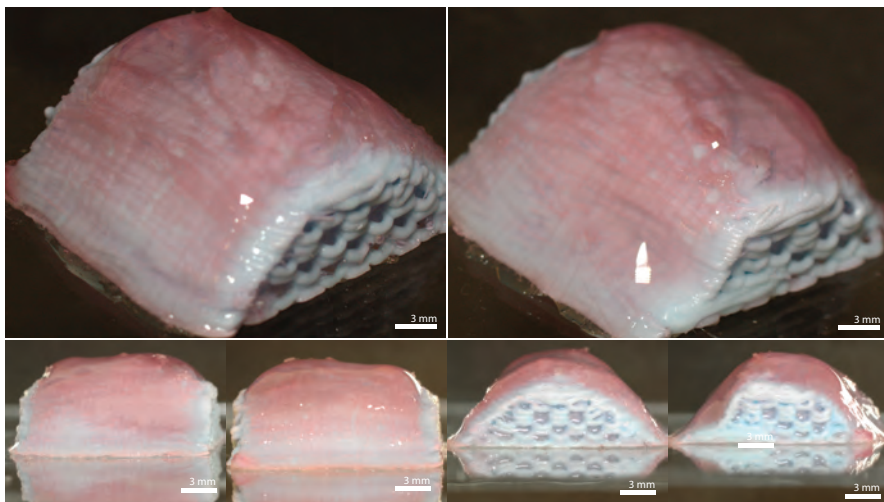


Figure 9. Completely resurfaced, large patient-specific, biofabricated implant.

Discussion

Current developments in (bio)fabrication technologies allow for multi-material and multi-scale fabrication resulting in tissue structures that more closely mimic native tissues.^{80,276,340} These developments have progressively improved the resolution of osteochondral plugs that are fabricated to treat AC and osteochondral defects.^{81,202,273} Although promising *in vitro* results have been shown, and mechanical stability of structurally strong plugs has been shown *in vivo*, these plugs are still relatively small and do not directly translate to patient-specific treatments. In this study, the first steps in the transition from the osteochondral plug towards larger, patient-specific and mechanical competent implants have been made.

Despite the fabrication challenges, engineering large tissue structures generally pose the challenge of nutrient and waste exchange to provide a biological environment in which the cells can produce matrix components and mature the engineered tissue.^{150,343} Multiple strategies to overcome this challenge have been tried such as incorporation of (micro-) channels within printed constructs²⁴⁷, controlled delivery mechanisms³⁴⁴, and modular scaffold designs³⁴⁵ to mature the tissue prior to eventual assembly. The *in vitro* culture of this study shows that for the 2 mm thick cartilage layer, nutrient and waste exchange did not prevent matrix distribution in larger implants. Although there was less sGAG/DNA production for the 12 mm and 24 mm diameter constructs as compared to the 6 mm diameter construct, an increase in sGAGs was still found for all these constructs over the course of 28 days. Moreover, placing both the 6- and 24-mm constructs on a transwell culture system to allow nutrient and waste exchange from more directions, did not affect matrix deposition in these constructs as compared to the flat plate culture system that reflects the same amount of nutrient and waste exchange as engineered cartilage of an osteochondral implant has. This suggests that the 2 mm thickness is not a limiting factor for cartilage-like matrix formation. Multiple *in vitro* studies that use 2 mm thick discs as a culture system for articular cartilage-like tissue formation support this result.^{84,167,274} Additionally, in a study that used aggregates to resurface the large tibia plateau, ample matrix distribution and tissue maturation in terms of type II collagen alignment were shown.³¹⁹ Although that study did not use a gel as a cell carrier, it does show that a 2 mm thick tissue does not have to be a limiting factor for articular cartilage-like tissue formation and maturation.

Another challenge of fabricating larger implants is the cell source and cell availability as cell-laden hydrogels generally use high cell densities to achieve matrix production throughout the entire construct. Achieving high cell numbers can be challenging with commonly used chondrocytes and MSCs as these lose chondrogenic potential after



multiple proliferation cycles. Equine derived ACPCs do not show this limited proliferative capacity and can therefore be expanded to high cell quantities.^{34,167} An additional benefit of ACPCs as opposed to MSCs is that the former do not tend to go into hypertrophic growth and subsequent osteogenic lineage. The cells used in this study are caprine-derived cells from articular cartilage tissue that show the potential to differentiate into the adipogenic, osteogenic, and chondrogenic lineage. Although no specific ACPC markers are known, it is important to test the chondrogenic capacity of these cells after multiple proliferation cycles to more thoroughly understand if the behaviour of these cells is similar to that of equine-derived ACPCs. Other approaches to deal with the challenge of cell availability are by co-culture of different cell types²⁹⁶, use of extracellular vesicles that act as stimulating communication units between the cells³⁴⁶, or increasing cell-cell contact by aggregating^{97,319} and preculturing chondrocytes and use these as building blocks for tissue maturation.

In vivo implantation of osteochondral plugs at orthotopic locations that include high loading regimes commonly results in unexpected outcomes, even when using materials that have shown promise in *in vitro* studies as well as in ectopic *in vivo* studies (Diloksumpan *et al. Under review*). The combination of loading and degradation of the material potentially induces micro-movements of the implant which subsequently results in bone resorption around it.³⁴⁷ Furthermore, if the implant loosens, this allows for infiltration of the synovial fluid to the bone tissue, which subsequently results in further bone degradation and thus intensifies the problem.³⁴⁸ To prevent micromovement and to further understand the role of mechanical loading on our implants, this study showed the effect of implant size on the mechanical properties of these implants under physiological loading conditions by using a DLP fabricated replica of the knee joint. Here, we show that an increase in implant size results in a decrease in implant stiffness during axial compression. Additionally, the maximum force of the implants decreased for larger implants as compared to smaller implants. Permanent deformation of the implants was both shown after axial compression and after flexion and extension. The 2-fold difference in stiffness between small and large implants during axial compression, and the 3-fold difference in maximum force during flexion-extension, highlight the importance of implant size as well as different testing regimes. In future research, this data can be incorporated in a finite element (FE) model that can be used to predict the mechanical loads on the implant and helps to improve the design of the bone component. This important step towards patient-specific implant stability, should also include the structural elements of the engineered cartilage component on top of the bone component as well.

To achieve larger patient-specific implants that include MEW fibres as the structural elements of the cartilage-component, it is important to maintain a constant electrical field strength by applying a constant collector to spinneret distance.³⁴⁹ Therefore, the curvature of the joint has to be followed with a constant distance between the collecting joint and the MEW printhead. As part of this study, a software tool has been developed to automatically generate a machine-specific g-code that accurately deposits MEW boxes on top of the complex MgP-PCL joint structure. The percentage of resurfacing was shown to be only 71% when exactly following the contours of the STL file, which can be explained by a deviation between the position of the printhead and the position where the actual fibre is deposited, caused by the viscoelastic behaviour of melt electrowritten PCL (also referred to as the “jetlag”). The piling up of fibres with this low percentage of resurfacing can be explained by the charge accumulation at the higher parts of the implant and the electrostatic autofocussing effect that favours vertical layer stacking.²⁹⁰ Manual extension of the printhead trajectory after automatic generation of g-code was performed to achieve 96% of resurfacing. This manual extension could potentially be avoided by direct feedback based on in-line monitoring of the jetlag and direct automatic extension of this printhead trajectory based on this jetlag. Additionally, although MEW onto the convex geometries was shown to be accurate, the accuracy decreased for the concave geometries. As this study only included a correction in z-direction and used a 3-axis platform, this might be improved by including an extra rotational axis to achieve a jet that is always normal-to-surface. With a normal-to-surface jet, even more control over fibre positioning could be achieved and other MEW designs on non-planar surfaces could be explored. For example, by applying an offset in the printhead trajectory, out-of-plane, arched structures have been established.³⁵⁰ This approach can be explored to mimic the structurally important “Benninghoff arcades”⁴⁰ and subsequently aid in further approximating the mechanical properties of AC tissue, which is a key requirement for regenerating AC tissue.¹⁰⁰

Conclusion

This study provides a roadmap for the successful scale-up from an osteochondral plug towards larger patient-specific implants for the treatment of joint damage. The mechanical characterization under physiological conditions shows that the implant size affects the stiffness of the implant (under axial loading) and maximum force (under flexion-extension). Large implants show lower stiffness, lower maximum force, and more permanent deformation as compared to small implants. Increased implant size did not limit cartilage-like tissue formation and additionally submerging the bottom of the construct in culture medium did not result in an increase in matrix production in neither the small or larger implants. This study provides an effective tool to automatically generate g-code to achieve a constant collecting implant to printhead distance. This allows for accurate MEW reinforcing fibre deposition on implants with patient-specific geometry. Manual extension

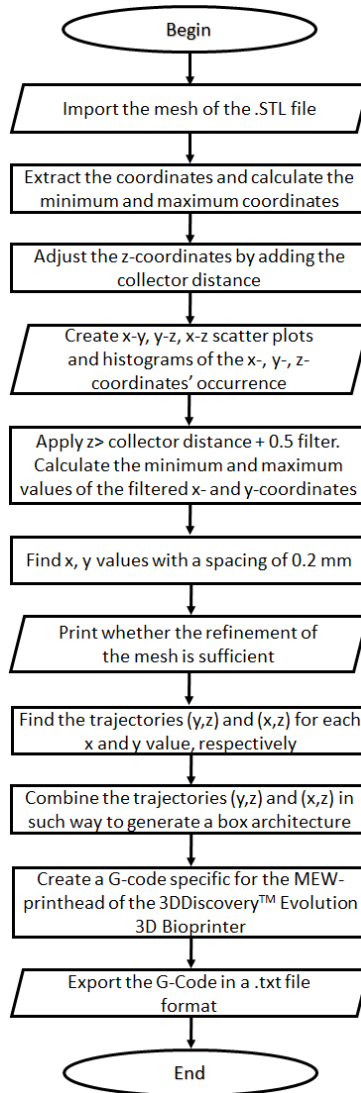


of the printing trajectory in the direction that included most deflection in z-direction was needed to completely cover the bone-component with reinforcing MEW fibres. This study showed successful fabrication of a multi-scale, patient-specific, large, mechanically stable, osteochondral implant with a complex geometry and an ability to form cartilage like matrix close to currently used smaller sized implants. These first steps are imperative for moving towards mechanically stable, multi-scale patient-specific osteochondral implants for the treatment of clinically relevant (osteo)chondral defects.

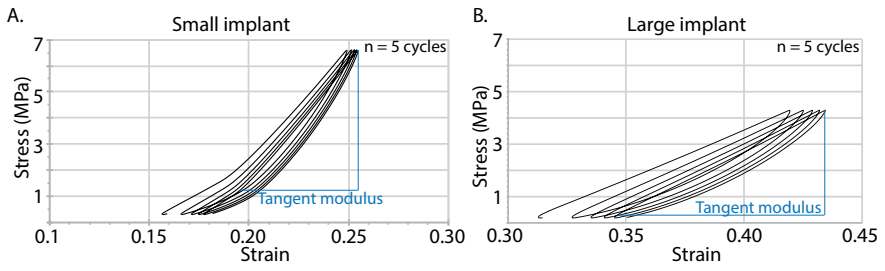
Acknowledgements

The primary antibodies against type II collagen type (II-II6B3) developed by T. F. Linsenmayer, was obtained from the DSHB, developed under the auspices of the NICHD and maintained by the University of Iowa, Department of Biology, Iowa City, IA. This work was financially supported by the European Research Council under grant agreement 647426 (3D-JOINT), EU funded E11312 Bioarchitect project, the Dutch Arthritis Society (Grants CO-14-1-001, LLP-12, and LLP-22), and Hofvijverkring.

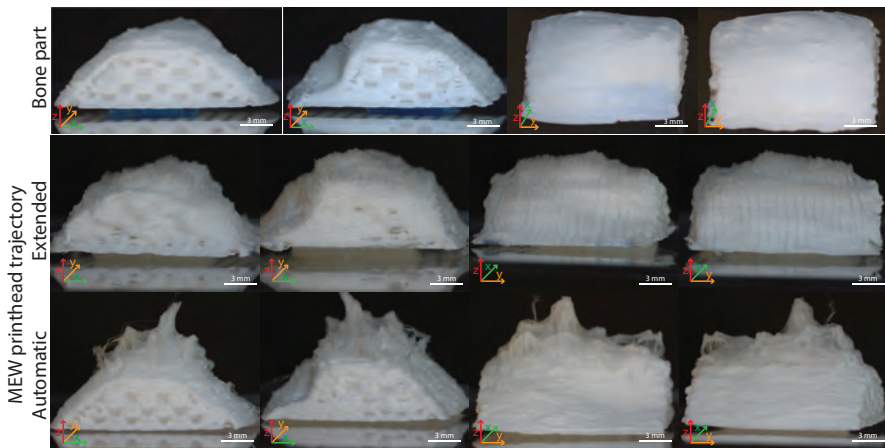
Supplementary figures



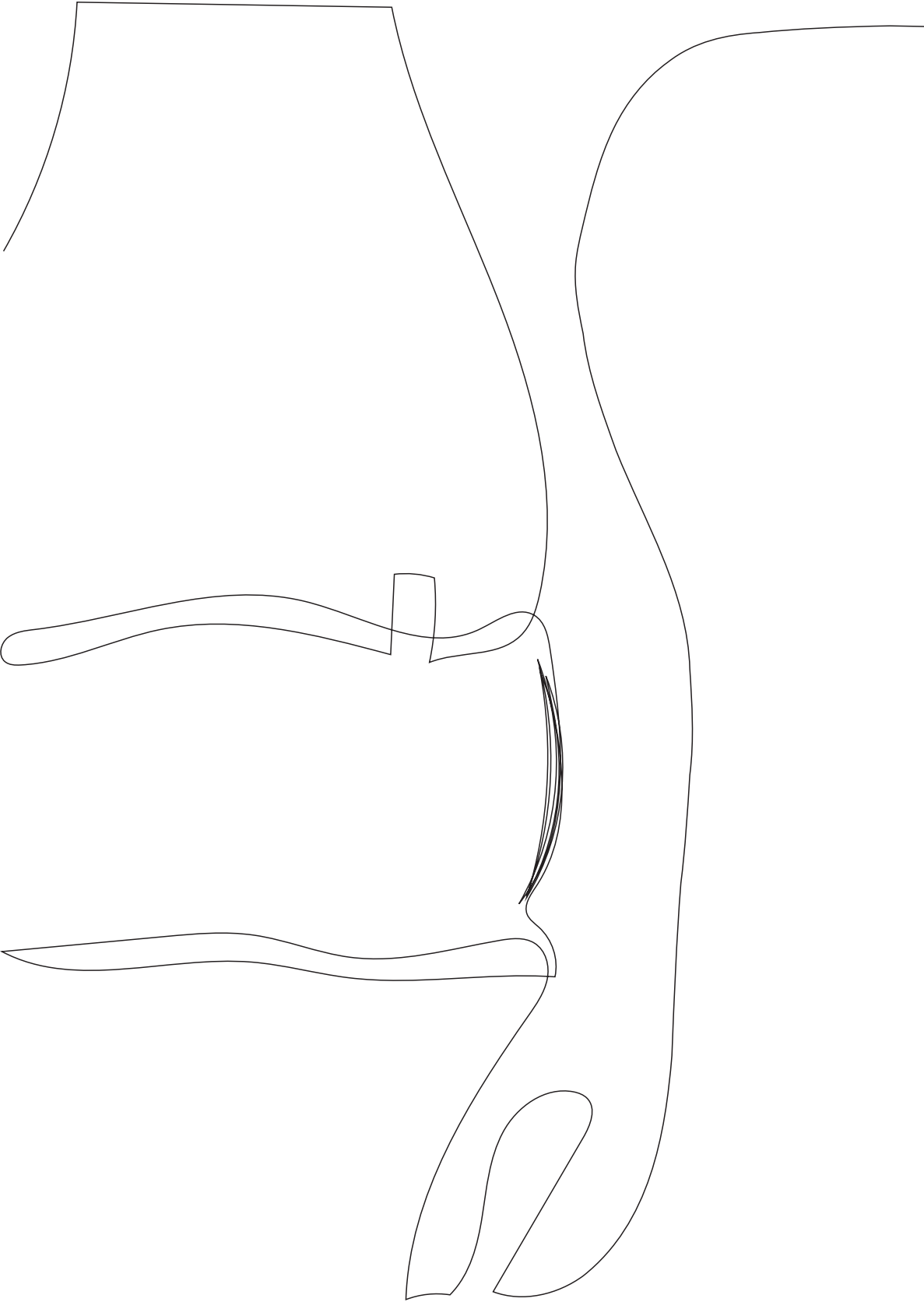
Supplementary Figure 1. Flowchart of automative g-code generation for MEW printhead trajectory.



Supplementary Figure 2. Stress-strain curves during cyclic axial compression. A) Small implant. B) Large implant.



Supplementary Figure 3. Macroscopic images from all sides of the bone part and the resurfaced implants with the manually extended and fully automatic code.



Chapter 10

General discussion and conclusion

Addressing the structural and mechanical challenges of the biofabricated osteochondral implant and how to further mimic native tissue architecture

The knee joint is a mechanically challenging environment for implantation due to the combination of compressive (up to 6 MPa³¹) and shear (up to 0,085 MPa³¹) loads that act on the articulating cartilage surface. A successful implant for (osteo)chondral tissue repair treatment requires similar mechanical properties as native tissue in order to survive and efficiently transfer loads. To address the structural and mechanical challenges of these implants, improving such mechanical properties of the load-transferring engineered chondral component, as well as the strength of the cartilage-to-bone interface, is vital. In this thesis, melt electrowriting (MEW) was used to expand the application of hydrogel-based materials to engineer (osteo)chondral implants by providing structural support to the cartilage component in both compression and shear, while also facilitating the strong interconnection between the cartilage and bone components. As hydrogels are intrinsically soft because of their low polymer volume, implantation of these hydrogels hitherto led to implant failure. Previously, MEW was used to mechanically reinforce soft cell-laden hydrogel constructs, which led to a significantly higher compressive modulus as compared to non-reinforced hydrogel constructs.^{84,92} Computational modelling showed that this effective reinforcing strategy is attributed to the load carrying-ability of the interconnections of the MEW fibres combined with the Poisson effect (*i.e.* the MEW fibres suppress lateral hydrogel expansion when the implant is submitted to compressive loads).⁹³ Other mechanical reinforcing strategies have been employed to improve the mechanical properties of cartilage implants, such as use of weaving technologies²⁹², interpenetrating networks (IPN)¹¹⁴, nano-particle reinforcement¹¹⁵, fused deposition modelling (FDM) fibre reinforcement^{82,86,253,336}, hydrogel-based reinforcement¹⁶³, and solution electrospinning⁸³. Reinforcement using fibre structures fabricated with FDM is most widely explored.^{82,150,184} This approach fabricates fibres with an average diameter of around 100 – 200 µm. Depending on the chosen design, the reinforcing material, and the method (print or cast) of including the (cell-laden) hydrogel, the compressive properties of FDM-reinforced hydrogel constructs can achieve values up to 6 MPa.^{82,86} Converged layer-by-layer printing of polycaprolactone (PCL) FDM reinforcement and a methacrylated hyaluronic acid (HAMA)-based bioink hampered optimal fusion of the thermoplastic PCL fibres and resulted in lower compressive properties (around 4 MPa) of the composite structure.³⁰⁵ Even lower compressive modulus values can be achieved for FDM-reinforced constructs. A compressive equilibrium modulus between 0.2 and 0.9 MPa resulted from the use of a double-offset printing design while co-printing FDM PCL fibres with an IPN hydrogel.⁸⁶ Although the values of FDM reinforced constructs covers such a wide range in compressive moduli, the thick fibre diameter of FDM scaffolds hampers efficient

interconnection of the non-fibrous components of the construct, which consequently limits homogeneous cartilage-like tissue deposition. Additionally, the stiff nature of the thick, high volume fraction of PCL fibres can result in stress-shielding and compromise matrix deposition, as chondrocytes are stimulated to produce neocartilage tissue by environmental mechanical cues.^{351–356} Furthermore, *in vivo* tissue remodelling should balance the degradation of the structural elements of the implant.^{357,358} Establishing this balance is even more challenging with use of thick, high volume fraction, structural elements. Although thick (diameter ~200 µm) hydrogel reinforcement allows for highly controllable degradation of the reinforcing component, the achieved compressive modulus of 138 to 263 kPa is more applicable for softer tissues.¹⁶³

The mechanical properties of native articular cartilage (AC) tissue are dependent on both the fibrous and non-fibrous components of the extracellular matrix (ECM). Yet, although glycosaminoglycans (GAGs) also contribute to the shear and compressive properties of AC tissue, their main function is to retain pretension in the collagen structure by attracting water.^{359–361} As GAG production has already been shown upon chondrogenic stimulation of mesenchymal stromal cells (MSCs), chondrocytes, and articular cartilage resident progenitor cells (ACPCs) in gelatin methacryloyl (gelMA)-based three-dimensional (3D) tissue cultures¹⁶⁷, the focus of this thesis was recreating the structure of the fibrous part (type II collagen) of the ECM. Collagen fibres are strong in tension and, therefore, able to counterbalance the swelling pressure and subsequently withstand compressive loading.³⁶² The zone-dependent directionality of the collagen fibres in AC leads to effective load transfer throughout the tissue. In fact, a strong correlation between the amount and directionality of collagen fibres and the AC shear modulus exists, as the shear loads are converted to stretching of the collagen fibres.^{41,361} The chosen fibre design in this thesis was inspired by the structural orientation of the collagen fibres in native AC tissue. A complex shear modulus up to 90 kPa, as well as compressive properties up to 600 kPa, were achieved and it was shown that these properties are dependent on the specific design and volume fraction of the MEW reinforcing fibres, as well as on the amount of *in vitro*-cultured cartilage-like matrix. Although MEW facilitated the reinforcement of hydrogel constructs in both shear and compression, and the implants survived the challenging *in vivo* conditions, the compressive properties of native AC tissue are still not matched.

To increase the compressive properties of regenerative implants, further mimicking the structural composition of native AC tissue is key. This will enable increased retainment of (swelling-inducing) GAGs and improve the intrinsic strength of the reinforcing fibres and the interconnection between the fibrous and non-fibrous components of the implant. In native AC tissue, type II collagen fibres comprise a complex hierarchy that includes attachment of type III and type IX collagen, the latter able to electrostatically

bind to aggrecan.^{363–365} This distinct architecture and composition of type II collagen fibres contributes to the entrapment of proteoglycans and may well be mimicked by through the use of (bio)fabrication technologies.

Recreation of the structurally important “Benninghoff” architecture with MEW potentially allows for further tissue mimicry and better load transfer. MEW has mainly been performed in an in-plane fashion, limiting the fabrication of arched structures. This thesis showed the first out-of-plane fabrication of MEW fibres (**Chapter 2**). Recently, it has been shown that by applying an offset in the printing trajectory using highly accurate MEW machines, more distinctive designs are possible which could potentially lead to the fabrication of arched structures with MEW.³⁵⁰ Alternatively, the arched architecture may well be fabricated with the use of hydrogel collector plates that guide the MEW fibre direction (**Chapter 5**).

The reinforcing material used in this thesis, PCL, is inert and does not interact with the hydrogels used, nor does it stimulate specific cell behaviour. The interaction between the reinforcing fibres and the cell-laden hydrogel could be improved by MEW of a methacrylate-functionalized blend of poly(hydroxymethylglycolide-co-ε-caprolactone)/poly(ε-caprolactone)(pHMGCL/PCL) that allows for a covalent grafting to the hydrogels used.¹⁸¹ To guide cell-growth and alignment, pHMGCL has been processed with MEW for cardiac tissue engineering.¹⁶⁹ The feasibility of processing such cell-interactive material with MEW is high, as MEW is a relatively new technique and the library of materials that could be processed with this system keeps expanding.^{90,366,367}

Retention of chondral implants in AC defects remains challenging and using an osteal-anchor has been proven effective in a press-fit method for implantation of a cartilage tissue construct.³³⁶ To firmly connect the engineered cartilage part to the osteal anchor, the design of the interface between cartilage and bone should be carefully considered. Combining MEW and extrusion-based printable calcium phosphate (pCaP) printing results in a strong connection between the cartilage-to-bone interface (**Chapter 3**). Apart from enabling effective integration of the cartilage and bone compartments within an engineered osteochondral plug, this approach may also be applicable to other engineered tissue interfaces, such as the tendon-to-bone interface. The design of the interconnection between mechanically dissimilar materials can be established more easily now that MEW technology is converged with the bioprinting process in a single biofabrication system.

Taken together, by using native tissue as an inspiration for the design of the structural elements of the chondral unit and the interface between cartilage and bone, mechanically reinforced implants that withstand the challenging *in vivo* environment could be achieved. A secure connection between the cartilage-to-bone interface was combined with a

reinforced cartilage compartment that showed a compressive modulus of 600 kPa and a complex shear modulus of 90 kPa. However, the compressive properties are not equal to native tissue and further mimicking of the structural type II collagen architecture may aid to provide even further improvement of the mechanical stability.

Role of converging (bio)fabrication technologies to further mimic osteochondral tissue architecture

Articular cartilage is a highly organised tissue with over 200 different proteins³⁶, and the multi-scale organization of these components facilitates its load-bearing function. The relation between the form and function of native tissue is well accepted.⁸⁰ Thus, to generate functional osteochondral implants, it is vital to mimic its native tissue architecture. To aid in generating grafts that show mature tissue mimicry, high resolution, multi-scale and multi-material fabrication is required. Although current singular (bio)fabrication technologies are not yet able to generate the high-resolution, multi-scale architecture of native (osteo)chondral tissue, these technologies are maturing towards creating clinically relevant tissue grafts.⁸⁰

Here, fabrication of multi-scale osteochondral implants was achieved by convergence of (bio)fabrication technologies. This thesis shows the first-time convergence of MEW and extrusion-based bioprinting within a single bioprinting platform (**Chapter 5**). By doing so, control over fibre reinforcing design, as well as zonal distribution of multiple cell-types, densities, and matrix components has been achieved. Although other studies have converged FDM printing with hydrogel printing⁸², or electrohydrodynamic printing with FDM printing²⁰⁰, the exhibited level of hierarchy in the fibrous and non-fibrous component has not been shown before. One of the limitations of this converged approach is, however, the long manufacturing time that can negatively affect cell behaviour. This challenge might be overcome by decreasing fabrication time by use of multiple printing heads³⁶⁸, different needle head designs that enable simultaneous multi-fibre deposition^{108,369–371}, or by implementing systems that locally stimulate a higher humidity to ensure a water-rich environment for the cells.

To fully mimic native AC tissue, a higher spatial resolution of the non-fibrous components is needed. While extrusion-based bioprinting with cell-laden hydrogels generally results in fibre diameters of around 200-300 μm , extrusion-based 3D-printing with shrinkable hydrogels can eventually yield in channels of 180 μm in diameter after shrinking twice in size.³⁷² Although promising, this system is not yet tested with cells and can only be used along with a cell-seeding strategy. Alternatively, volumetric bioprinting shows high potential, as the resolution achieved outperforms the resolution and design freedom of regular extrusion-based hydrogel depositing technologies.³⁷³ Yet, multi-material printing

and convergence of volumetric printing and reinforcing strategies have not yet been employed. As a high-resolution fibre deposition technology, MEW has also been used to process hydrogel scaffolds. However, besides being a time consuming process to eventually deposit cells, stacking of these hydrogel fibres and thereby building higher 3D structures, remains a challenge.³⁷⁴ Other ways to achieve higher spatial resolution in tissue mimicry is by smart needle design, *e.g.* micro-fluidic-inspired needle designs to mix hydrogels and deposit a gradient of cells or matrix components within the same hydrogel strand.³⁷⁵ Examples of advanced use of smart cartridge¹⁵⁰ or needle design include multi-material extrusion²⁶⁰, and using a multi-material multi-nozzle 3D printing system, which resulted in printing of voxels with a diameter that resembles the diameter of the nozzle thus eliminating the Barus-effect that is in part responsible for the increased diameter of hydrogel fibres.³⁷⁶ Alternative approaches to achieve hierarchy in 3D scaffolds that do not involve increasing the actual resolution of the deposited hydrogel filaments exist such as the use of pre-functionalized materials that stimulate specific cell behaviour^{307,377,378} or the use of combined external stimuli, *e.g.* the magnetic field, temperature and light, which resulted in cell alignment in an initially anisotropic cell-laden hydrogel.³⁷⁹ Based on the potential of all these individual technologies, it is even more evident that convergence of technologies holds promise for the future of tissue mimicry.

As demonstrated in **Chapter 4**, convergence of technologies is challenging as the optimal printing environment might differ between technologies. It is envisioned that artificial intelligence (AI) will be of particular value for further integration of different fabrication technologies for tissue mimicry. For example, by facilitating decision-making and optimal design both the efficient use of machine and (cell-laden) bioinks will be improved and progress in tissue mimicry will be accelerated. Furthermore, upon development of sensors (*e.g.* optical²³⁷, pH, temperature, humidity) as well as in software tools that make predictions based on analysis of large data sets, AI might aid in real-time monitoring and subsequent controlling of high-throughput biofabrication processes.^{238,239} Real-time monitoring and controlling of high-resolution fabrication can lead to less print-failure and make the overall process more efficient. This advanced approach requires expensive multi-disciplinary knowledge which can be stimulated by overarching grants and the increased commercialisation of biofabrication technologies. Commercialisation increases the availability of affordable bioprinting solutions that in turn stimulates development in bioprinting and biomaterial research. This increase in development and lower costs of biofabrication technologies will also accelerate clinical translation of 3D bioprinting technologies in the upcoming years. This consequently aids in achieving the envisioned solution of using biofabrication technologies to generate an osteochondral implant with an architecture that is inspired by native tissue as a therapeutic treatment for cartilage defects.

Translation of diarthrodial joint resurfacing

In view of the ultimate translation of the biofabricated osteochondral plug towards a potential patient-specific therapeutic solution for AC defects, translational challenges and long-term *in vivo* implant evaluation were addressed in this thesis, and implants that display the anatomical features of the joint were generated. First, the effects of frequently used (bio)materials and anatomically relevant geometries on the accuracy of MEW fibre deposition were evaluated (**Chapter 6**). The main finding was that it is feasible to accurately deposit MEW fibres on electrically conductive materials (e.g. hydrogels) and on less conductive materials (e.g. bioceramics and thermoplasts) if a constant electrical field strength was considered and the electrical force was directed perpendicular, normal, to the collecting material. Having explored and optimized the MEW process over a range of anatomically relevant collector materials, another existing challenge lies in the generation of a printhead trajectory to resurface non-planar collecting geometries. As MEW is typically used to fabricate 3D fibre meshes on uniform flat or rotating³⁸⁰ collector plates there is a lack of software tools to generate more complex MEW printhead trajectories. None exists that actually allows a continuous printhead trajectory that follows a predetermined curvature that is based on an .STL file. To facilitate user-friendly g-code generation for the resurfacing of anatomically relevant geometries based on a computed tomography (CT) scan, a program that semi-automatically generates g-code to resurface the geometry of an standard tessellation language (.STL) file was developed (**Chapter 9**). The impact of such a program for research involving MEW onto non-planar structures lies in the quicker, automatized way in which patient-specific resurfacing trajectories can be determined. The studies in this thesis focussed on effective resurfacing of convex geometries and further research regarding the resurfacing of concave shapes is still required. Following the findings regarding the resurfacing of convex geometries described in this thesis, it seems reasonable to also assume that maintaining a constant distance between the spinneret and the surface of the implant, *i.e.* by following the implant-specific curvature while assuring a perpendicular (normal) direction of the printhead to the surface of the implant, will also result in control over fibre deposition of concave geometries. It is envisioned that a combination of automatic g-code generation and the addition of an extra rotational axis in either the spinneret or the collector plate¹²³, will aid in achieving accurate MEW fibre deposition on concave and convex geometries.

To translate biofabricated osteochondral implants towards a therapeutic solution for the treatment osteochondral (OC) defects, orthotopic long-term *in vivo* evaluation in a relevant animal model is crucial. **Chapter 8** describes the results of the *in vivo* evaluation of biofabricated osteochondral plugs that were orthotopically implanted for 6 months in an equine OC defect model. The equine model has been shown to be a relevant, yet challenging, model for orthotopic *in vivo* studies^{27,177,178} and equine (pony) joints are

roughly similar in size and have similar cartilage thickness and biochemical composition compared to the human knee joint.²⁷ Furthermore, (degenerative) joint disease is as prevalent in horses as it is in humans, thus signifying a comparable unmet clinical need.³³²

Although a number *in vivo* studies with biofabricated implants have been performed for cartilage repair, these were mainly focussed on the biocompatibility of the materials used by subcutaneous or ectopic implantation.^{324–327,375} Orthotopically implanted hydrogels generally failed in the mechanically challenging joint environment.^{336,381} The study presented in this thesis (**Chapter 8**) was the first to show that a fully biofabricated osteochondral implant can survive the mechanically challenging environment in the joint. The structural integrity of the implants, achieved by introducing hierarchy in fibre-orientation, was of pivotal importance for survival of these implants and the use of pre-cultured cells seemed less important. This is in line with recent research that calls for the use of biofabrication technologies to include the structural components and achieve mechanically stable osteochondral grafts.¹⁰⁰ A further, more fundamental understanding in the formation and maturation of the structural fibrous components (e.g. the type II collagen network) is needed. Advanced biofabrication technologies potentially aids in stimulating the development of the eventual mechanical tissue structure, while providing a degradable framework that provides this structure during such development.

Whether or not to use cells and if so, which type (e.g. chondrocytes, chondrons, MSCs, ACPCs), which origin (e.g. allogeneic or autologous) and whether or not to preculture them, remains topic of debate. A good example of efficient cell-therapy for the treatment of chondral defects is the coculture of chondrons and MSCs.²⁹⁶ By combining autologous MSCs with chondrons, less chondrons are needed to still achieve cell-cell communication. This cell combination is implanted with fast degrading fibrin glue and without a pre-cultured matrix to begin with. Alternatively, ACPCs also seemed a promising alternative cell source as they have an unlimited proliferative capacity and are not prone to go into a hypertrophic phenotype and the subsequent osteogenic lineage as seen in MSCs.^{34,167} In this thesis, allogenic ACPCs were used, and although literature suggests that use of allogenic ACPCs should be reconsidered as adverse effects were shown after 12 months of implantation in the equine model³⁸², the studies presented here did not elicit any adverse immune reaction to these allogenic ACPCs.

One of the most interesting findings from the *in vivo* study in this thesis is that the cell-free plugs eventually performed similar in neocartilage tissue formation and mechanical properties as compared to the pre-cultured cell-laden plugs. Thus, osteochondral defects may well be treated with mechanically stable, cell-free implants that exhibit a patient-specific shape. Cell-free approaches to repair osteochondral defects have been used

before by implantation of synthetic scaffolds.^{48,75,383} Furthermore, bottom up approaches for the repair of chondral defects that use cells combined with fast degrading fibrin glue suggest that the initial cell organization might not be needed to achieve repair tissue that eliminates clinical symptoms.^{384,385} As it is shown that the structural stability is imperative, biofabrication technology may well aid in the fabrication of patient-specific mechanical stable implants that allow for ample neo-cartilage formation. The patient-specific fit is important to prevent infiltration of synovial fluid to the bone, where this potentially leads to osteolysis and subsequent implant failure.^{347,348} Previously, successful cartilage tissue regeneration in the rabbit shoulder has been established by use of a cell-free, human transforming growth factor- β 3 (TGF- β 3)-laden, patient-specific implant.³⁸⁶ Although promising, the difference in the regenerative capacity of articular cartilage between rabbits and human has to be considered.^{387,388}

The ability to treat osteochondral defects with patient-specific implants eliminates the use of expensive pre-culture systems and complicated translation of cell-based strategies for the regeneration of smaller, yet critical-sized osteochondral defects. Even though the defects (diameter = 6 mm) that were used in the equine model were considered critical size defects³⁸⁹, for smaller osteochondral defects the presence of a mechanically stable structure that limits leakage of cells and matrix-components, might be sufficient to regenerate such defects. Still, whether these mechanically stable structures actually limit matrix component leakage or not, is yet to be studied. The origin of the infiltrated cells, as well as the long-term effect of cartilage matrix formed by these infiltrated cells is unknown. However, if long-term effects are promising, and the nature of these infiltrating cells is known, it would be valuable to study to which extent, *e.g.* defect size, this cell-free approach would work. The clinical impact of such an off-the-shelf therapeutic strategy would be tremendous, even if it would only hold true for smaller sized defects. Due to the high volume of large implants, it is still envisioned that including cells will aid in the production and maturation of large quantities of neo-cartilage matrix for larger defect treatment.

Irrespective of cell-source and nature, the question remains whether newly produced cartilage-like matrix can eventually be organized in such way that it takes over the structural function of the biodegradable reinforcing framework, which is even more important for large implants. The implants of the *in vivo* study performed in this thesis did not show the distinct collagen alignment after 6 months of implantation. It might be that remodelling of an already precultured matrix is actually limiting tissue maturation as compared to non-precultured implants where matrix can directly be deposited at the required location. Next to the aforementioned envisioned strategies to increase the resolution of biofabrication technologies, dynamic culture systems^{319,355,390} that induce biomechanical

stimulation might aid to increase the level of maturation of larger pre-cultured implants. Upon combining this level of maturation with the mechanically stable implants, *in vivo* remodelling of the already pre-cultured matrix might be reduced or eliminated. To better understand the role of maturation and *in vivo* remodelling of deposited matrix components, a mechanically stable, statically precultured implant should be compared to a dynamically precultured implant that already shows the matured cartilage structure, as well as to a cell-free control.

The bone component of the osteochondral implants functioned as an anchor for the chondral region of the implant.³³⁶ Where the initially used pCaP allowed for a secure interconnection between the cartilage-to-bone interface via incorporation of MEW fibres in both the bone and cartilage phase, and the osteoinductive properties of this material were demonstrated *in vivo*³³⁵, the brittleness of pCaP posed a challenge during implantation. Partial failure of the brittle pCaP material upon implantation potentially leads to an imperfect fit and (micro-) movement along bone tissue, which subsequently results in osteolysis.³⁴⁷ Therefore, a more resilient bone-like material was used for later studies in this thesis. Medical grade PCL was combined with magnesium phosphate and strontium ions (MgPSr-PCL30), which resulted in an extrusion-based 3D printable bone material that posed less of a challenge during implantation, yielded an elastic modulus of around 40 MPa, and promoted *in vivo* bone regeneration in the non-load bearing tuber coxae model.³⁴¹ Although **Chapter 9** suggest that there is a good interconnection between extrusion based 3D printed MgP-PCL and MEW PCL fibres, the strength of the cartilage-to-bone interface needs to be quantified, using similar approaches as described for the evaluation of the pCaP material (**Chapter 4**).

Implantation of a biodegradable material that has a structural function at a load bearing location is challenging and the relation between degradation and stress distribution needs to be thoroughly studied. **Chapter 9** elucidates the difference in stress distribution for differently sized bone implants. Data from this chapter could be used in future research to develop a computational model that has significant potential to provide further insight into the optimal internal design of implants to achieve sufficient strength and neo-bone tissue ingrowth. Additionally, upon including the effect of the cartilage part on the stress distribution for large, patient-specific implants, optimization of the integration strategies between the cartilage-to-bone interface (**Chapter 4**) can be achieved.

Taken together, there is potential to use highly organized osteochondral plugs for the treatment of AC defects. Clinical translation of biofabricated implants for osteochondral defects still faces challenges, including compliance to Good Manufacturing Practice protocols and the use of clinically approved materials.³⁹¹ Nonetheless, the mechanical

stability of a biofabricated osteochondral plug with hierarchy in cell-deposition and fibre-orientation does show promise for clinical translation.

This thesis focussed on fabricating osteochondral implants for (osteo)chondral defects in the knee joint. Although the biomechanical properties of AC are joint-dependent and related to loading patterns, *e.g.* human articular hip cartilage is stiffer, less thick, and less permeable as compared to human knee cartilage, the methods used in this thesis are possibly translatable to other diarthrodial joint structures as well.³⁹²

Impact of highly organized osteochondral structures beyond diarthrodial joint resurfacing

The potential use of biofabrication technologies to generate highly organized osteochondral structures does extend beyond the use as an implant to treat OC defects and may also be of benefit for the fabrication of preclinical models. Promising results from *in vitro* studies do not always directly translate to positive results in *in vivo* studies. In turn, positive *in vivo* results are not directly translatable to human therapeutic strategies, in part because of species-to-species differences.³⁹³ Advanced *in vitro* models and organ-on-chip technologies might provide a way to bridge the gap between *in vitro* studies and clinical translation.³⁹⁴ Organ-on-chip platforms are microfluidics-based multichannel devices used to mimic the native microenvironment of a specific tissue. As the platforms are relatively small in size, they offer great potential for high-throughput and patient-specific testing. By integrating multisensory systems to such platforms, continuous monitoring of biomarkers and cellular response can be achieved.³⁹⁵ Once the tissue specific microenvironment is established in an organ-on-chip model, different chips can be combined to mimic the complete system that is involved in specific pathologies. For example, a joint-on-a-chip model would combine an osteochondral unit-on-chip with a synovial membrane-on-chip, Hoffa's fat pad-on-chip, ligament-on-chip, meniscus-on-chip, and a tendon-on-chip to recapitulate the complex joint environment where the healthy situation could be studied and compared with pathological situations such as osteoarthritis (OA).³⁹⁴ A few examples of osteochondral unit-on-chip-systems have been shown, yet these systems lack mechanical stimulation, are not connected to other relevant tissues in the joint and may therefore not be feasible as a model to bridge between *in vitro* and *in vivo* studies.³⁹⁶⁻³⁹⁸

Especially to recapitulate the mechanical stress distribution, multi-scale biofabrication of anatomically relevant geometries might aid to improve the joint-on-chip development and therewith allow for high-throughput and patient-specific testing. Additionally, fundamental research questions related to healthy AC tissue maturation, ideal cell source,

or patient-specific biomaterial degradation may, albeit in part, be answered by these sophisticated organ-on-chip platforms.

Conclusion

The main aim of this thesis was to fabricate a functional osteochondral implant (**Figure 1**), inspired by native tissue architecture, through the combination of 3D (bio) fabrication technologies. By improving the mechanical properties of hydrogel constructs with smart fibre design fabricated with melt electrowriting (MEW), and converging MEW into the extrusion-based bioprinting process, mechanically stable osteochondral implants with hierarchy in fibre orientation and cell distribution were successfully developed.

The *in vivo* evaluation of these implants in a relevant animal model supported the idea that the structural elements are critical for the success of these implants and additionally suggest that cells might not be required for the regeneration of smaller osteochondral defects. Together with the translation from a relatively small osteochondral cylindrical implant to a completely resurfaced, patient-specific, clinically relevant-sized implant, the potential to use advanced biofabrication technologies for implant fabrication for surgical treatment of osteochondral defects was shown.

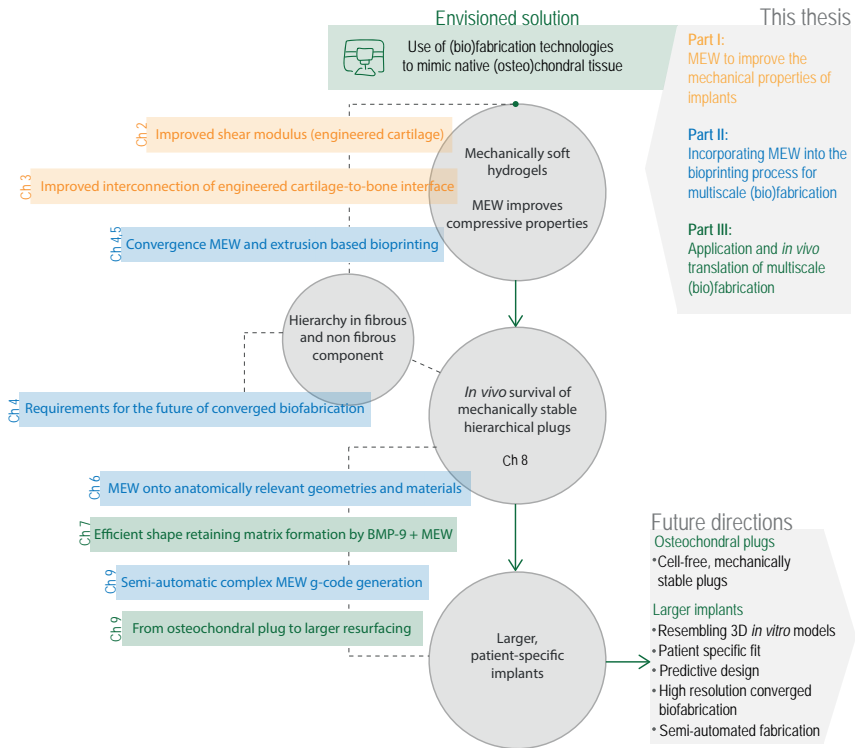
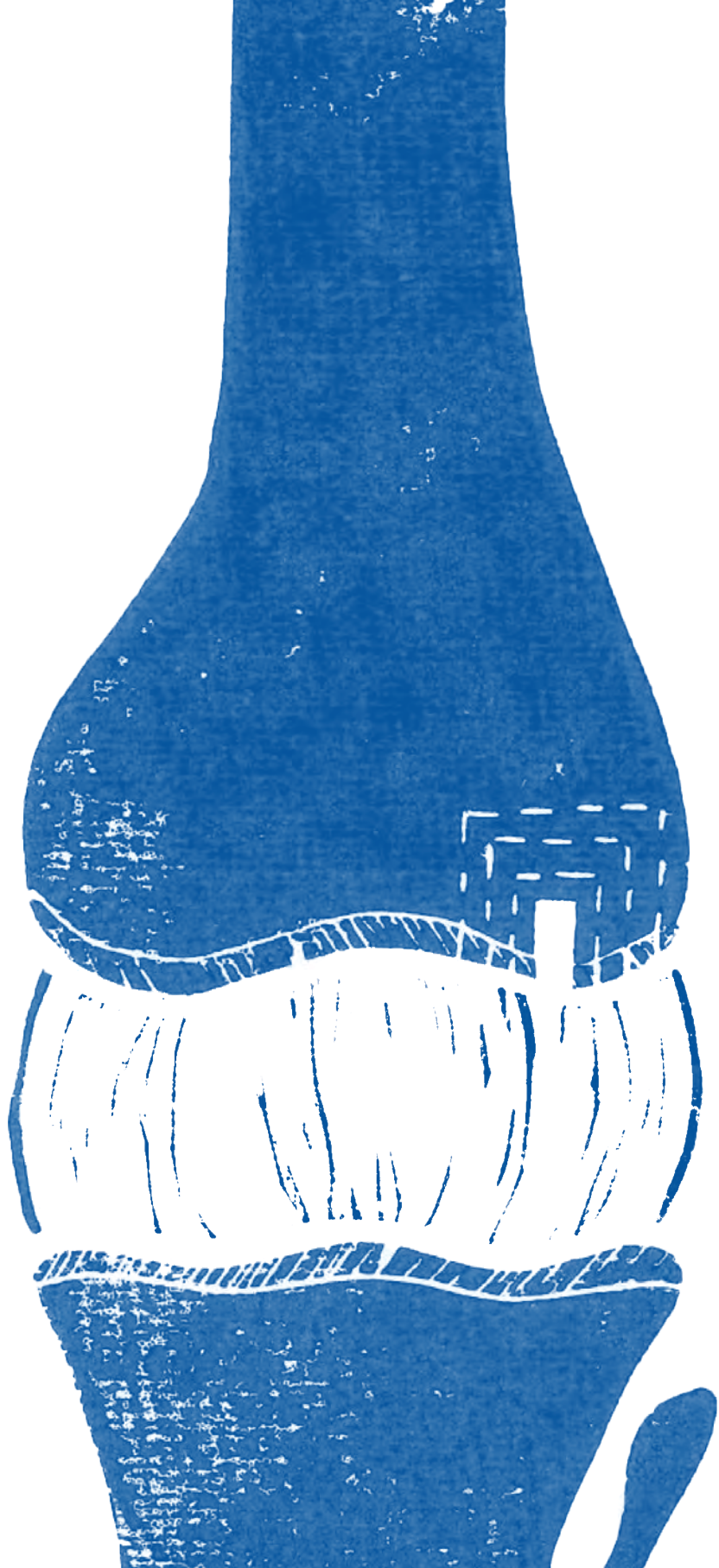


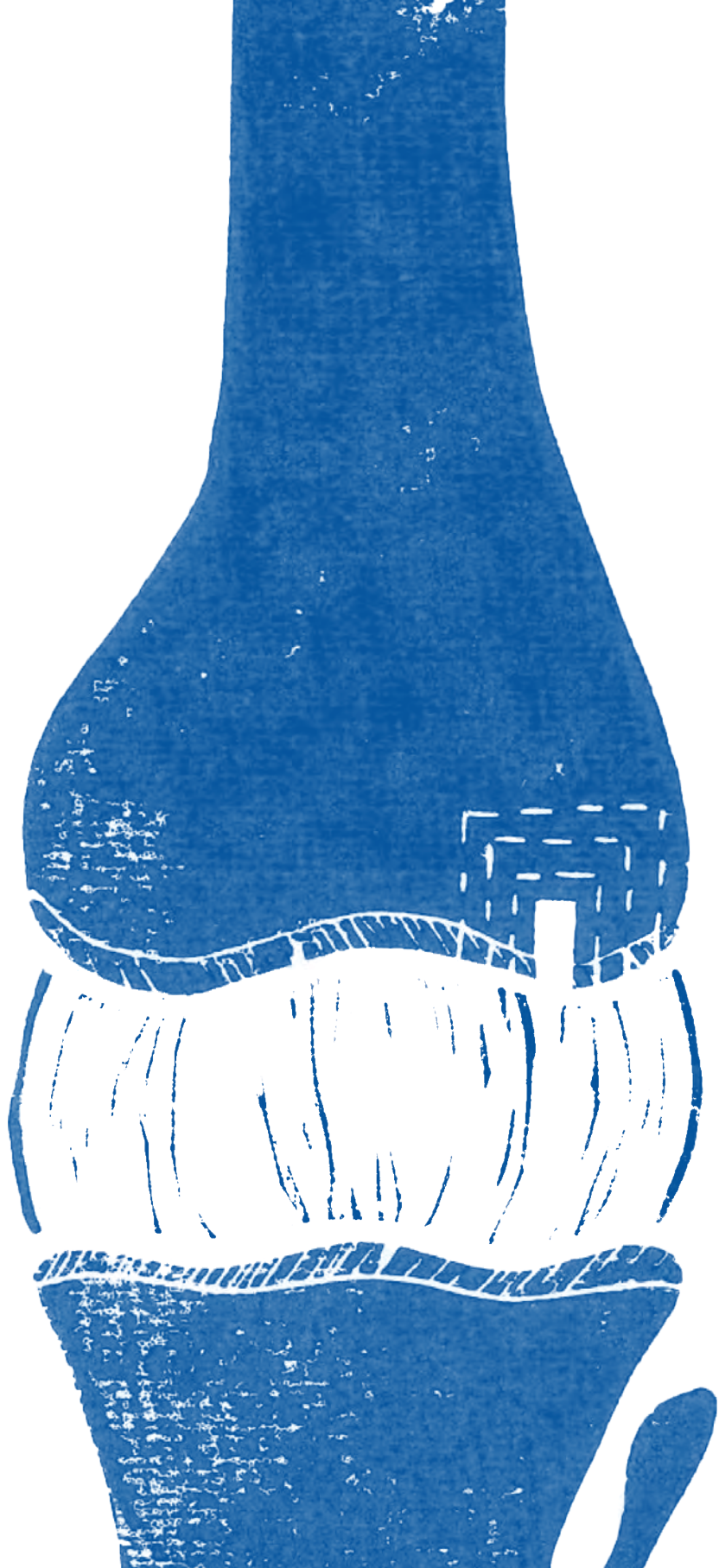
Figure 1. Flowchart of the steps taken from mechanically soft hydrogels to larger resurfacing of a patient-specific implant, and future directions to take. MEW = melt electrowriting. Ch = chapter.



Annex



A



Annex 1

Melt electrowriting of a mechanically stable 3D meniscus scaffold and co-culture of meniscus- and mesenchymal stromal cells.

Jasmijn V. Korpershoek¹

Mylène de Ruijter¹

Bastiaan F. Terhaard¹

Michella H. Hagmeijer¹

Miguel Castilho^{1,2}

Jos Malda^{1,3}

Lucienne A. Vonk^{1,#}

Manuscript in preparation

¹ Department of Orthopaedics, Regenerative Medicine Utrecht, UMC Utrecht, University of Utrecht, The Netherlands.

² Department of Biomedical Engineering, Eindhoven University of Technology, The Netherlands

³ Department of Clinical Sciences, Faculty of Veterinary Medicine, Utrecht University, The Netherlands.

[#]Current address: CO.DON AG, Warthestraße 21, D-14513 Teltow, Germany

A

Introduction

The human meniscus is a fibrocartilaginous tissue in the knee joint that can be divided in an inner zone composed of cartilage-like tissue, and an outer zone with a more fibrous phenotype^{399,400}. It plays a crucial role in load transmission in the knee due to an organized network of radial and circumferential collagen fibres^{399,401,402}. Meniscus injury affects young and active patients, as well as the elderly and is highly disabling. Successful surgical repair of meniscal tears is limited to the outer, vascularized region in young patients, as compared to the minimally regenerative inner zone and to older patients^{403,404}. Treatment, therefore, often involves meniscectomy, removal of the damaged part of the meniscus. Meniscectomy relieves symptoms in the short term, but is related to a high risk of osteoarthritis in the long term due to the loss of contact area and altered load bearing^{405–407}. Current strategies for replacement of the meniscus have important drawbacks. Transplantation of meniscus allografts is costly and conclusive evidence on long-term effectiveness is lacking^{408,409}. The Collagen Meniscus Implant (CMI®; Stryker, Kalamazoo, MI), a clinically available implant composed of bovine type 1 collagen, offers short term clinical improvement, but tissue deposition is limited in the long-term⁴¹⁰. Moreover, it does not account for the zonal organization and direction of collagen fibres in the meniscus. The clinical need for a durable meniscus implant is, therefore, unmet. Ideally, such an implant should allow for sufficient dampening and load transfer in order to withstand the challenging *in vivo* conditions. To improve durability and reactivity to the joint environment, it should be biocompatible and exhibit optimal pore size and pore interconnectivity to achieve cell infiltration and tissue ingrowth⁴¹¹. It should not lead to kissing lesions of opposing cartilage surfaces as these might eventually lead to articular cartilage defects and related pathological conditions.

A potential solution to the limited mechanical properties of current implants could lie in mimicking the fibre architecture of meniscus tissue. Recent developments in fibre deposition technologies seem promising for mimicking such complexity at native tissue resolution. For meniscus tissue engineering, materials like alginate, gelatin blends, and silk fibroin have been tested as cell carriers.⁴¹² Some of these materials were bioprinted, and even combined with other additive manufacturing technologies, such as the combination of extrusion-based printing of alginate and exposure to acoustic waves to induce cell-alignment while crosslinking the alginate biomaterial.⁴¹³ However, these biomaterials degrade too quickly *in vivo*, or are not able to fulfil the load transferring function of the meniscus as they collapse under the intense loading conditions in the joint. (Bio) fabrication technologies, such as fused deposition modelling (FDM), can fabricate a polymeric framework that can be combined with biomaterials to mechanically reinforce them.^{414,415} FDM has also been combined with nano-fibre producing technologies, such

as solution electrospinning, however, additional FDM support is still needed to achieve aligned solution electrospun nano-fibres.⁴¹⁶ Limitations of using FDM to generate this framework include limited pore-interconnectivity and mechanical properties that are not sufficient for load transfer and mechanotransduction. Additionally, the polymeric fibres resulting from FDM potentially lead to kissing lesions on the femoral and tibial articulating cartilage surfaces. Nano- to microfibre deposition technologies, such as random fibre deposition with solution electrospinning and controlled and aligned fibre deposition with melt electrowriting (MEW), have been used to reinforce hydrogels in biofabrication of other joint-related tissue equivalents.^{84,199} Controlled deposited microfibres made with MEW allow for sufficient pore interconnectivity, have a less rough/stiff surface as compared to FDM polymeric fibres, and are able to achieve tissue equivalents that more closely resemble the fibrous architecture of native tissue.

Pre-seeding a construct with cells can stimulate tissue formation and reactivity to the joint environment, and thereby enhance the long-term performance of a meniscus scaffold. In order to facilitate clinical translation of a pre-seeded construct, the number of autologous cells should not exceed the number that can be harvested during a single surgical procedure. A sufficient number of cells/stimuli for tissue formation can be achieved by combining recycled autologous meniscus cells obtained from the damaged and meniscectomized area with allogeneic MSCs. Increased cartilage formation using these cell combinations was already shown in a human clinical trial for cartilage defects⁴¹⁷, and *in vitro* for meniscus⁴¹⁸.

In this study, we show proof-of-concept of a meniscus construct made from medical-grade materials with MEW pre-seeded with a clinically feasible cell-source and number for one-stage treatment of meniscal injury. Our construct is inspired by nature where the radial and circumferential fibres establish the base for the mechanical properties. We hypothesize that these biofabricated constructs are mechanically superior, and biologically non-inferior to the clinically used CMI®. This study highlights the potential of translating biofabrication to the clinic.

Materials and Methods

Scaffold design and printability

Scaffold design was based on native meniscus fibre architecture. MEW was used to deposit micro-meter scale fibres in a circumferential (**Figure 1A**) and radial (**Figure 1B**) manner. These two layer types were deposited with a programmed inter fibre spacing of 225 µm or 160 µm (**Figure 1C**). The ratio of circumferential : radial fibres was 14:2 or

12:4 (**Figure 1C,D**). To allow for high throughput testing, the meniscus scaffolds were scaled down a factor 4 to fit into 24 well culture plates. Melt electrowriting was performed with polycaprolactone (PCL, PURASORB, Corbion, The Netherlands) at 90 °C, a collector distance of 5 mm, collector velocity of 10 mm/s, voltage of 10 kV, at a pressure of 0.118 MPa (3D Discovery, regenHU, Switzerland). Printability was assessed by measuring the fibre diameter and inter fibre spacing along the circumferential and radial lengths of the prints. These measurements were performed on images taken with scanning electron microscope (SEM, Phenom Pro Desktop SEM, Thermo Fischer Scientific, USA) by using Fiji software (ImageJ, version 2.0.0-rc-54/1.51h). SEM was performed with an accelerating voltage of 10 kV to image the MEW fibres. Prior to imaging, samples were coated with 2 nm of gold to improve imaging quality. Homogeneity of the fibre diameter was assessed by the standard deviation and the measured inter fibre spacing was compared to the programmed inter fibre spacing. To assess printability of the ratio of circumferential : radial fibres, SEM imaging was used with the same parameters as for the fibre measurements. Prior to *in vitro* culture, scaffolds were treated with 1M NaOH in H₂O to increase hydrophilicity and improve immersion of the scaffolds with fibrin glue.

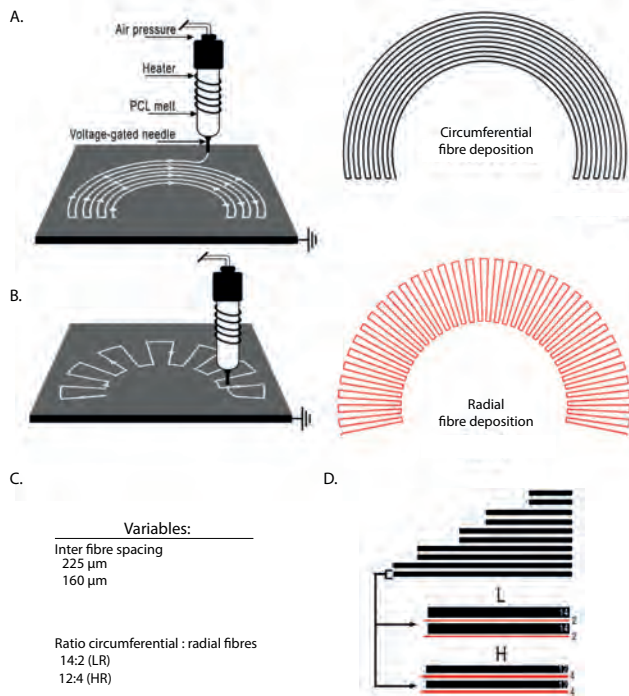


Figure 1. Scaffold design inspired by native fibre architecture. A) Printhead trajectory of MEW circumferential fibres. B) Printhead trajectory of MEW radial fibres. C) Variables in design include variety in inter fibre spacing and in the ratio between the circumferential and radial fibres. D) Illustration of variety in design of the ratio of circumferential and radial fibres.

Cell isolation and culture

Primary human meniscus cells were isolated from osteoarthritic menisci obtained after total knee arthroplasty from 3 donors. The tissue was handled anonymously according to the guidelines of the Federation of Dutch Medical Scientific Societies⁴¹⁹ and as approved by the ethical review board of the University Medical Center Utrecht. Briefly, menisci were cut into 1-2 mm cubical pieces and digested in Dulbecco's modified Eagle's medium (DMEM; Gibco, The Netherlands) with 0.2% pronase (Roche Diagnostics GmbH, Mannheim, Germany), 100 U/ml penicillin (Gibco) and 100 µg/ml streptomycin (Gibco) (1% p/s) at 37°C for 2 hours followed by an overnight digestion in DMEM with 0.075% collagenase type 2 (Worthington Biochemical Corporation, Lakewood, NJ, USA), 1% p/s, and 10% heat-inactivated Fetal Bovine Serum (FBS; Biowest, The Netherlands) at 37°C. The digested tissue was run over a 70µm strainer (Greiner Bio-One International GmbH, Austria) to remove debris, after which meniscus cells were cultured up to passage 2 in DMEM with 1% p/s and 10% FBS. The use of human MSCs was approved by the institutional ethical review board (TCBio 08-001 and 18/739). MSCs were obtained from bone marrow aspirates obtained from 3 donors after written informed consent was obtained. Briefly, bone marrow aspirate was Ficoll separated, and MSCs were expanded up to passage 4-5 in αMEM (minimal essential medium, Gibco) with 10% FBS, 1% 20 mM l-ascorbic acid-2-phosphate (1 % ASAP; Sigma-Aldrich), and 1% p/s.

CMI preparation

Eight CMIs[®] were cut using a negative mold and scalpel in order to obtain 4 times smaller scale model. Prior to seeding the downscaled CMIs[®] with cells, the implants were treated with 1% p/s and 50µg/ml gentamicin in PBS for 7 days and dried overnight.

Cell seeding

Cell seeding efficiency was determined by measuring DNA content on the scaffold and in the medium. DNA was measured with a Picogreen assay (Invitrogen, USA) according to the manufacturer's protocol, with excitation at 485 nm and emission at 535 using a Fluoroskan Ascent device (Thermo Fischer Scientific, USA). In order to seed the implants and scaffolds with cells, MSCs and meniscus cells were mixed in a 20:80 ratio in a 1:15 dilution of fibrinogen (Tisseel, Baxter BV, The Netherlands) in PBS. For seeding, the implants and scaffolds were placed in a seeding mold, after which 30 µl fibrinogen solution containing a total of 1.5×10^5 cells was added. The 30 µl of 1:50 diluted thrombin in PBS was added and the fibrin glue was allowed to gelate for 20 minutes at 37°C. The seeded scaffolds and implants were cultured at 37°C/5% CO₂ for 4 weeks in suspension plates (Greiner Bio-One International GmbH, Austria) in DMEM with 1% p/s, 2% human serum albumin (HSA; Sanquin Blood Supply Foundation, the Netherlands), 2% insulin-transferrin-

selenium-ethanolamine (ITS-X; Gibco, USA), and 1% L-ascorbic acid 2-phosphate (ASAP, Sigma Aldrich), with medium changes twice a week.

Mechanical testing

Compressive properties were assessed on a Q800 Dynamical Mechanical Analyser (DMA, T.A. Instruments, USA) using confined compression of the implants and scaffolds with an aluminium custom-made loading head in the negative shape of the constructs (**Figure 3**). A preload of 0.001N was applied after which the constructs were compressed until 30% of the original height at a 20% strain per minute rate. The compressive modulus was calculated from the slope of the linear part of the stress-strain curves at 10% - 15% strain.

Biochemical assays

After 4 weeks of culture, implants and scaffolds were digested at 60°C overnight in papain solution (50 µg/mL papain; Sigma-Aldrich, 0.2 M NaH₂PO₄, 0.1M EDTA, 0.01M cysteine, pH 6). Proteoglycan content was assessed using a Dimethylmethylene Blue (DMMB; pH 3) assay to quantify sulfated glycosaminoglycans. Absorbance was measured at 525 and 596 nm and chondroitin-6-sulfate (Sigma-Aldrich) was used as a standard. DNA content was quantified using the Quant-iT PicoGreen kit (Invitrogen) according to the manufacturer's protocol, with excitation at 485 nm and emission at 535 using a Fluoroskan Ascent device (Thermo Fischer Scientific).

Statistics

Data were analysed using IBM SPSS (version 15.0.0.2, Chicago, Illinois)/ Prism GraphPad (version 8.3, San Diego, California). Fibre diameter and inter fibre spacing were measured for 5 different samples. Differences were considered significant if $p < 0.05$, unpaired t-test (fibre diameter and inter fibre spacing), or ANOVA, post hoc Bonferroni (compressive modulus cell-free scaffolds ($n = 3$) and cell seeding efficiency ($n = 3$)). Data from the cell-laden compressive modulus and biochemical assays after 28 days of culture has not been tested on significant differences due to a lack of samples at this point ($n = 2$ instead of $n = 3$, work in progress).

Results and Discussion

Melt electrowriting (MEW) of radial and circumferential fibres (**Figure 1**), inspired by native fibre architecture, was successfully achieved. A clear distinction between the radial and circumferential fibres could be observed upon alternating these layers for both 225 µm and 160 µm fibre spacings (**Figure 2A**). Translating the MEW printing head in radial or circumferential trajectory resulted in an average fibre diameter of $15.91 \mu\text{m} \pm$

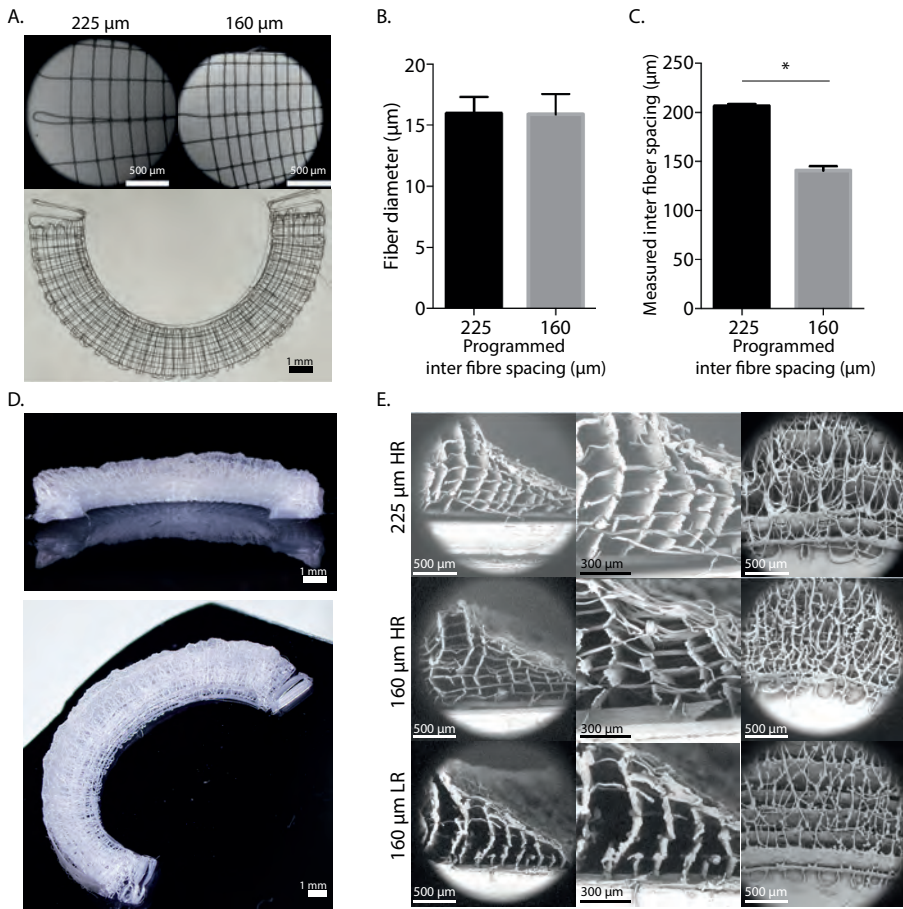


Figure 2. Printability of radial and circumferential MEW fibres to achieve a wedge-shaped meniscus. A) Top view of a single layer of radial and circumferential fibres. B) Fibre diameter of fibres for both inter fibre spacings. C) Measured inter fibre spacing for both programmed inter fibre spacings. D) Macroscopic image of a printed scaffold. E) SEM images of scaffolds with both inter fibre spacings and the different ratios of circumferential and radial fibres. * = $p < 0.05$, t-test.

1.55 μm and 15.75 $\mu\text{m} \pm 1.58 \mu\text{m}$, for the 225 μm and 160 μm programmed inter fibre spacing, respectively (**Figure 2B**). Additionally, the measured inter fibre spacing was close to the programmed line spacing (**Figure 2C**). The achieved fibre diameter is in line with previously reported MEW PCL fibre diameters and could potentially be changed by adapting the pressure that is applied to the polymer melt.¹⁵⁵ Previous studies that fabricated meniscus constructs were performed with FDM printing of PCL and resulted in fibre diameters at least 10 times bigger (100 μm – 400 μm), which underscores the potential of MEW as a (bio)fabrication technology to develop meniscus scaffolds. One

of the limitations of the scaffolds produced in this study is that they are scaled down resulting in significantly smaller scaffolds compared to the native meniscus. While this was done to decrease the fabrication-related challenges, as well as to facilitate biological evaluation, previous studies have already shown that scaffolds up to 8 mm in height can be fabricated with MEW.²⁹⁰ However, it has to be tested whether this still allows for a high resolution and accurate deposition of both the circumferential and radial fibres.

The native meniscus wedge-like shape was observed (**Figure 2D,E**). Moreover, fibre stacking was sufficiently accurate to provide porosity in x-, y-, and z-direction (**Figure 2E**).

The custom-made holder for compressive analysis of the wedge-shaped meniscus scaffold (**Figure 3A-C**) allowed mechanical testing of the melt electrowritten meniscus scaffolds and the CMI implants. The compressive modulus of the cell-free MEW-reinforced fibrin scaffolds is higher compared to the cell-free CMI scaffold (**Figure 3D**). No statistical differences were found between the different fibre designs. Although no statistical analysis can be performed at this stage as of a lack of samples, after 28 days of culture, the HR design seems to show a higher compressive modulus as compared to the CMI and LR designs (**Figure 3E**). However, no clear differences seem to be shown between the cell-laden and cell-free constructs.

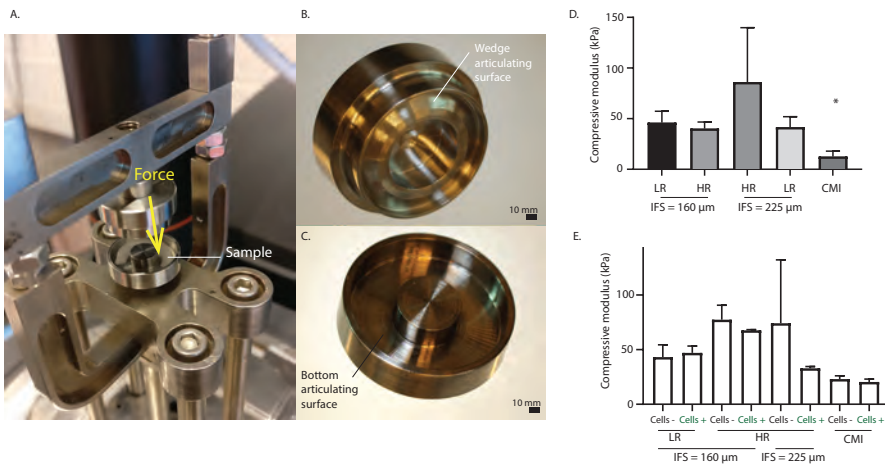


Figure 3. Mechanical characterization of meniscus implants and scaffolds. A) Compressive testing system. B) Custom made scaffold holder for compression of the wedge surface (top) C) Custom made scaffold holder for compression (bottom). D) Compressive modulus of the different implant designs and CMI at day 1, no cells. E) Compressive modulus of the different implant designs and CMI after 28 days of culture. IFS = Inter fibre spacing. * = $p < 0.05$, ANOVA, post hoc Bonferroni.

Cell seeding efficiency was similar for all scaffolds and comparable to cell seeding in typically used fibrin glue without a MEW scaffold (**Figure 4A**). DNA predominantly remained on the scaffolds and the DNA loss in the medium only occurred in the first 4 days (**Supplementary Figure 1**). Although no statistical analysis has been performed because of a lack of samples, this data suggests an increase in GAGs/DNA for all cell-laden scaffolds after 28 days of *in vitro* culture (**Figure 4B**).

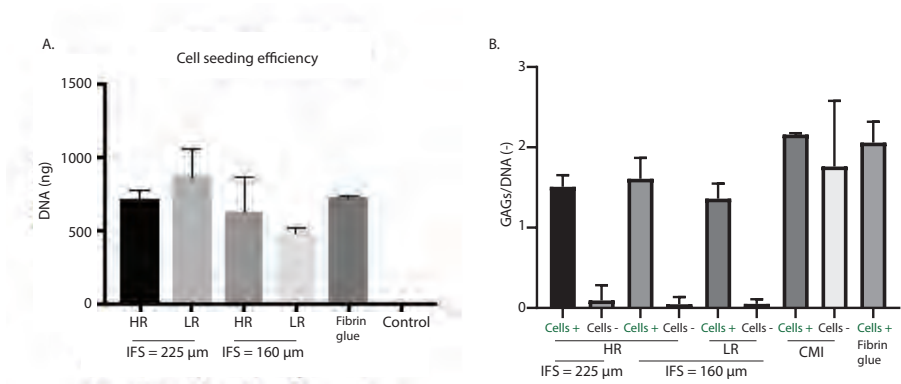
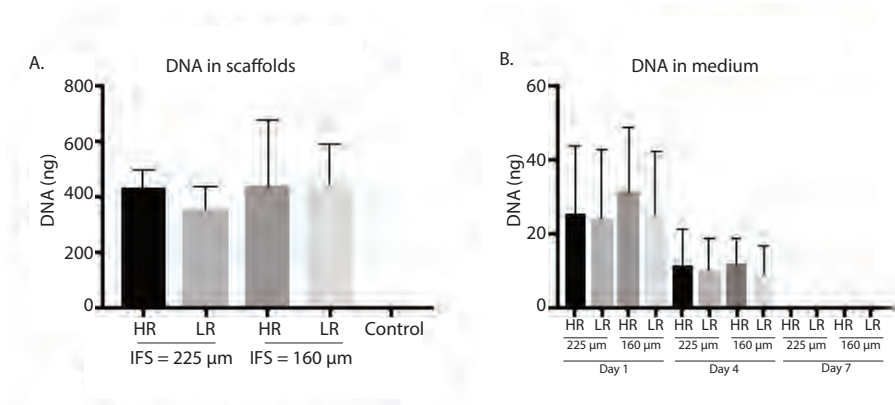


Figure 4. Cell behaviour on MEW scaffolds as compared to CMI and fibrin glue. A) Cell seeding efficiency of co-culture of meniscus cells and MSCs (20 : 80 ratio) on different scaffolds. B) Quantification of GAGs/DNA in different constructs after 28 days of culture. IFS = inter fibre spacing.

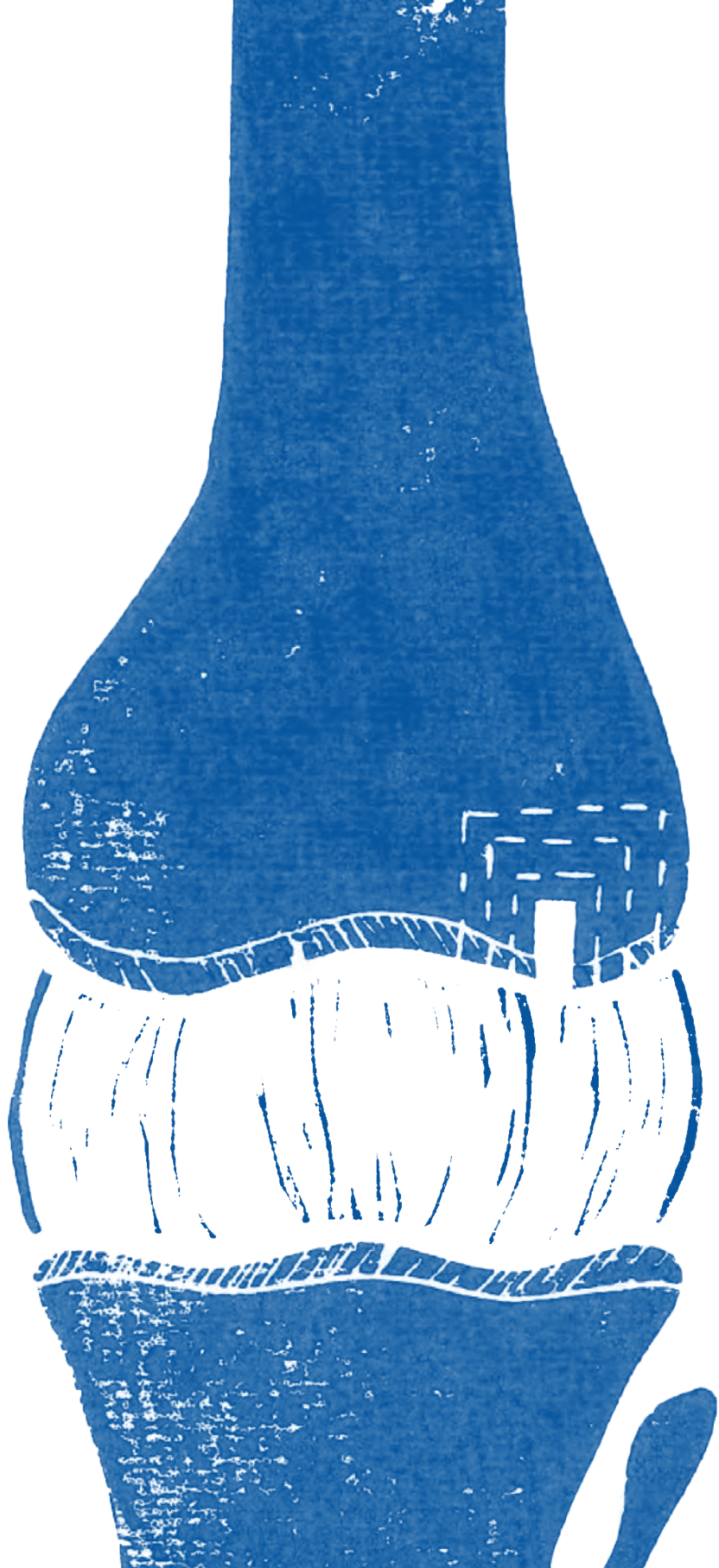
Conclusion

Melt electrowriting can be used to fabricate 3D meniscus scaffolds with a combination of circumferential and radial fibre orientation, similar to what is seen in native tissue. Scaffolds made with MEW, combined with fibrin glue as a cell-carrier, provided a good culture system for a co-culture of meniscus cells and MSCs, with a high cell seeding efficiency. Including MEW fibres seems to reinforce cell-laden fibrin glue constructs and seems to result in a higher compressive modulus as compared to the golden standard CMI implants.

Supplementary data



Supplementary figure 1. Cell seeding efficiency of co-culture of meniscus cells and MSCs (20 : 80 ratio) on different scaffolds. A) DNA in scaffolds B) DNA in medium. IFS = inter fibre spacing



Annex 2

Multi-scale 3D biofabrication enables generation of clinically relevant-sized diarthrodial joint tissue structures

Mylène de Ruijter¹

Nasim Golafshan¹

Paulina Nunez Bernal¹

Paweena Diloksumpan²

Inge Dokter¹

Joost van Duijn¹

Li Lv³

Sushila Maharjan³

Riccardo Levato^{1,2}

Yu Shrike Zhang³

Miguel Castilho^{1,4}

Jos Malda^{1,2}

Manuscript in preparation

¹ Department of Orthopaedics, Regenerative Medicine Utrecht, UMC Utrecht, University of Utrecht, The Netherlands.

² Department of Clinical Sciences, Utrecht University, The Netherlands.

³ Division of Engineering in Medicine, Brigham and Women's Hospital, Department of Medicine, Harvard Medical School, Cambridge, MA 02139, USA

⁴ Department of Biomedical Engineering, Eindhoven University of Technology, The Netherlands

Background

In this thesis, the role of multi-scale biofabrication for osteochondral tissue in the knee joint has been shown. However, the potential of this technology extends beyond osteochondral tissue. Other diarthrodial joint tissue structures can potentially be mimicked by use of multi-scale biofabrication as well. Here, the potential of the use of multi-scale 3D biofabrication for the enthesis (tendon-to-bone interface), as well as towards human-scale perfusable meniscus implant is shown.

Materials and methods

Fabrication entheses

Polycaprolactone (PCL, PURAC, Corbion, The Netherlands) was combined with Magnesium phosphate (MgP) as previously described (**Chapter 9** and Golafshan *et al*, *under review*). The combination of PCL and MgP (MgP-PCL) was extruded through a conical 22G nozzle (Nordson EFD, USA) with an air pressure of 0.06 to 0.22 MPa and translation velocity of 5 mm/s at room temperature in a porous grid structure with 3 extra closed layers at the edge (3D Discovery evolution, regenHU, Switzerland). These closed layers were used to interconnect PCL microfibres that were deposited with melt electrowriting (MEW, voltage = 8 kV, collector distance = 6 mm, collector velocity = 15 mm/s, air pressure = 0,12 MPa, temperature = 90°C (3D Discovery evolution, regenHU, Switzerland)). The PCL microfibres were deposited in a pattern that started with a straight line and ended in eight diverging fibres that were partly deposited onto the closed MgP-PCL layers at the edge. Starting with a layer of MgP-PCL, ten layers of MEW fibres were alternated with one layer of MgP-PCL until a total of 10 layers of MgP-PCL was achieved. Additionally, MEW of PCL microfibres was also performed on a rotating mandrel (diameter = 1 mm) to achieve tubular structures that were eventually meant to combine multiple straight ends of the microfibres that were interconnected into the MgP-PCL layers.

Tenocyte harvest and culture

Equine derived tenocytes were isolated from the patellar tendon of three skeletally mature equine donors. These donors had been donated to science by their owners and procedures were followed according to the guidelines of the Ethical and Animal Welfare body of Utrecht University. Briefly, vessel-free areas from the patellar tendon were sliced into 3 – 4 mm patches and placed into a 6-well plate. Without media, these plates are incubated at 37°C for 1 hour to ensure attachment of the tendon-patches to the plate. Culture medium consisting of Dulbecco's modified eagle medium (31966, Thermo Fisher Scientific, USA), supplemented with 10% fetal bovine serum (Gibco, Thermo Fisher

Scientific, USA), 1% non-essential amino acids (100X, Gibco, Thermo Fisher Scientific, USA), and 1% penicillin/streptomycin (Gibco, Thermo Fisher Scientific, USA) was gently added until the tendon samples were fully submerged. After 5-10 days, cells were migrated out of the tendon biopsies, and transferred to T75 culture flasks for further expansion with the above mentioned medium. Medium was refreshed twice per week.

To assess metabolic activity of tenocytes cultures with different medium types (adipogenic (same as in **Chapter 9**), osteogenic (same as in **Chapter 9**), and chondrogenic medium (same as in **Chapter 9**) with and without 0.1% recombinant human transforming growth factor- β 1 (TGF- β 1) (10 ng/mL, Prepotech, UK) simulation), and different hydrogel concentrations, tenocytes (2×10^6 cells/ml) were embedded in 5%, 10%, and 15% (w/v) gelatin methacryloyl (gelMA) (80% DoF, synthesized as previously described²⁵⁸) and crosslinked with Irgacure 2959 (0.1% (w/v) in phosphate-buffered saline (PBS), BASF, Ludwigshafen, Germany) in UV light (UVP CL-1000 Ultraviolet Crosslinker) for 15 minutes. *In vitro* culture was done up to 28 days and medium was refreshed three times per week. Metabolic activity was measured with an Alamar Blue staining (Resazurin sodium salt, Alfa Aesar), according to manufacturer's protocol with an incubation time of 4 hours. Additionally, tenocytes were characterized using immunohistochemistry with anti-tenomodulin antibody (1: 500 dilution, AB81328, Abcam). First, *in vitro* cultured constructs were formalin-fixed. Pronase (1 mg/mL, Roche, USA) was used for antigen retrieval, and sections were blocked with bovine serum albumin prior to antibody incubation (anti-tenomodulin antibody (1: 500 dilution, AB81328, Abcam)). Samples were washed and confocal microscopy (Leica SP8X, Germany) was used to characterize tenocytes by means of positive staining for tenomodulin and assess tenocyte morphology.

SEM imaging

Scanning electron microscopy (SEM) (Phenom Pro Desktop SEM, Thermo Fischer Scientific, USA) was performed with an accelerating voltage of 10 kV to image the melt electrowritten PCL microfibrils in between the MgP-PCL layers. Prior to imaging, samples were coated with 2 nm of gold to improve imaging quality.

Fabrication of perfusable tubes combined with melt electrowritten microfibre meshes.

To show the first steps in combining PCL melt electrowritten meshes and co-axial printed perfusable channels, a two-step approach was used. First, microfibre PCL meshes with an inter fibre spacing of 400 μ m with a height of 0.5 mm were fabricated with MEW (voltage = 8 kV, collector distance = 6 mm, collector velocity = 15 mm/s, air pressure = 0,12 MPa, temperature = 90°C (3D Discovery evolution, regenHU, Switzerland)). Co-axial printing was performed with the equipment and materials as described by Qingmeng *et al.*⁴²⁰

Briefly, a 7% gelMA- 2% alginate-hydrogel along with 0.25% (w/v) photoinitiator⁴²⁰ as a shell material with a calcium chloride (CaCl₂) core was done on top of these MEW meshes in different patterns using a custom made co-axial system.⁴²⁰ After fabrication, the co-axial tubes were crosslinked with 3% CaCl₂ and 1 minute of UV-crosslinking (wavelength: 360–480 nm, power: 6.9 mW/cm²). The hollow tubes were perfused with fluorescent micro-beads diluted in PBS.

Statistics

Data is presented as mean ± standard deviation. The *in vitro* culture experiments are performed in triplicate. Differences between groups were considered significant if $p < 0.05$, ANOVA, post hoc Bonferroni.

Results and discussion

Enthesis

The enthesis is the tendon-to-bone interface and has a load transferring function and is integrated with the smaller collagen fibres into the bone. The tendon is a densely packed fibrous tissue that consists of multiple collagen fibres (1-20 µm) that are surrounded by primary fibre bundles (15 - 400 µm) which are subsequently surrounded by secondary fibre bundles. These bundles are in turn surrounded by the endotendon, which also contains tenocytes, together forming the tendon (**Figure 1A, B**).^{421,422} Convergence of multi-scale biofabrication technology allows for the fabrication of the architecture of the enthesis. The bone protruding collagen fibres can be fabricated by means of melt electrowriting (MEW) (**Figure 1C**). These fibres can subsequently be intertwined with a 3D printable bone component, such as MgP-PCL used in this thesis (**Figure 1D**). The MEW fibres are well stacked and connect into the bone-reflecting material. By using a rotating mandrel, the primary fibre bundle can be replicated (**Figure 1E**).

The enthesis shows a mineralized gradient between the bone and tendon and tenocytes were extracted and 3D cultured in gelMA hydrogel under different culture conditions (**Figure 2**). Where the tenocytes show a flattened, fibroblastic morphology on cover glass, they became round-shaped once put in 5%, 10%, or 15% gelatin methacryloyl (gelMA) hydrogel, irrespective of the culture medium used (**Figure 2A**). All conditions did show tenomodulin - positive stained cells.

Over the course of 28 days of *in vitro* culture, the tenocytes were metabolic active under all conditions. Tenocytes cultured in the osteogenic medium showed an increased metabolic activity in the 5% 10% and 15% gelMA as compared to the 2D plate culture, as well as to

the tenocytes cultured in chondrogenic medium, with or without TGF- β 1 (**Figure 2B**). Tenocytes cultured in adipogenic medium also showed a higher metabolic activity upon culture in 10% or 15% gelMA as compared to the 2D cultured group and the chondrogenic stimulated tenocytes (**Figure 2B**). What this increase in metabolic activity means for the matrix distribution of the tenocytes is yet to be determined. Additionally, as the enthesis shows a gradient in mineralization, a coculture of tenocytes and mesenchymal stromal cells (MSCs) that are both stimulated by osteogenic medium might help in establishing this gradient.

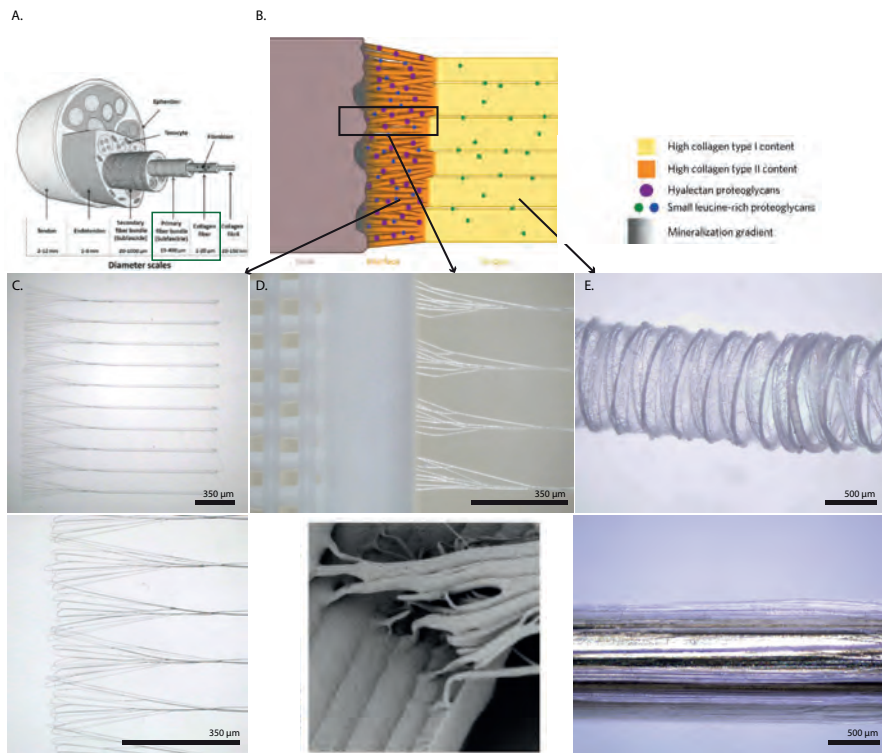


Figure 1. Convergence of (bio)fabrication technologies to fabricate the multi-scale enthesis. A-B) Schematics of the architecture of the tendon-to-bone interface (enthesis) adapted from Beldjilali-Labro M *et al.* and Rossetti *et al.*^{421,422} C) MEW PCL microfibres to represent the collagen fibres. D) Interconnection between the MEW PCL microfibres and the MgP-PCL printed bone representative. E) MEW PCL microfibres, deposited on a rotational mandrel to surround the collagen representing fibres and together represent the primary fibre bundles.

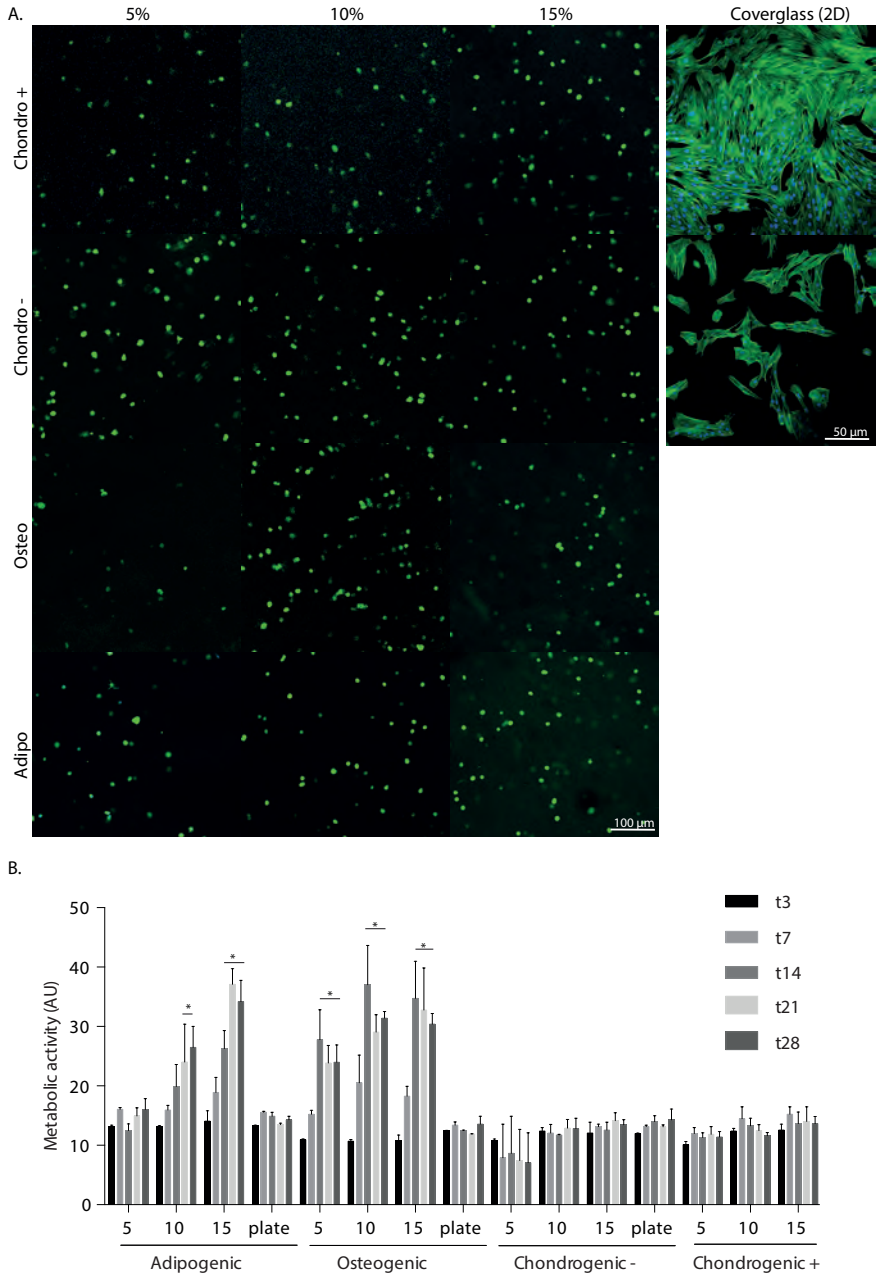


Figure 2. Tenocytes embedded in different % of gelMA and cultured with different media. A) Cell morphology after 14 days of culture. Green indicates positive staining for tenomodulin. B) Metabolic activity over the course of 28 days of culture. "5", "10", and "15" reflect the percentage of 3D gelMA, "plate" reflects 2D cover glass culture. * = Statistically different from 2D culture ($p < 0.05$), ANOVA post hoc Bonferroni.

Human-sized meniscus – perfusion

The human meniscus is a large, partly vascularized, tissue. To tissue engineer a human sized meniscus, perfusion is needed to mimic the architecture and to maintain cell viability throughout the entire tissue. One of the biofabrication techniques that allows the creation of large perfusion is co-axial extrusion-based bioprinting. Co-axial extrusion based bioprinting can combined with MEW to create large tissue sheets. The typical woodpile-structure (**Figure 3A**) could be used to create subunits that can subsequently be perfused around subunits. The MEW mesh could be used to generate large neo-tissue, such as was explored for articular cartilage in Chapter 7, or for adipose tissue tissue.³⁰⁸ The perfusable channels maintain shape upon the MEW meshes (**Figure 3B**), even when they intersect (**Figure 3B2**). The complex vasculature of the red-red zone of the meniscus (**Figure 3C**) was used as inspiration for the simplified printing path that was used for perfusion through engineered meniscus construct (**Figure 3D**). This printing path can be alternated with MEW meshes (**Figure 3E**) to allow perfusion through the different layers of the construct. Further studies with cell-laden MEW meshes would show if this perfusion helps in the *in vitro* culture and engineering of human sized meniscus tissue.

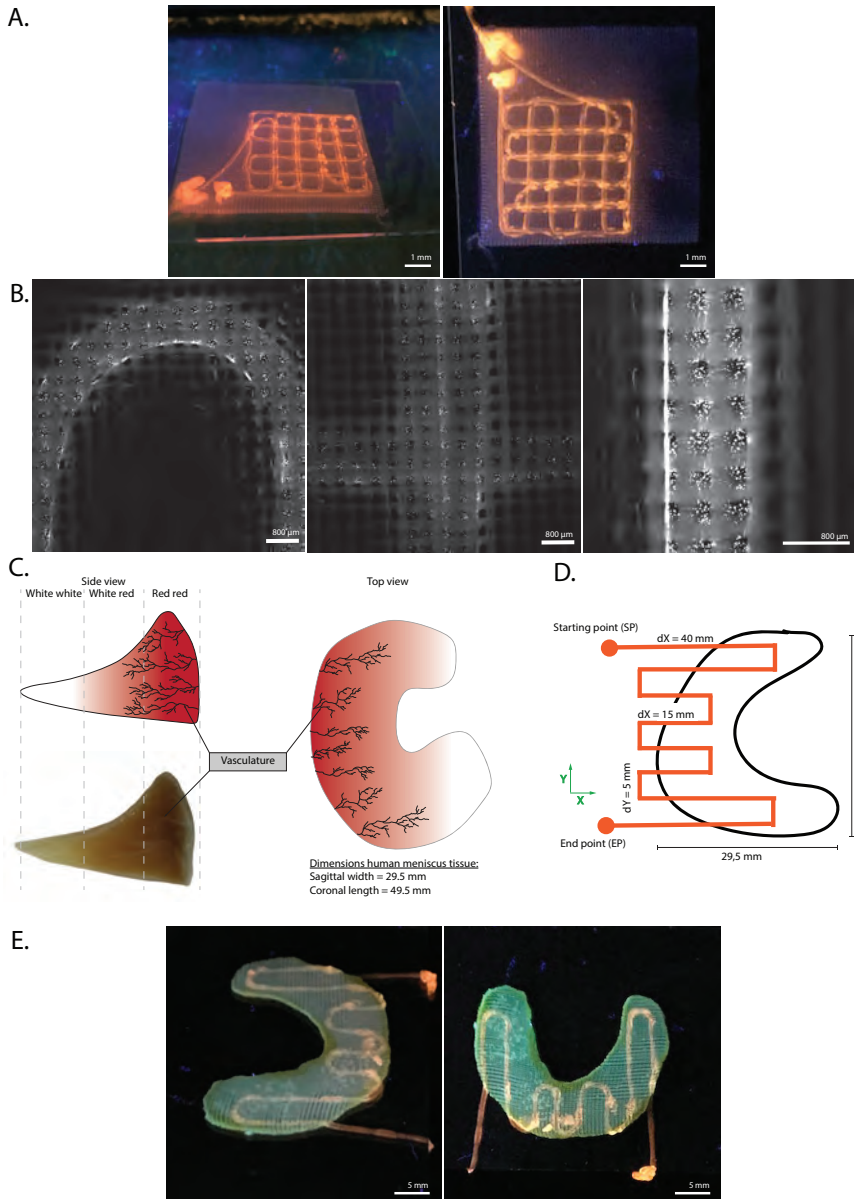
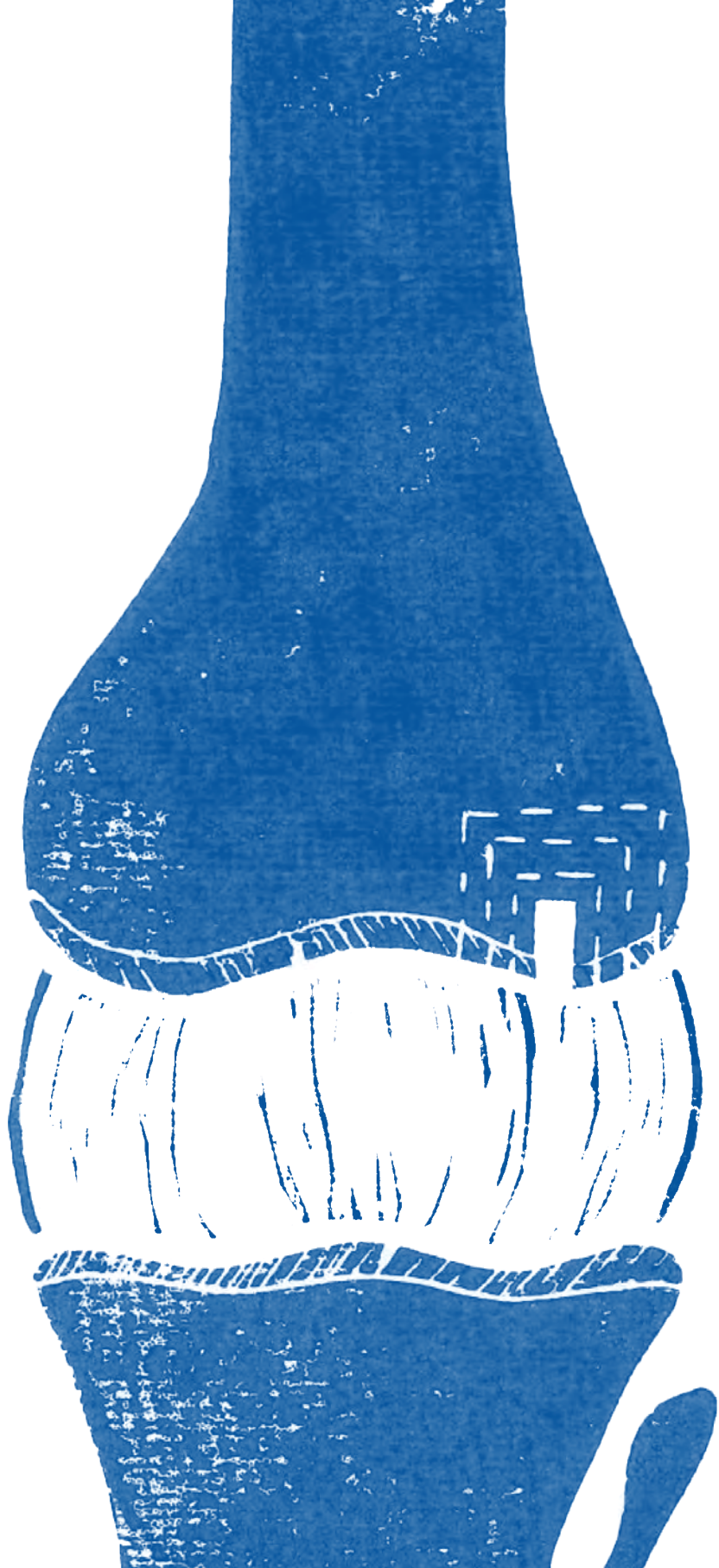


Figure 3. Combining co-axial extrusion based printing with MEW to achieve larger scale tissue fabrication. A) Woodpile-structure on top of a MEW mesh to allow perfusion of smaller tissue units. B) Macroscopic image of shape of co-axial fibres and MEW meshes. C) Schematic of native meniscus tissue. D) Co-axial printhead trajectory. E) Proof of principle in establishing a large perfusable network on a human sized meniscus shape.

Conclusion

Here two approaches are presented where convergence of advanced biofabrication technologies can aid in the generation of multi-scale, multi-material tissue equivalents. For example, the form of the enthesis can possibly be mimicked by convergence of melt electrowriting and extrusion-based printing of MgP-PCL. This allows multi-scale fabrication and could, therefore, enable 3D culture systems that better reflect the native tissue environment. The optimal gel and culture conditions of the tenocytes, and matrix distribution of such, has yet to be determined.

A human-sized meniscus could potentially be perfused by converging co-axial extrusion based printing with MEW. The design of large perfusable channels can be inspired by the vasculature in the native red-red zone. By alternating MEW with perfusable channels, engineering a human-sized meniscus might be feasible.



References

Annex. References

1. World Health Organization. Aging and Health. <https://www.who.int/news-room/fact-sheets/detail/ageing-and-health>.
2. Kontis V, Bennett JE, Mathers CD, Li G, Foreman K, Ezzati M. Future life expectancy in 35 industrialised countries: projections with a Bayesian model ensemble. *Lancet (London, England)*. 2017;389(10076):1323-1335. doi:10.1016/S0140-6736(16)32381-9
3. Andrews RM, Tan EJ, Varma VR, et al. Positive Aging Expectations Are Associated With Physical Activity Among Urban-Dwelling Older Adults. *Gerontologist*. 2017;57(suppl_2):S178-S186. doi:10.1093/geront/gnx060
4. Lee I-M, Shiroma EJ, Lobelo F, Puska P, Blair SN, Katzmarzyk PT. Effect of physical inactivity on major non-communicable diseases worldwide: an analysis of burden of disease and life expectancy. *Lancet (London, England)*. 2012;380(9838):219-229. doi:10.1016/S0140-6736(12)61031-9
5. Menec VH. The relation between everyday activities and successful aging: a 6-year longitudinal study. *J Gerontol B Psychol Sci Soc Sci*. 2003;58(2):S74-82. doi:10.1093/geronb/58.2.s74
6. Wen CP, Wai JPM, Tsai MK, et al. Minimum amount of physical activity for reduced mortality and extended life expectancy: a prospective cohort study. *Lancet (London, England)*. 2011;378(9798):1244-1253. doi:10.1016/S0140-6736(11)60749-6
7. Bauman A, Merom D, Bull FC, Buchner DM, Fiatarone Singh MA. Updating the Evidence for Physical Activity: Summative Reviews of the Epidemiological Evidence, Prevalence, and Interventions to Promote "Active Aging". *Gerontologist*. 2016;56 Suppl 2:S268-80. doi:10.1093/geront/gnw031
8. Montero-Fernandez N, Serra-Rexach JA. Role of exercise on sarcopenia in the elderly. *Eur J Phys Rehabil Med*. 2013;49(1):131-143.
9. Colcombe S, Kramer AF. Fitness effects on the cognitive function of older adults: a meta-analytic study. *Psychol Sci*. 2003;14(2):125-130. doi:10.1111/1467-9280.t01-1-01430
10. Kramer AF, Erickson KI. Capitalizing on cortical plasticity: influence of physical activity on cognition and brain function. *Trends Cogn Sci*. 2007;11(8):342-348. doi:10.1016/j.tics.2007.06.009
11. Strohle A. Physical activity, exercise, depression and anxiety disorders. *J Neural Transm*. 2009;116(6):777-784. doi:10.1007/s00702-008-0092-x
12. Hunter DJ, Bierma-Zeinstra S. Osteoarthritis. *Lancet*. 2019;393(10182):1745-1759. doi:10.1016/S0140-6736(19)30417-9
13. Silverwood V, Blagojevic-Bucknall M, Jinks C, Jordan JL, Protheroe J, Jordan KP. Current evidence on risk factors for knee osteoarthritis in older adults: A systematic review and meta-analysis. *Osteoarthritis Cartil*. 2015;23(4):507-515. doi:10.1016/j.joca.2014.11.019
14. Muthuri SG, Hui M, Doherty M, Zhang W. What if we prevent obesity? Risk reduction in knee osteoarthritis estimated through a meta-analysis of observational studies. *Arthritis Care Res*. 2011;63(7):982-990. doi:10.1002/acr.20464
15. Mandelbaum BR, Browne JE, Fu F, et al. Articular cartilage lesions of the knee. *Am J Sports Med*. 1998;26(6):853-861. doi:10.1177/03635465980260062201
16. Bruns J, Werner M, Habermann C. Osteochondritis Dissecans: Etiology, Pathology, and Imaging with a Special Focus on the Knee Joint. *Cartilage*. 2018;9(4):346-362. doi:10.1177/1947603517715736
17. Buckwalter JA, Mankin HJ. Articular cartilage: degeneration and osteoarthritis, repair, regeneration, and transplantation. *Instr Course Lect*. 1998;47:487—504. <http://europepmc.org/abstract/MED/9571450>.
18. Buckwalter J. Articular Cartilage: Injuries and Potential for Healing. *J Orthopaedic Sport Phys Ther*. 1998;28(4):192-202.
19. Davies-Tuck ML, Wluka AE, Wang Y, et al. The natural history of cartilage defects in people with knee osteoarthritis. *Osteoarthritis Cartil*. 2008;16(3):337-342. doi:10.1016/j.joca.2007.07.005
20. Ng M, Fleming T, Robinson M, et al. Global, regional, and national prevalence of overweight and obesity in children and adults during 1980-2013: a systematic analysis for the Global Burden of Disease Study 2013. *Lancet (London, England)*. 2014;384(9945):766-781. doi:10.1016/S0140-6736(14)60460-8

21. World Health Organization. Obesity and overweight. <https://www.who.int/news-room/fact-sheets/detail/obesity-and-overweight>.
22. Sowers MR, Karvonen-Gutierrez CA. The evolving role of obesity in knee osteoarthritis. *Curr Opin Rheumatol*. 2010;22(5):533-537. doi:10.1097/BOR.0b013e32833b4682
23. Mundermann A, Dyrby CO, Andriacchi TP. Secondary gait changes in patients with medial compartment knee osteoarthritis: increased load at the ankle, knee, and hip during walking. *Arthritis Rheum*. 2005;52(9):2835-2844. doi:10.1002/art.21262
24. J.J. Caron, R.J.H. Custers PJE. Chirurgische behandeling van (osteo) chondrale defecten in de knie. *Standpunt van Ned Orthop Ver*. 2019.
25. Curl WW, Krome J, Gordon ES, Rushing J, Smith BP, Poehling GG. Cartilage injuries: A review of 31,516 knee arthroscopies. *Arthroscopy*. 1997;13(4):456-460. doi:10.1016/S0749-8063(97)90124-9
26. Hjelle K, Solheim E, Strand T, Muri R, Brittberg M. Articular cartilage defects in 1,000 knee arthroscopies. *Arthroscopy*. 2002;18(7):730-734. doi:10.1053/jars.2002.32839
27. Malda J, Benders KEMM, Klein TJ, et al. Comparative study of depth-dependent characteristics of equine and human osteochondral tissue from the medial and lateral femoral condyles. *Osteoarthr Cartil*. 2012;20(10):1147-1151. doi:10.1016/j.joca.2012.06.005
28. Mancini IADD, Rieppo L, Pouran B, et al. Effects of body mass on microstructural features of the osteochondral unit: A comparative analysis of 37 mammalian species. *Bone*. 2019;127(July):664-673. doi:10.1016/j.bone.2019.07.001
29. Hirschmann MT, Müller W. Complex function of the knee joint: the current understanding of the knee. *Knee Surgery, Sport Traumatol Arthrosc*. 2015;23(10):2780-2788. doi:10.1007/s00167-015-3619-3
30. Miller RH. Joint Loading in Runners Does Not Initiate Knee Osteoarthritis. *Exerc Sport Sci Rev*. 2017;45(2):87-95. doi:10.1249/JES.000000000000105
31. Hayes WC, Mockros LF. Viscoelastic properties of human articular cartilage. *J Appl Physiol*. 1971;31(4):562-568. doi:10.1152/jappl.1971.31.4.562
32. Hunziker EB, Quinn TM, Hauselmann H-J. Quantitative structural organization of normal adult human articular cartilage. *Osteoarthr Cartil*. 2002;10(7):564-572. doi:10.1053/joca.2002.0814
33. Dowthwaite GP, Bishop JC, Redman SN, et al. The surface of articular cartilage contains a progenitor cell populations. *J Cell Sci*. 2004;117(6):889-897. doi:10.1242/jcs.00912
34. Williams R, Khan IM, Richardson K, et al. Identification and clonal characterisation of a progenitor cell sub-population in normal human articular cartilage. *PLoS One*. 2010;5(10). doi:10.1371/journal.pone.0013246
35. Klein TJ, Chaudhry M, Bae WC, Sah RL. Depth-dependent biomechanical and biochemical properties of fetal, newborn, and tissue-engineered articular cartilage. *J Biomech*. 2007;40(1):182-190. doi:10.1016/j.jbiomech.2005.11.002
36. Hsueh M-F, Khabut A, Kjellström S, Önerfjord P, Kraus VB. Elucidating the Molecular Composition of Cartilage by Proteomics HHS Public Access TOC Graphic. *J Proteome Res*. 2016;15(2):374-388. doi:10.1021/acs.jproteome.5b00946
37. Hynes RO, Naba A. Overview of the matrisome-An inventory of extracellular matrix constituents and functions. *Cold Spring Harb Perspect Biol*. 2012;4(1):1-16. doi:10.1101/cshperspect.a004903
38. Klein TJ, Ph D, Malda J, et al. Tissue Engineering of Articular Cartilage with Biomimetic Zones. 2009;15(2).
39. Sophia Fox AJ, Bedi A, Rodeo SA. The basic science of articular cartilage: Structure, composition, and function. *Sports Health*. 2009;1(6):461-468. doi:10.1177/1941738109350438
40. Benninghoff A. Form und bau der gelenknorpel in ihren beziehungen zur funktion. 1925.
41. Zhu W, Mow VC, Koob TJ, Eyre DR. Viscoelastic shear properties of articular cartilage and the effects of glycosidase treatments. *J Orthop Res*. 1993;11(6):771-781. doi:10.1002/jor.1100110602
42. M. Brittberg, A. Lindahl, A. Nilsson, C. Ohlsson, O. Isaksson LP. Treatment of deep cartilage defects in the knee with autologous chondrocyte transplantation. *N Engl J Med*. 1994;331(14):889-895.

43. Hunter W. On the structure and diseases of articulating cartilage. *Philos Trans R Soc L.* 1743;42b:514-521.
44. Bekkers JEJ, Inklaar M, Saris DBF. Treatment selection in articular cartilage lesions of the knee: a systematic review. *Am J Sports Med.* 2009;37 Suppl 1:148S-55S. doi:10.1177/0363546509351143
45. Steadman JR, Briggs KK, Rodrigo JJ, Kocher MS, Gill TJ, Rodkey WG. Outcomes of microfracture for traumatic chondral defects of the knee: Average 11-year follow-up. *Arthrosc J Arthrosc Relat Surg.* 2003;19(5):477-484. doi:https://doi.org/10.1053/jars.2003.50112
46. Bark S, Piontek T, Behrens P, Mkalaluh S, Varoga D, Gille J. Enhanced microfracture techniques in cartilage knee surgery: Fact or fiction? *World J Orthop.* 2014;5(4):444-449. doi:10.5312/wjo.v5.i4.444
47. Benthien JP, Behrens P. Autologous Matrix-Induced Chondrogenesis (AMIC): Combining Microfracturing and a Collagen I/III Matrix for Articular Cartilage Resurfacing. *Cartilage.* 2010;1(1):65-68. doi:10.1177/1947603509360044
48. Pina S, Rebelo R, Correlo VM, Oliveira JM, Reis RL. Bioceramics for Osteochondral Tissue Engineering and Regeneration. *Adv Exp Med Biol.* 2018;1058:53-75. doi:10.1007/978-3-319-76711-6_3
49. Fuchs A, Eberbach H, Izadpanah K, Bode G, Sudkamp NP, Feucht MJ. Focal metallic inlay resurfacing prosthesis for the treatment of localized cartilage defects of the femoral condyles: a systematic review of clinical studies. *Knee Surg Sports Traumatol Arthrosc.* 2018;26(9):2722-2732. doi:10.1007/s00167-017-4714-4
50. Bartlett W, Skinner JA, Gooding CR, et al. Autologous chondrocyte implantation versus matrix-induced autologous chondrocyte implantation for osteochondral defects of the knee: a prospective, randomised study. *J Bone Joint Surg Br.* 2005;87(5):640-645. doi:10.1302/0301-620X.87B5.15905
51. Saris DBF, Vanlauwe J, Victor J, et al. Characterized chondrocyte implantation results in better structural repair when treating symptomatic cartilage defects of the knee in a randomized controlled trial versus microfracture. *Am J Sports Med.* 2008;36(2):235-246. doi:10.1177/0363546507311095
52. Fickert S, Gerwien P, Helmert B, et al. One-Year Clinical and Radiological Results of a Prospective, Investigator-Initiated Trial Examining a Novel, Purely Autologous 3-Dimensional Autologous Chondrocyte Transplantation Product in the Knee. *Cartilage.* 2012;3(1):27-42. doi:10.1177/1947603511417616
53. Hangody L, Kish G, Karpati Z, Udvarhelyi I, Szigeti I, Bely M. Mosaicplasty for the treatment of articular cartilage defects: application in clinical practice. *Orthopedics.* 1998;21(7):751-756.
54. Bobic V. Arthroscopic osteochondral autograft transplantation in anterior cruciate ligament reconstruction: a preliminary clinical study. *Knee Surg Sports Traumatol Arthrosc.* 1996;3(4):262-264. doi:10.1007/bf01466630
55. Gortz S, Bugbee WD. Fresh osteochondral allografts: graft processing and clinical applications. *J Knee Surg.* 2006;19(3):231-240. doi:10.1055/s-0030-1248112
56. Pisanu G, Cottino U, Rosso F, et al. Large osteochondral allografts of the knee: Surgical technique and indications. *Joints.* 2018;6(1):42-53. doi:10.1055/s-0038-1636925
57. Solheim E, Hegna J, Strand T, Harlem T, Inderhaug E. Randomized Study of Long-term (15-17 Years) Outcome After Microfracture Versus Mosaicplasty in Knee Articular Cartilage Defects. *Am J Sports Med.* 2017;46(4):826-831. doi:10.1177/0363546517745281
58. Jasper LL, Jones CA, Mollins J, Pohar SL, Beaupre LA. Risk factors for revision of total knee arthroplasty: a scoping review. *BMC Musculoskelet Disord.* 2016;17(1):182. doi:10.1186/s12891-016-1025-8
59. Mithoefer K, Williams RJ 3rd, Warren RF, et al. The microfracture technique for the treatment of articular cartilage lesions in the knee. A prospective cohort study. *J Bone Joint Surg Am.* 2005;87(9):1911-1920. doi:10.2106/JBJS.D.02846
60. Kreuz PC, Steinwachs MR, Erggelet C, et al. Results after microfracture of full-thickness chondral defects in different compartments in the knee. *Osteoarthr Cartil.* 2006;14(11):1119-1125. doi:10.1016/j.joca.2006.05.003

61. Shive MS, Stanish WD, McCormack R, et al. BST-CarGel(R) Treatment Maintains Cartilage Repair Superiority over Microfracture at 5 Years in a Multicenter Randomized Controlled Trial. *Cartilage*. 2015;6(2):62-72. doi:10.1177/1947603514562064
62. Gao L, Orth P, Cucchiariini M, Madry H. Autologous Matrix-Induced Chondrogenesis: A Systematic Review of the Clinical Evidence. *Am J Sports Med*. 2019;47(1):222-231. doi:10.1177/0363546517740575
63. Steinwachs M. New technique for cell-seeded collagen-matrix-supported autologous chondrocyte transplantation. *Arthroscopy*. 2009;25(2):208-211. doi:10.1016/j.arthro.2008.10.009
64. Rapko S, Baron U, Hoffmuller U, Model F, Wolfe L, Olek S. DNA methylation analysis as novel tool for quality control in regenerative medicine. *Tissue Eng*. 2007;13(9):2271-2280. doi:10.1089/ten.2006.0444
65. Saris DBF, Vanlauwe J, Victor J, et al. Treatment of symptomatic cartilage defects of the knee: characterized chondrocyte implantation results in better clinical outcome at 36 months in a randomized trial compared to microfracture. *Am J Sports Med*. 2009;37 Suppl 1:10S-19S. doi:10.1177/0363546509350694
66. Knutsen G, Drogset JO, Engebretsen L, et al. A randomized trial comparing autologous chondrocyte implantation with microfracture. Findings at five years. *J Bone Joint Surg Am*. 2007;89(10):2105-2112. doi:10.2106/JBJS.G.00003
67. Knutsen G, Engebretsen L, Ludvigsen TC, et al. Autologous chondrocyte implantation compared with microfracture in the knee. A randomized trial. *J Bone Joint Surg Am*. 2004;86(3):455-464. doi:10.2106/00004623-200403000-00001
68. Ferruzzi A, Buda R, Faldini C, et al. Autologous chondrocyte implantation in the knee joint: open compared with arthroscopic technique. Comparison at a minimum follow-up of five years. *J Bone Joint Surg Am*. 2008;90 Suppl 4:90-101. doi:10.2106/JBJS.H.00633
69. Jones KJ, Kelley BV, Arshi A, McAllister DR, Fabricant PD. Comparative Effectiveness of Cartilage Repair With Respect to the Minimal Clinically Important Difference. *Am J Sports Med*. 2019;47(13):3284-3293. doi:10.1177/0363546518824552
70. Siebold R, Suezter F, Schmitt B, Trattning S, Essig M. Good clinical and MRI outcome after arthroscopic autologous chondrocyte implantation for cartilage repair in the knee. *Knee Surg Sports Traumatol Arthrosc*. 2018;26(3):831-839. doi:10.1007/s00167-017-4491-0
71. Bentley G, Biant LC, Carrington RWJ, et al. A prospective, randomised comparison of autologous chondrocyte implantation versus mosaicplasty for osteochondral defects in the knee. *J Bone Joint Surg Br*. 2003;85(2):223-230. doi:10.1302/0301-620x.85b2.13543
72. Sherman SL, Thyssen E, Nuelle CW. Osteochondral Autologous Transplantation. *Clin Sports Med*. 2017;36(3):489-500. doi:10.1016/j.csm.2017.02.006
73. Familiari F, Cinque ME, Chahla J, et al. Clinical Outcomes and Failure Rates of Osteochondral Allograft Transplantation in the Knee: A Systematic Review. *Am J Sports Med*. 2018;46(14):3541-3549. doi:10.1177/0363546517732531
74. Frank RM, Lee S, Cotter EJ, Hannon CP, Leroux T, Cole BJ. Outcomes of Osteochondral Allograft Transplantation With and Without Concomitant Meniscus Allograft Transplantation: A Comparative Matched Group Analysis. *Am J Sports Med*. 2018;46(3):573-580. doi:10.1177/0363546517744202
75. Matta C, Szűcs-Somogyi C, Kon E, et al. Osteogenic differentiation of human bone marrow-derived mesenchymal stem cells is enhanced by an aragonite scaffold. *Differentiation*. 2019;107:24-34. doi:10.1016/j.diff.2019.05.002
76. Kon E, Filardo G, Brittberg M, et al. A multilayer biomaterial for osteochondral regeneration shows superiority vs microfractures for the treatment of osteochondral lesions in a multicentre randomized trial at 2 years. *Knee Surg Sports Traumatol Arthrosc*. 2018;26(9):2704-2715. doi:10.1007/s00167-017-4707-3
77. Brix M, Kaipel M, Kellner R, et al. Successful osteoconduction but limited cartilage tissue quality following osteochondral repair by a cell-free multilayered nano-composite scaffold at the knee. *Int Orthop*. 2016;40(3):625-632. doi:10.1007/s00264-016-3118-2

78. Christensen BB, Foldager CB, Jensen J, Jensen NC, Lind M. Poor osteochondral repair by a biomimetic collagen scaffold: 1- to 3-year clinical and radiological follow-up. *Knee Surg Sports Traumatol Arthrosc.* 2016;24(7):2380-2387. doi:10.1007/s00167-015-3538-3
79. Groen WM, Diloksumpan P, van Weeren PR, Levato R, Malda J. From intricate to integrated: Biofabrication of articulating joints. *J Orthop Res.* 2017;35(10):2089-2097. doi:10.1002/jor.23602
80. Levato R, Jungst T, Scheuring RG, Blunk T, Groll J, Malda J. From shape to function: the next step in bioprinting. *Adv Mater.* 2020;32(12):1906423. doi:10.1002/adma.201906423
81. Daly AC, Freeman FE, Gonzalez-Fernandez T, Critchley SE, Nulty J, Kelly DJ. 3D Bioprinting for Cartilage and Osteochondral Tissue Engineering. *Adv Healthc Mater.* 2017;6(22):1-20. doi:10.1002/adhm.201700298
82. Schuurman W, Khristov V, Pot MW, Van Weeren PR, Dhert WJA, Malda J. Bioprinting of hybrid tissue constructs with tailorable mechanical properties. *Biofabrication.* 2011;3(2). doi:10.1088/1758-5082/3/2/021001
83. Coburn J, Gibson M, Bandalini PA, et al. Biomimetics of the Extracellular Matrix: An Integrated Three-Dimensional Fiber-Hydrogel Composite for Cartilage Tissue Engineering. *Smart Struct Syst.* 2011;7(3):213-222. doi:10.12989/sss.2011.7.3.213
84. Visser J, Melchels FPW, Jeon JE, et al. Reinforcement of hydrogels using three-dimensionally printed microfibrils. *Nat Commun.* 2015;6:1-10. doi:10.1038/ncomms7933
85. Bas O, De-Juan-Pardo EM, Chhaya MP, et al. Enhancing structural integrity of hydrogels by using highly organised melt electrospun fibre constructs. *Eur Polym J.* 2015;72:451-463. doi:https://doi.org/10.1016/j.eurpolymj.2015.07.034
86. Schipani R, Scheurer S, Florentin R, Critchley SE, Kelly DJ. Reinforcing interpenetrating network hydrogels with 3D printed polymer networks to engineer cartilage mimetic composites. *Biofabrication.* 2020.
87. Shin YM, Hohman MM, Brenner MP, Rutledge GC. Electrospinning: A whipping fluid jet generates submicron polymer fibers. *Appl Phys Lett.* 2001;78(8):1149-1151. doi:10.1063/1.1345798
88. Hochleitner G, Jüngst T, Brown TD, et al. Additive manufacturing of scaffolds with sub-micron filaments via melt electrospinning writing. *Biofabrication.* 2015;7(3):35002. doi:10.1088/1758-5090/7/3/035002
89. Dalton PD. Melt electrospinning with additive manufacturing principles. *Curr Opin Biomed Eng.* 2017;2:49-57. doi:10.1016/j.cobme.2017.05.007
90. Robinson TM, Huttmacher DW, Dalton PD. The Next Frontier in Melt Electrospinning: Taming the Jet. *Adv Funct Mater.* 2019;29(44). doi:10.1002/adfm.201904664
91. Brown TD, Dalton PD, Huttmacher DW. Direct writing by way of melt electrospinning. *Adv Mater.* 2011;23(47):5651-5657. doi:10.1002/adma.201103482
92. Bas O, De-Juan-Pardo EM, Meinert C, et al. Biofabricated soft network composites for cartilage tissue engineering. *Biofabrication.* 2017;9(2):25014. doi:10.1088/1758-5090/aa6b15
93. Castillo M, Hochleitner G, Wilson W, et al. Mechanical behavior of a soft hydrogel reinforced with three-dimensional printed microfibre scaffolds. *Sci Rep.* 2018;8(1):1-10. doi:10.1038/s41598-018-19502-y
94. Li K, Tashman S, Fu F, Harner C, Zhang X. Automating analyses of the distal femur articular geometry based on three-dimensional surface data. *Ann Biomed Eng.* 2010;38(9):2928-2936. doi:10.1007/s10439-010-0064-9
95. de Windt TS, Saris DBF, Slaper-Cortenbach ICM, et al. Direct Cell-Cell Contact with Chondrocytes Is a Key Mechanism in Multipotent Mesenchymal Stromal Cell-Mediated Chondrogenesis. *Tissue Eng Part A.* 2015;21(19-20):2536-2547. doi:10.1089/ten.TEA.2014.0673
96. Morgan BJ, Bauza-Mayol G, Gardner OFW, et al. Bone Morphogenetic Protein-9 Is a Potent Chondrogenic and Morphogenic Factor for Articular Cartilage Chondroprogenitors. *Stem Cells Dev.* May 2020. doi:10.1089/scd.2019.0209

97. Moreira Teixeira LS, Leijten JCH, Sobral J, et al. High throughput generated micro-aggregates of chondrocytes stimulate cartilage formation in vitro and in vivo. *Eur Cell Mater.* 2012;23:387-399. doi:10.22203/ecm.v023a30
98. Trounson A, McDonald C. Stem Cell Therapies in Clinical Trials: Progress and Challenges. *Cell Stem Cell.* 2015;17(1):11-22. doi:10.1016/j.stem.2015.06.007
99. Marks P, Gottlieb S. Balancing Safety and Innovation for Cell-Based Regenerative Medicine. *N Engl J Med.* 2018;378(10):954-959. doi:10.1056/NEJMs1715626
100. Malda J, Groll J, van Weeren PR. Rethinking articular cartilage regeneration based on a 250-year-old statement. *Nat Rev Rheumatol.* 2019;15(10):571-572. doi:10.1038/s41584-019-0278-7
101. Dalton PD, Vaquette C, Farrugia BL, Dargaville TR, Brown TD, Hutmacher DW. Electrospinning and additive manufacturing: converging technologies. *Biomater Sci.* 2013;1(2):171-185. doi:10.1039/c2bm00039c
102. Hutmacher DW, Schantz T, Zein I, Ng KW, Teoh SH, Tan KC. Mechanical properties and cell cultural response of polycaprolactone scaffolds designed and fabricated via fused deposition modeling. *J Biomed Mater Res.* 2001;55(2):203-216. doi:10.1002/1097-4636(200105)55:2<203::aid-jbm1007>3.0.co;2-7
103. Hanson Shepherd JN, Parker ST, Shepherd RF, Gillette MU, Lewis JA, Nuzzo RG. 3D Microperiodic Hydrogel Scaffolds for Robust Neuronal Cultures. *Adv Funct Mater.* 2011;21(1):47-54. doi:10.1002/adfm.201001746
104. Lewis JA. Direct ink writing of 3D functional materials. *Adv Funct Mater.* 2006;16(17):2193-2204. doi:10.1002/adfm.200600434
105. Smay JE, Gratson GM, Shepherd RF, Cesarano J, Lewis JA. Directed colloidal assembly of 3D periodic structures. *Adv Mater.* 2002;14(18):1279-1283. doi:10.1002/1521-4095(20020916)14:18<1279::AID-ADMA1279>3.0.CO;2-A
106. Brown TD, Slotosch A, Thibaudeau L, et al. Design and fabrication of tubular scaffolds via direct writing in a melt electrospinning mode. *Biointerphases.* 2012;7(1-4):13. doi:10.1007/s13758-011-0013-7
107. Hochleitner G, Youssef A, Hrynevich A, et al. Fibre pulsing during melt electrospinning writing. *BioNanoMaterials.* 2016;17(3-4):159-171. doi:10.1515/bnm-2015-0022
108. Brown TD, Dalton PD, Hutmacher DW. Melt electrospinning today: An opportune time for an emerging polymer process. *Prog Polym Sci.* 2016;56:116-166. doi:10.1016/j.progpolymsci.2016.01.001
109. Bognitzki M, Czado W, Frese T, et al. Nanostructured fibers via electrospinning. *Adv Mater.* 2001;13(1):70-72.
110. Gibson PW, Schreuder-Gibson HL, Rivin D, Schreuder-Gibson HL, Rivin D. Electrospun fiber mats: transport properties. *AIChE J.* 1999;45(1):190-195. doi:10.1002/aic.690450116
111. Reneker DH, Chun I. Nanometre diameter fibres of polymer, produced by electrospinning. *Nanotechnology.* 1996;7(3):216.
112. Muerza-Cascante ML, Haylock D, Hutmacher DW, Dalton PD. Melt electrospinning and its technologization in tissue engineering. *Tissue Eng Part B Rev.* 2015;21(2):187-202. doi:10.1089/ten.TEB.2014.0347
113. Malda J, Visser J, Melchels FP, et al. 25th anniversary article: Engineering hydrogels for biofabrication. *Adv Mater.* 2013;25(36):5011-5028. doi:10.1002/adma.201302042
114. Prielipp H, Knechtel M, Claussen N, et al. Strength and fracture toughness of aluminum/alumina composites with interpenetrating networks. *Mater Sci Eng A.* 1995;197(1):19-30. doi:https://doi.org/10.1016/0921-5093(94)09771-2
115. Shin SR, Bae H, Cha JM, et al. Carbon Nanotube Reinforced Hybrid Microgels as Scaffold Materials for Cell Encapsulation. *ACS Nano.* 2012;6(1):362-372. doi:10.1021/nn203711s
116. Kai D, Prabhakaran MP, Stahl B, Eblenkamp M, Wintermantel E, Ramakrishna S. Mechanical properties and in vitro behavior of nanofiber-hydrogel composites for tissue engineering applications. *Nanotechnology.* 2012;23(9):95705. doi:10.1088/0957-4484/23/9/095705

117. Engh CA, Bobyn JD, Glassman AH. Porous-coated hip replacement. The factors governing bone ingrowth, stress shielding, and clinical results. *J Bone Joint Surg Br.* 1987;69(1):45-55.
118. Hochleitner G, Hümmer JF, Luxenhofer R, Groll J. High definition fibrous poly (2-ethyl-2-oxazoline) scaffolds through melt electrospinning writing. *Polymer (Guildf).* 2014;55(20):5017-5023.
119. Chen F, Hochleitner G, Woodfield T, Groll J, Dalton PD, Amsden BG. Additive Manufacturing of a Photo-Cross-Linkable Polymer via Direct Melt Electrospinning Writing for Producing High Strength Structures. *Biomacromolecules.* 2016;17(1):208-214. doi:10.1021/acs.biomac.5b01316
120. Chiu-Webster S, Lister JR. The fall of a viscous thread onto a moving surface: a 'fluid-mechanical sewing machine.' *J Fluid Mech.* 2006;569:89-111.
121. Brun P-T, Audoly B, Ribe NM, Eaves TS, Lister JR. Liquid ropes: a geometrical model for thin viscous jet instabilities. *Phys Rev Lett.* 2015;114(17):174501.
122. Morris SW, Dawes JHP, Ribe NM, Lister JR. Meandering instability of a viscous thread. *Phys Rev E.* 2008;77(6):66218.
123. Jungst T, Muerza-Cascante ML, Brown TD, et al. Melt electrospinning onto cylinders: Effects of rotational velocity and collector diameter on morphology of tubular structures. *Polym Int.* 2015;64(9):1086-1095. doi:10.1002/pi.4948
124. Chang C, Tran VH, Wang J, Fuh Y-K, Lin L. Direct-write piezoelectric polymeric nanogenerator with high energy conversion efficiency. *Nano Lett.* 2010;10(2):726-731.
125. Lee SW, Lee HJ, Choi JH, et al. Periodic array of polyelectrolyte-gated organic transistors from electrospun poly(3-hexylthiophene) nanofibers. *Nano Lett.* 2010;10(1):347-351. doi:10.1021/nl903722z
126. Skylar-Scott MA, Gunasekaran S, Lewis JA. Laser-assisted direct ink writing of planar and 3D metal architectures. *Proc Natl Acad Sci U S A.* 2016;113(22):6137-6142. doi:10.1073/pnas.1525131113
127. Pouran B, Arbabi V, Bleys RLAW, van Weeren PR, Zadpoor AA, Weinans H. Solute transport at the interface of cartilage and subchondral bone plate: effect of micro-architecture. *J Biomech.* 2017;52:148-154.
128. Deymier AC, An Y, Boyle JJ, et al. Micro-mechanical properties of the tendon-to-bone attachment. *Acta Biomater.* 2017;56:25-35.
129. Nover AB, Lee SL, Georgescu MS, et al. Porous titanium bases for osteochondral tissue engineering. *Acta Biomater.* 2015;27:286-293.
130. Yuk H, Zhang T, Lin S, Parada GA, Zhao X. Tough bonding of hydrogels to diverse non-porous surfaces. *Nat Mater.* 2016;15(2):190-196.
131. Zhao Y, Li M, Liu B, et al. Ultra-tough injectable cytocompatible hydrogel for 3D cell culture and cartilage repair. *J Mater Chem B.* 2018;6(9):1351-1358.
132. Means AK, Shrode CS, Whitney L V, Ehrhardt DA, Grunlan MA. Double network hydrogels that mimic the modulus, strength, and lubricity of cartilage. *Biomacromolecules.* 2019;20(5):2034-2042.
133. Lima EG, Chao PG, Ateshian GA, et al. The effect of devitalized trabecular bone on the formation of osteochondral tissue-engineered constructs. *Biomaterials.* 2008;29(32):4292-4299.
134. Jiang J, Tang A, Ateshian GA, Guo XE, Hung CT, Lu HH. Bioactive stratified polymer ceramic-hydrogel scaffold for integrative osteochondral repair. *Ann Biomed Eng.* 2010;38(6):2183-2196.
135. Jeon JE, Vaquette C, Theodoropoulos C, Klein TJ, Huttmacher DW. Multiphasic construct studied in an ectopic osteochondral defect model. *J R Soc Interface.* 2014;11(95):20140184.
136. Seol Y, Park JY, Jeong W, Kim T, Kim S, Cho D. Development of hybrid scaffolds using ceramic and hydrogel for articular cartilage tissue regeneration. *J Biomed Mater Res Part A.* 2015;103(4):1404-1413.
137. Scotti C, Wirz D, Wolf F, et al. Engineering human cell-based, functionally integrated osteochondral grafts by biological bonding of engineered cartilage tissues to bony scaffolds. *Biomaterials.* 2010;31(8):2252-2259.
138. Levingstone TJ, Matsiko A, Dickson GR, O'Brien FJ, Gleeson JP. A biomimetic multi-layered collagen-based scaffold for osteochondral repair. *Acta Biomater.* 2014;10(5):1996-2004.

139. Li C, Ouyang L, Pence IJ, et al. Buoyancy-Driven Gradients for Biomaterial Fabrication and Tissue Engineering. *Adv Mater*. 2019;31(17):1900291.
140. Bian W, Lian Q, Li D, et al. Morphological characteristics of cartilage-bone transitional structures in the human knee joint and CAD design of an osteochondral scaffold. *Biomed Eng Online*. 2016;15(1):82.
141. Holmes B, Zhu W, Li J, Lee JD, Zhang LG. Development of novel three-dimensional printed scaffolds for osteochondral regeneration. *Tissue Eng Part A*. 2015;21(1-2):403-415.
142. Erisken C, Kalyon DM, Wang H. Functionally graded electrospun polycaprolactone and β -tricalcium phosphate nanocomposites for tissue engineering applications. *Biomaterials*. 2008;29(30):4065-4073.
143. Erisken C, Kalyon DM, Wang H, Örnek-Ballanco C, Xu J. Osteochondral tissue formation through adipose-derived stromal cell differentiation on biomimetic polycaprolactone nanofibrous scaffolds with graded insulin and Beta-glycerophosphate concentrations. *Tissue Eng Part A*. 2011;17(9-10):1239-1252.
144. Shim J-H, Jang K-M, Hahn SK, et al. Three-dimensional bioprinting of multilayered constructs containing human mesenchymal stromal cells for osteochondral tissue regeneration in the rabbit knee joint. *Biofabrication*. 2016;8(1):14102.
145. Levato R, Visser J, Planell JA, Engel E, Malda J, Mateos-Timoneda MA. Biofabrication of tissue constructs by 3D bioprinting of cell-laden microcarriers. *Biofabrication*. 2014;6(3):35020.
146. Castro NJ, O'Brien J, Zhang LG. Integrating biologically inspired nanomaterials and table-top stereolithography for 3D printed biomimetic osteochondral scaffolds. *Nanoscale*. 2015;7(33):14010-14022.
147. Aydogdu MO, Oner ET, Ekren N, et al. Comparative characterization of the hydrogel added PLA/ β -TCP scaffolds produced by 3D bioprinting. *Bioprinting*. 2019;13:e00046.
148. Moxon SR, Cooke ME, Cox SC, et al. Suspended manufacture of biological structures. *Adv Mater*. 2017;29(13):1605594.
149. Pati F, Jang J, Ha D-H, et al. Printing three-dimensional tissue analogues with decellularized extracellular matrix bioink. *Nat Commun*. 2014;5(1):1-11.
150. Kang H-W, Lee SJ, Ko IK, Kengla C, Yoo JJ, Atala A. A 3D bioprinting system to produce human-scale tissue constructs with structural integrity. *Nat Biotechnol*. 2016;34(3):312-319. doi:10.1038/nbt.3413
151. Kim BS, Jang J, Chae S, et al. Three-dimensional bioprinting of cell-laden constructs with polycaprolactone protective layers for using various thermoplastic polymers. *Biofabrication*. 2016;8(3):35013.
152. Mouser VHM, Levato R, Bonassar LJ, et al. Three-Dimensional Bioprinting and Its Potential in the Field of Articular Cartilage Regeneration. *Cartilage*. 2017;8(4):327-340. doi:10.1177/1947603516665445
153. Ahlfeld T, Doberenz F, Kilian D, et al. Bioprinting of mineralized constructs utilizing multichannel plotting of a self-setting calcium phosphate cement and a cell-laden bioink. *Biofabrication*. 2018;10(4):45002.
154. de Ruijter M, Ribeiro A, Dokter I, Castilho M, Malda J. Converged Biofabrication: Simultaneous Micropatterning of Fibrous Meshes and Bioinks for the Fabrication of Living Tissue Constructs (Adv. Healthcare Mater. 7/2019). *Adv Healthc Mater*. 2019;8(7):1970024. doi:10.1002/adhm.201970024
155. Hrynevich A, Bilge S, Haigh JN, et al. Dimension-Based Design of Melt Electrowritten Scaffolds. 2018:1-6. doi:10.1002/smll.201800232
156. Carrodeguas RG, De Aza S. α -Tricalcium phosphate: Synthesis, properties and biomedical applications. *Acta Biomater*. 2011;7(10):3536-3546.
157. Dziadek M, Kudlackova R, Zima A, et al. Novel multicomponent organic-inorganic WPI/gelatin/CaP hydrogel composites for bone tissue engineering. *J Biomed Mater Res Part A*. 2019;107(11):2479-2491.
158. Sadowska J-M, Guillem-Marti J, Montufar EB, Espanol M, Ginebra M-P. Biomimetic versus sintered calcium phosphates: The in vitro behavior of osteoblasts and mesenchymal stem cells. *Tissue Eng Part A*. 2017;23(23-24):1297-1309.

159. Lode A, Meissner K, Luo Y, et al. Fabrication of porous scaffolds by three-dimensional plotting of a pasty calcium phosphate bone cement under mild conditions. *J Tissue Eng Regen Med*. 2014;8(9):682-693.
160. Epple M. Review of potential health risks associated with nanoscopic calcium phosphate. *Acta Biomater*. 2018;77:1-14.
161. Bobo D, Robinson KJ, Islam J, Thurecht KJ, Corrie SR. Nanoparticle-based medicines: a review of FDA-approved materials and clinical trials to date. *Pharm Res*. 2016;33(10):2373-2387.
162. Zhou H, Lee J. Nanoscale hydroxyapatite particles for bone tissue engineering. *Acta Biomater*. 2011;7(7):2769-2781.
163. Melchels FPW, Blokzijl MM, Levato R, et al. Hydrogel-based reinforcement of 3D bioprinted constructs. *Biofabrication*. 2016;8(3):035004. doi:10.1088/1758-5090/8/3/035004
164. Ginebra M-P, Fernandez E, De Maeyer EAP, et al. Setting reaction and hardening of an apatitic calcium phosphate cement. *J Dent Res*. 1997;76(4):905-912.
165. Karageorgiou V, Kaplan D. Porosity of 3D biomaterial scaffolds and osteogenesis. *Biomaterials*. 2005;26(27):5474-5491.
166. Gleeson JP, Plunkett NA, O'Brien FJ. Addition of hydroxyapatite improves stiffness, interconnectivity and osteogenic potential of a highly porous collagen-based scaffold for bone tissue regeneration. *Eur Cell Mater*. 2010;20(218):30.
167. Levato R, Webb WR, Otto IA, et al. The bio in the ink: cartilage regeneration with bioprintable hydrogels and articular cartilage-derived progenitor cells. *Acta Biomater*. 2017;61:41-53. doi:10.1016/j.actbio.2017.08.005
168. Van Den Bulcke AI, Bogdanov B, De Rooze N, Schacht EH, Cornelissen M, Berghmans H. Structural and Rheological Properties of Methacrylamide Modified Gelatin Hydrogels. *Biomacromolecules*. 2000;1(1):31-38. doi:10.1021/bm990017d
169. Castilho M, Feyen D, Flandes-Iparraguirre M, et al. Melt Electrospinning Writing of Poly-Hydroxymethylglycolide-co-ε-Caprolactone-Based Scaffolds for Cardiac Tissue Engineering. *Adv Healthc Mater*. 2017;6(18):1700311. doi:10.1002/adhm.201700311
170. Schuurman W, Levett PA, Pot MW, et al. Gelatin-methacrylamide hydrogels as potential biomaterials for fabrication of tissue-engineered cartilage constructs. *Macromol Biosci*. 2013;13(5):551-561.
171. Lim KS, Schon BS, Mekhileri N V, et al. New visible-light photoinitiating system for improved print fidelity in gelatin-based bioinks. *ACS Biomater Sci Eng*. 2016;2(10):1752-1762.
172. Lim KS, Levato R, Costa PF, et al. Bio-resin for high resolution lithography-based biofabrication of complex cell-laden constructs. *Biofabrication*. 2018;10(3):34101. doi:10.1088/1758-5090/aac00c
173. Ribeiro A, Blokzijl MM, Levato R, et al. Assessing bioink shape fidelity to aid material development in 3D bioprinting. *Biofabrication*. 2017;10(1):14102.
174. Ajaxon I, Acciaoli A, Lionello G, et al. Elastic properties and strain-to-crack-initiation of calcium phosphate bone cements: Revelations of a high-resolution measurement technique. *J Mech Behav Biomed Mater*. 2017;74:428-437.
175. Hannink G, Arts JJC. Bioresorbability, porosity and mechanical strength of bone substitutes: what is optimal for bone regeneration? *Injury*. 2011;42:S22-S25.
176. Dorozhkin S V. Self-setting calcium orthophosphate formulations. *J Funct Biomater*. 2013;4(4):209-311.
177. Hurtig MB, Buschmann MD, Fortier LA, et al. Preclinical studies for cartilage repair: recommendations from the International Cartilage Repair Society. *Cartilage*. 2011;2(2):137-152.
178. McGowan KB, Stiegman G. Regulatory challenges for cartilage repair technologies. *Cartilage*. 2013;4(1):4-11.
179. Khattak SF, Bhatia SR, Roberts SC. Pluronic F127 as a cell encapsulation material: utilization of membrane-stabilizing agents. *Tissue Eng*. 2005;11(5-6):974-983.
180. Golub EE, Boesze-Battaglia K. The role of alkaline phosphatase in mineralization. *Curr Opin Orthop*. 2007;18(5):444-448.

181. Boere KWM, Visser J, Seyednejad H, et al. Covalent attachment of a three-dimensionally printed thermoplast to a gelatin hydrogel for mechanically enhanced cartilage constructs. *Acta Biomater.* 2014;10(6):2602-2611. doi:10.1016/j.actbio.2014.02.041
182. Shepherd DE, Seedhom BB. The 'instantaneous' compressive modulus of human articular cartilage in joints of the lower limb. *Rheumatology (Oxford).* 1999;38(2):124-132.
183. St-Pierre J-P, Gan L, Wang J, Pilliar RM, Gryn timer MD, Kandel RA. The incorporation of a zone of calcified cartilage improves the interfacial shear strength between in vitro-formed cartilage and the underlying substrate. *Acta Biomater.* 2012;8(4):1603-1615.
184. Daly AC, Critchley SE, Rencsok EM, Kelly DJ. A comparison of different bioinks for 3D bioprinting of fibrocartilage and hyaline cartilage. *Biofabrication.* 2016;8(4):45002. doi:10.1088/1758-5090/8/4/045002
185. Levett PA, Melchels FPW, Schrobback K, Hutmacher DW, Malda J, Klein TJ. Chondrocyte redifferentiation and construct mechanical property development in single-component photocrosslinkable hydrogels. *J Biomed Mater Res A.* 2014;102(8):2544-2553. doi:10.1002/jbm.a.34924
186. Akkineni AR, Luo Y, Schumacher M, Nies B, Lode A, Gelinsky M. 3D plotting of growth factor loaded calcium phosphate cement scaffolds. *Acta Biomater.* 2015;27:264-274.
187. de Ruijter M, Hrynevich A, Haigh JN, et al. Out-of-Plane 3D-Printed Microfibers Improve the Shear Properties of Hydrogel Composites. *Small.* 2018;14(8):1-6. doi:10.1002/smll.201702773
188. Bas O, Elena M D-J-P, Meinert C, et al. Biofabricated soft network composites for cartilage tissue engineering. *Biofabricated soft network composites for cartilage tissue engineering.* *Biofabrication.* 2017.
189. Hurle K, Neubauer J, Bohner M, Doebelin N, Goetz-Neunhoeffler F. Effect of amorphous phases during the hydraulic conversion of α -TCP into calcium-deficient hydroxyapatite. *Acta Biomater.* 2014;10(9):3931—3941. doi:10.1016/j.actbio.2014.03.017
190. Barba A, Diez-Escudero A, Maazouz Y, et al. Osteoinduction by Foamed and 3D-Printed Calcium Phosphate Scaffolds: Effect of Nanostructure and Pore Architecture. *ACS Appl Mater Interfaces.* 2017;9(48):41722-41736. doi:10.1021/acsami.7b14175
191. Van Der Wolk R. Thematic Network on Improving Organ Donation and Transplantation in the EU 2019. 2019.
192. Starzl TE. History of clinical transplantation. *World J Surg.* 2000;24(7):759-782.
193. Moroni L, Burdick JA, Highley C, et al. Biofabrication strategies for 3D in vitro models and regenerative medicine. *Nat Rev Mater.* 2018;3(5):21-37.
194. De Luca M, Aiuti A, Cossu G, Parmar M, Pellegrini G, Robey PG. Advances in stem cell research and therapeutic development. *Nat Cell Biol.* 2019;21(7):801-811.
195. Sart S, Ma T, Li Y. Preconditioning stem cells for in vivo delivery. *Biores Open Access.* 2014;3(4):137-149.
196. Czerniecki SM, Cruz NM, Harder JL, et al. High-throughput screening enhances kidney organoid differentiation from human pluripotent stem cells and enables automated multidimensional phenotyping. *Cell Stem Cell.* 2018;22(6):929-940.
197. Sachs N, Tsukamoto Y, Kujala P, Peters PJ, Clevers H. Intestinal epithelial organoids fuse to form self-organizing tubes in floating collagen gels. *Development.* 2017;144(6):1107-1112.
198. Weiss LE, Merz R, Prinz FB, et al. Shape deposition manufacturing of heterogeneous structures. *J Manuf Syst.* 1997;16(4):239-248.
199. de Ruijter M, Ribeiro A, Dokter I, Castilho M, Malda J. Simultaneous Micropatterning of Fibrous Meshes and Bioinks for the Fabrication of Living Tissue Constructs. *Adv Healthc Mater.* 2019;8(7):1800418. doi:10.1002/adhm.201800418
200. Wei C, Dong J. Hybrid hierarchical fabrication of three-dimensional scaffolds. *J Manuf Process.* 2014;16(2):257-263. doi:https://doi.org/10.1016/j.jmapro.2013.10.003
201. Lee S-J, Nowicki M, Harris B, Zhang LG. Fabrication of a highly aligned neural scaffold via a table top stereolithography 3D printing and electrospinning. *Tissue Eng Part A.* 2017;23(11-12):491-502.

202. Diloksumpan P, de Ruijter M, Castilho M, et al. Combining multi-scale 3D printing technologies to engineer reinforced hydrogel-ceramic interfaces. *Biofabrication*. 2020;12(2):025014. doi:10.1088/1758-5090/ab69d9
203. Ma X, Zhang L, Tan J, et al. Continuous manufacturing of nanofiber yarn with the assistance of suction wind and rotating collection via needleless melt electrospinning. *J Appl Polym Sci*. 2017;134(20).
204. Betsch M, Cristian C, Lin Y, et al. Incorporating 4D into bioprinting: Real-time magnetically directed collagen fiber alignment for generating complex multilayered tissues. *Adv Healthc Mater*. 2018;7(21):1800894.
205. Miri AK, Nieto D, Iglesias L, et al. Microfluidics-enabled multimaterial maskless stereolithographic bioprinting. *Adv Mater*. 2018;30(27):1800242.
206. Lee A, Hudson AR, Shiwardski DJ, et al. 3D bioprinting of collagen to rebuild components of the human heart. *Science (80-)*. 2019;365(6452):482-487.
207. Martin JJ, Fiore BE, Erb RM. Designing bioinspired composite reinforcement architectures via 3D magnetic printing. *Nat Commun*. 2015;6(1):1-7.
208. Hinton TJ, Jallerat Q, Palchesko RN, et al. Three-dimensional printing of complex biological structures by freeform reversible embedding of suspended hydrogels. *Sci Adv*. 2015;1(9):e1500758.
209. Grigoryan B, Paulsen SJ, Corbett DC, et al. Multivascular networks and functional intravascular topologies within biocompatible hydrogels. *Science (80-)*. 2019;364(6439):458-464.
210. Foresti D, Kroll KT, Amissah R, et al. Acoustophoretic printing. *Sci Adv*. 2018;4(8):eaat1659.
211. Chansoria P, Shirwaiker R. characterizing the process physics of Ultrasound-Assisted Bioprinting. *Sci Rep*. 2019;9(1):1-17.
212. Liu F, Wang W, Mirihanage W, Hinduja S, Bartolo PJ. A plasma-assisted bioextrusion system for tissue engineering. *CIRP Ann*. 2018;67(1):229-232.
213. Liu T, Pang Y, Zhou Z, Yao R, Sun W. An integrated cell printing system for the construction of heterogeneous tissue models. *Acta Biomater*. 2019;95:245-257.
214. Skylar-Scott MA, Uzel SGM, Nam LL, et al. Biomanufacturing of organ-specific tissues with high cellular density and embedded vascular channels. *Sci Adv*. 2019;5(9):eaaw2459.
215. Mekhileli NV, Lim KS, Brown GCJ, et al. Automated 3D bioassembly of micro-tissues for biofabrication of hybrid tissue engineered constructs. *Biofabrication*. 2018;10(2):24103. doi:10.1088/1758-5090/aa9ef1
216. Xu T, Binder KW, Albanna MZ, et al. Hybrid printing of mechanically and biologically improved constructs for cartilage tissue engineering applications. *Biofabrication*. 2012;5(1):15001. doi:10.1088/1758-5082/5/1/015001
217. Boccaccio A, Uva AE, Fiorentino M, Lamberti L, Monno G. A mechanobiology-based algorithm to optimize the microstructure geometry of bone tissue scaffolds. *Int J Biol Sci*. 2016;12(1):1.
218. Lee JM, Yeong WY. Design and printing strategies in 3D bioprinting of cell-hydrogels: A review. *Adv Healthc Mater*. 2016;5(22):2856-2865.
219. Castilho M, Rodrigues J, Vorndran E, et al. Computational design and fabrication of a novel bioresorbable cage for tibial tuberosity advancement application. *J Mech Behav Biomed Mater*. 2017;65:344-355.
220. Dias MR, Guedes JM, Flanagan CL, Hollister SJ, Fernandes PR. Optimization of scaffold design for bone tissue engineering: a computational and experimental study. *Med Eng Phys*. 2014;36(4):448-457.
221. Zhao F, Vaughan TJ, McNamara LM. Quantification of fluid shear stress in bone tissue engineering scaffolds with spherical and cubical pore architectures. *Biomech Model Mechanobiol*. 2016;15(3):561-577.
222. Deaton JD, Grandhi R V. A survey of structural and multidisciplinary continuum topology optimization: post 2000. *Struct Multidiscip Optim*. 2014;49(1):1-38.
223. Arabnejad S, Johnston B, Tanzer M, Pasini D. Fully porous 3D printed titanium femoral stem to reduce stress-shielding following total hip arthroplasty. *J Orthop Res*. 2017;35(8):1774-1783.

224. Giorgi M, Verbruggen SW, Lacroix D. In silico bone mechanobiology: modeling a multifaceted biological system. *Wiley Interdiscip Rev Syst Biol Med*. 2016;8(6):485-505.
225. Vetsch JR, Müller R, Hofmann S. The evolution of simulation techniques for dynamic bone tissue engineering in bioreactors. *J Tissue Eng Regen Med*. 2015;9(8):903-917.
226. Bose S, Vahabzadeh S, Bandyopadhyay A. Bone tissue engineering using 3D printing. *Mater today*. 2013;16(12):496-504.
227. Phillips ATM, Villette CC, Modenese L. Femoral bone mesoscale structural architecture prediction using musculoskeletal and finite element modelling. *Int Biomech*. 2015;2(1):43-61.
228. Villette CC, Phillips ATM. Informing phenomenological structural bone remodelling with a mechanistic poroelastic model. *Biomech Model Mechanobiol*. 2016;15(1):69-82.
229. Villette CC, Phillips ATM. Microscale poroelastic metamodel for efficient mesoscale bone remodelling simulations. *Biomech Model Mechanobiol*. 2017;16(6):2077-2091.
230. Hambli R, Katerchi H, Benhamou C-L. Multiscale methodology for bone remodelling simulation using coupled finite element and neural network computation. *Biomech Model Mechanobiol*. 2011;10(1):133-145.
231. Mehrian M, Geris L. Optimizing neotissue growth inside perfusion bioreactors with respect to culture and labor cost: a multi-objective optimization study using evolutionary algorithms. *Comput Methods Biomech Biomed Engin*. 2020;23(7):285-294.
232. Jungst T, Pennings I, Schmitz M, Rosenberg AJWPWP, Groll J, Gawlitta D. Heterotypic scaffold design orchestrates primary cell organization and phenotypes in cocultured small diameter vascular grafts. *Adv Funct Mater*. 2019;29(43):1905987. doi:10.1002/adfm.201905987
233. Saidy NT, Wolf F, Bas O, et al. Biologically inspired scaffolds for heart valve tissue engineering via melt electrowriting. *Small*. 2019;15(24):1900873.
234. D O'Connell C, Di Bella C, Thompson F, et al. Development of the Biopen: a handheld device for surgical printing of adipose stem cells at a chondral wound site. *Biofabrication*. 2016;8(1):15019.
235. Hakimi N, Cheng R, Leng L, et al. Handheld skin printer: in situ formation of planar biomaterials and tissues. *Lab Chip*. 2018;18(10):1440-1451.
236. Berdeu A, Laperrousaz B, Bordy T, et al. Lens-free microscopy for 3D+ time acquisitions of 3D cell culture. *Sci Rep*. 2018;8(1):1-9.
237. Ruland A, Gilmore KJ, Daikuara LY, Fay CD, Yue Z, Wallace GG. Quantitative ultrasound imaging of cell-laden hydrogels and printed constructs. *Acta Biomater*. 2019;91:173-185.
238. Baumann F, Schön M, Eichhoff J, Roller D. Concept development of a sensor array for 3D printer. *Procedia CIRP*. 2016;51(1):24-31.
239. Wang J, Ma Y, Zhang L, Gao RX, Wu D. Deep learning for smart manufacturing: Methods and applications. *J Manuf Syst*. 2018;48:144-156.
240. Groll J, Boland T, Blunk T, et al. Biofabrication: Reappraising the definition of an evolving field. *Biofabrication*. 2016;8(1). doi:10.1088/1758-5090/8/1/013001
241. Melchels FPW, Domingos MAN, Klein TJ, Malda J, Bartolo PJ, Hutmacher DW. Additive manufacturing of tissues and organs. *Prog Polym Sci*. 2012. doi:10.1016/j.progpolymsci.2011.11.007
242. Chang R, Nam J, Sun W. Direct cell writing of 3D microorgan for in vitro pharmacokinetic model. *Tissue Eng Part C Methods*. 2008;14(2):157-166.
243. Hutmacher DW. Biomaterials offer cancer research the third dimension. *Nat Mater*. 2010;9(2):90-93.
244. Derby B. Printing and prototyping of tissues and scaffolds. *Science (80-)*. 2012;338(6109):921-926.
245. Hollander AP, Dickinson SC, Kafienah W. Stem cells and cartilage development: complexities of a simple tissue. *Stem Cells*. 2010;28(11):1992-1996.
246. Ren X, Wang F, Chen C, Gong X, Yin L, Yang L. Engineering zonal cartilage through bioprinting collagen type II hydrogel constructs with biomimetic chondrocyte density gradient. *BMC Musculoskelet Disord*. 2016;17(1):301.
247. Kolesky DB, Truby RL, Gladman AS, Busbee TA, Homan KA, Lewis JA. 3D bioprinting of vascularized, heterogeneous cell-laden tissue constructs. *Adv Mater*. 2014;26(19):3124-3130. doi:10.1002/adma.201305506

248. Byambaa B, Annabi N, Yue K, et al. Bioprinted osteogenic and vasculogenic patterns for engineering 3D bone tissue. *Adv Healthc Mater.* 2017;6(16):1700015.
249. Horváth L, Umehara Y, Jud C, Blank F, Petri-Fink A, Rothen-Rutishauser B. Engineering an in vitro air-blood barrier by 3D bioprinting. *Sci Rep.* 2015;5(1):1-8.
250. Moutos FT, Freed LE, Guilak F. A biomimetic three-dimensional woven composite scaffold for functional tissue engineering of cartilage. *Nat Mater.* 2007;6(2):162-167.
251. Liao I, Moutos FT, Estes BT, Zhao X, Guilak F. Composite three-dimensional woven scaffolds with interpenetrating network hydrogels to create functional synthetic articular cartilage. *Adv Funct Mater.* 2013;23(47):5833-5839.
252. Akbari M, Tamayol A, Laforte V, et al. Composite living fibers for creating tissue constructs using textile techniques. *Adv Funct Mater.* 2014;24(26):4060-4067.
253. Mouser VHM, Abbadessa A, Levato R, et al. Development of a thermosensitive HAMA-containing bio-ink for the fabrication of composite cartilage repair constructs. *Biofabrication.* 2017;9(1):015026. doi:10.1088/1758-5090/aa6265
254. Lee J-S, Hong JM, Jung JW, Shim J-H, Oh J-H, Cho D-W. 3D printing of composite tissue with complex shape applied to ear regeneration. *Biofabrication.* 2014;6(2):24103.
255. Darnell M, Mooney DJ. Leveraging advances in biology to design biomaterials. *Nat Mater.* 2017;16(12):1178-1185.
256. Dalton PD, Brown TD, Hutmacher DW. Melt electrospinning writing fibrous scaffolds for regenerative medicine. In: *JOURNAL OF TISSUE ENGINEERING AND REGENERATIVE MEDICINE.* Vol 6. WILEY-BLACKWELL 111 RIVER ST, HOBOKEN 07030-5774, NJ USA; 2012:372-373.
257. Criscenti G, Vasilevich A, Longoni A, et al. 3D screening device for the evaluation of cell response to different electrospun microtopographies. *Acta Biomater.* 2017;55:310-322.
258. Melchels FPWW, Dhert WJAA, Hutmacher DW, Malda J. Development and characterisation of a new bioink for additive tissue manufacturing. *J Mater Chem B.* 2014;2(16):2282-2289. doi:10.1039/c3tb21280g
259. Klotz BJ, Gawlitta D, Rosenberg AJWP, Malda J, Melchels FPW. Gelatin-methacryloyl hydrogels: towards biofabrication-based tissue repair. *Trends Biotechnol.* 2016;34(5):394-407.
260. Liu W, Zhang YS, Heinrich MA, et al. Rapid continuous multimaterial extrusion bioprinting. *Adv Mater.* 2017;29(3):1604630. doi:10.1002/adma.201604630
261. Zeltinger J, Sherwood JK, Graham DA, Müller R, Griffith LG. Effect of pore size and void fraction on cellular adhesion, proliferation, and matrix deposition. *Tissue Eng.* 2001;7(5):557-572.
262. Malda J, Rouwkema J, Martens DE, et al. Oxygen gradients in tissue-engineered PEGT/PBT cartilaginous constructs: measurement and modeling. *Biotechnol Bioeng.* 2004;86(1):9-18.
263. Prockop DJ. Marrow stromal cells as stem cells for nonhematopoietic tissues. *Science (80-).* 1997;276(5309):71-74.
264. Friedenstein AJ, Gorskaja JF, Kulagina N. Fibroblast precursors in normal and irradiated mouse hematopoietic organs. *Exp Hematol.* 1976;4(5):267.
265. Wakitani S, Saito T, Caplan AL. Myogenic cells derived from rat bone marrow mesenchymal stem cells exposed to 5-azacytidine. *Muscle Nerve Off J Am Assoc Electrodagn Med.* 1995;18(12):1417-1426.
266. Alice J SF, Asheesh B, Scoot A R. The Basic Science of Articular Cartilage : *Sports Health.* 2009;1(6):461-468. doi:10.1177/1941738109350438
267. Mancini IAD, Rieppo L, Pouran B, Afara IO, Braganca FMS. Effects of body mass on microstructural features of the osteochondral unit: A comparative analysis of 37 mammalian species. *Bone.* 2019;127(February):664-673. doi:10.1016/j.bone.2019.07.001
268. Schuurman W, Gawlitta D, Klein TJ, et al. Zonal Chondrocyte Subpopulations Reacquire Zone-Specific Characteristics during in Vitro Redifferentiation. *Am J Sports Med.* 2009;37(1_suppl):97S-104S. doi:10.1177/0363546509350978

269. Kingsbury SR, Gross HJ, Isherwood G, Conaghan PG. Original article Osteoarthritis in Europe : impact on health status , work productivity and use of pharmacotherapies in five European countries. 2020;(January 2014):937-947. doi:10.1093/rheumatology/ket463
270. Richter DL, Jr RCS, Wascher DC. Knee Articular Cartilage Repair and Restoration Techniques : A Review. 2015;8(2):153-160. doi:10.1177/1941738115611350
271. Kraeutler MJ, Belk JW, Purcell JM, Mccarty EC. Microfracture Versus Autologous Chondrocyte Implantation for Articular Cartilage Lesions in the Knee A Systematic Review of 5-Year Outcomes. :995-999. doi:10.1177/0363546517701912
272. Afghah F, Dikyol C, Altunbek M, Koc B. applied sciences Biomimicry in Bio-Manufacturing : Developments in Melt Electrospinning Writing Technology Towards Hybrid Biomanufacturing. 2019.
273. de Ruijter M, Ribeiro A, Dokter I, Castilho M, Malda J. Simultaneous Micropatterning of Fibrous Meshes and Bioinks for the Fabrication of Living Tissue Constructs. *Adv Healthc Mater.* 2018;1800418:1800418. doi:10.1002/adhm.201800418
274. Castilho M, Mouser V, Chen M, Malda J, Ito K. Bi-layered micro-fibre reinforced hydrogels for articular cartilage regeneration. *Acta Biomater.* 2019;95:297-306. doi:10.1016/j.actbio.2019.06.030
275. Onofrillo C, Duchi S, Cathal D, et al. Direct Writing Electrospinning of Scaffoldolds with Multidimensional Fiber Architecture for Hierarchical Tissue Engineering. *Biomaterials.* 2017;197(January):38187-38200. doi:10.1021/acsami.7b07151
276. Castilho M, Ruijter M De, Beirne S, et al. Multitechnology Biofabrication : A New Approach for the Manufacturing of Functional Tissue Structures ? *Trends Biotechnol.* 2020:1-13. doi:10.1016/j.tibtech.2020.04.014
277. Rosell-Illompart J. Ultrafast 3D printing with submicrometer features using electrostatic jet de flection. 2000;(2020):1-9.
278. Wang B, Zhou W, Chang MW, Ahmad Z, Li JS. Impact of substrate geometry on electrospun fiber deposition and alignment. *J Appl Polym Sci.* 2017;134(19):1-11. doi:10.1002/app.44823
279. Yan H, Liu L, Zhang Z. Alignment of electrospun nanofibers using dielectric materials. *Appl Phys Lett.* 2009;95(14). doi:10.1063/1.3242378
280. Ding H, Cao K, Zhang F, Boettcher W, Chang RC. A Fundamental Study of Charge Effects on Melt Electrowritten Polymer Fibers. *Mater Des.* 2019;178:107857. doi:10.1016/j.matdes.2019.107857
281. Castilho M, van Mil A, Maher M, et al. Melt Electrowriting Allows Tailored Microstructural and Mechanical Design of Scaffolds to Advance Functional Human Myocardial Tissue Formation. *Adv Funct Mater.* 2018;28(40):1-10. doi:10.1002/adfm.201803151
282. Wunner FM, Mieszczanek P, Bas O, et al. Printomics: the high-throughput analysis of printing parameters applied to melt electrowriting. *Biofabrication.* 2019;11(2):25004. doi:10.1088/1758-5090/aafc41
283. Mitchell SB, Sanders JE. A unique device for controlled electrospinning. *Wiley Intersci.* 2005. doi:10.1002/jbm.a.30673
284. Brown TD, Edin F, Detta N, Skelton AD, Hutmacher DW, Dalton PD. Melt electrospinning of poly(ϵ -caprolactone) scaffolds: Phenomenological observations associated with collection and direct writing. *Mater Sci Eng C.* 2015;45:698-708. doi:10.1016/j.msec.2014.07.034
285. Woodruff MA, Hutmacher DW. Progress in Polymer Science The return of a forgotten polymer — Polycaprolactone in the 21st century. 2010;35:1217-1256. doi:10.1016/j.progpolymsci.2010.04.002
286. Yang J, Zhang YS, Yue K, Khademhosseini A. Cell-laden hydrogels for osteochondral and cartilage tissue engineering. *Acta Biomater.* 2017;57:1-25. doi:10.1016/j.actbio.2017.01.036
287. Liu M, Zeng X, Ma C, et al. Injectable hydrogels for cartilage and bone tissue engineering. 2017;(November 2016). doi:10.1038/boneres.2017.14
288. Hamadouche M, Sedel L. Ceramics in orthopaedics. *Bone Joint J.* 2014;(April). doi:10.1302/0301-620X.82B8.11744

289. Wei C, Dong J. Development and Modeling of Melt Electrohydrodynamic-Jet Printing of Phase-Change Inks for High-Resolution Additive Manufacturing. *J Manuf Sci Eng.* 2014;136(6):061010. doi:10.1115/1.4028483
290. Wunner FM, Wille ML, Noonan TG, et al. Melt Electrospinning Writing of Highly Ordered Large Volume Scaffold Architectures. *Adv Mater.* 2018;1706570:1-6. doi:10.1002/adma.201706570
291. Liashenko, Ievgenii. Rosell-Illompart, Joan. Cabot A. Ultrafast 3D printing with submicrometer features using electrostatic jet deflection. *Nat Commun.* 2020;11(753):1-9. doi:10.1038/s41467-020-14557-w
292. Moutos FT, Glass KA, Compton SA, et al. Anatomically shaped tissue-engineered cartilage with tunable and inducible anticytokine delivery for biological joint resurfacing. *Proc Natl Acad Sci.* 2016;113(31):E4513 LP-E4522. doi:10.1073/pnas.1601639113
293. Wluka AE, Ding C, Jones G, Cicuttini FM. The clinical correlates of articular cartilage defects in symptomatic knee osteoarthritis: A prospective study. *Rheumatology.* 2005. doi:10.1093/rheumatology/kei018
294. Grande DA, Schwartz JA, Brandel E, Chahine NO, Sgaglione N. Articular Cartilage Repair: Where We Have Been, Where We Are Now, and Where We Are Headed. *Cartilage.* 2013. doi:10.1177/1947603513494402
295. Devitt BM, Bell SW, Whitehead TS. Cartilage Preservation and Restoration Techniques: Evidence-Based Practice. *Manag Knee Osteoarthr Younger, Act Patient.* 2016;51-65.
296. de Windt TS, Vonk LA, Slaper-Cortenbach ICM, et al. Allogeneic Mesenchymal Stem Cells Stimulate Cartilage Regeneration and Are Safe for Single-Stage Cartilage Repair in Humans upon Mixture with Recycled Autologous Chondrons. *Stem Cells.* 2017;35(1):256-264. doi:10.1002/stem.2475
297. Dominici M, Le Blanc K, Mueller I, et al. Minimal criteria for defining multipotent mesenchymal stromal cells. The International Society for Cellular Therapy position statement. *Cytotherapy.* 2006;8(4):315-317. doi:10.1080/14653240600855905
298. Visser J, Gawlitta D, Benders KEM, et al. Endochondral bone formation in gelatin methacrylamide hydrogel with embedded cartilage-derived matrix particles. *Biomaterials.* 2015. doi:10.1016/j.biomaterials.2014.10.020
299. Khan IM, Bishop JC, Gilbert S, Archer CW. Clonal chondroprogenitors maintain telomerase activity and Sox9 expression during extended monolayer culture and retain chondrogenic potential. *Osteoarthr Cartil.* 2009. doi:10.1016/j.joca.2008.08.002
300. Alsalameh S, Amin R, Gemba T, Lotz M. Identification of Mesenchymal Progenitor Cells in Normal and Osteoarthritic Human Articular Cartilage. *Arthritis Rheum.* 2004. doi:10.1002/art.20269
301. McCarthy HE, Bara JJ, Brakspear K, Singhrao SK, Archer CW. The comparison of equine articular cartilage progenitor cells and bone marrow-derived stromal cells as potential cell sources for cartilage repair in the horse. *Vet J.* 2012. doi:10.1016/j.tvjl.2011.08.036
302. Morgan B, Bauza-Mayol G, Gardner O, et al. BMP9 is a potent chondrogenic and morphogenic factor for articular cartilage-derived chondroprogenitors. *Stem Cells Dev.* 2020. doi:10.1089/scd.2019.0209
303. Li Z, Cao B, Wang X, Ye K, Li S, Ding J. Effects of RGD nanospacing on chondrogenic differentiation of mesenchymal stem cells. *J Mater Chem B.* 2015. doi:10.1039/c5tb00455a
304. Feng Q, Wei K, Lin S, et al. Mechanically resilient, injectable, and bioadhesive supramolecular gelatin hydrogels crosslinked by weak host-guest interactions assist cell infiltration and in situ tissue regeneration. *Biomaterials.* 2016. doi:10.1016/j.biomaterials.2016.05.043
305. Mouser VHM, Levato R, Mensinga A, Dhert WJA, Gawlitta D, Malda J. Bio-ink development for three-dimensional bioprinting of hetero-cellular cartilage constructs. *Connect Tissue Res.* 2018;00(00):1-15. doi:10.1080/03008207.2018.1553960
306. Lim KS, Abinzano F, Bernal PN, et al. One-Step Photoactivation of a Dual-Functionalized Bioink as Cell Carrier and Cartilage-Binding Glue for Chondral Regeneration. *Adv Healthc Mater.* 2020. doi:10.1002/adhm.201901792

307. Bertlein S, Hochleitner G, Schmitz M, et al. Permanent Hydrophilization and Generic Bioactivation of Melt Electrowritten Scaffolds. *Adv Healthc Mater.* 2019;8(7):1-8. doi:10.1002/adhm.201801544
308. McMaster R, Hoefner C, Hrynevich A, et al. Tailored Melt Electrowritten Scaffolds for the Generation of Sheet-Like Tissue Constructs from Multicellular Spheroids. *Adv Healthc Mater.* 2019;8(7):e1801326. doi:10.1002/adhm.201801326
309. Hills RL, Belanger LM, Morris EA. Bone morphogenetic protein 9 is a potent anabolic factor for juvenile bovine cartilage, but not adult cartilage. *J Orthop Res.* 2005. doi:10.1016/j.orthres.2004.12.009
310. van Caam A, Madej W, Thijssen E, et al. Expression of TGF β -family signalling components in ageing cartilage: Age-related loss of TGF β and BMP receptors. *Osteoarthr Cartil.* 2016;24(7):1235-1245. doi:10.1016/j.joca.2016.02.008
311. van Caam A, Blaney Davidson E, Garcia de Vinuesa A, et al. The high affinity ALK1-ligand BMP9 induces a hypertrophy-like state in chondrocytes that is antagonized by TGF β 1. *Osteoarthr Cartil.* 2015. doi:10.1016/j.joca.2015.02.007
312. Blunk T, Sieminski AL, Appel B, et al. Bone morphogenetic protein 9: A potent modulator of cartilage development in vitro. *Growth Factors.* 2003. doi:10.1080/0897719031000148822
313. Majumdar MK, Wang E, Morris EA. BMP-2 and BMP-9 promote chondrogenic differentiation of human multipotential mesenchymal cells and overcome the inhibitory effect of IL-1. *J Cell Physiol.* 2001. doi:10.1002/jcp.10025
314. Yan S, Zhang R, Wu K, et al. Characterization of the essential role of bone morphogenetic protein 9 (BMP9) in osteogenic differentiation of mesenchymal stem cells (MSCs) through RNA interference. *Genes Dis.* 2018. doi:10.1016/j.gendis.2018.04.006
315. Lamplot JD, Qin J, Nan G, et al. BMP9 signaling in stem cell differentiation and osteogenesis. *Am J Stem Cells.* 2013.
316. Yu L, Dawson LA, Yan M, et al. BMP9 stimulates joint regeneration at digit amputation wounds in mice. *Nat Commun.* 2019. doi:10.1038/s41467-018-08278-4
317. Dexheimer V, Gabler J, Bomans K, Sims T, Omlor G, Richter W. Differential expression of TGF- β superfamily members and role of Smad1/5/9-signalling in chondral versus endochondral chondrocyte differentiation. *Sci Rep.* 2016. doi:10.1038/srep36655
318. Longobardi L, Li T, Tagliaferro L, et al. Synovial Joints: from Development to Homeostasis. *Curr Osteoporos Rep.* 2015. doi:10.1007/s11914-014-0247-7
319. Daly AC, Kelly DJ. Biofabrication of spatially organised tissues by directing the growth of cellular spheroids within 3D printed polymeric microchambers. *Biomaterials.* 2019;197(January):194-206. doi:10.1016/j.biomaterials.2018.12.028
320. Cosgrove BD, Mui KL, Driscoll TP, et al. N-cadherin adhesive interactions modulate matrix mechanosensing and fate commitment of mesenchymal stem cells. *Nat Mater.* 2016;15(12):1297-1306. doi:10.1038/nmat4725
321. Bian L, Guvendiren M, Mauck RL, Burdick JA. Hydrogels that mimic developmentally relevant matrix and N-cadherin interactions enhance MSC chondrogenesis. *Proc Natl Acad Sci.* 2013;110(25):10117-10122. doi:10.1073/pnas.1214100110
322. Poole AR, Kojima T, Yasuda T, Mwale F, Kobayashi M, Lavery S. Composition and structure of articular cartilage: A template for tissue repair. *Clin Orthop Relat Res.* 2001;(391 SUPPL.):26-33. doi:10.1097/00003086-200110001-00004
323. MacCONAILL MA. The movements of bones and joints; the mechanical structure of articulating cartilage. *J Bone Joint Surg Br.* 1951;33B(2):251-257.
324. You F, Chen X, Cooper DML, Chang T, Eames BF. Homogeneous hydroxyapatite/alginate composite hydrogel promotes calcified cartilage matrix deposition with potential for three-dimensional bioprinting. *Biofabrication.* 2018;11(1):15015. doi:10.1088/1758-5090/aaf44a

325. Apelgren P, Karabulut E, Amoroso M, et al. In Vivo Human Cartilage Formation in Three-Dimensional Bioprinted Constructs with a Novel Bacterial Nanocellulose Bioink. *ACS Biomater Sci Eng.* 2019;5(5):2482-2490. doi:10.1021/acsbiomaterials.9b00157
326. Apelgren P, Amoroso M, Lindahl A, et al. Chondrocytes and stem cells in 3D-bioprinted structures create human cartilage in vivo. *PLoS One.* 2017;12(12):e0189428. doi:10.1371/journal.pone.0189428
327. Kunisch E, Knauf A-K, Hesse E, et al. StarPEG/heparin-hydrogel based in vivo engineering of stable bizonal cartilage with a calcified bottom layer. *Biofabrication.* 2018;11(1):15001. doi:10.1088/1758-5090/aae75a
328. Lee CH, Cook JL, Mendelson A, Moiola EK, Yao H, Mao JJ. Regeneration of the articular surface of the rabbit synovial joint by cell homing: a proof of concept study. *Lancet (London, England).* 2010;376(9739):440-448. doi:10.1016/S0140-6736(10)60668-X
329. Critchley S, Sheehy EJ, Cunniffe G, et al. 3D printing of fiber-reinforced cartilaginous templates for the regeneration of osteochondral defects. *Acta Biomater.* 2020;(xxxx). doi:10.1016/j.actbio.2020.05.040
330. Strauss EJ, Goodrich LR, Chen C-T, Hidaka C, Nixon AJ. Biochemical and biomechanical properties of lesion and adjacent articular cartilage after chondral defect repair in an equine model. *Am J Sports Med.* 2005;33(11):1647-1653. doi:10.1177/0363546505275487
331. Griffin DJ, Bonnevie ED, Lachowsky DJ, et al. Mechanical characterization of matrix-induced autologous chondrocyte implantation (MACI®) grafts in an equine model at 53 weeks. *J Biomech.* 2015;48(10):1944-1949. doi:10.1016/j.jbiomech.2015.04.010
332. Hoemann C, Kandel R, Roberts S, et al. International Cartilage Repair Society (ICRS) Recommended Guidelines for Histological Endpoints for Cartilage Repair Studies in Animal Models and Clinical Trials. *Cartilage.* 2011;2(2):153—172. doi:10.1177/1947603510397535
333. Schindelin J, Arganda-Carreras I, Frise E, et al. Fiji: an open-source platform for biological-image analysis. *Nat Methods.* 2012;9(7):676-682. doi:10.1038/nmeth.2019
334. Doube M, Klosowski MM, Arganda-Carreras I, et al. BoneJ: Free and extensible bone image analysis in ImageJ. *Bone.* 2010;47(6):1076-1079. doi:10.1016/j.bone.2010.08.023
335. Diloksumpan P, Bolaños RV, Cokelaere S, et al. Orthotopic Bone Regeneration within 3D Printed Bioceramic Scaffolds with Region-Dependent Porosity Gradients in an Equine Model. *Adv Healthc Mater.* 2020;9(10):e1901807. doi:10.1002/adhm.201901807
336. Mancini IADD, Vindas Bolaños RA, Brommer H, et al. Fixation of hydrogel constructs for cartilage repair in the equine model: a challenging issue. *Tissue Eng Part C Methods.* 2017;23(11):804-814. doi:10.1089/ten.tec.2017.0200
337. Vindas Bolaños RA, Cokelaere SM, Estrada McDermott JM, et al. The use of a cartilage decellularized matrix scaffold for the repair of osteochondral defects: the importance of long-term studies in a large animal model. *Osteoarthr Cartil.* 2017;25(3):413-420. doi:10.1016/j.joca.2016.08.005
338. Maroudas 1976 - swelling pressure and collagen tension. 1976.
339. Hedegaard CL, Mata A. Integrating self-assembly and biofabrication for the development of structures with enhanced complexity and hierarchical control. *Biofabrication.* 2020;12(3):32002. doi:10.1088/1758-5090/ab84cb
340. Dalton PD, Woodfield TBF, Mironov V, Groll J. Advances in Hybrid Fabrication toward Hierarchical Tissue Constructs. *Adv Sci (Weinheim, Baden-Wuerttemberg, Ger.)* 2020;7(11):1902953. doi:10.1002/advs.201902953
341. Golafshan, Nasim; Vorndran, Elke; Zaharievski, Stefan; Brommer, Harold; Babu Kadumudi, Firoz; Dolatshahi-Pirouz, Alireza; Gbureck, Uwe; van Weeren, René; Castilho, Miguel; Malda J. Tough magnesium phosphate-based 3D printed implants induce bone regeneration in an equine defect model. *Under Rev.*
342. Taylor WR, Ehrig RM, Heller MO, Schell H, Seebeck P, Duda GN. Tibio-femoral joint contact forces in sheep. *J Biomech.* 2006;39(5):791-798. doi:https://doi.org/10.1016/j.jbiomech.2005.02.006
343. Standards EBC, Willson K, Ke D, Kengla C, Atala A, Murphy S V. Chapter 5. 2140.

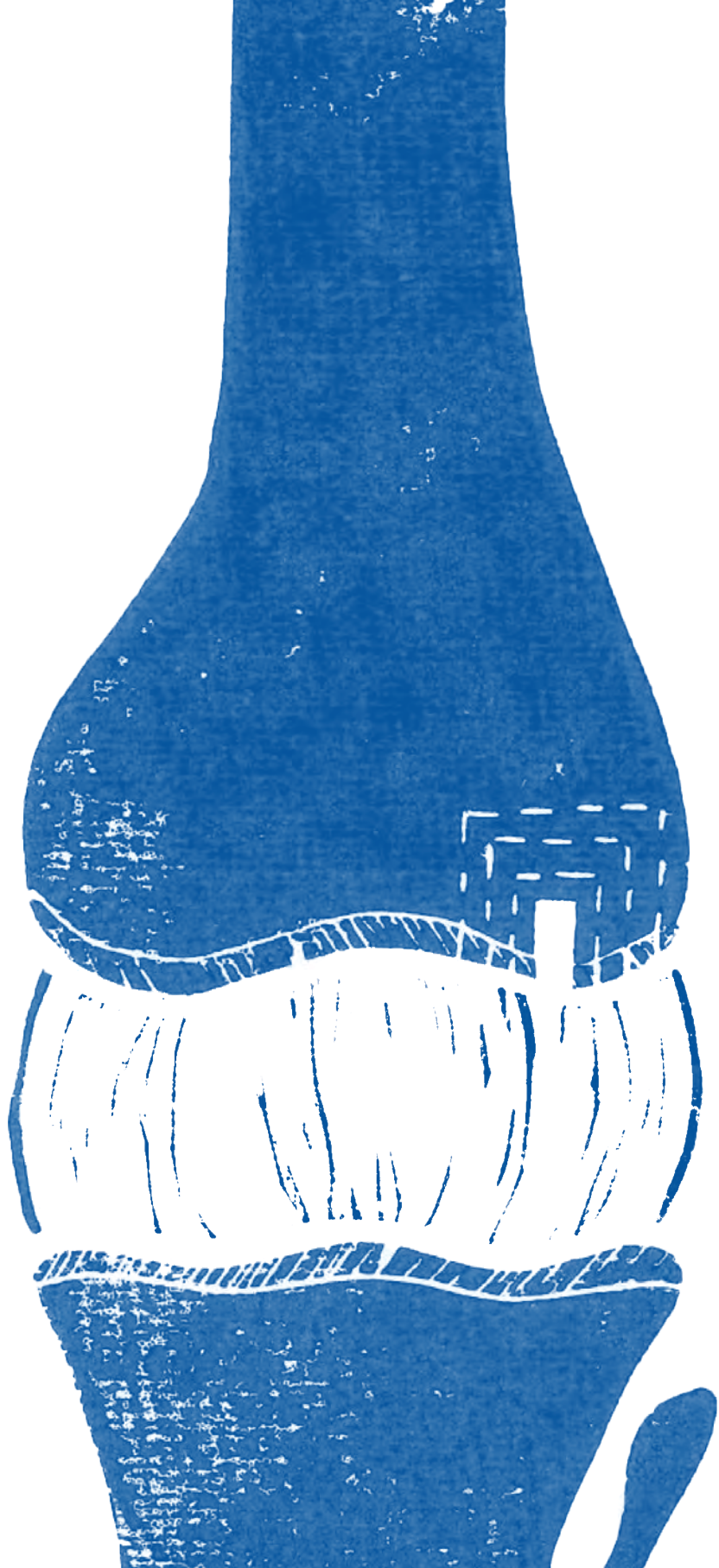
344. Poldervaart MT, Wang H, van der Stok J, et al. Sustained release of BMP-2 in bioprinted alginate for osteogenicity in mice and rats. *PLoS One*. 2013;8(8):e72610. doi:10.1371/journal.pone.0072610
345. Otto IA, Melchels FPW, Zhao X, et al. Auricular reconstruction using biofabrication-based tissue engineering strategies. *Biofabrication*. 2015;7(3):32001. doi:10.1088/1758-5090/7/3/032001
346. Vonk LA, van Dooremalen SFJ, Liv N, et al. Mesenchymal Stromal/stem Cell-derived Extracellular Vesicles Promote Human Cartilage Regeneration In Vitro. *Theranostics*. 2018;8(4):906-920. doi:10.7150/thno.20746
347. Albrektsson T, Becker W, Coli P, Jemt T, Mölne J, Sennerby L. Bone loss around oral and orthopedic implants: An immunologically based condition. *Clin Implant Dent Relat Res*. 2019;21(4):786-795. doi:10.1111/cid.12793
348. Kold SE, Hickman J, Melsen F. An experimental study of the healing process of equine chondral and osteochondral defects. *Equine Vet J*. 1986;18(1):18-24. doi:10.1111/j.2042-3306.1986.tb03529.x
349. Peiffer Q.C., de Ruijter M., van Duijn J., Crottet D., Dominic E., Malda J. CM. Melt electrowriting onto anatomically relevant substrates: Resurfacing a diarthrodial joint. *Under Rev*.
350. Liashenko I, Hrynevich A, Dalton PD. Designing Outside the Box: Unlocking the Geometric Freedom of Melt Electrowriting using Microscale Layer Shifting. *Adv Mater*. May 2020:e2001874. doi:10.1002/adma.202001874
351. Ahearne M. Introduction to cell-hydrogel mechanosensing. *Interface Focus*. 2014;4(2):20130038. doi:10.1098/rsfs.2013.0038
352. Glatt V, Evans CH, Stoddart MJ, Antonio S, Clinic M. orthopaedic regenerative medicine. 2020;37(6):1263-1269. doi:10.1002/jor.24205.Regenerative
353. Jeon JE, Schrobback K, Huttmacher DW, Klein TJ. Dynamic compression improves biosynthesis of human zonal chondrocytes from osteoarthritis patients. *Osteoarthr Cartil*. 2012;20(8):906-915. doi:10.1016/j.joca.2012.04.019
354. Wimmer MA, Grad S, Kaup T, et al. Tribology approach to the engineering and study of articular cartilage. *Tissue Eng*. 2004;10(9-10):1436-1445. doi:10.1089/ten.2004.10.1436
355. Schätti O, Grad S, Goldhahn J, et al. A combination of shear and dynamic compression leads to mechanically induced chondrogenesis of human mesenchymal stem cells. *Eur Cell Mater*. 2011;22:214-225. doi:10.22203/ecm.v022a17
356. Li Z, Yao S-J, Alini M, Stoddart MJ. Chondrogenesis of human bone marrow mesenchymal stem cells in fibrin-polyurethane composites is modulated by frequency and amplitude of dynamic compression and shear stress. *Tissue Eng Part A*. 2010;16(2):575-584. doi:10.1089/ten.TEA.2009.0262
357. Huttmacher DW. Scaffolds in tissue engineering bone and cartilage. *Biomaterials*. 2000;21(24):2529-2543. doi:https://doi.org/10.1016/S0142-9612(00)00121-6
358. Guilak F, Butler DL, Goldstein SA. Functional tissue engineering: the role of biomechanics in articular cartilage repair. *Clin Orthop Relat Res*. 2001;(391 Suppl):S295-305.
359. Ateshian GA. The role of interstitial fluid pressurization in articular cartilage lubrication. *J Biomech*. 2009;42(9):1163-1176. doi:10.1016/j.jbiomech.2009.04.040
360. Kempson GE, Muir H, Swanson SA, Freeman MA. Correlations between stiffness and the chemical constituents of cartilage on the human femoral head. *Biochim Biophys Acta*. 1970;215(1):70-77. doi:10.1016/0304-4165(70)90388-0
361. Mow VC, Holmes MH, Michael Lai W. Fluid transport and mechanical properties of articular cartilage: A review. *J Biomech*. 1984;17(5):377-394. doi:10.1016/0021-9290(84)90031-9
362. Cohen NP, Foster RJ, Mow VC. Composition and dynamics of articular cartilage: Structure, function, and maintaining healthy state. *J Orthop Sports Phys Ther*. 1998;28(4):203-215. doi:10.2519/jospt.1998.28.4.203
363. Eyre DR, Weis MA, Wu JJ. Articular cartilage collagen: An irreplaceable framework? *Eur Cells Mater*. 2006;12:57-63. doi:10.22203/eCM.v012a07

364. Vaughan L, Mendler M, Huber S, et al. D-periodic distribution of collagen type IX along cartilage fibrils. *J Cell Biol.* 1988;106(3):991-997. doi:10.1083/jcb.106.3.991
365. Kapyla J, Jaalinoja J, Tulla M, et al. The fibril-associated collagen IX provides a novel mechanism for cell adhesion to cartilaginous matrix. *J Biol Chem.* 2004;279(49):51677-51687. doi:10.1074/jbc.M409412200
366. Florczak S, Lorson T, Zheng T, et al. Melt electrowriting of electroactive poly (vinylidene difluoride) fibers. 2019;(November 2018). doi:10.1002/pi.5759
367. Haigh JN, Dargaville TR, Dalton PD. Additive manufacturing with polypropylene microfibers. *Mater Sci Eng C.* 2017;77:883-887. doi:10.1016/j.msec.2017.03.286
368. Wunner FM, Eggert S, Maartens J, et al. Design and Development of a Three-Dimensional Printing High-Throughput Melt Electrowriting Technology Platform. *3D Print Addit Manuf.* 2019;6(2):82-90. doi:10.1089/3dp.2017.0149
369. Koenig K, Beukenberg K, Langensiepen F, Seide G. A new prototype melt-electrospinning device for the production of biobased thermoplastic sub-microfibers and nanofibers. *Biomater Res.* 2019;23:10. doi:10.1186/s40824-019-0159-9
370. SalehHudin HS, Mohamad EN, Mahadi WNL, Muhammad Afifi A. Multiple-jet electrospinning methods for nanofiber processing: A review. *Mater Manuf Process.* 2018;33(5):479-498. doi:10.1080/10426914.2017.1388523
371. Li X, Zhang Y, Li H, Chen H, Ding Y, Yang W. Effect of oriented fiber membrane fabricated via needleless melt electrospinning on water filtration efficiency. *Desalination.* 2014;344:266-273. doi:10.1016/j.desal.2014.04.003
372. Gong J, Schuurmans CCLL, Genderen AM van, et al. Complexation-induced resolution enhancement of 3D-printed hydrogel constructs. *Nat Commun.* 2020;11(1):1-14. doi:10.1038/s41467-020-14997-4
373. Bernal PN, Delrot P, Loterie D, et al. Volumetric Bioprinting of Complex Living-Tissue Constructs within Seconds. *Adv Mater.* 2019;31(42). doi:10.1002/adma.201904209
374. Nahm D, Weigl F, Schaefer N, et al. A versatile biomaterial ink platform for the melt electrowriting of chemically-crosslinked hydrogels. *Mater Horizons.* 2020;7(3):928-933. doi:10.1039/c9mh01654f
375. Idaszek J, Costantini M, Karlsen TA, et al. 3D bioprinting of hydrogel constructs with cell and material gradients for the regeneration of full-thickness chondral defect using a microfluidic printing head. *Biofabrication.* 2019;11(4):44101. doi:10.1088/1758-5090/ab2622
376. Skylar-Scott MA, Mueller J, Visser CW, Lewis JA. Voxelated soft matter via multimaterial multinozzle 3D printing. *Nature.* 2019;575(7782):330-335. doi:10.1038/s41586-019-1736-8
377. Coad BR, Jasieniak M, Griesser SS, Griesser HJ. Controlled covalent surface immobilisation of proteins and peptides using plasma methods. *Surf Coatings Technol.* 2013;233:169-177. doi:10.1016/j.surfcoat.2013.05.019
378. Stewart CAC, Akhavan B, Hung J, et al. Multifunctional Protein-Immobilized Plasma Polymer Films for Orthopedic Applications. *ACS Biomater Sci Eng.* 2018;4(12):4084-4094. doi:10.1021/acsbmaterials.8b00954
379. Tognato R, Armiento AR, Bonfrate V, et al. A Stimuli-Responsive Nanocomposite for 3D Anisotropic Cell-Guidance and Magnetic Soft Robotics. *Adv Funct Mater.* 2019;29(9):1-10. doi:10.1002/adfm.201804647
380. McColl E, Groll J, Jungst T, Dalton PD. Design and fabrication of melt electrowritten tubes using intuitive software. *Mater Des.* 2018;155:46-58. doi:10.1016/j.matdes.2018.05.036
381. Chimene D, Kaunas R, Gaharwar AK. Hydrogel bioink reinforcement for additive manufacturing: a focused review of emerging strategies. *Adv Mater.* 2020;32(1):1902026.
382. Frisbie DD, McCarthy HE, Archer CW, Barrett MF, McIlwraith CW. Evaluation of articular cartilage progenitor cells for the repair of articular defects in an equine model. *J Bone Jt Surg - Am Vol.* 2015;97(6):484-493. doi:10.2106/JBJS.N.00404

383. Slynarski K, de Jong WC, Snow M, Hendriks JAA, Wilson CE, Verdonk P. Single-Stage Autologous Chondrocyte-Based Treatment for the Repair of Knee Cartilage Lesions: Two-Year Follow-up of a Prospective Single-Arm Multicenter Study. *Am J Sports Med.* 2020;48(6):1327-1337. doi:10.1177/0363546520912444
384. Makris EA, Gomoll AH, Malizos KN, Hu JC, Athanasiou KA. Repair and tissue engineering techniques for articular cartilage. *Nat Rev Rheumatol.* 2015;11(1):21-34. doi:10.1038/nrrheum.2014.157
385. Mastbergen SC, Saris DBF, Lafeber FPJG. Functional articular cartilage repair: here, near, or is the best approach not yet clear? *Nat Rev Rheumatol.* 2013;9(5):277-290. doi:10.1038/nrrheum.2013.29
386. Lee CH, Cook JL, Mendelson A, et al. Regeneration of the articular surface of the rabbit synovial joint by cell homing: a proof of concept study. *Lancet (London, England).* 2010;376(9739):440-448. doi:10.1016/S0140-6736(10)60668-X
387. Smith DW, Gardiner BS, Davidson JB, Grodzinsky AJ. Computational model for the analysis of cartilage and cartilage tissue constructs. *J Tissue Eng Regen Med.* 2016;10(4):334-347.
388. Ap Gwynn I, Wade S, Ito K, Richards RG, Archer C. Novel aspects to the structure of rabbit articular cartilage. *Eur Cells Mater.* 2002;4:18-29. doi:10.22203/eCM.v004a02
389. Salonius E, Rieppo L, Nissi MJ, et al. Critical-sized cartilage defects in the equine carpus. *Connect Tissue Res.* 2019;60(2):95-106. doi:10.1080/03008207.2018.1455670
390. Li Z, Kupcsik L, Yao S-J, Alini M, Stoddart MJ. Mechanical load modulates chondrogenesis of human mesenchymal stem cells through the TGF-beta pathway. *J Cell Mol Med.* 2010;14(6A):1338-1346. doi:10.1111/j.1582-4934.2009.00780.x
391. O'Donnell BT, Ives CJ, Mohiuddin OA, Bunnell BA. Beyond the Present Constraints That Prevent a Wide Spread of Tissue Engineering and Regenerative Medicine Approaches. *Front Bioeng Biotechnol.* 2019;7:95. doi:10.3389/fbioe.2019.00095
392. Athanasiou KA, Agarwal A, Dzida FJ. Comparative study of the intrinsic mechanical properties of the human acetabular and femoral head cartilage. *J Orthop Res.* 1994;12(3):340-349. doi:10.1002/jor.1100120306
393. Denayer T, Stöhrn T, Van Roy M. Animal models in translational medicine: Validation and prediction. *New Horizons Transl Med.* 2014;2(1):5-11. doi:10.1016/j.nhtms.2014.08.001
394. Piluso S, Li Y, Abinzano F, et al. Mimicking the Articular Joint with In Vitro Models. *Trends Biotechnol.* 2019;37(10):1063-1077. doi:10.1016/j.tibtech.2019.03.003
395. Zhang YS, Aleman J, Shin SR, et al. Multisensor-integrated organs-on-chips platform for automated and continual in situ monitoring of organoid behaviors. *Proc Natl Acad Sci U S A.* 2017;114(12):E2293-E2302. doi:10.1073/pnas.1612906114
396. Lin H, Lozito TP, Alexander PG, Gottardi R, Tuan RS. Stem cell-based microphysiological osteochondral system to model tissue response to interleukin-1B. *Mol Pharm.* 2014;11(7):2203-2212. doi:10.1021/mp500136b
397. Lozito TP, Alexander PG, Lin H, Gottardi R, Cheng AW, Tuan RS. Osteoarthritis is a disease of the osteochondral junction. 2010;4(Suppl 1):1-6. <http://stemcellres.com/content/4/S1/S6>.
398. Jusoh N, Oh S, Kim S, Kim J, Jeon NL. Microfluidic vascularized bone tissue model with hydroxyapatite-incorporated extracellular matrix. *Lab Chip.* 2015;15(20):3984-3988. doi:10.1039/c5lc00698h
399. Melrose J, Smith S, Cake M, Read R, Whitelock J. Comparative spatial and temporal localisation of perlecan, aggrecan and type I, II and IV collagen in the ovine meniscus: An ageing study. *Histochem Cell Biol.* 2005;124(3-4):225-235. doi:10.1007/s00418-005-0005-0
400. McDevitt CA, Webber RJ. The ultrastructure and biochemistry of meniscal cartilage. *Clin Orthop Relat Res.* 1990;(252):8-18. doi:10.1097/NCN.0b013e31823ea54e
401. Herwig J, Egner E, Buddecke E. Chemical changes of human knee joint menisci in various stages of degeneration. *Ann Rheum Dis.* 1984;43(4):635-640. doi:10.1136/ard.43.4.635
402. Petersen W, Tillmann B. Collagenous fibril texture of the human knee joint menisci. *Anat Embryol (Berl).* 1998;(197):317-324.

403. King D. The healing of semilunar cartilages. 1936. *Clin Orthop Relat Res.* 1990;(252):4-7.
404. Starke C, Kopf S, Petersen W, et al. Meniscal repair. *Arthroscopy.* 2009;25(9):1033-1044. doi:10.1016/j.arthro.2008.12.010
405. Englund M, Roemer FW, Hayashi D, Crema MD, Guermazi A. Meniscus pathology, osteoarthritis and the treatment controversy. *Nat Rev Rheumatol.* 2012;8(7):412-419. doi:10.1038/nrrheum.2012.69
406. McDermott I, Amis A. The consequences of meniscectomy. *J Bone Joint Surg Br.* 2006;88(12):1549-1556. doi:10.1302/0301-620X.88B12.18140
407. Englund M, Roos EM, Lohmander LS. Impact of type of meniscal tear on radiographic and symptomatic knee osteoarthritis: A sixteen-year followup of meniscectomy with matched controls. *Arthritis Rheum.* 2003;48(8):2178-2187. doi:10.1002/art.11088
408. Waugh N, Mistry H, Metcalfe A, et al. Meniscal allograft transplantation after meniscectomy: clinical effectiveness and cost-effectiveness. *Knee Surgery, Sport Traumatol Arthrosc.* 2019;27(6):1825-1839. doi:10.1007/s00167-019-05504-4
409. ElAttar M, Dhollander A, Verdonk R, Almqvist KF, Verdonk P. Twenty-six years of meniscal allograft transplantation: Is it still experimental? A meta-analysis of 44 trials. *Knee Surgery, Sport Traumatol Arthrosc.* 2011;19(2):147-157. doi:10.1007/s00167-010-1351-6
410. Zaffagnini S, Giordano G, Vascellari A, et al. Arthroscopic collagen meniscus implant results at 6 to 8 years follow up. *Knee Surgery, Sport Traumatol Arthrosc.* 2007;15(2):175-183. doi:10.1007/s00167-006-0144-4
411. Yusuke Nakagawa, Lisa A. Fortier, Jeremy J. Maolchiro Sekiya SA. 3D-printed artificial meniscus. *Bio-orthopaedics A New Approach.* 2017:419-433. doi:10.1007/978-3-662-54181-4
412. Murphy CA, Costa JB, Silva-Correia J, Oliveira JM, Reis RL, Collins MN. Biopolymers and polymers in the search of alternative treatments for meniscal regeneration: State of the art and future trends. *Appl Mater Today.* 2018;12:51-71. doi:10.1016/j.apmt.2018.04.002
413. Chansoria P, Narayanan LK, Schuchard K, Shirwaiker R. Ultrasound-assisted biofabrication and bioprinting of preferentially aligned three-dimensional cellular constructs. *Biofabrication.* 2019;11(3):35015. doi:10.1088/1758-5090/ab15cf
414. Lee CH, Rodeo SA, Fortier LA, Lu C, Eriskin C, Mao JJ. Protein-releasing polymeric scaffolds induce fibrochondrocytic differentiation of endogenous cells for knee meniscus regeneration in sheep. *Sci Transl Med.* 2014;6(266):266ra171. doi:10.1126/scitranslmed.3009696
415. Warren PB, Huebner P, Spang JT, Shirwaiker RA, Fisher MB. Engineering 3D-Bioploted scaffolds to induce aligned extracellular matrix deposition for musculoskeletal soft tissue replacement. *Connect Tissue Res.* 2017;58(3-4):342-354. doi:10.1080/03008207.2016.1276177
416. Sooriyaarachchi D, Wu J, Feng A, Islam M, Tan GZ. Hybrid Fabrication of Biomimetic Meniscus Scaffold by 3D Printing and Parallel Electrospinning. *Procedia Manuf.* 2019;34:528-534. doi:https://doi.org/10.1016/j.promfg.2019.06.216
417. de Windt T, Vonk L, Slaper-Crtenbach I, et al. Allogeneic MSCs and recycled autologous chondrons mixed in a one-stage cartilage cell transplantation: a first-in-man trial in 35 patients. *Stem Cells.* 2017;35(8):1984-1993.
418. Hagmeijer M, Vonk L, Fenu M, van Keep Y, Krych A, Saris D. Meniscus regeneration combining meniscus and mesenchymal stromal cells in a degradable meniscus implant: an in vitro study. *Eur Cells Mater.* 2019;38:51-62. doi:10.22203/eCM.v038a05
419. Federa. Human Tissue and Medical Research: Code of Conduct for responsible use.
420. Pi Q, Maharjan S, Yan X, et al. Digitally Tunable Microfluidic Bioprinting of Multilayered Cannular Tissues. *Adv Mater.* 2018;30(43):1-10. doi:10.1002/adma.201706913
421. Beldjilali-Labro M, Garcia Garcia A, Farhat F, et al. Biomaterials in Tendon and Skeletal Muscle Tissue Engineering: Current Trends and Challenges. *Mater (Basel, Switzerland).* 2018;11(7). doi:10.3390/ma11071116

422. Rossetti L, Kuntz LA, Kunold E, et al. The microstructure and micromechanics of the tendon-bone insertion. *Nat Mater*. 2017;16(6):664-670. doi:10.1038/nmat4863
423. ICRS cartilage injury evaluation package. https://cartilage.org/society/publications/icrs-score/icrs_evaluation/. Accessed July 14, 2020.
424. The third industrial revolution. *Econ*. 2012.
425. Wilson WCJ, Boland T. Cell and organ printing 1: protein and cell printers. *Anat Rec A Discov Mol Cell Evol Biol*. 2003;272(2):491-496. doi:10.1002/ar.a.10057
426. Keriquel V, Guillemot F, Arnault I, et al. In vivo bioprinting for computer- and robotic-assisted medical intervention: preliminary study in mice. *Biofabrication*. 2010;2(1):14101. doi:10.1088/1758-5082/2/1/014101
427. Nakamura M, Kobayashi A, Takagi F, et al. Biocompatible inkjet printing technique for designed seeding of individual living cells. *Tissue Eng*. 2005;11(11-12):1658-1666. doi:10.1089/ten.2005.11.1658
428. Hull CW, Arcadia, Calif. United States Patent (19). 1984;(19):16.
429. Melchels FPW, Feijen J, Grijpma DW. A review on stereolithography and its applications in biomedical engineering. *Biomaterials*. 2010;31(24):6121-6130. doi:https://doi.org/10.1016/j.biomaterials.2010.04.050
430. Colosi C, Shin SR, Manoharan V, et al. Microfluidic Bioprinting of Heterogeneous 3D Tissue Constructs Using Low-Viscosity Bioink. *Adv Mater*. 2016;28(4):677-684a. doi:10.1002/adma.201503310
431. Jungst T, Smolan W, Schacht K, Scheibel T, Groll J. Strategies and Molecular Design Criteria for 3D Printable Hydrogels. *Chem Rev*. 2016;116(3):1496-1539. doi:10.1021/acs.chemrev.5b00303
432. Kristen M, Ainsworth MJ, Chirico N, et al. Fiber Scaffold Patterning for Mending Hearts: 3D Organization Bringing the Next Step. *Adv Healthc Mater*. 2020;9(1). doi:10.1002/adhm.201900775
433. Hoch E, Tovar GEM, Borchers K. Bioprinting of artificial blood vessels: Current approaches towards a demanding goal. *Eur J Cardio-thoracic Surg*. 2014;46(5):767-778. doi:10.1093/ejcts/ezu242
434. van der Valk DC, van der Ven CFT, Blaser MC, et al. Engineering a 3d-bioprinted model of human heart valve disease using nanoindentation-based biomechanics. *Nanomaterials*. 2018;8(5). doi:10.3390/nano8050296
435. Yanez M, Rincon J, Dones A, De Maria C, Gonzales R, Boland T. In vivo assessment of printed microvasculature in a bilayer skin graft to treat full-thickness wounds. *Tissue Eng Part A*. 2015;21(1-2):224-233.
436. Kingsley DM, Roberge CL, Rudkouskaya A, et al. Laser-based 3D bioprinting for spatial and size control of tumor spheroids and embryoid bodies. *Acta Biomater*. 2019;95:357-370.
437. Duan B, Hockaday LA, Kang KH, Butcher JT. 3D bioprinting of heterogeneous aortic valve conduits with alginate/gelatin hydrogels. *J Biomed Mater Res Part A*. 2013;101(5):1255-1264.
438. Gudapati H, Dey M, Ozbolat I. A comprehensive review on droplet-based bioprinting: past, present and future. *Biomaterials*. 2016;102:20-42.
439. Ouyang L, Highley CB, Sun W, Burdick JA. A generalizable strategy for the 3D bioprinting of hydrogels from nonviscous photo-crosslinkable inks. *Adv Mater*. 2017;29(8):1604983.
440. He J, Zhao X, Chang J, Li D. Microscale Electro-Hydrodynamic Cell Printing with High Viability. *Small*. 2017;13(47):1702626.



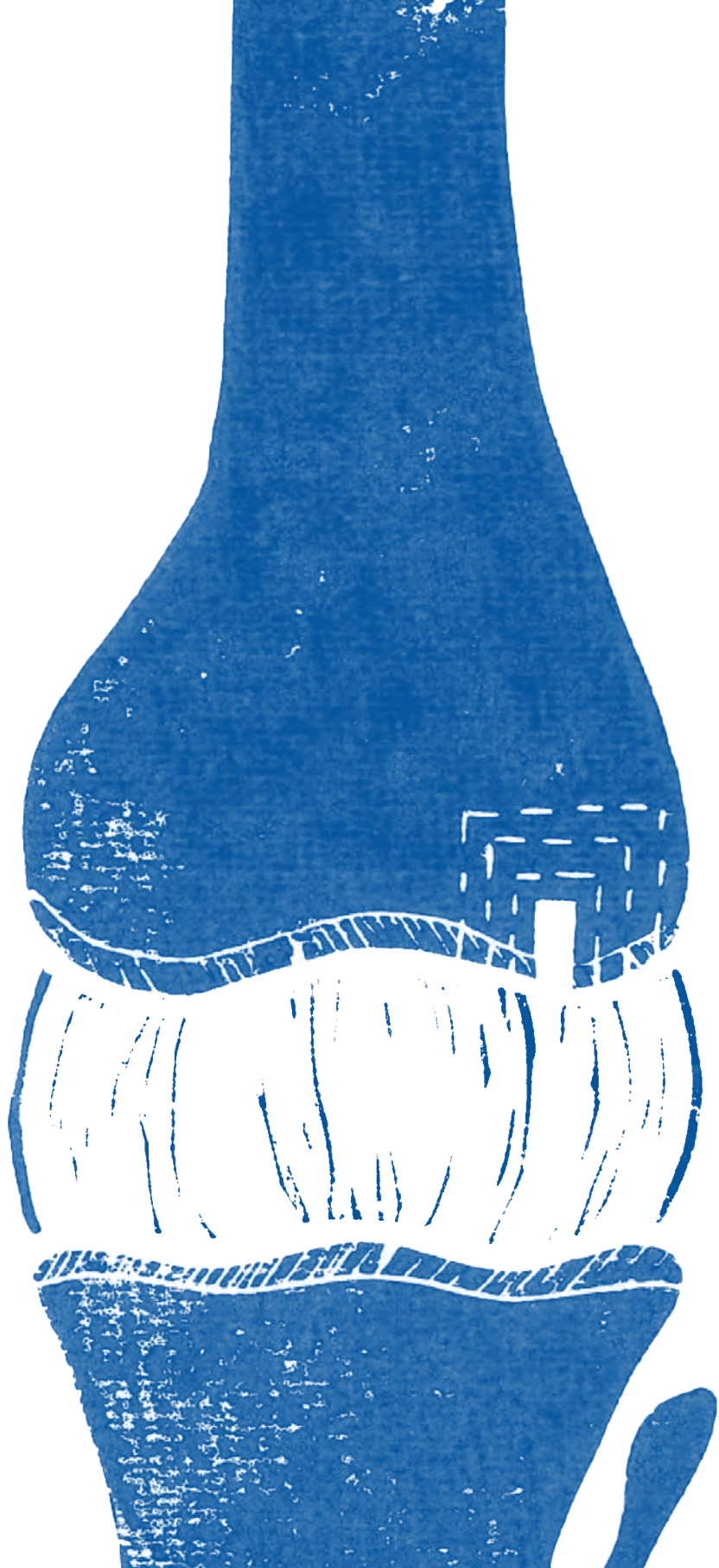
List of abbreviations

A

List of abbreviations

2D	Two-dimensional
3D	Three-dimensional
AC	Articular cartilage
ACI	Autologous chondrocyte implantation
ACPC	Articular cartilage-resident progenitor cell
AM	Additive manufacturing
ASAP	L-ascorbic acid-2-phosphate
BMP-9	Bone morphogenic protein 9
CAD	Computer aided design
CAM	Computer aided manufacturing
CD	Collector distance
CT	Computed tomography
CTS	Critical translation speed
DLP	Digital light processing
DMA	Dynamic mechanical analysis
DMEM	Dulbecco's modified eagle medium
DMSO	Dimethylsulphoxide
DNA	Deoxyribonucleic acid
EBP	Extrusion based bioprinting
ECM	Extra cellular matrix
EDTA	Ethylenediaminetetraacetic acid
FBS	Fetal bovine serum
FDM	Fused deposition modelling
FGF	Fibroblast growth factor
GAG	Glycosaminoglycan
gelMA	gelatin methacryloyl
GMP	Good manufacturing practice
HA	Hyaluronic acid
HAMA	Methacrylated hyaluronic acid
ICRS	International cartilage regeneration & joint preservation society
IFD	Inter fibre distance
IHC	Immunohistochemistry
ITS-X	Insulin-transferrin-selenium-ethanolamine
MA	Methacrylate
MACI	Matrix-induced autologous chondrocyte implantation

MEW	Melt electrowriting
MMA	Polymethylmethacrylate
MSC	Mesenchymal stromal cell
NaOH	Sodium hydroxide
NEAA	non-essential amino acids solution
OA	Osteoarthritis
OAG	Osteochondral allografting
OAT	Osteochondral autologous transplantation
OC	Osteochondral
PAAM	Poly acrylamide
PBS	Phosphate-buffered saline
PCL	Polycaprolactone
pHEMA	poly(2-hydroxyethyl methacrylate)
PID	Proportional integral derivative
PTA	Programmed translation accuracy
RNA	Ribonucleic acid
SEM	Scanning electron microscopy
SES	Solution electrospinning
STL	Standard tessellation language
TE	Tissue engineering
TEMED	Tetramethylethylenediamide
TGF- β 1	Transforming growth factor beta
TKR	Total knee replacement
USA	United States of America
UV	Ultra violet
WOMAC	Western Ontario and McMaster universities osteoarthritis index



Summary

Summary

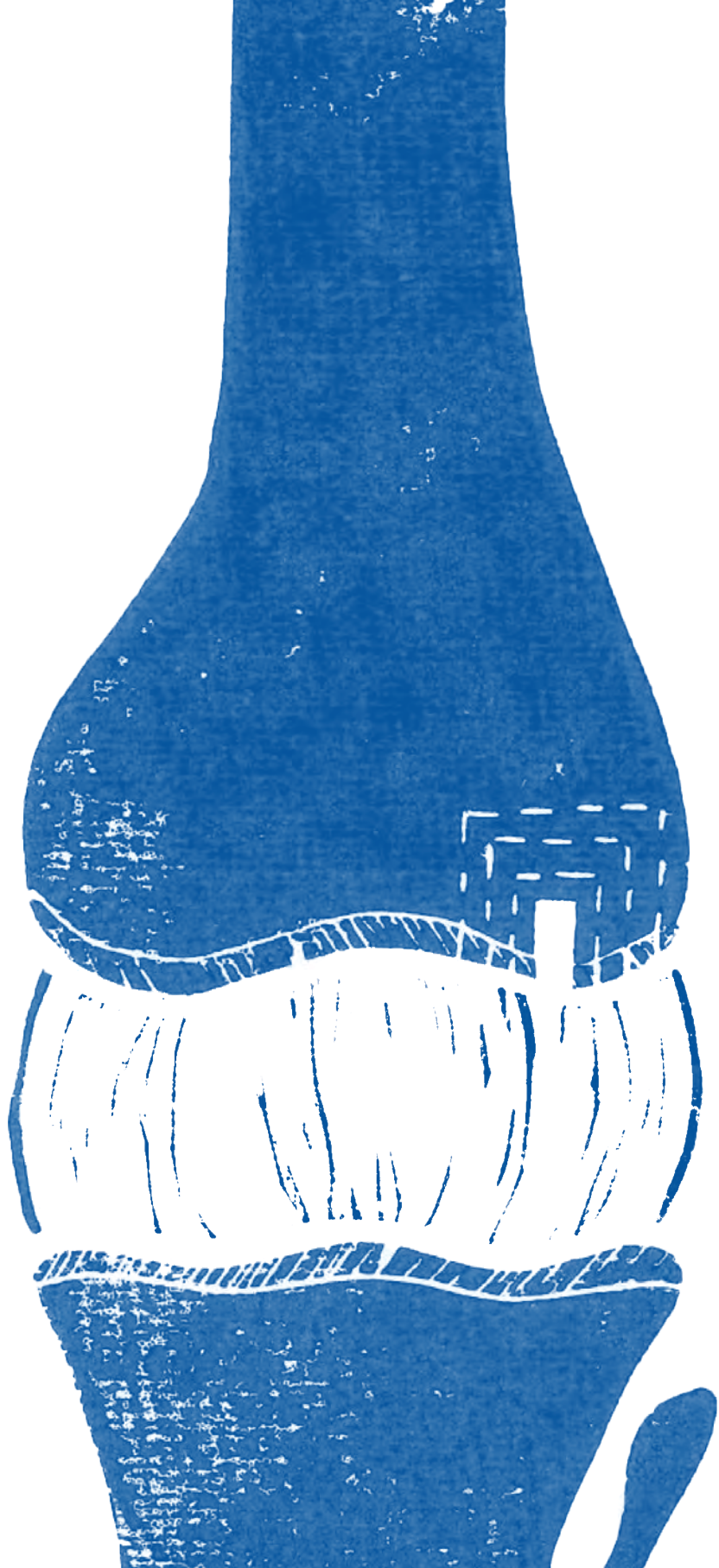
In the quest to find new treatments for (osteo)chondral defects and to eliminate or postpone total knee replacement surgery, the potential of 3D bioprinting for the fabrication of biodegradable, patient-specific (osteo)chondral implants has been explored. The overarching aim of this thesis was to fabricate a functional (osteo)chondral implant, inspired by native tissue architecture and use of biodegradable materials, by combining advanced 3D (bio)fabrication technologies.

Part I demonstrated how melt electrowriting (MEW) was used to improve the mechanical properties of (osteo)chondral implants. It was previously shown that incorporation of organised microfibre meshes in hydrogel-based cartilage constructs results in increased compressive properties. Here, it was shown that microfibres, deposited in an out-of-plane fashion, improve the shear properties of hydrogel scaffolds while using only a limited volume fraction of biodegradable polymer fibres (**Chapter 2**). Additionally, microfibre meshes were used to improve the interconnection between the cartilage-to-bone interface by interlocking them within a printed calcium phosphate-based (pCaP) bone cement structure (**Chapter 3**).

To further address the zonal structure and composition of the native cartilage tissue through the layered deposition of cells and matrix components, the incorporation of the MEW-based production of microfibres within the bioprinting process was explored in **Part II**. First, the state-of-the-art concept of combining different manufacturing processes into a single biofabrication platform was reviewed and future perspectives of such approaches were discussed (**Chapter 4**). Further, it demonstrated, for the first time, the successful convergence of MEW and extrusion-based bioprinting into a single printing platform enabling control over the fibrous and non-fibrous components of chondral grafts (**Chapter 5**). Moreover, the potential of this converged approach for resurfacing anatomically relevant structures and clinically relevant materials was demonstrated. The importance of ensuring a constant electrical field strength and directing the electrical force normal to the collecting structure for accurate microfibre patterning on non-planar surfaces was shown (**Chapter 6**).

Part III subsequently addressed the pre-clinical application of the developed multi-scale (bio)fabrication approaches. First, it was shown that bone morphogenetic protein 9 (BMP-9) can be used to stimulate articular cartilage resident chondroprogenitor cells (ACPCs) to produce large quantities of reinforced cartilage-like matrix in a time-efficient manner which holds promise for the clinical translation of large biofabricated implants (**Chapter 7**). Next, long-term *in vivo* evaluation showed that pre-cultured osteochondral

plugs with hierarchy in both cell density and microfibre organization were stable enough to withstand the mechanically challenging environment of the stifle joint in an equine model. This study highlights the importance of structural reinforcement and suggests that the use of transplanted cells is, in fact, secondary to the presence of a mechanically stable structure (**Chapter 8**). Upscaling from relatively small osteochondral plugs to larger patient-specific implants demonstrated that the size of the implants significantly affected the stiffness of the implants and that the design of the implant should take into account the position of implantation to effectively restore mechanical functioning of the joint. Additionally, this study introduced a new computer aided design (CAD) to computer aided manufacturing (CAM) software tool to more easily generate the MEW printing trajectory for the resurfacing of patient-specific geometries (**Chapter 9**). Taken together, this thesis shows accurate fabrication of an osteochondral implant, inspired by native tissue architecture, and demonstrates the potential of using converged biofabrication strategies for the treatment of joint defects.



Nederlandse samenvatting

In de zoektocht naar nieuwe behandelingen ten behoeve van (osteo)chondrale defecten waardoor metalen totale knie prothesen uit te stellen of te elimineren zijn, is de potentie van 3D bioprinten voor de fabricatie van biodegradeerbare, patiënt-specifieke (osteo)chondrale implantaten onderzocht. Het overkoepelende doel van dit proefschrift was het fabriceren van een functioneel (osteo)chondraal implantaat, geïnspireerd door de natuurlijke weefsel architectuur en gemaakt van biodegradeerbare materialen, door het combineren van vergevorderde 3D(bio)fabricatie technologieën.

Deel I demonstreerde hoe melt electrowriting (MEW) gebruikt is om de mechanische eigenschappen van (osteo)chondrale implantaten te verbeteren. Voorheen is laten zien dat het incorporeren van georganiseerde micro-vezel matjes in hydrogel scaffolds resulteerde in verhoogde compressieve eigenschappen. In dit proefschrift is gedemonstreerd dat deze techniek tevens gebruikt kan worden om vezels te printen die een “out-of-plane” ontwerp hebben en hierdoor een verhoogde resistentie tegen afschuifkrachten geven wanneer deze micro-vezels gecombineerd worden met hydrogelen (**Hoofdstuk 2**). Micro-vezel matjes zijn tevens gecombineerd met een printbaar calcium-fosfaat-gebaseerd bot-achtig cement (pCaP) om de interconnectie tussen gefabriceerd kraakbeen-achtig weefsel en gefabriceerd bot-achtig weefsel te verstevigen (**Hoofdstuk 3**).

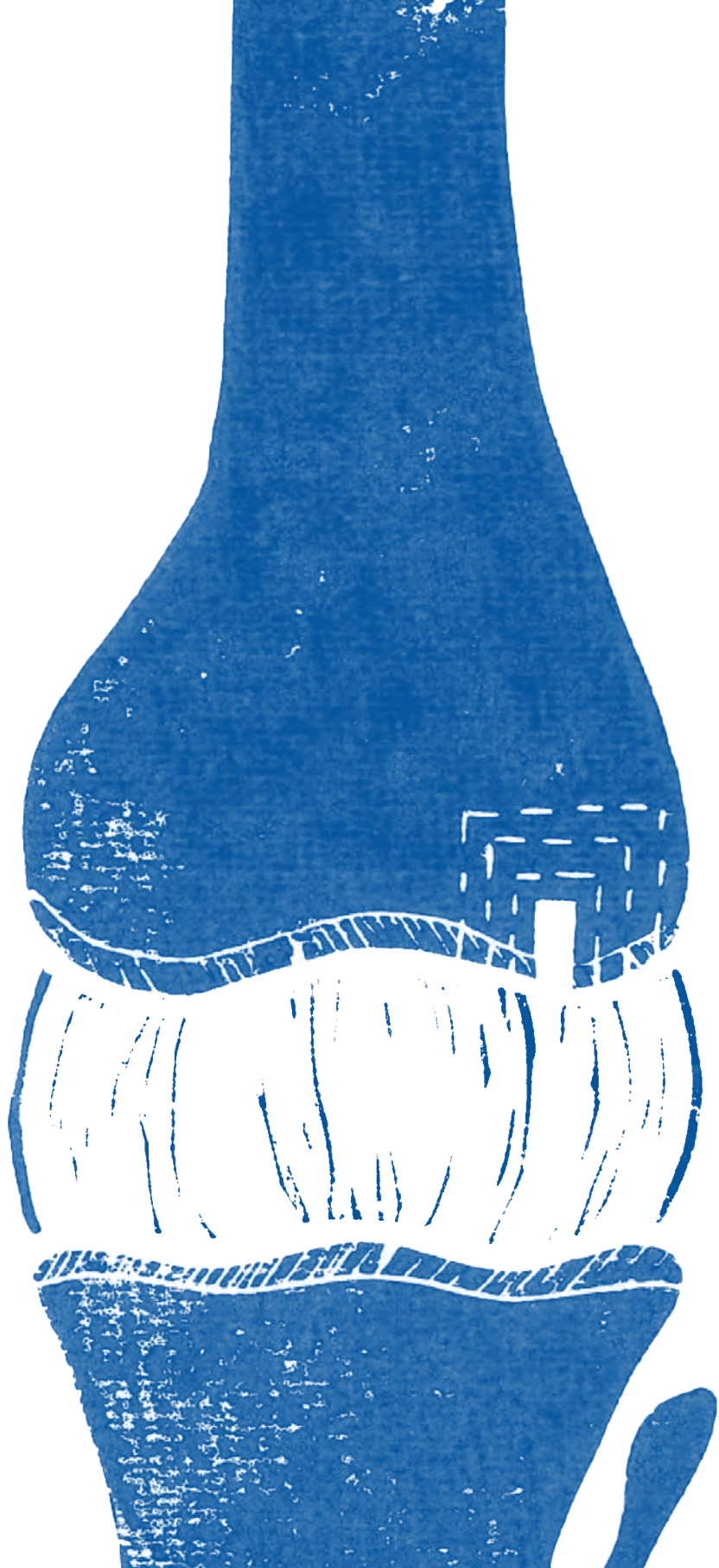
Om de hiërarchische architectuur van natuurlijk articulaire kraakbeen weefsel verder na te kunnen bootsen door middel van gelaagde depositie van cellen en kraakbeenachtige matrix componenten, is de fabricatie van micro-vezels (door middel van MEW) geïncorporeerd in het hydrogel bioprint proces in **deel II** van dit proefschrift. Eerst is het vernieuwende concept van het combineren van verschillende fabricatie technieken om tot een enkel-staps biofabricatie platform te komen belicht, waarbij tevens het toekomstperspectief van een dussdanig platform wordt aangestipt (**Hoofdstuk 4**). In **Hoofdstuk 5** is voor het eerst de combinatie van 3D bioprinten en micro-vezel depositie (door middel van MEW) in een enkel-staps platform aangetoond. Dit platform resulteerde in gelijktijdige controle over zowel de fibreuze als niet-fibreuze componenten van de kraakbeenachtige matrix. De potentie om dit enkel-staps biofabricatie platform te gebruiken voor anatomisch relevante structuren (zoals het femurcondyl) is onderzocht door accurate micro-vezel depositie te bewerkstelligen op convexe geometrieën van verschillende klinisch-relevante materialen (**Hoofdstuk 6**). In deze studie is het belang van een constant elektrisch veld sterkte alsmede de richting van de elektrische kracht ten opzichte van het oppervlak aangetoond.

Deel III van dit proefschrift beschrijft de preklinische applicatie van de ontwikkelde multi-schaal (bio)fabricatie technologieën. Eerst is aangetoond dat stimulatie van kraakbeen-progenitor cellen met de groeifactor bone morphogenic protein 9 (BMP-9) kan resulteren

in efficiënte productie van grote hoeveelheden kraakbeen-achtig weefsel (**Hoofdstuk 7**). Deze BMP-9 stimulatie heeft potentie voor het fabriceren van grotere bio-gefabriceerde implantaten. Daarna heeft lange-termijn *in vivo* evaluatie in een groot en relevant diermodel (paard) aangetoond dat pre-geconditioneerde osteochondrale pluggen met een hiërarchie in vezel-oriëntatie en cel-distributie mechanisch stabiel genoeg zijn om de mechanisch uitdagende omgeving van de knie te overleven (**Hoofdstuk 8**). Deze studie toont het belang van structurele elementen en impliceert dat deze structurele elementen mogelijk belangrijker zijn voor de regeneratie van osteochondrale defecten dan het gebruik van getransplanteerde cellen.

Het opschalen van relatief kleine osteochondrale pluggen naar grotere patiënt-specifieke implantaten demonstreert dat de grootte van het implantaat significant invloed heeft op de mechanische stijfheid van het implantaat wanneer dit onder mechanisch fysiologische condities wordt belast. Het ontwerp van het implantaat dient overwogen te worden om de mechanische functionaliteit effectief te kunnen herstellen. Daarnaast heeft deze studie een nieuwe software tool geïntroduceerd om de generatie van het micro-vezel depositie print pad aan te kunnen passen aan de patiënt-specifieke geometrieën (**Hoofdstuk 9**).

Dit proefschrift laat accurate fabricatie zien van een osteochondraal implantaat waarvan het ontwerp is geïnspireerd door de natuurlijke articulaire kraakbeen weefsel architectuur. Het potentieel van gebruik van gecombineerde biofabricatie technieken voor de fabricatie van implantaten, ten behoeven van de behandeling van gewrichts-defecten is aangetoond en bediscussieerd in **Hoofdstuk 10**.



Acknowledgements

Micro-scale, macro-scale, en multi-scale zijn termen die veelvuldig aan bod gekomen zijn in dit proefschrift. Als onderzoeker realiseer ik mij dat de kennis die verworven is tijdens de onderzoeken die beschreven staan in dit proefschrift slechts micro-scale kan zijn ten opzichte van de totale wetenschap alsmede ten opzichte van de reeds verworven kennis binnen de weefsel-wereld. Echter, ik geloof ook dat de uiteindelijke toepassing van de, in dit proefschrift, verworven kennis intens waardevol kan zijn voor diegene die baat hebben bij therapieën die mogelijk op delen van dit onderzoek gebaseerd kunnen zijn. De totale potentiële impact van dit proefschrift beschrijf ik dan ook graag als multi-scale. Echter, de steun en bijdrage van hierna beschreven personen met betrekking tot het ontstaan en volbrengen van dit proefschrift is beter te omschrijven is als yotta-scale. Jullie zijn mij dierbaar en mijn dank voor jullie steun en input is oneindig.

Promotor en co-promotor

Geachte Professor dr. ir. Malda, beste **Jos**,

Van friet op station Duisburg, naar lunch op de Chinese Muur, sushi in Kyoto, en gember in Hong Kong: wat hebben we veel meegemaakt in de afgelopen 4 jaar. Allereerst bedankt voor het vertrouwen dat jij vanaf het begin van mijn promotie (of eigenlijk daarvoor?) in mij hebt gehad. Al op dag 1 graptten wij over het aantal papers dat deel uit kon maken van dit proefschrift. Hoewel dat aantal (bijna) is gehaald, maakte dit aantal ook al vrij snel niet meer uit. Onder jouw begeleiding ontstond er een mooi proefschrift met een duidelijke lijn en interessante onderzoeken. Hierdoor kwam er al snel ruimte om meer risicovolle projecten te proberen, om side-projecten op te zetten, en samenwerkingen aan te gaan. Hoewel natuurlijk niet al deze projecten gebracht konden worden naar het niveau dat ik uiteindelijk wilde zien, ben ik evengoed enorm trots op wat we wel bereikt hebben in dit proefschrift, en op wat ik heb mogen leren in de weg hiernaartoe. Ja, echt! Dit alles was niet gelukt zonder zo een fijne promotor als jij, daarvoor dank. Jouw enthousiasme, kennis, snelheid van denken en verbanden leggen, en het vertrouwen dat jij uitstraalt, werkt onnoemelijk inspirerend. Bedankt voor de ruimte die jij geeft, de kansen die jij creëert, en de tijd die je neemt als dit nodig is, hierdoor heb ik een rijke en leuke 4 jaar mogen genieten. Bedankt voor alles dat ik van je heb mogen leren. Ik zal altijd terugkijken op een mooie promotietijd, kan vertrouwen op de basis die hier is gelegd, en hoop zeker dat we elkaar nog lang tegen zullen blijven komen in deze mooie 3D weefsel-wereld. Ik wens je al het goeds voor de toekomst, samen met Annelie en de kids. Benieuwd naar de lijnen die jij uit gaat zetten en de resultaten die uit het "Malda-Team" mogen komen. Ik kan trots eindigen met: Bedankt voor alles, ik had mij geen betere PhD-tijd voor kunnen stellen. Het ga je goed!

Dear dr. ir. Castilho, dear **Miguel**,

“Almost there”, the engineer and the hybrid. Even though I was your first PhD student to supervise, and started without a full engineering background (hybrid), I do believe we have come pretty far. I am happy with the road we’ve taken and think we both learned a lot along the way. I am very grateful for your guidance and the opportunities that you have provided during my PhD. From helping designing a new MEW device together with the MTKF to including me in the meetings with RegenHU about the Bioarchitect project, where I could learn more about valorisation and business. Your talent and expertise is widely spread and appreciated among the different departments. Yet, you always found a way to help out when needed, to call and tell me it would all work out when I was overanalysing a micro-scale detail, or to remind me about the opportunities that lie ahead in terms of projects, collaborations, and conferences. Our meetings were one of the constant highlights where we had more time to discuss current projects and future research ideas. I am utterly impressed by the amount of ideas and enthusiasm you have for science, thank you so much for sharing that. Over these years I have learned a lot from you, and can only describe you as an extremely talented and smart but also very kind and polite person that enjoys science, Portugal and surfing, yet dislikes eating cow-skin (Biofabrication 2017), and does not sleep well if the bed is right above a loud bar (Biofabrication 2019, Sorry!). Dear Miguel, thank you for everything, it was a pleasure to have you as a co-promotor, you are the best, and I am proud that we “are there”.

Review committee

Beste Prof. dr. Marianne **Verhaar**, Prof. dr. Roos **Masereeuw**, Dear Prof. dr. Lorenzo **Moroni**, Dr. David **Hoey**, Prof. dr. Liam **Grover**, thank you for your enthusiasm and taking the time to read and evaluate this thesis. I am honoured to have the opportunity to discuss the findings in my thesis with such well-appreciated scientists.

Paranimfen

Dear **Paulina**, from student to paranimph, I am super glad to have met you. Your easy-going character, combined with your Mexican passion, hardworking attitude and kind personality, makes it hard to not be friends with you. No wonder Sam felt right at home from the first minute you got him. I am super proud of how you managed and matured your initial student project and maybe even more so on how well you are doing within your PhD. You definitely bring more colour to the lab. Thank you for everything you’ve done, from 8 am meetings to proof reading the final sections of this thesis. You are the best!

Beste **Inge**, wat heb ik een geluk gehad dat jij aangenomen was op het 3D joint project. Niet alleen was het zonder jou een heel veel dunner proefschrift geworden, had ik veel langere dagen mogen draaien, en hadden we lang niet zoveel kennis kunnen verwerven uit side-projecten, ook was het een stuk minder gezellig geweest. Wat was het fijn om met jou samen te werken, lekker no-nonsense en aanpakken. Voornamelijk tijdens de converged printing studies waren wij een goed geoliede machine waarbij jij de cellen regelde en ik volledig kon focussen op de fabricatie. Onze trip naar team Dublin was ook erg leerzaam en gezellig, ik ben blij dat we dat hebben kunnen doen. Ik wens jou al het geluk in de toekomst, bedankt voor alles!

Collegas van het UMC, de UU, en daarbuiten

My PhD time would not have been the same without the colleagues that I have worked with. I really enjoyed my time at the orthopaedics department and look back at fruitful discussions, retreats, Orthoski-trips, conference visits, borrels and many more fun and valuable activities. **Anita, Imke, Maaïke, Huub, Mechteld, Nienke, Nada, Leonardo, Michiel, Bruce, Koen W, Koen D, Floris, Jelle, Justin, Sebastiaan, Rob, Willem Paul, Jasper, Kelly, Saber, Razmara, Jonneke, Isabel, Erin, Maarten, Vivian, Pedro, Alexandre, Kim van D** thanks for everything and I wish you all the best. **Harrie** Weinans, **Keita** Ito, **Jacqueline** Alblas, **Laura** Creemers, bijzonder bedankt voor alle waardevolle feedback tijdens de researchmeetings. **Roel**, bedankt voor de altijd waardevolle klinische input, alsmede voor de feedback op de introductie van dit proefschrift. **Michelle**, bedankt voor die aller- aller eerste stage, dit is het moment geweest dat ik wist dat ik het onderzoek in wilde. Ik heb enorm veel van je geleerd, bedankt voor alles. Ik wens je al het geluk samen met Kevin en de kids. **Debby**, bedankt voor het vertrouwen dat jij tijdens de master al liet zien. Altijd een voorbeeld voor de RMT studenten, veel geluk in de toekomst. **Lizette**, het is erg leuk om met jou samen te werken, bedankt voor jouw waardevolle advies. **Alessia**, impressed by your passion for research and climbing (yes, climbing), sorry for the times I scared you in the early mornings in the lab. **Iris P**, bescheiden, maar wat een mooi proefschrift heb jij afgeleverd. **Chella**, New Orleans (ORS) room-mate, bedankt voor alles. Het bedenken en opstarten van het MEWnicusproject was leuk, succes met de opleiding. **Jasmijn**, het MEWnicusproject verder uitwerken en uitvoeren was fijn om samen te doen, zeker met jouw vrolijke daadkrachtige instelling. **Lucienne**, onnoemelijk veel kennis op zoveel verschillende vlakken en daarbij zo aardig en geduldig. Bedankt voor al jouw input en advies, ik heb dit altijd als zeer waardevol ervaren. Ik wens jou en jouw gezin al het beste, en hopelijk tot ziens in Berlijn. **Joao**, most valuable player of team "We don't fall". I don't remember when we actually started climbing together, yet I would not like to miss our sessions for the world. Although the result of "you pick" is always interesting, I do enjoy how we push each other with our different climbing styles and look forward to future outdoor adventures. We have only

worked together on a few projects, yet your interest and passion for science have always been very clear, I honestly believe you will do great things in the future. Thanks for being a good friend, keep your harness tight and please don't fall (this is not sarcastic). **Mattie, Anneloes, Inge D**, without you, the lab would not be running as smoothly. Thank you for all the help and advice along the way. **Mattie**, koning van de histologie. Niet alleen het waardevolle lab-advies, maar ook de goede restaurant-tips zijn altijd erg gewaardeerd. **Anneloes**, koningin van de PCR, inspirerend om te zien hoe graag jij nieuwe dingen leert, ook erg leuk dat je nu ook ontspanning kan vinden in het klimmen. **Inge D**, zie boven. **Riccardo**, impressed but certainly not surprised that you received the ERC grant. You were always there for advice and help when needed, I have learned a lot from you, thank you. It is inspiring to see you work in the lab. Wish you all the best and please keep "making the exception the rule". **Susanna**, your chemical knowledge is beyond what I can even imagine, thanks for all the nice chats in the lab, your presence always brightens the room. **Yang**, the most kind, knowledgeable and fun flow-specialist I know. **Paweena**, bench-neighbour, 3D-joint mate, ICRS Macau room-mate. I have really enjoyed spending time with you and I will stand by my previous statement that you are one of the most brilliant people I've ever met. It was very special to be paranimph at your defense. Thanks for everything. **Irina**, thank you for all your valuable input and "gezelligheid", it was fun sharing the Biofabrication 2017 experience with you. Your baking- and art-skills are always amazing, still waiting for you to open that bakery. Wish you all the best, you will do great! **Sammy**, we met in Würzburg and I'm glad you have joined the team! Looking forward to your next discoveries (and camping adventures). **Joost, Quentin, Andrei, Madison, Martina**, thank you for being the core of the MEW lab and help in keeping things running as we want them to run. **Joost**, jouw enthousiasme is geweldig, het maakte niet uit of dat nu over machines, wetenschap, of campers ging. Bedankt ook dat je altijd bereidt was om mee te denken en in te springen wanneer de machines faalde. **Quentin**, it was a pleasure to work together on the curved-surfaces paper, thank you for your down-to-earth vibes, and dead-lift motivations. **Andrei**, from supervisor in Würzburg to colleague in Utrecht. You are such a kind and knowledgeable person that keeps inspiring me to do cool science until it is as perfect as it can get. I am really glad that you are happy in Utrecht and value your friendship a lot. **Madison**, I don't think I have ever met such an organized person as yourself. Thank you for all the joy you bring in the lab (e.g. googly eyes), your energy is contagious. **Nasim**, thank you for working together on the PCL-MgP materials, I still think it is impressive how you approached this. Looking forward to our future projects, they will be great. **Brenda**, bedankt voor het altijd oplossen van de meestal bizarre (of onhandige) uitdagingen. Niets is te gek, jij regelt het wel. Het was daarbij altijd gezellig om even bij je binnen te lopen. Veel geluk in het nieuwe huis, wordt vast prachtig! **Inge van H(eld)**, bedankt voor alles! Zo krachtig en altijd bereidt om te helpen. Ik wens jou heel veel succes en plezier in de toekomst. **Margot**, LR-buurvrouw, room-mate in Berlijn, en nu

samenwerken op RegMedXB. Het is altijd leuk om met jou samen te werken. Jouw kritische blik op de bio is altijd zeer waardevol, bedankt! **Florencia**, "How are you doing?" "You look fancy today!", it is always fun to have you around in the lab. You are such a friendly person and great teacher to everyone around you, absolutely amazing. Thank you so much for everything, also for all the work of the BMP-9 chapter, it was fun to work with you. Wish you all the best with Stijn and Thomas. **Iris**, vanaf dag 1 klikte het goed tussen ons en ontstond er een goede vriendschap. Hoewel totaal andere projecten (3D Joint, 3D Ear), hebben we toch nog samen kunnen werken op jouw printpaper, wat ben ik daar trots op! Ik vind het erg mooi om te zien hoe jij (o.a. met Gezond Kompas) anderen wilt inspireren met jouw visie om gezondheidszorg weer over gezondheid te laten gaan. Blijf doen wat goed voelt en ga waar je voor wilt gaan, als krachtig en oprecht mens red jij het écht wel! Het was een eer om paranimf te mogen zijn op jouw dag, dat blijft een extra mooie herinnering. Ook zal ik vaak met plezier terugdenken aan onze koffiemomenten op het strand, de orthoski, wijn in Würzburg, en onze ontbijtmeetings in Utrecht. Bedankt voor alle mooie en leerzame momenten. **Margo**, wat ben jij een vriendelijk, tof, en oprecht mens met vele talenten! Het is inspirerend hoe jij nieuwe dingen die totaal buiten je comfortzone liggen op pakt. Van neurowetenschappen naar 3D printen van gedecellularizeerde kraakbeen matrix. Van kitesurfen naar boulderen, topopen, voor klimmen en buiten multi-pitches. Ik hoop dat we nog vaak met tuigjes, poeder, walkietalkies ("noem je me nou dik?" "Ik wil niet stoken, maar zoiets hoorde ik ook"), en klipjes de hoogte in mogen. Bedankt voor jouw hulp tijdens de laatste loodjes en de perspectieven die jij als geen ander kan geven. Blijf je eigen pad volgen, geen berg is te hoog voor jou (🎵 English (us)).

Beste **Ferry**, bedankt voor de tweede stage en daarmee de springplank richting deze PhD positie. Jouw kennis en kijk op de wetenschap alsmede de rust die jij hierbij uitstraalt zijn altijd inspirerend geweest. Op goed advies probeer ik nog vaak "vrijdagmiddag experimenten" in te plannen. Ik leer nog altijd veel van je, zal dat altijd blijven doen, en ben blij dat we nog contact hebben. Ik wens jou heel veel geluk toe met Willeke, Amy, Zoë, Zara, en Dash, wat hebben jullie het mooi in Edinburg.

De collega's van de diergeneeskunde, gezondheidszorg paard waren gelukkig nooit ver weg. Beste **Lotte, Ineke, Maria, Nikae, Saskia, Filipe, en Harold**, het was enorm fijn om met jullie samen te werken, bedankt voor alle inzichten en kennis die jullie mij hebben gegeven. Natuurlijk ook bedankt voor al jullie hulp tijdens de *in vivo* studies, jullie expertise is enorm waardevol en zal dat ook nog heel lang zijn. Geachte Prof. van Weeren, beste **René**, bedankt voor alle hulp. Jouw zicht op het gehele plaatje, de bredere zin van wetenschap, en de grotere concepten binnen en buiten ons veld is uniek. Ik zal nooit vergeten hoe snel jij een gestructureerde discussie wist te maken van mijn "whirlpool". Ook bedankt voor de gastvrijheid tijdens de Normandië retraites, naast dat deze effectief

waren voor de groepsconnectie, en voor het besef dat onze bredere (historische) kennis aan verbetering toe was, heb ik hier hele goede herinneringen aan en was het beide keren iets om naar uit te kijken, dank je wel!

Students

Although I asked a lot of each of you, you have all done an amazing job during your internships and I hope you look back at it with as much fun as I do. Spending time with you in the lab was one of the most exciting things to do as you are all so very talented, motivated, and smart which resulted in interesting discussions, new creative experimental plans, and quite some geeky jokes. **Max**, bedankt voor het werk met zwellende hydrogelen. **Kylee**, I hope you will never lose your sense of humor, you will do absolutely great! **Christina**, thank you for your work during the EuroStars Program. **Paulina**, "It just crosslinks all the time, so annoying!". **Anastasia**, thank you for your help in the work about guiding MEW fibers over hydrogel structures. **Bastiaan**, bedankt voor jouw inzet op het MEWniscus samenwerkingsproject met Jasmijn, jij gaat sowieso mooie dingen doen! **Shaiv**, thank you for your work on the computational modelling of the shear modulus of MEW-gelMA composites and the subsequent development of a testing system. **Ioanna**, thank you for working on the final chapter of this thesis, where everything came together. Trust your talents, they will get you where you want to go! **Kim, Leah, Josse**, thank you for your trust in letting me guide you through your writing assignments, your fresh thoughts were always inspiring.

Collaborations

During these 4 years of my PhD, I had the opportunity to collaborate with a lot of extremely smart and talented scientists from all over the world. I would like to thank some of these in particular:

Team Würzburg,

Dear Prof. Groll, **Jürgen**, dear Prof. Dalton, **Paul**, thank you for the great time I've had during my research stay in Würzburg. You have introduced me to the wonders of melt electrowriting and my chemical knowledge has definitely benefitted from working in your lab as well. I will always look back at a great experience and sincerely enjoyed doing research in your lab, thank you! **Moataz, Jodie, Andrei, Tomasz, Gernot**, thank you including me in the MEW-team, without each of you, it would never have been so much fun and the project could never have been evolved into its final stage. **Tomasz**, always good to see you. I enjoyed our interesting conversations, our shared airbnb in Ohio and I'm curious about your next achievements in science and photography. Thank you. **Jodie, Daimon**, although we have met in Würzburg, I'm extremely happy that we still see each

other in Mannheim and Utrecht, spending time with you two is always a good idea. Thank you for being our friends.

Team Dublin,

Dear Prof. Kelly, **Daniel**, dear Prof. Brama, **Pieter**, dear **Ross, Pierluca, Fiona, Rosanna, Dave, Ines, Xavi**, thank you for the interesting overarching discussions during our visits to Dublin and your visit to Utrecht. Your enthusiasm is noticeable and it was always good to discuss the challenges that we all face. I have learned a lot from each of you, and had great fun getting to know you. Thank you!

Team Boston,

Dear Prof. Zhang, **Yu Shrike, Sushila** Maharjan, **Li** Lv, thank you for showing me around in the Boston lab and teaching me the tips and tricks of coaxial printing.

Team QUT,

Dear Prof. Pivonka, **Peter**, dear **Paige** Little, and **Roderick** Verberne, thank you for the collaboration and work on the *ex vivo* model of Chapter 9.

Team RegenHU,

Dear **Dominic, Denis, Mauro**, thank you for the interesting discussions in the Bioarchitect project meetings. I have learned a lot from your side and it was a pleasure to work with you. Thank you!

Vrienden

Kim A, Lisa, Nicole, Britt, Annelot, Saskia, Fleur en **Yvette**, wat fijn dat onze middelbare school groep nog altijd bij elkaar is. Ontspanning is belangrijk en jullie zijn er altijd om mij daaraan te helpen herinneren. Van dansen (?) met uitsmijters op de Heemskerke feestweek en kampioen worden op badminton invitatietoernooien, tot wijn in Würzburg, Lundt, de katjeskelder, of Manchester, gezellig is het altijd. **Remco, Bart, Jasper, Renee, Tom, Simon, Alex**, en de kids **Luuk** en **Jonna**, jullie maken deze groep nog meer compleet! Bedankt voor al jullie steun en vriendschap, zonder jullie was het niet op deze manier gelukt.

Kim V en **Frank**, ook jullie maken alles een stuk leuker en gezelliger. Of we nou handballen (oké, vroeger dan), koffie drinken, hardlopen, of lekker aan het strand eten, het is altijd goed! Lieve Kim, bedankt dat je er bent, onze vriendschap betekent veel en ik kijk uit naar onze IJsland trip. Ik wens jullie samen veel geluk in jullie nieuwe paleis (ballonnen voor de housewarming zijn besteld).

Familie

Al een geruime tijd kan ik mij gelukkig prijzen dat ik mij bij twee families thuis mag voelen, niet enkel in mijn gezin van herkomst, *de Ruijter*, maar ook bij de *van Duijn*-en (Rik).

van Duijn

Lieve **Pieter, Wilma, Renee, Martin, Jaxx** en **Maci**, bedankt dat het altijd zo gezellig is als we samen zijn. De diners, lunches, gebak-en/of-pepernoot-momenten zijn altijd iets om naar uit te kijken vanwege de leuke en interessante gesprekken (en natuurlijk ook het lekkere eten). Ik hoop dat we snel weer eens met zijn allen op vakantie kunnen. En Jaxx, ik denk dat jij wel een PhD in dino's (Paleontologie) kan halen als je later groot bent.

de Ruijter

Een van de meest memorabele reizen die ik tijdens mijn PhD gemaakt heb is samen met jullie, langs de kust van Noorwegen. Bedankt voor deze mooie momenten, ik denk er nog vaak aan terug.

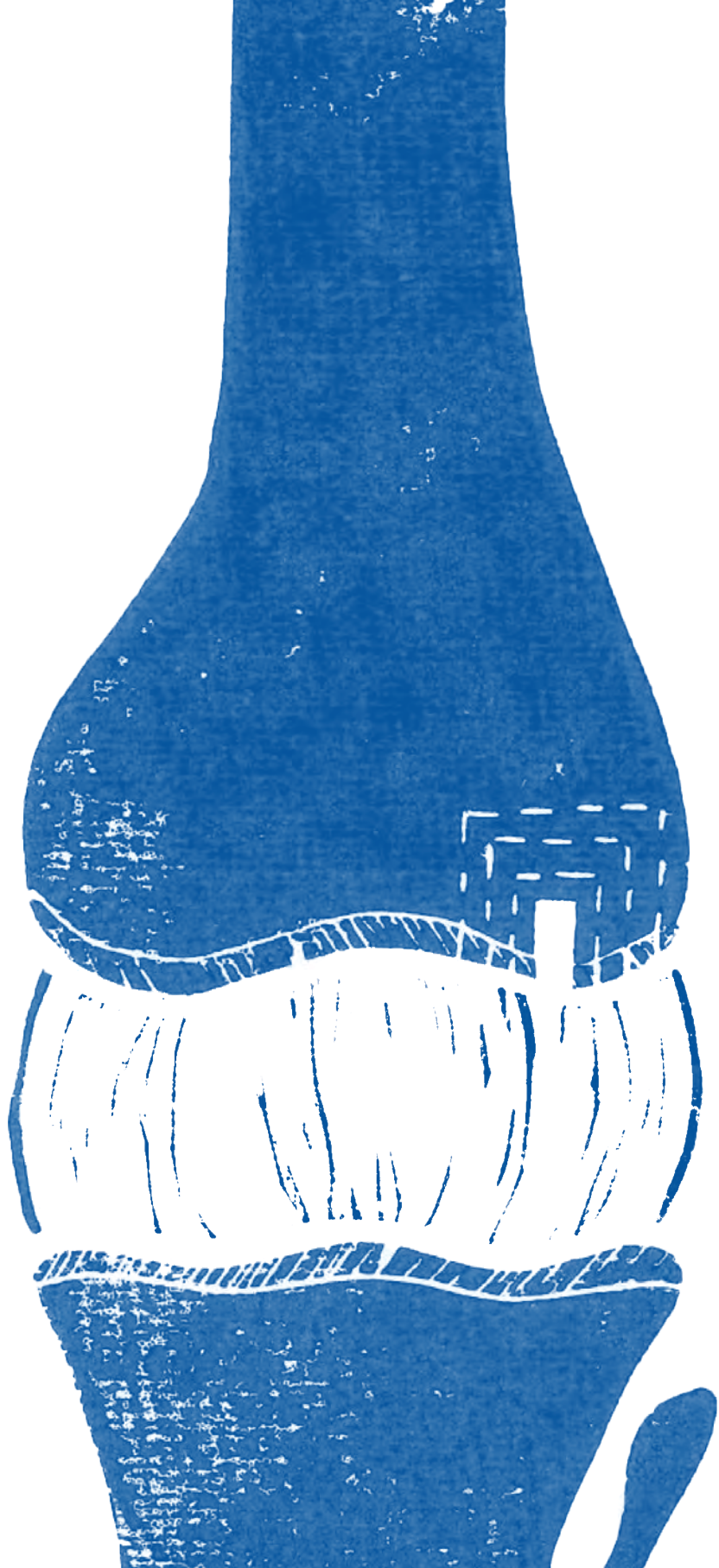
Lieve **Bas, Jill** en **Floris**, het is altijd leuk om even langs te lopen en te kletsen tijdens een kopje koffie. **Bas**, ik ben trots dat jij mijn broer bent, en had met geen ander willen opgroeien. Ik vind het erg fijn om te zien hoe leuk jullie het met zijn 3-en (bijna 4-en) voor elkaar hebben. **Jill**, jouw enthousiasme en vrolijkheid straalt zeker door naar het hele gezin! **Floris**, wat ben jij een geweldig vrolijk mannetje en wat tref jij het met zulke lieve zorgzame ouders, ik weet zeker dat jij nog vele avonturen met ze gaat beleven.

lieve **Pap** en **Mam**, alles begint bij de basis en ik ben dan ook erg dankbaar voor jullie jarenlange support. Dankzij jullie heb ik altijd het idee gehad dat ik alles kon leren, doen, en worden wat ik wilde, zolang ik maar mijn best deed. De insteek dat de wereld wat dat betreft onbegrensd was heeft zeker geholpen in het behalen van mijn PhD. Het oppakken van interdisciplinaire en uitdagende projecten was leuk, omdat ik van huis uit heb meegekregen dat niets onmogelijk is. **Pap**, jij kan werkelijk alles maken en het mee mogen helpen met jouw klussen heeft ongetwijfeld gezorgd voor het ontwikkelen van mijn praktische skills en inzicht en ik kijk daar met enorm veel plezier op terug. **Mam**, het plannen en doorzetten maar tegelijkertijd flexibel opstellen is onmisbaar in het behalen van een PhD en ik durf te stellen dat ik deze eigenschap van jou heb verkregen. Daarnaast

heb ik heb veel plezier beleefd aan onze gezamenlijke trips (o.a. Kopenhagen, Stockholm) en kijk ik uit naar de volgende. Pap en Mam, bedankt voor alles.

De allerbeste

Lieve **Rik**, jouw onvoorwaardelijke steun tijdens mijn PhD is in geen enkele scale te beschrijven. Bedankt voor hoe jij met mij deze weg belopen hebt en voor al het geduld dat hiervoor nodig was. Van in het weekend “pim-pam-pipetteren” tot het nalezen van stukken of feedback geven op presentaties. Eigenlijk ben jij inmiddels ook expert op 3D printen van kraakbeen. Ik ben elke dag weer ongelooflijk trots op wie jij bent, wat jij doet, en hoe wij samen zijn. Wat ben ik blij dat jij de stap gezet hebt om te beginnen met RWX en Zolder.io, kiest voor wat je leuk vindt en vertrouwt op wat je kan. Rik, met jou is alles leuker en ik kijk enorm uit naar onze volgende avonturen. Altijd samen, ik hou van jou.



Publications

A

This thesis is based upon the following publications:

Out-of-plane 3D-Printed Microfibres Improve the Shear Properties of Hydrogel Composites.

Mylène de Ruijter, Andrei Hrynevich, Jodie N. Haigh, Gernot Hochleitner, Miguel Castilho, Jürgen Groll, Jos Malda, Paul D. Dalton

Small. 2018 Feb;14(8). DOI: 10.1002/smll.201702773. Epub 2017 Dec 14.

Combining multi-scale 3D printing technologies to engineer reinforced hydrogel-ceramic interfaces.

Paweena Diloksumpan, Mylène de Ruijter, Miguel Castilho, Uwe Gbureck, Tina Vermonden, P. René van Weeren, Jos Malda, Riccardo Levato

Biofabrication. 2020 Feb 19;12(2):025014. DOI: 10.1088/1758-5090/ab69d9.

Multi-technology biofabrication: a new standard for manufacturing of functional tissues.

Miguel Castilho, Mylène de Ruijter, Stephen Beirne, Claire C. Villette, Keita Ito, Gordon G. Wallace, Jos Malda

Trends in Biotechnology. 2020 May 25;S0167-7799(20)30119-0. DOI: 10.1016/j.tibtech.2020.04.014

Simultaneous Micro-Patterning of Fibrous Meshes and Bioinks for the Fabrication of Living Tissue Constructs.

Mylène de Ruijter, Alexandre Ribeiro, Inge Dokter, Miguel Castilho, Jos Malda

Advanced Healthcare Materials. 2019 Apr;8(7):e1800418. DOI: 10.1002/adhm.201800418
Epub 2018 Jun 17.

Front cover 2019, special issue: Building Blocks for Biofabricated Models

Melt electrowriting onto anatomically relevant substrates: Resurfacing a diarthrodial joint.

Mylène de Ruijter*, Quentin C. Peiffer*, Joost van Duijn, Denis Crottet, Dominic, Ernst, Jos Malda, Miguel Castilho

Materials & Design. 2020 Oct; 195, 109025 DOI:10.1016/j.matdes.2020.109025

* = Authors contributed equally

Bone morphogenic protein 9 stimulates efficient cartilage-like matrix production by articular cartilage-resident chondroprogenitor cells onto 3D melt electrowritten scaffolds.

Florencia Abinzano, [Mylène de Ruijter](#), Anneloes Mensinga, Miguel Castilho, I. M. Khan, P. René van Weeren, Riccardo Levato, Jos Malda

Manuscript in preparation

Pivotal importance of reinforcement of cartilage implants confirmed in challenging large animal model; presence of transplanted cells probably secondary.

[Mylène de Ruijter](#), Paweena Diloksumpan, Inge Dokter, Harold Brommer, Ineke H. Smit, Riccardo Levato, P. René van Weeren, Miguel Castilho, Jos Malda

Submitted

Scaling up from osteochondral plug to patient-specific condyle resurfacing: fabrication, *in vitro* characterization, and mechanical characterization under physiological conditions of clinically relevant osteochondral implants.

[Mylène de Ruijter](#), Nasim Golafshan, Inge Dokter, Ioanna Gkoni, Roderick Verberne, Joao Garcia, Laura Creemers, P. René van Weeren, Pieter. A.J. Brama, Daniel J Kelly, Keita Ito, Paige Little, Peter Pivonka, Jos Malda, Miguel Castilho

Manuscript in preparation

Papers not included in this thesis

Biocompatible hydrogel-based inks for cell electrowriting of well-organized, micrometer size three-dimensional living structures.

Miguel Castilho*, Riccardo Levato*, Paulina Nunez Bernal, [Mylène de Ruijter](#), Christina Y. Sheng, Joost van Duijn, Susanna Piluso, Keita Ito, Jos Malda.

Submitted

* = Authors contributed equally

The Complexity of Joint Regeneration: How an Advanced Implant could Fail by Its *In Vivo* Proven Bone Component.

Paweena Diloksumpan, Florencia Abinzano, [Mylène de Ruijter](#), Anneloes Mensinga, Saskia Plomp, Ilyas Khan, Harold Brommer, Ineke Smit, Miguel Castilho, P. René van Weeren, Jos Malda, and Riccardo Levato.

Submitted

Hydrogel-based reinforcement of 3D bioprinted constructs.

Ferry P.W. Melchels*, Maarten M. Blokzijl*, Riccardo Levato, Quentin C. Peiffer, [Mylène de Ruijter](#), Wim E. Hennink, Tina Vermonden, Jos Malda

Biofabrication. 2016 Jul 19;8(3):035004. DOI: 10.1088/1758-5090/8/3/035004

* = Authors contributed equally

Biofabrication of a shape-stable auricular structure for the reconstruction of ear deformities.

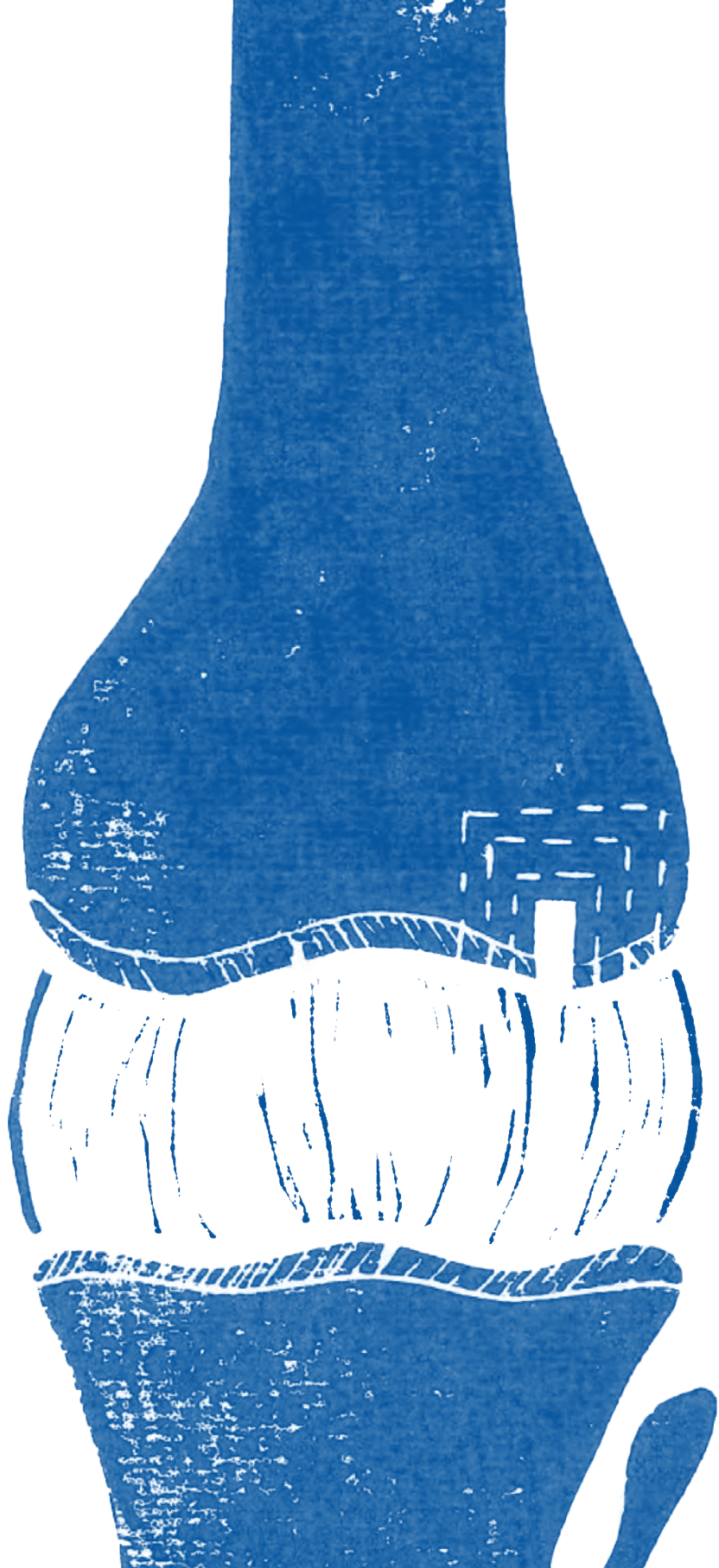
Iris Otto, Pamela Capendale, João Garcia, [Mylène de Ruijter](#), Rob van Doremalen, Miguel Castilho, Taylor Lawson, Mark Grinstaff, Corstiaan Breugem, Moshe Kon, Riccardo Levato, Jos Malda.

Submitted

3D bioprinting of methacrylated hyaluronic acid (MeHA) hydrogel with intrinsic osteogenicity.

Michelle T. Poldervaart, Birgit Goversen, [Mylène de Ruijter](#), Anna Abbadessa, Ferry P. W. Melchels, F. Cumhur Öner, Wouter J. A. Dhert, Tina Vermonden, Jacqueline Alblas

PLoS One. 2017 Jun 6;12(6):e0177628. DOI: 10.1371/journal.pone.0177628



Curriculum Vitae



A

Mylène de Ruijter was born in Heemskerk, The Netherlands, on the 16th of August 1989. After graduating high school (Beverwijk), she obtained a bachelor in Biomedical Sciences at the VU University, Amsterdam, with a minor in Biomedical Engineering at the TU Delft, Delft. During this time, she performed research on acetabular reaming and did an internship on 3D bioprinting for bone regeneration. She pursued research-oriented education further with the research master Regenerative Medicine and Technology (University of Utrecht, TU Eindhoven) where her internships were focused on 3D bioprinting of aggregates for cartilage



tissue engineering (Utrecht), as well as on improving the shear properties of cell-laden cartilage constructs by creating out-of-plane fibers with melt electrowriting (Würzburg, supervision by Prof. Dr. Paul D. Dalton). During these internships, she presented her results at various international conferences and got awarded a merit-award at the World Biomaterials Congress in 2016 (Montreal, Canada). Her PhD work started in the summer of 2016, was performed at the department of Orthopaedics (UMC Utrecht) and was part of a larger project called 3D-joint, funded by the European Research Council. During this project Mylène was supervised by Dr. ir. Miguel Castilho and Prof. Dr. ir. Jos Malda. Her research focused on the fabrication of mechanically stable implants for cartilage and osteochondral defects by converging different biofabrication technologies. The results of her PhD research are described and discussed in this thesis. She presented her PhD research at multiple (inter)national conferences where she met many researchers from the field, was awarded travel grants (Berlin, Germany 2018, Hernstein, Austria 2017) and was nominated for the Prof. dr. ir. Rik Huiskesprijs (2020). Furthermore, she was awarded a Hofvijverkring fellowship (2019) which allowed her to visit and collaborate with the lab of Prof. Dr. Daniel J. Kelly (Trinity College, Dublin) and Dr. Yu Shrike Zhang (Harvard Medical School, and Brigham and Women's hospital, Boston). Next to her research activities, Mylène was actively involved in education and outreach activities by supervising master and bachelor students, giving lectures at university-courses and summer schools, co-moderating an e-course on Biofabrication, helping with the annual U-talent program for high-school students and by presenting her and her group's research to the general public at national science days. Mylène is currently working within the RegMedXB consortium at the department of Orthopaedics (UMC Utrecht).

